

Department of

Earth and Environmental Sciences

PhD program Chemical, Geological and Environmental Sciences Cycle XXXIII

Curriculum in Geological Sciences

THE ANOMALY OF RIFT-PARALLEL TRANSCURRENT FAULTS

Surname Russo Name Elena

Registration number 709319

Tutor: prof. ZANCHI Andrea

Supervisor: prof. TIBALDI Alessandro

Co-Supervisor: dr. BONALI Fabio Luca

Co-Supervisor: dr. WAITE Gregory P.

Coordinator: prof.ssa FREZZOTTI Maria Luce

ACADEMIC YEAR 2020/2021

Acknowledgments

I would like to express my sincere gratitude to my supervisor prof. Alessandro Tibaldi for the support and encouragement and stimulating questions that he has given to me throughout my PhD: his guidance helped me in all the time of research and writing of this thesis. Also, I would like to say a special thank you to my co-supervisor, dr. Fabio Luca Bonali. His support, guidance and overall insights have made this PhD an inspiring experience for me. The meetings and conversations with prof. Tibaldi and dr. Bonali were vital in inspiring me to think outside the box, from multiple perspectives to form a comprehensive and objective critique.

I would like to acknowledge my co-supervisor dr. Greg Waite from the Michigan Technological University, and also dr. Jamie Farrell and dr. Fred Massin, for all the work done together, in particular for their continuous support and helpful discussion.

During the second year of my PhD, I have enjoyed a month-long stay at the Research Institute of Earthquake and Volcano Geology (Geological Survey of Japan, AIST, Tsukuba), and I would like to thank all the people I had the pleasure to meet and to work with during such amazing experience. Special thanks go to dr. Nobuo Geshi and dr. Tadashi Yamasaki, who supported me and gave me the chance to learn new advanced approaches and techniques that I can apply in the future in my research career.

I would like to acknowledge the reviewers of the present PhD thesis, dr. Rita De Nardis and dr. Joël Ruch: the possibility of viewing my thesis from their perspective helped me to improve it in the best way possible thanks to their scientific expertise.

I would also like to express my gratitude to dr. Fabio Marchese and dr. Luca Fallati, for their meaningful collaboration in the field in Iceland and for the pleasant times spent together. I would like to thank my parents, my boyfriend and my friends for supporting me. I feel a very profound gratitude for their continuous encouragement throughout the process of researching and writing of this thesis. Thank you.

Abstract

Fractures with transcurrent and oblique components of motion, parallel and coeval to rift zones, which developed at the surface and in the upper ten kilometers of the crust, have been recently documented in extensional volcano-tectonic contexts through earthquake focal mechanisms and Holocene field data. Their origin and development is still undefined, due to the fact that transcurrent motions both along normal faults and extensional fractures are incompatible with the stress field associated with rift zones and, furthermore, transcurrent movements along planes parallel to normal faults are not compatible with the extension required to form a rift. This anomaly is an issue of international interest for the scientific community: in fact, interpreting correctly geophysical data associated with magma upwelling, which also influences the genesis of faults and extension fractures at the surface, is a key point when monitoring active volcanic zones.

The present research focuses on the Yellowstone volcanic plateau, in the western United States, and the Theistareykir and Krafla Fissure Swarms, the westernmost rifts of the Northern Volcanic Zone, in northeast Iceland. Main aim is to define the partition of fault motions at planes with different kinematics, to study the temporal relations between transcurrent/transensional faults and normal faults, to evaluate the relations between transcurrent/transensional faults and magmatic intrusions and to analyze the variations of fault kinematics with depth.

A multidisciplinary approach has been adopted, that consists in the integration of new geological-structural field data acquired through classical methods, quantitative data collected on Orthomosaics and on Digital Surface Models (DSMs) elaborated through Structure from Motion photogrammetry techniques (SfM) applied to Unmanned Aerial Vehicles (UAVs) surveys, seismic data regarding both earthquakes of magmatic and tectonic origin and numerical models on sill and dyke-induced deformations.

The complex geometry and distribution of rift-parallel transcurrent faults is interpreted both considering the possible control of regional tectonics on the orientation of faults and the relation with seismic swarms, magmatic emplacement, that could cause the enlargement of pre-existing fractures or the development of new fractures and small faults, and surficial deformation phases. The predominance of strike-slip motions revealed by focal mechanism solutions during the 2010 Madison Plateau seismic swarm at Yellowstone lead to the development of a geomechanical model that explains the origin of left- or right-lateral kinematics as related to an horizontally-propagating dyke. Such fractures can be located in correspondence of the advancing fluid tip or at the sides of

the advancing magmatic body, as confirmed by both field data collected through classical methods and UAV surveys conducted in Iceland and by the numerical models developed to investigate horizontal dyke propagation.

List of Contents

	<i>Page</i>
Chapter 1: Introduction	10
1.1 <i>Aims and objectives</i>	
1.2 <i>Methodology</i>	
1.3 <i>Thesis structure</i>	
Chapter 2: Geological setting	15
2.1 <i>Yellowstone Volcanic Plateau</i>	
2.2 <i>Iceland: the Northern Volcanic Zone</i>	
Chapter 3: Methodology – Northern Volcanic Zone	32
3.1 <i>Field mapping</i>	
3.2 <i>Structure from Motion (SfM) techniques applied to UAV surveys</i>	
3.2.1 <i>Why UAVs and which kind is suitable for this research?</i>	
3.2.2 <i>Orthomosaics and DSMs reconstruction</i>	
3.2.3 <i>UAV surveys: testing flight heights</i>	
3.3 <i>Numerical modeling</i>	
Chapter 4: Results – Northern Volcanic Zone	54
4.1 <i>Northern Volcanic Zone: Theistareykir Fissure Swarm</i>	
4.1.1 <i>Entire Theistareykir Fissure Swarm</i>	
4.1.1.1 <i>Geometry of faults and extension fractures</i>	
4.1.1.2 <i>Opening directions</i>	
4.1.1.3 <i>Strike-slip components</i>	
4.1.1.4 <i>Extensional strain</i>	
4.1.2 <i>Theistareykir Fissure Swarm: focus on the central part of the rift</i>	

4.1.2.1 Key areas selection

4.1.2.2 Data collection

4.2 Northern Volcanic Zone: Krafla Fissure Swarm

4.2.1 Western part of the Krafla Fissure Swarm

4.2.1.1 High resolution outputs from photogrammetry processing

4.2.1.2 New geological-structural data

4.2.2 Focus on the Hituholar graben

4.2.2.1 General geometry of the studied structure

4.2.2.2 Secondary structures

4.3 Numerical modeling: dyke-induced stress change on transcurrent faults

Chapter 5: Discussion – Northern Volcanic Zone

97

5.1 Theistareykir Fissure Swarm

5.2 Krafla Fissure Swarm

Chapter 6: Methodology – Yellowstone volcanic plateau

107

6.1 Yellowstone volcanic plateau: seismic data and processing

6.2 Seismic data elaboration: hypocenters relocation and earthquakes selection

6.3 Focal mechanism solutions

6.4 Calculation of the state of stress from FMS

6.5 Seismic catalogue declustering and swarm identification

6.6 Numerical modeling

Chapter 7: Results – Yellowstone volcanic plateau

115

7.1 Faulting system

7.2 Earthquake relocations

7.3 Analysis of relocated seismicity

7.4 Quality selection

7.5 Focal mechanisms and kinematics

7.6 Calculation of the stress field and relation with surficial deformation

7.7 Numerical modeling

Chapter 8: Discussion – Yellowstone volcanic plateau 134

8.1 Seismic swarms and relation with strike-slip faulting mechanisms

8.2 Association between strike-slip faulting and deformation: a comparison with previous data

Chapter 9: Discussion - The origin of rift-parallel transcurrent faults in extensional volcano-tectonic settings 139

Chapter 10: Conclusions 147

Appendix 1: Extensional fractures at Theistareykir Fissure Swarm 149

Appendix 2: Extensional fractures at Krafla Fissure Swarm 185

Appendix 3: Examples of relocated earthquakes of the Yellowstone volcanic plateau 199

Appendix 4: Focal mechanism solutions of the Yellowstone volcanic plateau 221

Bibliography 227

Chapter 1

Introduction

1.1 Aims and objectives

Diffuse strike-slip motions in extensional settings, parallel and coeval to rift zones, have been documented over the past few decades along volcanotectonic zones through earthquake focal mechanisms and Holocene field data, such as across Iceland (e.g. [Khodayar and Einarsson, 2002](#); [Nanfito, 2011](#); [Proett, 2015](#); [Runnals, 2015](#); [Karson et al., 2015, 2018](#); [Karson, 2017](#); [Horst et al., 2018](#)), specifically at Bárðarbunga volcano ([Ágústsdóttir et al., 2016](#); [Hjartardóttir et al., 2016a](#); [Ruch et al., 2016](#)) and Theistareykir Fissure Swarm ([Tibaldi et al., 2016a,b](#); [Bonali et al., 2019a,b](#)), and in the United States, at Yellowstone ([Christiansen, 2001](#); [Waite and Smith, 2002, 2004](#); [Russo et al., 2017, 2020](#)) and Long Valley calderas ([Savage and Cockerham, 1984](#); [Shelly et al., 2013, 2016](#)).

Such rift-parallel faults with strike-slip components are not compatible with the extension required to form a rift ([Figure 1](#)). This anomaly is not only an issue of international interest for the scientific community, but it is also crucial for evaluating seismic and volcanic hazards. In fact, interpreting correctly geophysical data associated with magma upwelling, which also influences the genesis of faults and extension fractures at the surface, is a key point when monitoring active volcanic zones. Therefore, understanding the kinematics and origin of structures along volcanotectonic rifts is of paramount importance for both volcanic and seismic hazard assessments.

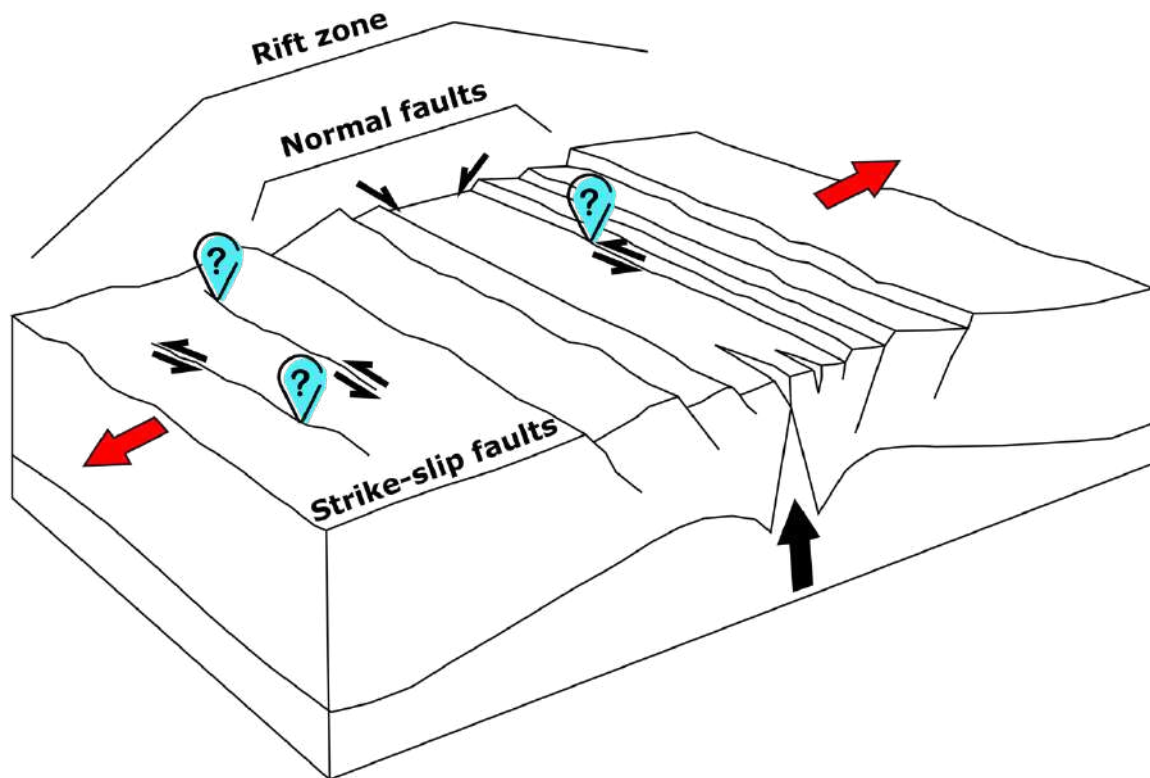


Figure 1 Sketch showing anomalous rift-parallel faults with strike-slip components (indicated through light blue question marks) which have been documented by past researches through Holocene field data and earthquake focal mechanisms and are not compatible with the extension required to form a rift (shown by red arrows).

My research project is focused on better understanding the characteristics and origin of strike-slip deformations that develop at the surface and in the upper ten kilometers of the crust in two specific extensional volcano-tectonic contexts: the Yellowstone volcanic plateau in western United States and the Northern Volcanic Zone in northeast Iceland, specifically focusing on the Theistareykir and Krafla Fissure Swarms. These areas share an extensional tectonic regime active at least since Pliocene times, complex volcano-tectonic structures, and multiple episodes of magma intrusions. According to previous studies (e.g. [Ruch et al., 2016](#); [Shelly et al., 2016](#); [Russo et al., 2017, 2020](#)), strike-slip motions in such contexts are linked to magmatic intrusions or movement of pressurized fluids, although it is also possible that transcurrent faulting might occur along structures oblique to the rift trend in consequence of regional tectonic stresses.

More in detail, at Yellowstone, numerous magmatic intrusions have been detected in form of sills and they have been related to episodes of deformations evidenced by GPS data, consisting in surface uplifting or downwarping ([Chang et al., 2007](#); [Puskas et al., 2007](#)). According to these works, the contraction or dilatation of magmatic bodies is at the origin of periods of subsidence or uplift in

the area, respectively. Recent researches have also enlightened the relations between surficial deformations, movement of magmatic fluids at depth and seismic activity (Waite and Smith, 2002, 2004; Shelly et al., 2013; Russo et al., 2017). In fact, the latter authors, through the analysis of seismic data from 1988 to 2010, found that strike-slip faults are confined to peripheral zones respect to the position of sills at depth and are due to local variations in the stress field for the propagation of magma, in contrast with classical models, which describe extensional movements in correspondence of the terminations of a horizontal intrusive body (Malthe-Sørenssen et al., 2004; Kavanagh et al., 2006).

In Iceland, rift-parallel structures with variable amounts of strike-slip component have been detected by previous studies and their nature is still undefined. The current hypothesis states that they are due to the northward and southward propagation of the rift, thus resulting in rotation of crustal blocks and in zones of localized deformation (Einarsson and Ericksson, 1982; Einarsson, 1991). Nevertheless, scientific debate is still going on. In fact, recent studies (e.g. Karson et al., 2015; Horst et al., 2018) showed that the northward propagation of the Northern Volcanic Zone results in a clockwise rotation of the crust west to the rift zone, thus explaining the presence of mainly sinistral transcurrent faults with a N-S direction. On the other hand, on the east side of the rift zone, the anticlockwise rotation of the crust should generate mainly right-lateral transcurrent faults. Thus, the rotation of blocks should be due to the increasing amount of opening by reaching greater distances from the tip of the rift south. But the presence also of dextral transcurrent faults on the western side and of sinistral components on the eastern side of the rift shows that the development of these structures is even more complicated.

In detail, the aim of the present PhD research is to: *i)* define the partition of fault motions at planes with different kinematics in rift zones; *ii)* study the temporal relations between faults with transcurrent/transensional components and normal faults associated with extensional tectonic regimes; *iii)* evaluate the relations between transcurrent/transensional faults and magmatic intrusions; and *iv)* analyze the variations of fault kinematics with depth.

1.2 Methodology

These goals have been reached through a multidisciplinary approach, that consists in the integration of: *i)* new geological-structural field data acquired through classical methods; *ii)* quantitative data collected on Orthomosaics and on Digital Surface Models (DSM) elaborated through Structure from Motion techniques (SfM) applied to Unmanned Aerial Vehicles (UAVs) surveys; *iii)* seismological

data regarding both earthquakes of magmatic and tectonic origin; and *iv*) numerical models on sill and dyke-induced deformations. These methodologies enlighten different perspectives on the scientific issue investigated in this research: in fact, seismic data elaboration allows to evaluate the location, geometry and kinematics of rift-parallel structures both at the near surface and within the upper crust, whereas field measurements and drone surveys allow to reconstruct the same characteristics at the surface, and thus to evaluate vertical variations.

Regarding my contribution in performing each methodology: the collection, elaboration and analysis of field data through classical methods and drone surveys was the result of a teamwork by me, prof. Alessandro Tibaldi, dr. Fabio Luca Bonali, dr. Luca Fallati and dr. Fabio Marchese, BSc and MSc students. Furthermore, I performed the elaboration of seismological data, with a support by dr. Greg Waite for hypocenter relocations and focal mechanisms calculation. Numerical models were developed by me.

The main outcome of the present research is a three-dimensional scenario (four-dimensional, when taking into account temporal variations of development of rift-parallel structures) that describes how structures develop transcurrent component of motions at the surface and in depth in extensional settings, thus contributing to a better assessment of volcanic hazard in both study areas. In fact, it is well known that magma movement at depth generates surficial deformations (and structures with strike-slip components are part of those), and by interpreting correctly these structures, new knowledges on geophysical data indicating the upwelling of magma can improve the understanding on how/where new eruptions might occur.

Note: The methodologies described above could not have been fully applied in both study areas: in fact, due to the COVID19 pandemic situation, the seismic analysis of Icelandic earthquakes (consisting in seismic data relocation and eventual focal mechanism solutions computation) at the Icelandic Meteorological Office, that had been planned in June-July 2020, could not have been performed. For the same reason, it was not possible to perform data collection in the field at Yellowstone.

1.3 Thesis structure

After an in-depth description of the geological settings of both areas ([Chapter 2](#)), this PhD thesis will be divided in two parts, one describing the methodology, results and discussion related to the Northern Volcanic Zone, based on extensive fieldwork through classical methods and UAV surveys

([Chapters 3, 4 and 5](#)), and the other describing the methodology, results and discussion related to the Yellowstone volcanic plateau, based on the analysis of seismic data ([Chapters 6, 7 and 8](#)). After that, an integrated discussion considering both study areas will follow ([Chapter 9](#)).

Chapter 2

Geological setting

2.1 Yellowstone Volcanic Plateau

The Yellowstone volcanic plateau is a long-lived, voluminous volcanic system located in the northeastern part of the tectonically active Basin and Range Province, 1600 km east of the western North American plate boundary (inset in [Fig. 2A](#)). It lies at the northeastern end of the age-transgressive 700-km-long Yellowstone-Snake River Plain (YSRP), a silicic volcanic province that originated ~ 17 Ma ago and influenced the composition and strength of the overriding North America plate ([Fig. 2B](#); [Morgan, 1971, 1972](#); [Matthews and Anderson, 1973](#); [Smith and Sbar, 1974](#); [Armstrong et al., 1975](#); [Smith, 1977](#); [Bonnichsen, 1982](#); [Leeman, 1982](#); [Morgan et al., 1984](#); [Pierce and Morgan, 1990, 1992](#); [Kuntz, 1992](#); [Smith and Braile, 1994](#); [Morgan et al., 1995](#); [DeNosaquo et al., 2009](#)). The geological setting of the YSRP is affected both by magmatic processes and by the regional NW-SE tectonic extension of the 30 Ma 800-km-wide Basin and Range Province, which is outlined by mountain ranges and parallel valleys delimited by normal faults ([Smith and Sbar, 1974](#); [Smith, 1977](#)).

The presence of a deep-seated mantle plume provides the source of heat of Yellowstone, which is defined as an intraplate hotspot, and is at the origin of a high total heat flux up to 1800 mW/m², which corresponds to more than 30-40 times the continental average heat flow ([Fournier et al., 1976, 1989](#); [Blackwell and Richards, 2004](#)). Among the main characteristics of hotspots, the formation of linear and time-transgressive volcanic chains accompanied by topographic swells resulting from hot buoyant material at the base of the plate has been fully recognized in several past researches ([Morgan, 1972](#); [Crough, 1978, 1983](#); [Davies, 1988](#); [Sleep, 1990, 1992](#); [Burov and Guillou-Frottier, 2005](#); [Burov et al., 2007](#); [Ito and van Keken, 2007](#)). According to calculations of intraplate vector motions (e.g. [Smith and Sbar, 1974](#)), the plate motion at Yellowstone is characterized by a ~257° azimuth and an apparent rate of 2.8 cm/yr, using a pole of rotation for the North American plate from [Atwater \(1970\)](#) ([Fig. 2B](#)). In fact, as can be noticed in [Fig. 2B](#), a decrease in age of the YSRP volcanic centres moving towards the northeast has been observed ([Smith and Sbar, 1974](#)).

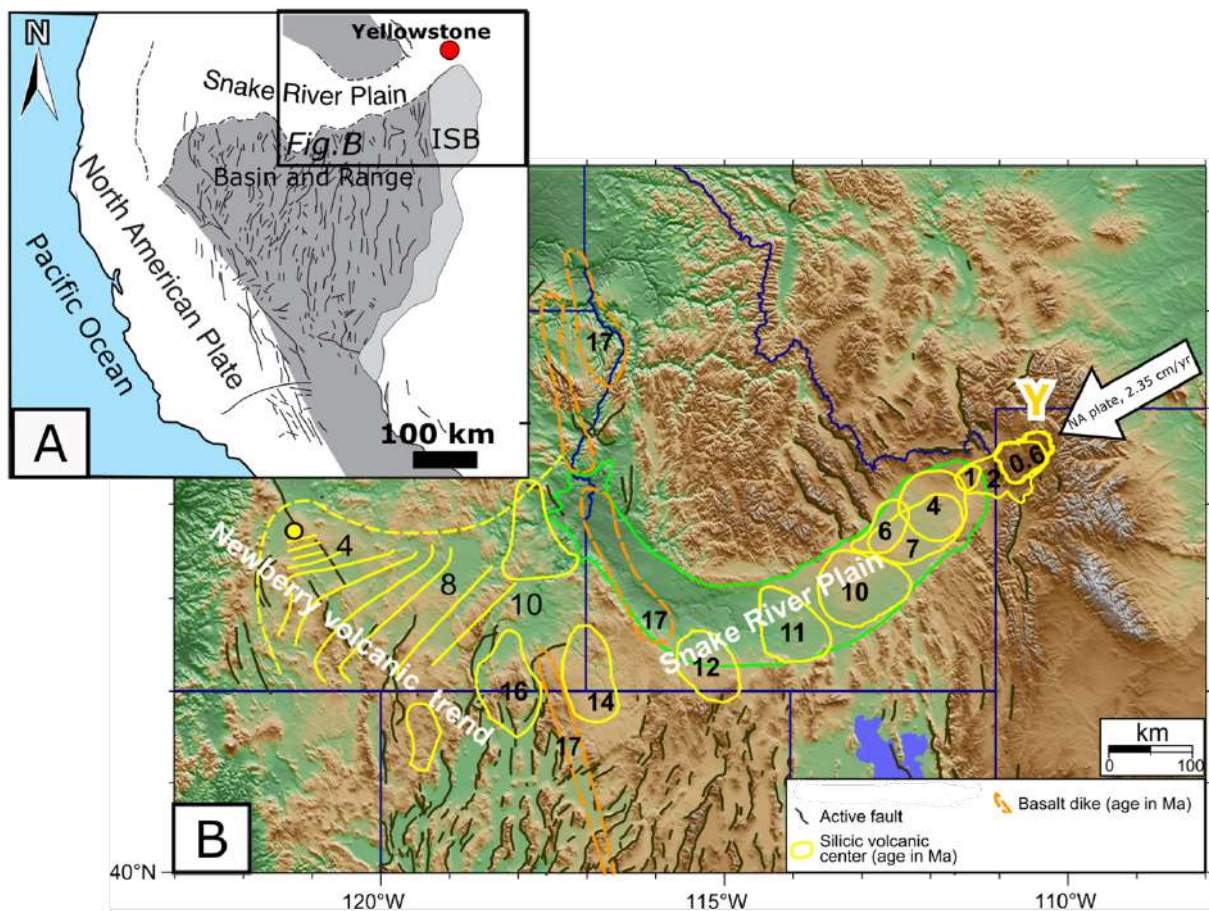


Figure 2 (A) Inset showing location of Yellowstone volcanic plateau and main faults of Basin and Range Province (modified after Nagorsen-Rinke et al., 2013 and Russo et al., 2020). ISB = Intermountain Seismic Belt. **Figure B** is located. (B) Track of the Yellowstone hotspot (Y) (after Smith and Siegel, 2000) showing the relative motion and age of YSRP silicic volcanic centers (Armstrong et al., 1975; Smith and Braile, 1984; Pierce and Morgan, 1990, 1992; Kuntz et al., 1992; Smith and Braile, 1994; Perkins and Nash, 2002). The direction of North America plate motion is represented by a large white arrow (Smith and Sbar, 1974). The topographically low area occupied by the Snake River Plain is outlined in green. Black lines show late Quaternary faults; Cenozoic basaltic dikes (age in Ma) are shown in yellow and orange (Zoback and Thompson, 1978; Camp, 1995; Glen and Ponce, 2002) (modified after Smith et al., 2009).

The Yellowstone crustal magma reservoir is composed by a 5-15% partially molten material, 90 km long and located at depths spanning from 5 to 17 km, thus being 2.5 times larger than previously estimated (Fig. 3; Husen et al., 2004; Farrell et al., 2014). This low V_p magma body extends 15 km

NE of the caldera and correlates with the location of the largest negative gravity anomaly, a nearly 80 mGal gravity low. The shallowest portion of the Yellowstone magma reservoir, which reaches depths shallower than 5 km, is located below the Hot Spring Basin Group (HSB) (Fig. 3), which is one of the most active thermal basins in the area located northeast respect to the caldera (Werner et al., 2008; DeNosaquo et al., 2009). Here, magmatic fluids have migrated away from the magma reservoir along existing fractures (Farrell et al., 2014).

Another large, shallow low V_p body has been recognized close to the NW boundary of the caldera and, due to the low V_p/V_s ratio, has been interpreted as a gas body composed by saturated CO_2 (Husen et al., 2004; Farrell et al., 2014).

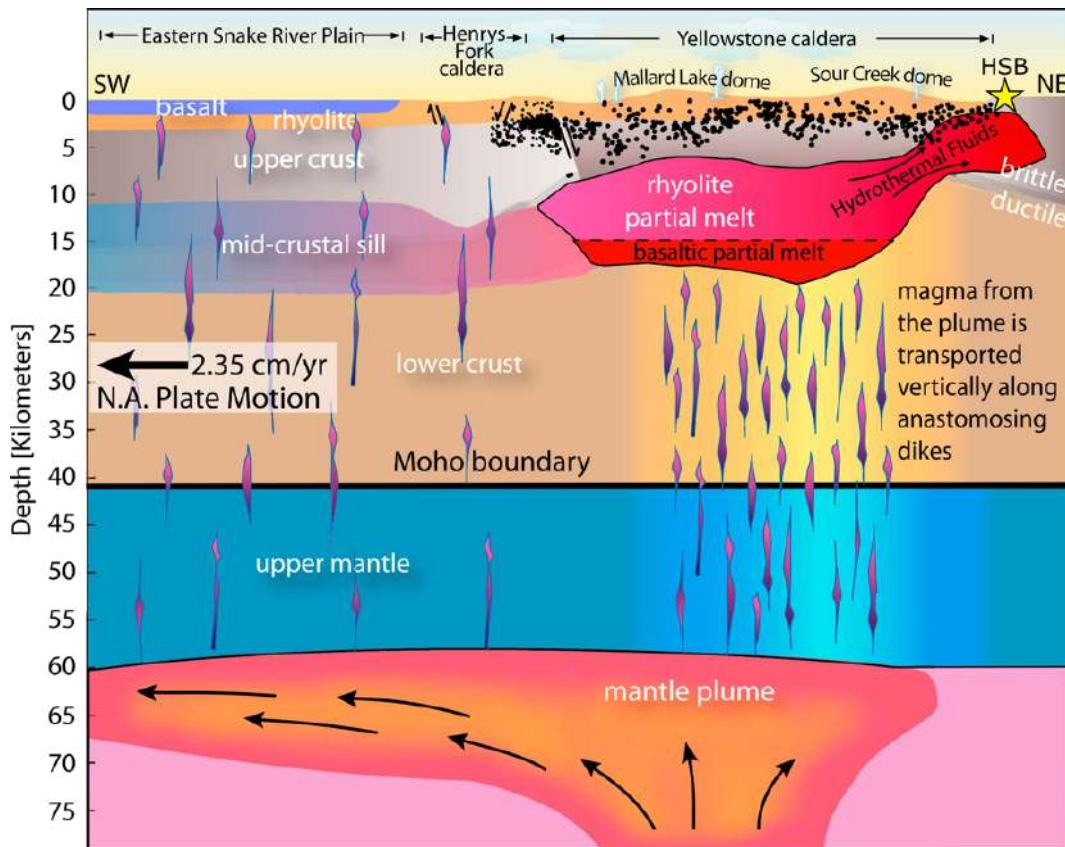


Figure 3 Sketch of the interaction between the Yellowstone hotspot plume and the North America plate (modified after DeNosaquo et al., 2009 and Farrell et al., 2014). HSB = Hot Spring Basin Group.

The buoyant rising through the upper mantle and lower crust of basaltic melt from the plume causes the partial melt of the silicic continental crust (Fig. 3; Farrell et al., 2014). The lithospheric cooling and contraction above such crystallizing fractionated magma reservoir forms the characteristic bimodal rhyolite-basalt volcanic system of the YSRP (shown in Figure 2). In fact, the Yellowstone Plateau is a clear example of a compositionally bimodal rhyolite-basalt igneous field; no

intermediate composition is present (Christiansen, 2001). The geological features in the area are the result of its violent volcanic past, consisting of three catastrophic caldera-forming eruptions at 2.1, 1.3 and 0.63 Ma, which erupted 2500 km³, 280 km³ and 1000 km³ of material, respectively (Christiansen, 2001).

Three major sheets of ash-flow tuffs make up the stratigraphic column, separated by unconformities: from oldest to youngest, *i*) the Huckleberry Ridge tuff, which corresponds to the development of the first caldera (2.1 Ma), *ii*) the Mesa Falls tuff (composed by the Island Park Rhyolite and Mount Jackson Rhyolite), which represents the second caldera formation (1.3 Ma), and *iii*) the Lava Creek tuff and the Plateau Rhyolite, corresponding to the 0.63 Ma 45 km x 70 km Yellowstone caldera (Fig. 4; Christiansen, 2001).

The 0.63 Ma Yellowstone caldera (third cycle) has an elliptical shape, elongated in an ENE-WSW direction, and is characterized by the presence of two resurgent domes (Figure 4): the eastern Sour Creek dome, which formed soon after the caldera, and the western Mallard Lake dome, which dates to about 0.16 Ma (Christiansen, 2001). Each dome has a ring-fracture zone, which delineates the margin of the post-caldera uplifted blocks, and a series of NW-striking faults with an average length of 754 meters that form a complex graben along the structural axis (Fig. 4). These faults are related to uplift and doming of the resurgent blocks, not to their collapse (Carr and Quinlivan, 1968; Smith, 1968). Furthermore, the youngest movements along these faults were recognized by Pierce (1973) as post-dating the last main glaciation of the Rocky Mountains (late Pleistocene).

Christiansen (2001) distinguished the above cited Quaternary faults mapped in Figure 4 between certain and concealed, based on the reliability of the location of the structures: the latter have a poorly defined trace in the field and are inferred on the basis of topography, whereas certain faults have been mapped by photogrammetry on a topographic basemap at a scale of 1:250,000 or more detailed (Machette, 2001). These are all mapped as normal faults, although a detailed reconstruction of their kinematics that could indicate strike-slip components is not available. A decrease in measured vertical offset has been observed when approaching the caldera, because of the coverage by volcanic rocks on the plateau, whereas at distance it is possible to observe cumulative displacements on faults over time in the order of 396 m (Love, 1961; Christiansen, 2001). Faults are characterized in most cases by linear trends in plan view, except in some areas as for example just outside the northeastern caldera rim, where they have an arcuate shape. This shape has been considered as influenced by movements of the Yellowstone magmatic body at depth in an area that did not have a strongly developed preexisting system of tectonic faults (e.g. Eaton et al.,

1975). Waldrop (1969) showed that these faults have had renewed rupture during late Quaternary times.

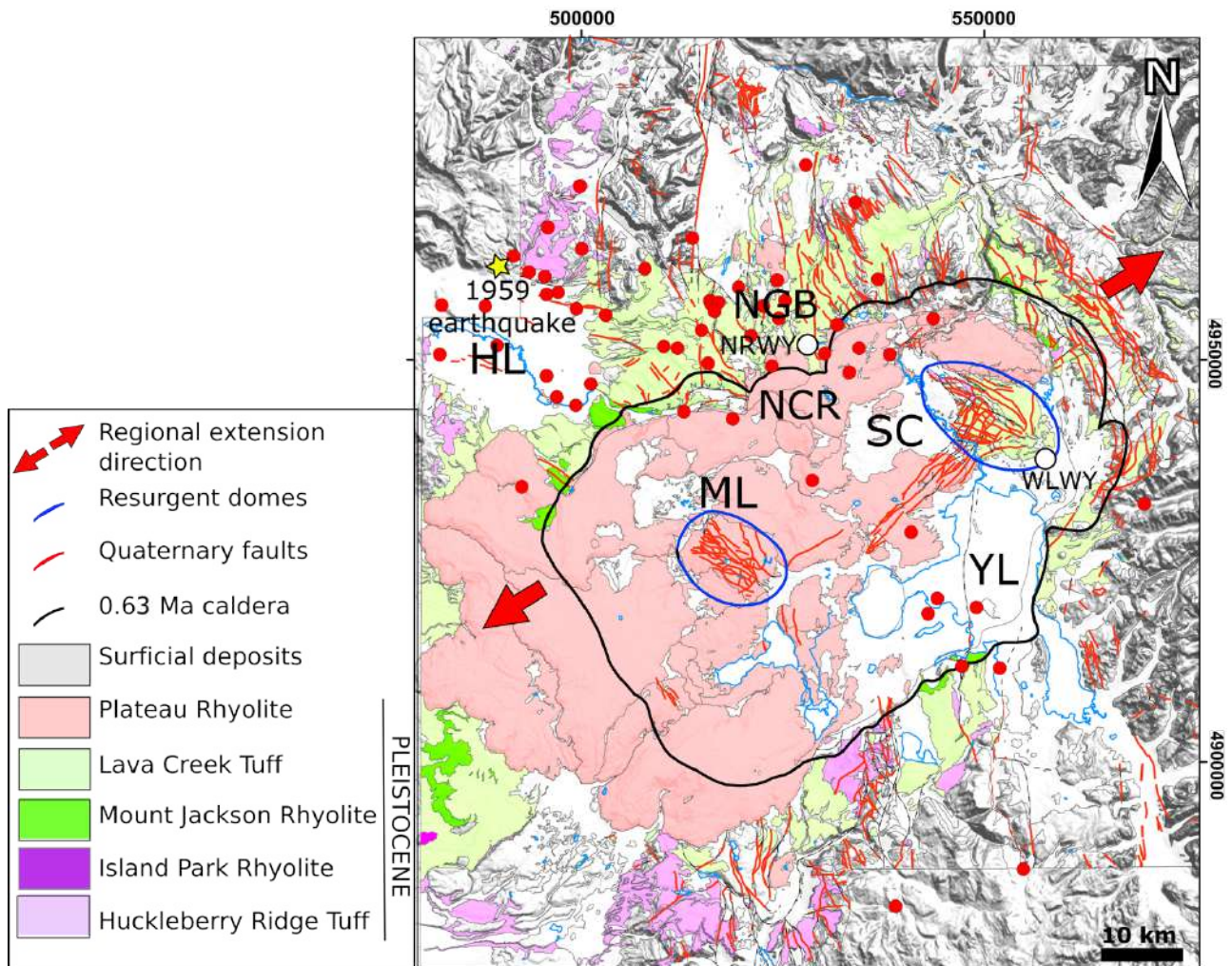


Figure 4 Geological map of Yellowstone volcanic plateau modified after Christiansen (2001). ML = Mallard Lake resurgent dome; SC = Sour Creek resurgent dome; YL = Yellowstone Lake; HL = Hebgen Lake; NGB = Norris Geyser Basin; NCR = Northern Caldera Rim. The 0.63 Ma caldera is shown as a black line, resurgent domes are represented as blue lines. Fault data, represented in red, after Christiansen (2001). Dashed lines indicate concealed faults. Red arrows represent the σ_3 direction (Puskas and Smith, 2009). Shaded view of the Digital Elevation Model (DEM) provided by the USGS National Elevation Dataset. Coordinate system: WGS84/UTM zone 12N; coordinates are expressed in meters. Location of NRWY and WLWY GPS stations is shown as white circles. Such stations have been chosen among the Yellowstone network according to previous studies (e.g. Chang et al., 2010) as the most representative of surficial deformations within the Yellowstone caldera and the Norris Geyser Basin, respectively. Location of the 1959 Hebgen Lake earthquake is shown as a yellow star,

red points represent earthquakes with magnitude values > 4 that occurred since 1947, derived from the USGS catalogue www.earthquake.usgs.gov (modified after Russo et al., 2020).

The geological characteristics of the Yellowstone volcanic plateau, in terms of faults geometry and earthquake occurrence, are influenced both by interacting tectonic and magmatic processes: in fact, past researches showed that magmatic activity can alter the behavior of nearby tectonic faults (e.g. [Hampel and Hetzel, 2008](#)).

Even though no magmatic eruptions have occurred at the Yellowstone volcanic plateau since ~70 ka ago within or near the caldera, the area is still volcanically active, with high hydrothermal and seismic activity and periods of magmatic-fluid-triggered deformation well-documented by Global Navigation Satellite Systems (GNSS) and Interferometric Synthetic Aperture Radar (InSAR) data recorded over the past several decades (e.g. [Wicks et al., 2006](#); [Chang et al., 2007, 2010](#)).

In fact, leveling, GPS, and InSAR measurements have captured periods of uplift and subsidence throughout the volcanic plateau ([Fig. 5](#); [Pelton and Smith, 1979](#); [Dzurisin et al., 1994](#); [Wicks et al., 1998, 2006](#); [Chang et al., 2007](#)). These episodes of deformation within and adjacent to the caldera have been attributed to combinations of two processes taking place beneath the caldera: pressurization and de-pressurization of an alternately self-sealed and leaking hydrothermal fluid reservoir that traps volatiles exsolved from a crystallizing rhyolitic magma reservoir, or transfer, formation and crystallization of rhyolitic or basaltic magma ([Wicks et al., 2006](#)). [Tizzani et al. \(2015\)](#) identified three deformation sources at the origin of caldera unrest, the Mallard Lake (ML) and Sour Creek (SC) resurgent domes and the Northern Caldera Rim area (NCR, [Fig. 4](#)), which are located below the brittle-ductile transition zone that is between 4 km and 6 km under the resurgent domes ([DeNosaquo et al., 2009](#)) and between 7 km and 9 km in the NGB region ([Smith et al., 2009](#); location in [Fig. 4](#)).

Deformation in the north rim has been defined as NRUA (North Rim Uplift Anomaly), which, together with NGB, is located at the intersection of the Norris-Mammoth corridor and an east-west trending zone of seismicity called the Norris-Hebgen seismic belt, which extends from the NGB to the east to the location of the 1959 Ms 7.5 earthquake to the west, which occurred few kilometers north of the Hebgen Lake (HL) (location in [Fig. 4](#); [White et al., 1988](#); [Waite and Smith, 2002](#)). The Norris-Mammoth corridor is characterized by active normal faults, hydrothermal features, and intense seismicity ([Waite and Smith, 2002](#)). It is in fact a rift-like zone with NNE-SSW extension ([Savage et al., 1993](#); [Waite and Smith, 2004](#)) that experienced minor postcaldera volcanism

(Christiansen, 2001; Morgan et al., 2017). Seismic activity that occurred in the above cited areas has been characterized by the presence of most earthquakes with magnitudes higher than 4 since 1947, acquired from the USGS earthquake catalogue, as shown in Figure 4.

More in detail, previous studies (e.g. Chang et al., 2010) have shown different phases of deformation recorded within the 0.63 Ma Yellowstone caldera and the Norris Geyser Basin (NGB) area, just north of the NCR (Fig. 4). Such deformations are not simultaneous: the crustal transfer of fluids outward from the caldera and inward from the Norris area could be the underlying cause of the deformation reversals observed in the Yellowstone area (e.g. Shelly et al., 2013). Figure 5 shows the deformation phases that occurred between 2010 and 2016: the caldera experienced subsidence at rates of about 1.5 cm/yr until the M_w 4.8 earthquake in March 2014, which was part of the Norris seismic swarm. In fact, this earthquake occurred at the same time of a reversal in the deformation from subsidence to uplift at about 10 cm/yr (Fig. 5; Chang et al., 2010). Within the Norris Geyser Basin area (location in Fig. 4) uplift began in the second half of 2013, reaching rates of over 15 cm/yr in the beginning of 2014. After the 2014 Norris earthquake, deformation near Norris reversed to rapid subsidence at a rate exceeding 20 cm/yr (Farrell et al., 2014; Stovall et al., 2014). In 2016, the 0.63 Ma Yellowstone caldera was subsiding, whereas the Norris Geyser Basin area was uplifting (Farrell, 2013).

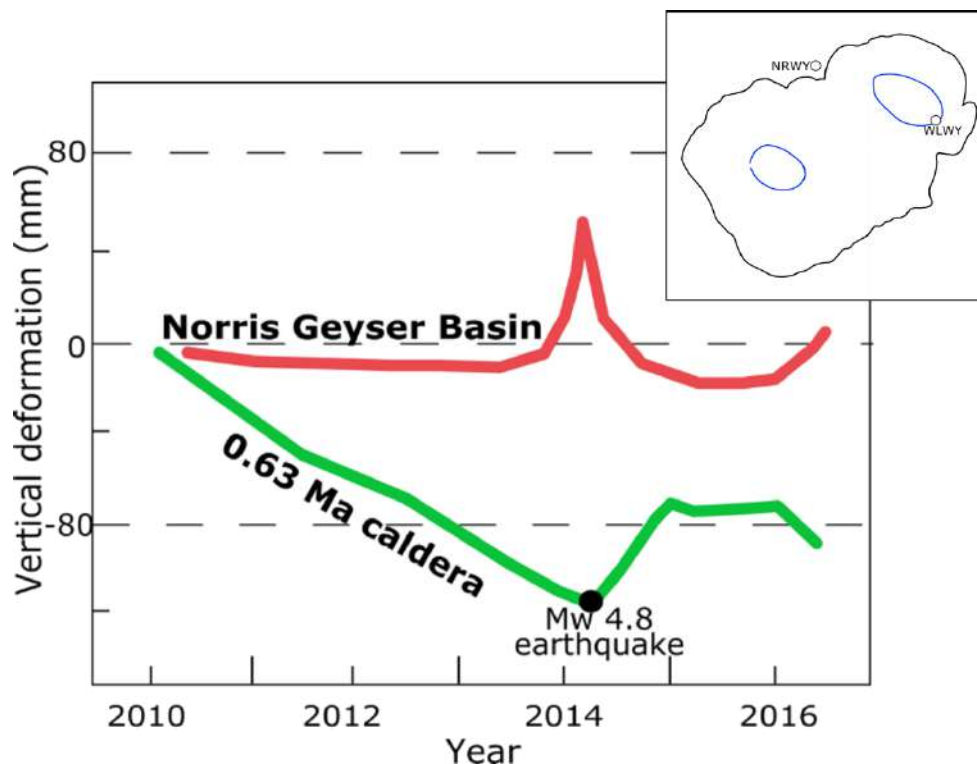


Figure 5 Vertical component of deformation between 2010 and 2016 documented by GPS stations WLWY and NRWY (located in the inset in the upper right corner and in Fig. 4) of the Yellowstone-

Contin network, representing intra-caldera and outer caldera (Norris Geyser Basin) deformation, respectively (modified after Russo et al., 2020).

Over the past decades, previous studies aimed at identifying spatial variations in seismic stress indicators at Yellowstone have been performed through the elaboration of focal mechanism solutions (FMS) (Figure 6; e.g. Waite and Smith, 2004; Russo et al., 2017, 2020). Waite and Smith (2004) calculated 364 FMS for the time interval 1973-1998 (Fig. 6A), which revealed predominant normal faults with varying orientations across the caldera. These authors were able to identify a rotation in T axis north of the caldera, where the densest seismicity is present, from N-S near the location of the 1959 Hebgen Lake (HL) earthquake (location in Fig. 4) to ENE-WSW 35 km east. The N-S extension has been interpreted as related to postseismic viscoelastic relaxation following the 1959 HL earthquake. Russo et al (2017) computed 369 FMS in the same area but over the time interval 1988-2010 (Fig. 6B), also taking into account stress inversion results from Waite and Smith (2004) (Fig. 6A), revealing the presence, apart from normal faults typical of the Basin and Range province, of subordinate strike-slip and few reverse motions, that have been compared with magma inflation and deflation phases. Furthermore, such authors identified temporal (respect to Waite and Smith, 2004) and spatial rotations in σ_3 direction both in the outer and inner part of the 0.63 Ma caldera.

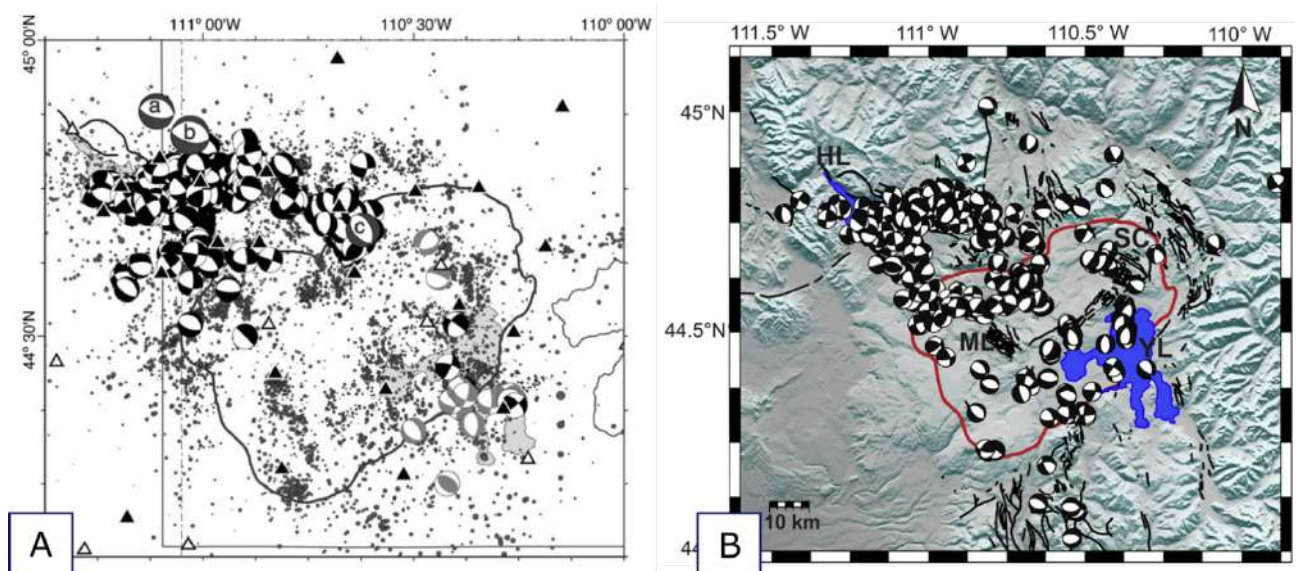


Figure 6 (A) Complete set of the 1973-1998 focal mechanism solutions calculated by Waite and Smith (2004) plotted over relocated epicenters (gray circles). The additional 18 events taken from a data set with less well constrained depths are plotted with gray compressional regions. Larger

mechanisms labeled 'a' and 'b' are 1959 M_s 7.5 Hebgen Lake main shock subevents (Doser, 1985). Mechanism 'c' is a composite solution of the main shock and aftershocks of the 1975 M_L 6.1 Norris Junction earthquake (Pitt et al., 1979). (B) Complete set of the 1988-2010 focal mechanism solutions calculated by Russo et al (2017). The red line represents the 0.63 Ma Yellowstone caldera boundary. ML = Mallard Lake resurgent dome; SC = Sour Creek resurgent dome; YL = Yellowstone Lake; HL = Hebgen Lake. The topographic data is provided by the USGS National Elevation Dataset.

2.2 Iceland: the Northern Volcanic Zone

Iceland is a peculiar geological spot, being crossed by the emerged North American and Eurasian plate boundary: it is volcanically and dynamically supported by the Iceland hotspot, centered beneath the western Vatnajökull icecap, and it is characterized by a series of rift zones linked by transform fault zones (Figure 7; Ward, 1971; Sæmundsson, 1978, 1979; White and McKenzie, 1989; Einarsson, 2008). The average thickness of the oceanic crust in Iceland is 29 km (Menke and Levin, 1994; Darbyshire et al., 2000; Allen et al., 2002; Brandsdóttir and Menke, 2008): in particular, the upper crust, which is 5 km to 10 km thick, is composed mainly by basaltic lavas and dykes, whereas the lower crust is made up of gabbroic material (Pálmason et al., 1978; Sæmundsson, 1979; Allen et al., 2002; Brandsdóttir and Menke, 2008). Rift zones of Iceland are composed by swarms of fissures, extension fractures and volcanic systems (Tryggvason, 1973; Sæmundsson, 1978; Hjartardóttir et al., 2015). The main volcanic systems of which Iceland is composed of, shown in Figure 7, are: the Western and Eastern Rift Zones (WRZ and ERZ), the South Iceland Seismic Zone (SISZ), which connects the ERZ with the Reykjanes Ridge (RR), and the Northern Volcanic Zone (NVZ) (Hjartardóttir et al., 2016b).

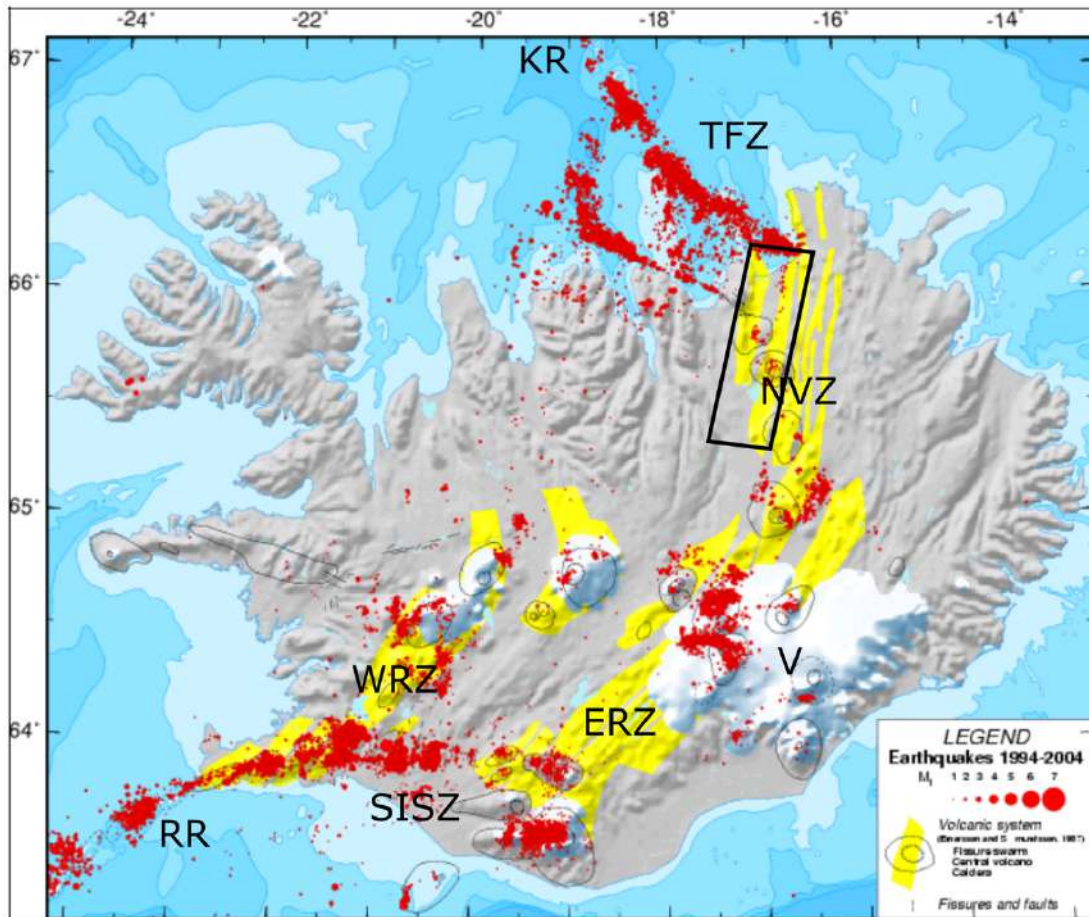


Figure 7 Main active rift zones of Iceland, marked by fissure swarms (yellow) and central volcanoes (black outlines) (Jóhannesson and Sæmundsson, 1998; Hjartardóttir et al., 2015). Seismicity along the Iceland plate boundary zones between 1994 and 2004 is shown as red points. KR = Kolbeinsey Ridge; RR = Reykjanes Ridge; WRZ = Western Rift Zone; ERZ = Eastern Rift Zone, NVZ = Northern Volcanic Zone, SISZ = South Iceland Seismic Zone, TFZ = Tjörnes Fracture Zone, V = Vatnajökull Glacial Icecap. Black rectangle indicates location of the study area of the present research. Map and epicenters from the Icelandic Meteorological Office provided by Gunnar B. Gudmundsson (modified after Karson et al., 2018).

According to previous studies, the NVZ and ERZ are propagating away from the Iceland hotspot, to the north and south respectively, resulting in abandoned rift zones, and migration of transform faults (Sæmundsson, 1974; Harðarson et al., 1997; Garcia et al., 2002; LaFemina et al., 2005; Einarsson, 2008; Karson, 2017). Furthermore, such propagation is supposed to be at the origin of block rotations along the margins of the propagating rift zones around a pole of rotation located at the rift tips (Figure 8; Hey et al., 1980; Schouten et al., 1993; Karson, 2017; Karson et al., 2018). Block rotations cause the development of widespread major rift-parallel strike-slip faulting cutting rocks

of various ages across Iceland (Figure 8; e.g. Proett, 2015; Runnals, 2015; Karson, 2017; Karson et al., 2018). Seismicity, which is concentrated at depths shallower than 15-20 km, occurs mainly along the transform fault and oblique rift zones (Figure 7; Stefánsson et al., 1993; Einarsson, 2008).

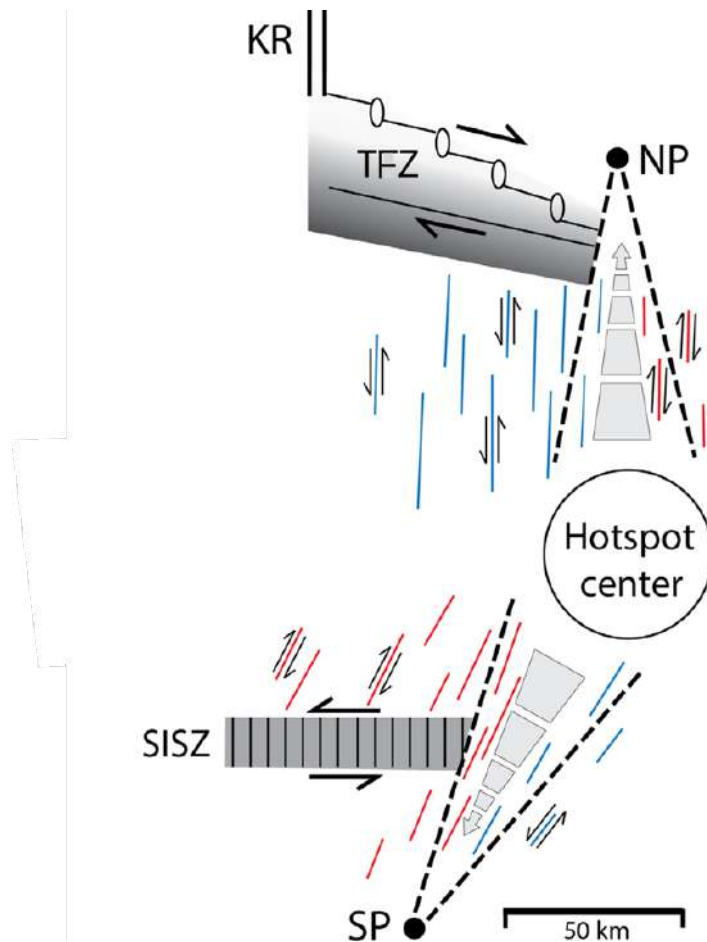


Figure 8 Tectonic sketch of the Iceland Plate Boundary Zone (PBZ). Wide, light gray arrows show flow of middle crust and mantle away from the hotspot toward propagating rift tips to the N (NP) and S (SP). Pseudofaults, shown as dashed lines, truncate transform fault structures of the SISZ and TFZ. Propagation causes rift-parallel strike-slip faulting, red-right-lateral and blue-left lateral (modified after Karson, 2017).

This research focuses on the Northern Volcanic Zone (NVZ), located in the north-eastern part of Iceland as shown in Figure 7, which represents the northernmost point of emersion of the Mid-Atlantic Ridge. The NVZ is connected to the Kolbeinsey Ridge (KR) through the Tjörnes Fracture Zone, a seismically active shear zone composed of three N120°-striking segments, named from north to south: the Grímsey Oblique Rift (also known as Grímsey Lineament), the Húsavík-Flatey Fault and

the Dalvík Lineament (Fig. 9; Einarsson, 1991; Magnúsdóttir and Brandsdóttir, 2011; Hjartardóttir et al., 2016b).

The NVZ, characterized by plate spreading with a rate of 2 cm/yr oriented N106°E (red arrows in Figure 9; DeMets et al, 1994; Hjartardóttir et al., 2016a), is composed of five volcano-tectonic rift zones (the Theistareykir, Krafla, Fremrinámar, Askja and Kverkfjöll volcanic systems; Hjartardóttir et al., 2016a,b), each composed of N-S to NNE-SSW trending swarms of normal faults, dry extension fractures and eruptive fissures, 5-20 km wide and 60-100 km long, and of a main volcano (Saemundsson, 1974).

For the purposes of this research, I focus on the two westernmost rifts of the NVZ, since they experienced recent major rifting episodes: in 2007-2009 within the Theistareykir Fissure Swarm (ThFS), and in 1724-1729 (a rifting episode known as the Mývatn fires episode) and 1975-1984 within the Krafla Fissure Swarm (KFS) (Bjornsson et al., 1977; Hofton and Foulger, 1996).

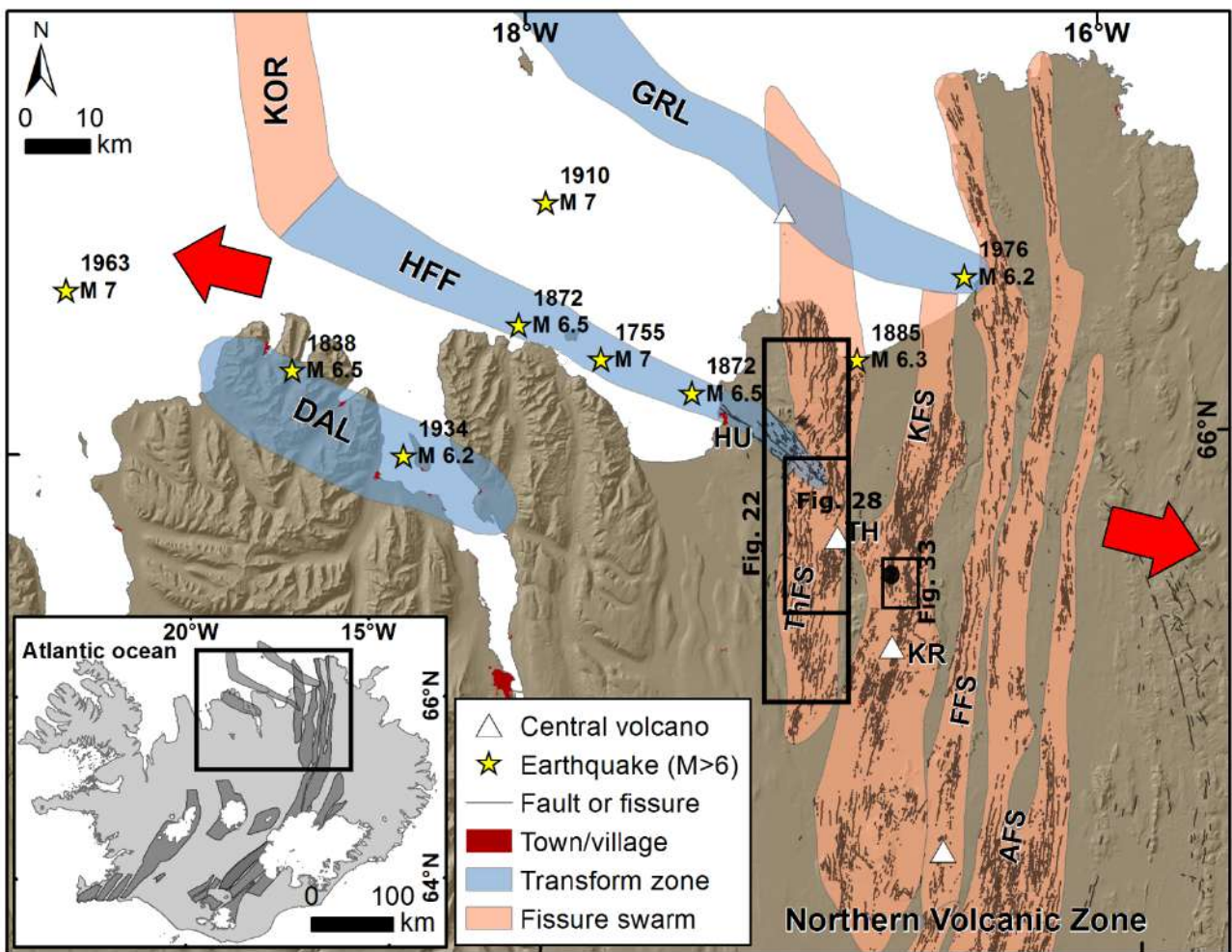


Figure 9 Tectonic setting of northeastern Iceland. The mid-Atlantic Ridge is here offset by the Húsavík-Flatey Fault (HFF) and by the Grimsey Volcanic Zone (GVZ) which is part of the Tjörnes transform zone. Orange stripes represent volcanotectonic rift zones, also termed “fissure swarms”,

belonging to the Northern Volcanic Zone (NVZ) (after [Hjartardóttir et al., 2015](#)). Faults and fissures (dark grey lines) are from [Magnúsdóttir and Brandsdóttir \(2011\)](#) and [Hjartardóttir et al. \(2012, 2015\)](#). Yellow stars locate historical earthquakes with $M > 6$ (after [Stefansson et al., 2008](#)). White triangles represent the main Quaternary central volcanoes. Inset shows the location of the area and the volcanotectonic rift zones of Iceland ([Einarsson and Saemundsson, 1987](#); [Hjartardóttir et al., 2015](#)). Red arrows indicate the plate spreading orientation ([DeMets et al., 1994](#); [Hjartardóttir et al., 2016a](#)). ThFS = Theistareykir Fissure Swarm; KFS = Krafla Fissure Swarm; TH = Theistareykir basaltic shield volcano; KR = Krafla central volcano; FFS = Fremrinámar Fissure Swarm; AFS = Askja Fissure Swarm; HU = Town of Húsavík; OB = Öxarfjörður Basin (modified after [Bonali et al., 2019b](#)). Black circle indicates location of [Figure 39](#).

The Theistareykir Fissure Swarm (ThFS) is an active, N-S trending, 70-km-long volcano-tectonic rift that forms the westernmost edge of the NVZ, marked by the presence of normal faults and extension fractures, parallel to sub-parallel to each other, striking mostly N00-30° ([Fig. 9](#); [Acocella et al., 2000](#); [Dauteuil et al., 2001](#); [Hjartardóttir et al., 2012, 2015](#); [Pasquaré Mariotto et al., 2015](#)). The ThFS is also dotted with a number of volcanic vents and is home to the major Theistareykir central volcano (TH; [Fig. 9](#)).

The intersection between the ThFS and the Husavík-Flatey Fault (HFF), characterized by dominant right-lateral strike-slip movements, was studied in detail by [Gudmundsson et al. \(1993\)](#), [Fjäder et al. \(1994\)](#), [Magnúsdóttir and Brandsdóttir \(2011\)](#), [Pasquaré Mariotto et al. \(2015\)](#), and [Tibaldi et al. \(2016a,b, 2018\)](#), while the HFF itself was first studied by [Einarsson \(1958\)](#) and mapped by [Saemundsson \(1974\)](#), [Opheim and Gudmundsson \(1989\)](#), [Gudmundsson et al. \(1993\)](#), [Garcia et al. \(2002\)](#), [Garcia and Dhont \(2005\)](#), [Gudmundsson \(2007\)](#), [Magnúsdóttir and Brandsdóttir \(2011\)](#), [Pasquaré Mariotto et al. \(2015\)](#), and [Tibaldi et al. \(2016a,b\)](#). The intersection between ThFS and HFF causes some structural changes, such as strike rotations ([Fig. 10](#); [Gudmundsson et al., 1993](#); [Fjäder et al., 1994](#); [Magnúsdóttir and Brandsdóttir, 2011](#); [Pasquaré Mariotto et al., 2015](#); [Tibaldi et al., 2016a,b](#)).

Furthermore, between the volcano and the ThFS – HFF intersection, normal faults dominate with a predominant westward dip direction in the eastern part of the rift and an eastward dip in the western part ([Tibaldi et al., 2016a,b](#)). Also, in the southernmost portion of the ThFS, normal faults dip mostly to the west, whereas approaching the Theistareykir volcano (located in [Fig. 9](#)), faults mostly dip east and then vanish in correspondence of the youngest products of this volcano

(Hjartardóttir and Einarsson, 2015; Khodayar et al., 2018). Hjartardóttir et al. (2016b) suggested that the HFF extends further east than the ThFS, even as far as the Krafla rift. This hypothesis is supported by Tibaldi et al. (2016a,b) and Tibaldi and Bonali (2018), who observed an interaction between the HFF and the structures of the ThFS. North of this junction, the faults terminate and only extension fractures are observed (Tibaldi et al., 2016b; Bonali et al., 2019b). Further north, the ThFS continues offshore within the Öxarfjörður Basin (Fig. 9; Einarsson, 2008; Hjartardóttir, 2013) and it connects to the Grimsey Lineament.

Along the ThFS, several depositional units crop out, represented by sedimentary sequences from Miocene to Pleistocene times, as well as lava flows of Pliocene, Pleistocene and Holocene age (Fig. 10; Saemundsson, 1974; Garcia et al., 2002). The latest eruption here took place about 2.4 ka BP, with the emission of the 'Theistareykjähraun' lava flows between the central volcano and the Husavik-Flatey Fault (Fig. 10; Saemundsson et al., 2012). Faults and extension fractures can be found in both pre-Last Glacial Maximum (LGM) and in post-LGM lithostratigraphic units (Fig. 10). Active vertical deformation at Theistareykir volcano, measured through GPS-based methods (Metzger et al., 2011), was interpreted as induced by inflation of the underlying magma chamber. During historical times, the following rifting and volcanic unrest episodes are documented: *i*) between 1867 and 1868, a M 6 earthquake hit in the northern part of the ThFS, accompanied by volcanic eruptions in the northern offshore sector of the rift (Thoroddsen, 1925; Halldórsson, 2005; Magnúsdóttir and Brandsdóttir, 2011); *ii*) between 1884 and 1885, an earthquake swarm culminated in a M 6.3 earthquake along the rift, near the coast (Fig. 9; Halldórsson, 2005); and *iii*) between 2007 and 2009 an 8-cm uplift in correspondence of an area centred on the Theistareykir volcano was recorded, and it was interpreted as the result of an inflation of the magma chamber below (Metzger et al., 2011; Metzger and Jónsson, 2014).

The second westernmost rift of the NVZ is the 100-km long Krafla Fissure Swarm (KFS), which, together with the associated Krafla central volcano (KR; Fig. 9) has been interested by the recentmost (1975-1984) volcanic and seismic activity within the NVZ. The Krafla volcano hosts an 8-km-wide caldera, which developed starting with a large eruption ~100,000 years ago and successively widened in east-west direction due to plate spreading (Saemundsson, 1991). It is essentially basaltic in composition, although more silicic products crop out in the surroundings of the caldera (Jónsson, 1994). According to previous research, the magma chamber is situated between 3 km and 7 km depth (Einarsson, 1978).

The fissure swarm that prolongs northward of the caldera mostly affects the post-glacial lava flows known as the Stóráviti lava shield, which have emplaced 10-12 ka ago (Sæmundsson, 1991; Mattsson and Höskuldsson, 2011). South of the caldera, the KFS is punctuated by numerous lava flows emplaced since 3000 yrs BP, while glacial deposits cover the southernmost part. Fractures within the swarm are mostly oriented N to NNE (Fig. 10; Angelier et al., 1997; Hjartardóttir et al., 2016a,b).

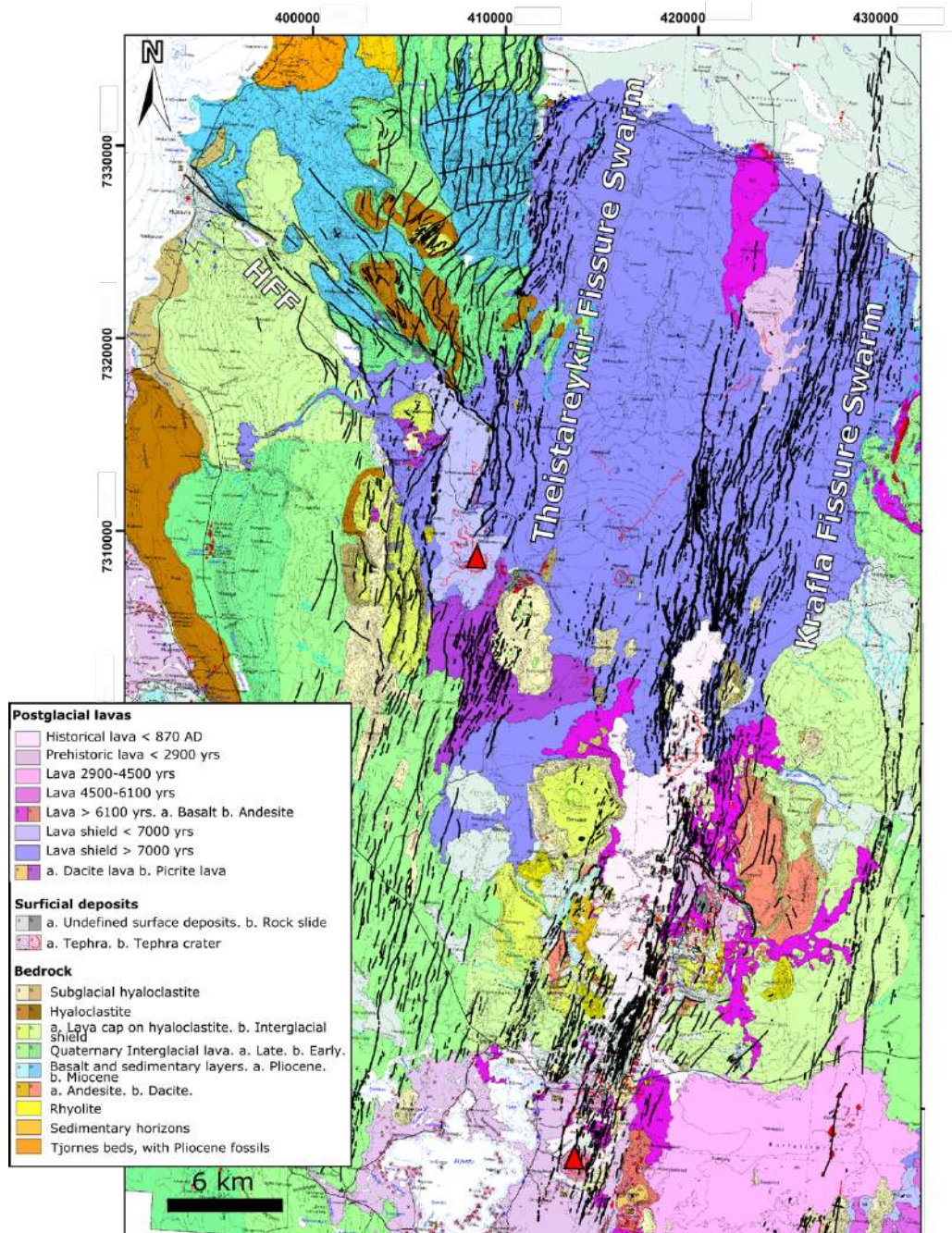


Figure 10 Geological map of the Theistareykir (ThFS) and Krafla Fissure Swarms (KFS) (modified after [Saemundsson et al, 2012](#)). Faults and fractures are indicated as black lines, courtesy of [Ásta Rut Hjartardóttir](#). Central volcanoes are indicated as red triangles.

Episodes of surficial deformation at Krafla have been interpreted as resulting from magma accumulation about 3 km below the volcano centre ([Tryggvason, 1978](#); [Bjornsson et al., 1979](#)). A series of inflation and deflation phases have been detected over the past decades, accompanied by rifting in the fault swarm and earthquakes, which typically start in the interior of the caldera structure and then propagate towards the north or south along the fracture/fault swarm. This pattern of earthquake activity is commonly accepted to derive from horizontal migration of magma away from the chamber zone located below the volcano ([Brandsdottir and Einarsson, 1979](#)). A major phase of deformation began at the KFS in December 1975 ([Bjornsson et al., 1977, 1979](#)) and lasted until 1984, accompanied by about 20 rifting episodes and numerous lava flows. During each rifting episode, magma escaped from the chamber below the Krafla volcano and intruded along the fissure swarm in the form of kms-long dykes ([Hofton and Foulger, 1996](#)). In nine of these episodes, a volcanic eruption did take place.

During the 1975-1984 period, total widening across the KFS amounts from 2 to 6 m, with local maximum of 9 m ([Bjornsson, 1985](#); [Gudmundsson 1995b](#)). GPS geodetic monitoring repeated several times in the successive years, revealed large, systematic, rift-normal expansion that was interpreted as post-rifting relaxation of compressional stress accumulated in the near-boundary region of the plates, in consequence of the 1975-1984 repeated dyke intrusions ([Foulger et al., 1992](#); [Heki et al., 1993](#); [Jahn et al., 1994](#); [Hofton and Foulger, 1996](#)). Satellite synthetic aperture radar data acquired in the years 1993-2008, show further rift expansion that was explained by the combination of plate spreading, viscoelastic relaxation following the 1975-1984 intrusions, and inflation/deflation of shallow magma chambers beneath the Theistareykir and Krafla central volcanoes ([Ali et al., 2014](#)). Finally, optical image correlation of declassified spy satellite and aerial photos show that during the 1975-1984 events, dykes typically propagated up to the surface in the caldera region and to a depth of about 3 km at the northern end of the KFS ([Hollingsworth et al., 2013](#)). This results in a widening of the grabens, produced by the dyking events, outward from the caldera.

Both the Theistareykir and the Krafla Fissure Swarm are characterized by widespread seismicity, as shown in [Figure 11](#), reaching a highest magnitude value of 5.2 (M_L). The presence of a main swarm

within the ThFS in correspondence of the geothermal field and of the Krafla caldera can be observed, as well as the alignment of epicentres according to the direction of the swarms of extension fractures and normal faults.

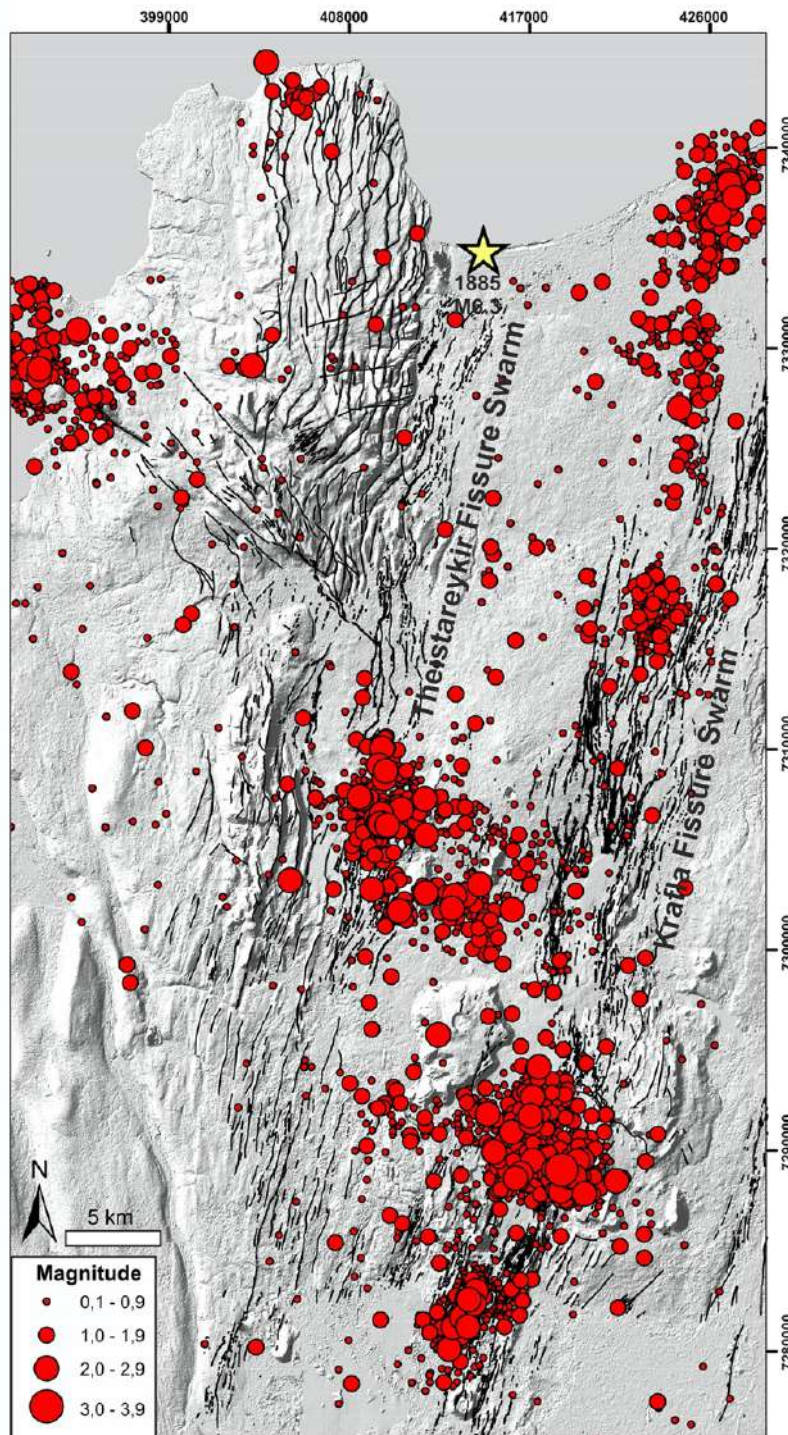


Figure 11 1991-2018 seismicity at Theistareykir and Krafla Fissure Swarms, scaled with magnitude. Fractures and faults are represented as black lines. Seismic catalogue is courtesy of Michelle J. Parks (Icelandic Meteorological Office). Coordinate system: UTM WGS84 zone 38N.

Chapter 3

Methodology – Northern Volcanic Zone

Regarding the Northern Volcanic Zone of Iceland, the present research integrates new geological-structural field data acquired through classical methods with quantitative data collected on Orthomosaics and on Digital Surface Models (DSM) elaborated through Structure from Motion techniques (SfM) applied to Unmanned Aerial Vehicles (UAVs) surveys.

3.1 Field mapping

The collection of field measurements has been performed in order to establish the geometry and kinematics of volcano-tectonic structures, focusing on the presence of lateral components of motion. Such structures have been classified into normal faults when associated with a continuous and appreciable vertical offset greater than 0.5 m, or as extension fractures when associated with a vertical offset lower than 0.5 m. More in detail, field measurements, located by differential GPS and managed in GIS environment, were regularly spaced along each structure.

Regarding extension fractures ([Figs. 12C-D-E](#)), the strike, amount of dilation and opening direction have been measured, with special attention on focusing on fractures unaffected by erosion, with a limited (or null) amount of sediments and without any fallen rocks on their sides: in fact, all these are factors that might alter the final measurement and that must be avoided so as to attain the greatest degree of accuracy. How were the amount of opening and the opening direction measured? Since lava flow columnar joints guided the formation of fractures at the surface, the fracture margins are irregular with several potential piercing points. The operator was thus able to measure by compass and laser rangefinder, with a great accuracy, the distance along the line connecting corresponding piercing points on each side of the extension fracture (e.g. [Fig. 12D](#); e.g. [Pasquarè Mariotto et al., 2015](#); [Bonali et al., 2019a](#)). In case the piercing points were not clearly visible, the dilation has been measured perpendicularly to the fracture azimuth and the opening direction has not been considered. In this latter case, all the measured extension fractures are about perpendicular to the spreading direction and thus the data on dilation amount can be considered as reliable.

In case fractures were filled by sediments, the amount of opening has been measured across the lower portions and only where fracture rock walls were detectable, so as to avoid any possible

overestimation of the dilation amount due to gravity, frost weathering, or a combination of both, which can create a funnel-shaped profile. In fact, in the field, an operator may be inclined to measure the amount of opening of fractures as the distance between the fracture rims. However, processes of erosion due to gravity, or cryoclastism, or a combination of them, might have enlarged the fracture near the topographic surface (white dashed line in Fig. 12F). This creates a funnel-shaped profile and, as a consequence, an overestimation of the dilation amount. A correct measurement should imply reaching down to a deeper level inside the fracture, in order to approach the original fracture walls (white line in Fig. 12F). In this case, a correct measurement by a field operator can be performed only if this level is reachable.

Regarding faults, field measurements comprised offset, strike, dip and spacing (Figs. 12A-B). Fault offset has been measured in the field by tape or laser rangefinder, by recognizing and quantifying displacements of piercing points such as stream beds, crests, lava flows and deposits, or by GPS measurements where the scarps were in the order of tens of meters. In most cases, the fault scarp is vertical and the strike-slip component is irrelevant, thus the net slip has been measured as coinciding with fault scarp height. As the downdip slip is the dominant one, the vertical offset has been measured in the field at intervals of 50 m, or continuously through drones, in order to come up with fault slip profiles, following Manighetti's approach (Manighetti et al., 1997, 2001). Points with accumulation of debris at the foothill of the fault scarp, which can bias the results, have been avoided. In any case, the studied deformations are of post-glacial age and are extremely fresh, thus erosion is not significant.

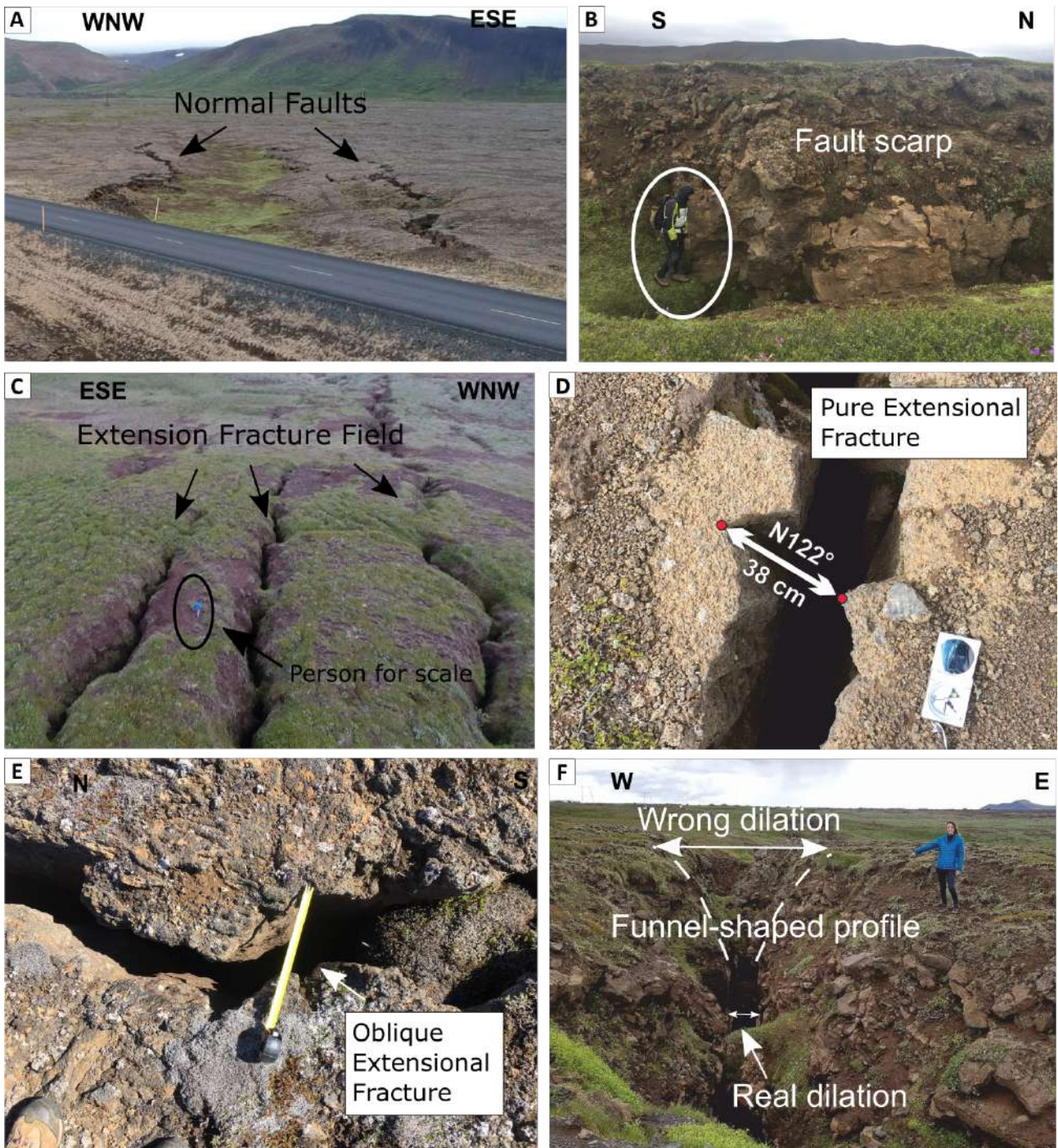


Figure 12 Examples of structures studied in the field. (A) Graben structures, with the two opposite-dipping normal faults, (B) Normal fault, person for scale, (C) UAV-captured picture of an extension fracture field, person for scale, (D) Example of piercing points along pure extension fracture, with indication of opening direction and amount of opening, (E) Example of piercing points along an oblique extension fracture, with a right lateral component, (F) Example of extension fracture with indication of real and wrong dilation, the latter caused by a funnel-shaped profile (Tibaldi et al., 2020b).

3.2 Structure from Motion (SfM) techniques applied to UAV surveys

3.2.1 Why UAVs and which kind is suitable for this research?

Unmanned Aerial Vehicles (UAVs) represent powerful tools for scientific purposes and have been extensively used for geological studies (e.g. Müller et al., 2017; Darmawan et al., 2018; Favalli et al., 2018; De Beni et al., 2019), thanks to a number of characteristics that make them more competitive and useful than satellites, giving the possibility to: *i)* choose appropriate data acquisition and time; *ii)* adjust flying altitude to obtain a very high spatial resolution; *iii)* repeat flights as much as necessary; *iv)* produce three-dimensional models of terrains from the acquired RGB data; *v)* survey vertical rock cliffs; *vi)* lower the cost of data acquisition respect than that of high-resolution satellite imagery; and *vii)* carry various types of sensors designed for specific purposes.

By using UAVs, it is possible to obtain a more comprehensive vision of volcano-tectonic structures from above, which might be very difficult to attain in the field, due to hard logistic conditions and the size of structures.

Different types of UAVs can be used for geological studies (Fig. 13): balloons, multi-rotor (Fig. 13B), fixed-wing (Fig. 13C) and hybrid (Fig. 13D). While balloons do not need fuel or a battery, on the other hand they cannot be remotely controlled. Hybrid types allow to switch between flying like a fixed-wing aircraft and hovering like a multi-rotor one: an example of Tailsitter VTOL (Vertical Take-off and Landing) is shown in Figure 13D (the picture is courtesy of Joël Ruch). The fixed-wing type can cover larger areas in a smaller time frame using high quality cameras, but such model is more difficult to be transported and more expensive than multi-rotor UAVs. Based on our experience, the latter can fly at very low heights attaining a great field resolution, and much more importantly, take-off and landing operations are easier than for fixed-wing models; this is crucial especially in difficult logistic terrains (e.g. outcropping lavas or remote beach areas, Bonali et al., 2019a; Fallati et al., 2019).

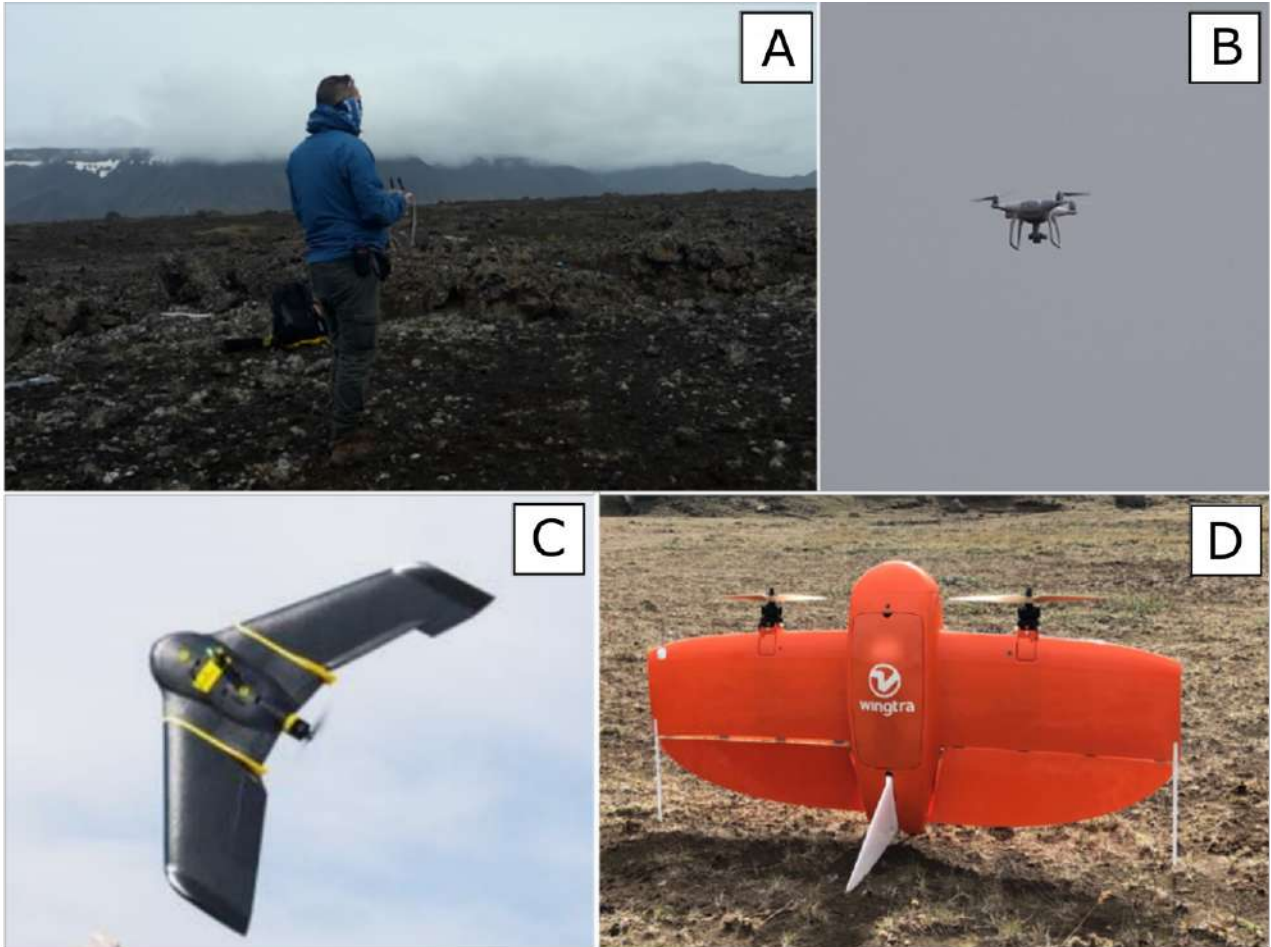


Figure 13 (A) UAV pilot at work, (B) Commercial UAV quadcopter in action, (C) Fixed wings UAV type, (D) VTOL (vertical take-off and landing) UAV type - this picture is courtesy of Joël Ruch (Bonali et al., 2020a).

For such reasons, we used the DJI Phantom 4 PRO quadcopter for the SfM reconstruction, that allowed to shoot photos at 20 Megapixels, including EXIF information (Exchangeable image file format) and GPS coordinates. UAV flight paths have been planned and managed using DJI Ground Station Pro software (<https://www.dji.com/ground-station-pro>). UAV photos have been captured every 2 seconds (equal time interval mode), with a constant velocity of 3 m/s (low speed) and in optimal light conditions suitable for the camera ISO range (100-1600), in order to: minimize the motion blur, avoid the rolling shutter effect, achieve well-balanced camera settings (exposure time, ISO, aperture), and ensure sharp and correctly exposed images with low noise (e.g. Vollgeer et al., 2016).

3.2.2 Orthomosaics and DSMs reconstruction

The workflow used for this research dedicated to Orthomosaics and Digital Surface Models (DSMs) production is based on [Bonali et al. \(2019a\)](#). In order to accurately co-register the resulting model to the World Geodetic System (WGS84) coordinates, Ground Control Points have been established, both around the model borders and in the central part, the latter aimed at reducing the ‘doming’ effect resulting from SfM processing ([Fig. 14A](#); e.g. [James and Robson, 2012](#); [Turner et al., 2012](#); [Westoby et al., 2012](#); [James et al., 2017](#)). Such targets were surveyed using the Emlid Reach RS© single frequency receivers in RTK configuration (with centimeter-level accuracy), linked in real time by NTRIP to the Icelandic CORS network (ICECORS - <https://www.lmi.is/en/icecors-network/>), used as reference station. Emlid Reach RS© runs an open-source RTK processing software called RTKLIB by [Takasu \(2009\)](#), that is available directly on receiver and doesn’t require any computer to run, if the base stations are at 15 km maximum distance from the rover. In our case, the medium distance from our rovers to the ICECORS network was 35 km, so an additional post-processing correction has been performed using the RTKLIB software for computers. All the z values (altitude a.s.l.) of the GCPs were corrected using the regional geoid model to obtain the orthometric height for the models. For surveying GCPs, artificial and natural markers easily recognizable on drone-captured photos have been used (e.g. [Figs. 14C-G](#)): the latter can be represented by very well visible stones (e.g. [Fig. 14F](#)), or lava flow borders (e.g. [Fig. 14G](#)), and have been often chosen since the unnecessary to retrieve them could significantly speed up the survey. As ecological target, we used five slices of bread forming an X on the ground ([Fig. 14E](#)). An example of an artificial marker has been the drone backpack, in particular one of the corners of its box ([Fig. 14D](#)).

Regarding the number of GCPs collected in each surveyed area, approaches adopted in previous researches have been taken into account: in physical geography, where SfM is used, it is recommended to use a minimum of three GCPs (or target) with XYZ coordinates to scale and georeference the point cloud ([Smith et al., 2016](#)). As a general rule, larger the number of GCPs, larger the final accuracy of the model. For example, [Javernick et al. \(2014\)](#) decided to use a large number of GCPs, even as high as 95, distributed throughout the study area in a 100 m grid, but with a low image overlap of 70-60%, the latter being an important parameter to obtain a greater alignment of images and to reduce the distortions on the resulting Orthomosaics, as suggested by [Gerloni et al. \(2018\)](#), [Bonali et al. \(2019b\)](#), [Krokos et al. \(2019\)](#) and [Antoniou et al. \(2019\)](#). Further authors considered a lower number of GCPs but a higher image overlap: for example, [Vollgger et al. \(2016\)](#) used 12 GCPs (randomly distributed) with an image overlap of 85-75 %, whereas [Esposito et](#)

al. (2017) used 15 GCPs (uniformly distributed over the area) with 80-60% of overlap. The UAV flight strategy adopted for the present research has been chosen to reach a good compromise between battery consumption, survey time, area extension, data resolution and accuracy of the models: photos have been collected in a range of 90-85% overlap along the path and 80-75% in lateral direction, thus allowing a larger areal coverage.

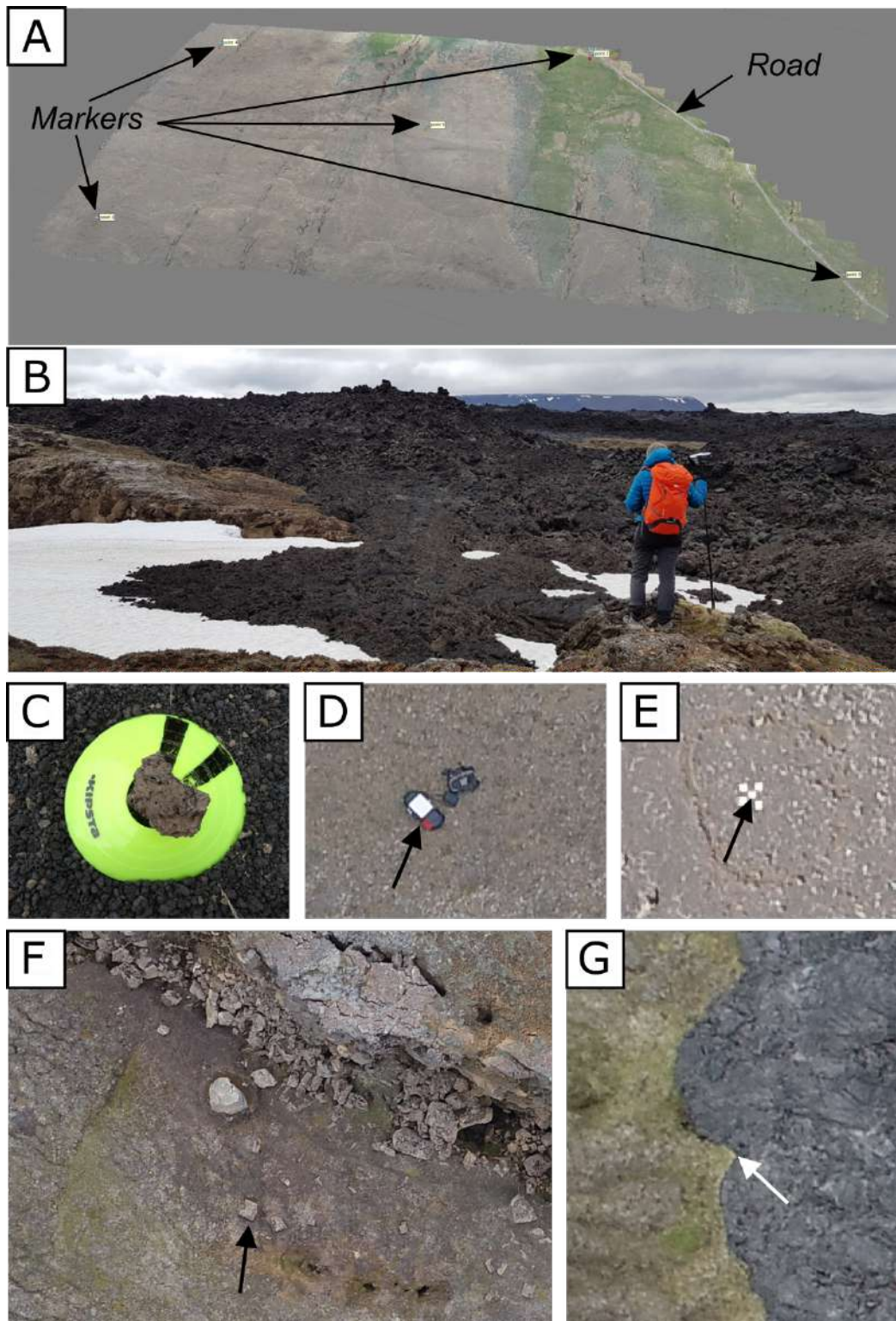


Figure 14 (A) Example of Ground Control Points used to georeference the model, (B) Operator collecting Ground Control Points on a natural target, (C) Artificial target as large as 20 cm, where the uppermost black band has been considered, (D) Corner of drone gray box (that is as large as 35 cm), (E) Five slices of bread adjusted to form a X, where we collected the corner of the central one (as large as 10 cm), (F) Lower right corner of massive rocks (the rock is as large as 1 m), (G) Lava flow margin where it forms a 90° angle (modified after [Bonali et al., 2020b](#)).

Another strategy to reduce the 'doming' effect on the resulting DTM/DSM (Tonkin and Midgley, 2016), consists of collecting aerial photos with an oblique inclination with respect to the ground (James and Robson, 2014). Nevertheless, this strategy results in greater consumption of the battery power and so it is useless for commercial UAVs equipped with low-cost GPS chipset, where GCPs collection is crucial to georeference the model; it is thus more efficient to design a GCPs survey as proposed in the present work.

The workflow used for the present research can be separated in two parts, dedicated to data collection (photos and Ground Control Points - GCPs) and to data processing and model reconstruction, respectively (Fig. 15A).

The first step of Part I consisted into the planning and management of UAV flight missions covering the areas to be surveyed, including paths orientations through the DJI Ground Station Pro software (<https://www.dji.com/ground-station-pro>). The flight strategy used in this work was selected in order to have a good compromise between survey time, battery consumption, area extension, data resolution and model accuracy. Many variables have been taken into account, including atmospheric conditions, for example the wind direction, that can affect UAV flight performance and therefore the quality of the captured images: it is much better to have the wind parallel to the main and longer paths (e.g. Fig. 15B). Furthermore, in order to reduce shadows around elevated features, we flew with the sun to the azimuth. Luckily, during the summer period in Iceland (July), the sun angle variation is minimal, and the illumination is almost uniform during the central part of the day. Part II of the workflow consists in data processing aimed at model reconstruction, in terms of DSMs and Orthomosaics. Photos have been processed with the use of Agisoft Metashape (<http://www.agisoft.com/>), a commercial Structure from Motion software (SfM). This software is becoming increasingly widely used in the geological community for both UAV and field-based SfM studies for its user-friendly interface, intuitive workflow and high quality of points clouds (Burns et al., 2017; Cook, 2017).

Matching features have been identified through SfM techniques in different photos, collected along a defined flight path (Fig. 15B), and were then combined to create a sparse and dense cloud (Figs. 15C-D), eventually a mesh, an Orthomosaic, and a DTM/DSM as final products (further details in Stal et al., 2012; Westoby et al., 2012). The first step was to obtain an initial low-quality photo alignment, only considering measured camera locations (Reference preselection mode). After that, photos with quality value <0.5, or out of focus, were excluded from further photogrammetric processing, as suggested in the user manual of the software (Agisoft LLC, 2018). The focal length and photo

dimensions were automatically detected by the program after the import of digital images and then used for the subsequent calibration of the intrinsic parameters of the camera (principal point coordinates, distortion coefficients). After this first quality check, we added Ground Control Points (GCPs) in all photos, where available, in order to: *i*) scale and georeference the point cloud (and thus the resulting model); *ii*) optimize extrinsic parameters, such as estimated camera locations and orientations; *iii*) improve the accuracy of the final model. We then realigned the photos using high accuracy settings: as a result of this step, camera location and orientation were better established, and the sparse point cloud was computed by the software (e.g. [Fig. 15C](#)).

The next step consisted in reconstructing the dense point cloud (e.g. [Fig. 15D](#)), calculated from the sparse point cloud, using a Mild depth filtering and medium quality settings. The mesh was reconstructed considering a Height field surface, the dense cloud as source data for a Medium number of Face count. Finally, since the DSM could be generated both by the Mesh and by the dense cloud as source data, we preferred the latter to obtain a better resolution, referring the DSM to the geographic coordinate system (WGS84); the Orthomosaic was generated considering the DSM as surface (and thus the WGS84 system).

On the Orthomosaics obtained through UAV surveys, the opening direction and net amount of opening of extension fractures have been quantified by assessing the direction and measuring the length of a line connecting two piercing points on each side of a fracture (in a GIS environment). All these measurements were made only along extension fractures that are at least 50 m away from a scarp, so as to avoid local gravity effects. Moreover, opening amounts were also collected along N109°-striking transects, each spaced 1 km in a N-S direction; this was done with the purpose of evaluating along-rift variations in the extensional strain parallel to the average direction of plate spreading affecting this part of Iceland ([DeMets et al., 1994, 2010](#); [Metzger et al., 2011](#); [Hjartardóttir et al., 2012](#); [Drouin et al., 2017](#)).

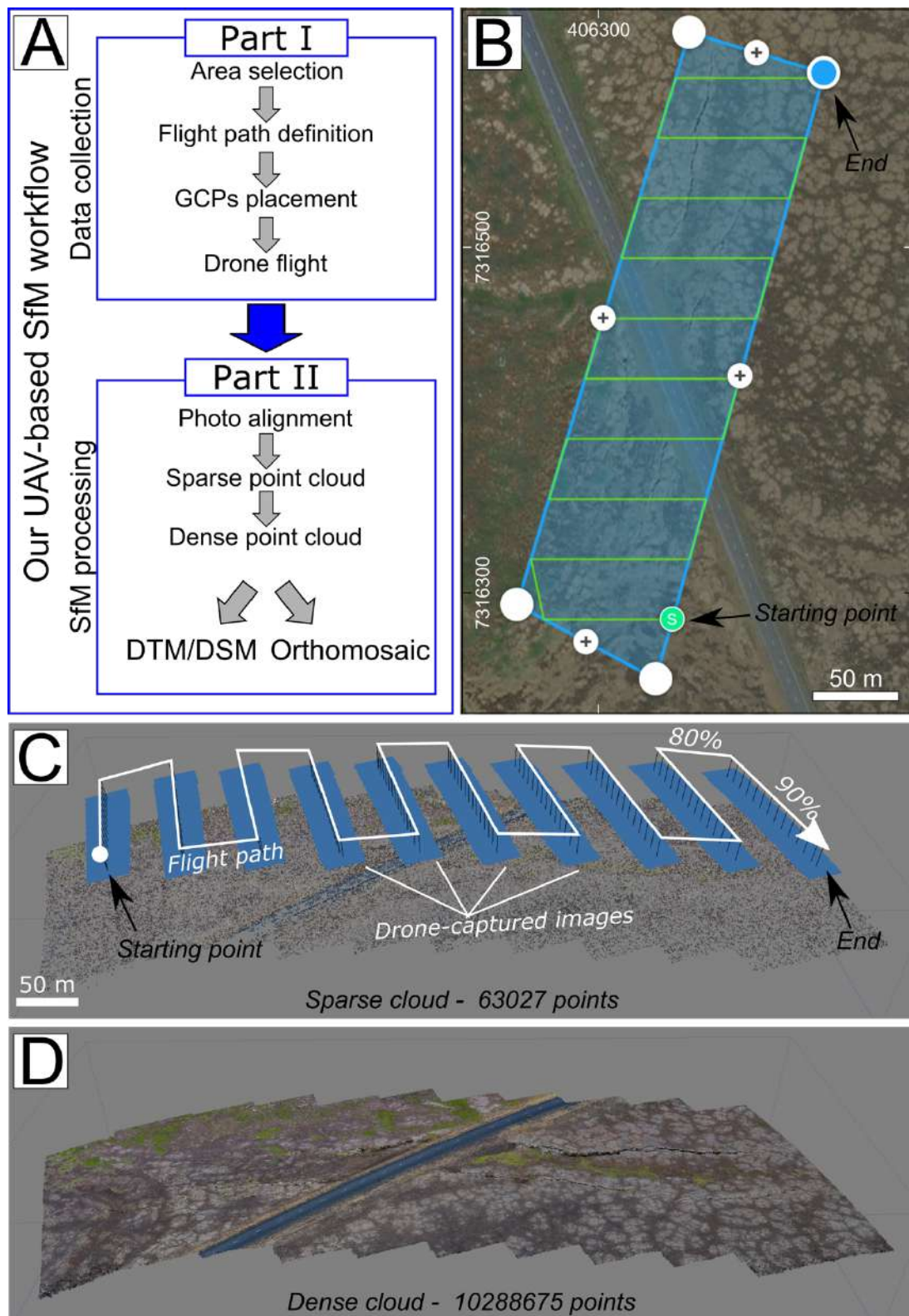


Figure 15 (A) Overall workflow used in the present research to generate DSMs and Orthomosaics using SfM software, (B) UAV flight path (green line) at 50m of flight height. Wind conditions have also been taken into account. Blue square indicates the surveyed area, (C) Sparse and (D) Dense cloud generated by SfM software. Suggested overlap among pictures is also reported. Computed

camera positions are represented as blue rectangles, black lines show the pitch angle and camera orientation (modified after [Bonali et al., 2019a](#)).

3.2.3 UAV surveys: testing flight heights

An assessment of the best flight height to be used during drone surveys of volcano-tectonic structures has been performed: in fact, UAV flights were completed at heights of 50 m and 100 m during a preliminary campaign within the Theistareykir Fissure Swarm in order to choose the best height for collecting the most-suitable data, with high quality, for volcano-tectonic purposes. Different aspects were taken into account: *i*) number of surveyed features; *ii*) time of flight; and *iii*) level of accuracy. Furthermore, to verify the accuracy of the resulting models, the same kind of quantitative measurements were taken in the same points both in the field and on Orthomosaics and DSMs, in order to make a comparison and thus to determine the accuracy of the remotely-quantified ones.

After the tests described in detail hereunder, the identified best height has been applied for all the UAV surveys of the present research. The resulting Orthomosaics and DSMs of Key area 1 (location shown in [Fig. 28](#)) from UAV flight heights of 50 meters and 100 meters are shown in [Figure 16](#): the resulting resolution that has been reached is of 2 cm and 8 cm respectively ([Bonali et al., 2019a](#)).

The area is characterized by the presence of two main normal faults, striking NNE-SSW, affecting the 2.4 ka old lavas. The main fault segments that outline the graben morphology (Faults n. 1, 2 and 3) are shown in [Figure 16D](#). Two fault scarps face to the WNW and one to the ESE, defining a graben that is about 30 m wide. Several extension fractures are also present. As shown in the DSMs ([Figs. 16C-D](#)), the western part of the area has a general altitude higher than the eastern part, and the central part of the graben is always located in the collapsed area. Furthermore, the western block of the graben is higher than the eastern one, as shown in the topographic profiles. The vertical offset of scarps measured at several locations in the field shows a maximum value of 2.35 m in the western and 1.4 m in the eastern part ([Fig. 16C](#)). These data have been compared to the vertical offset obtained by DSMs resulting from SfM ([Fig. 17F](#)): the difference in vertical offset is always lower than 0.25 m, whereas the averaged difference is equal to 0.13 m (st. dev. = 0.05) and 0.12 m (st. dev. = 0.07) (flight height of 50 and 100 m respectively).

Extension fractures have also been surveyed in order to collect and compare the fracture dilation and opening direction data measured in the field at 12 sites with measurements remotely

quantified on Orthomosaics from UAV surveys (Bonali et al., 2019a). Rose diagrams from field data and from UAV surveys reveal N-S to NNE-SSW-striking fractures (Figs. 17A-B-C), with opening directions ranging from N88° to N121° (Fig. 17D) and dilation ranging from 0.14 m to 1.07 m (Fig. 17F). Much more importantly, averaged opening direction is always between N106° and N108° and the difference between averaged values measured in the field and with the UAV (considering both 50 m and 100 m of flight height) is just 1.9° and 1.4°, respectively. More in detail, extension fractures show an average difference of measured dilation (between UAV and field data) of 0.04 m (st. dev. = 0.03) in the case of 50-m-flight height and 0.07 m (st. dev. = 0.05) in case of 100-m-flight height UAV surveys. The difference in opening direction is equal to 5.7° (st. dev. = 3.0) in the first case and 6° (st. dev. = 3.6) in the latter case (Fig. 17E). Moreover, the differences between measurements of vertical offsets are shown in Figure 17F: there is no clear tendency to overestimate or underestimate measurements if field results and UAV surveys are compared.

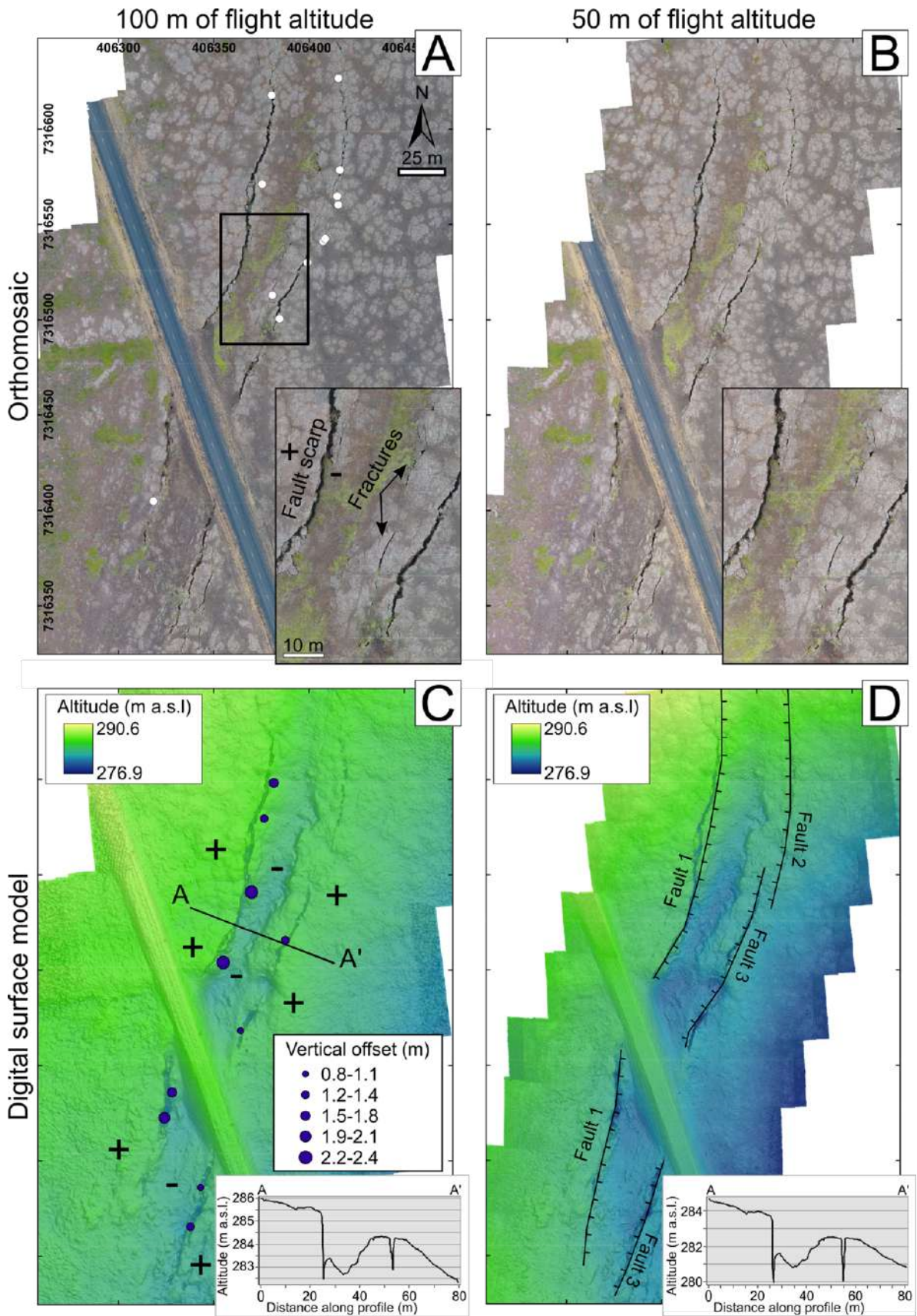


Figure 16 Orthomosaics (A-B) and Digital Surface Models (C-D) of Key area 1 (location in Fig. 28) from UAV surveys at a flight height of 100 m (A-C) and 50 m (B-D) respectively. In the lower right corner of **Figures A and B**, same detail of fracture field and fault scarps. In the lower right corner of

Figures C and D (DSMs), same topographic profile A-A' is represented. '+' and '-' symbols represent uplifted/subsided blocks. Altitudes are shown as a colour range (legend in figure). White dots in Figure A and blue dots (scaled with vertical offsets) in Figure C represent 10 sites of field measurements. Figure D contains faults n.1, 2 and 3; slip profiles of these faults are shown in Figure 17 (modified after Bonali et al., 2019a).

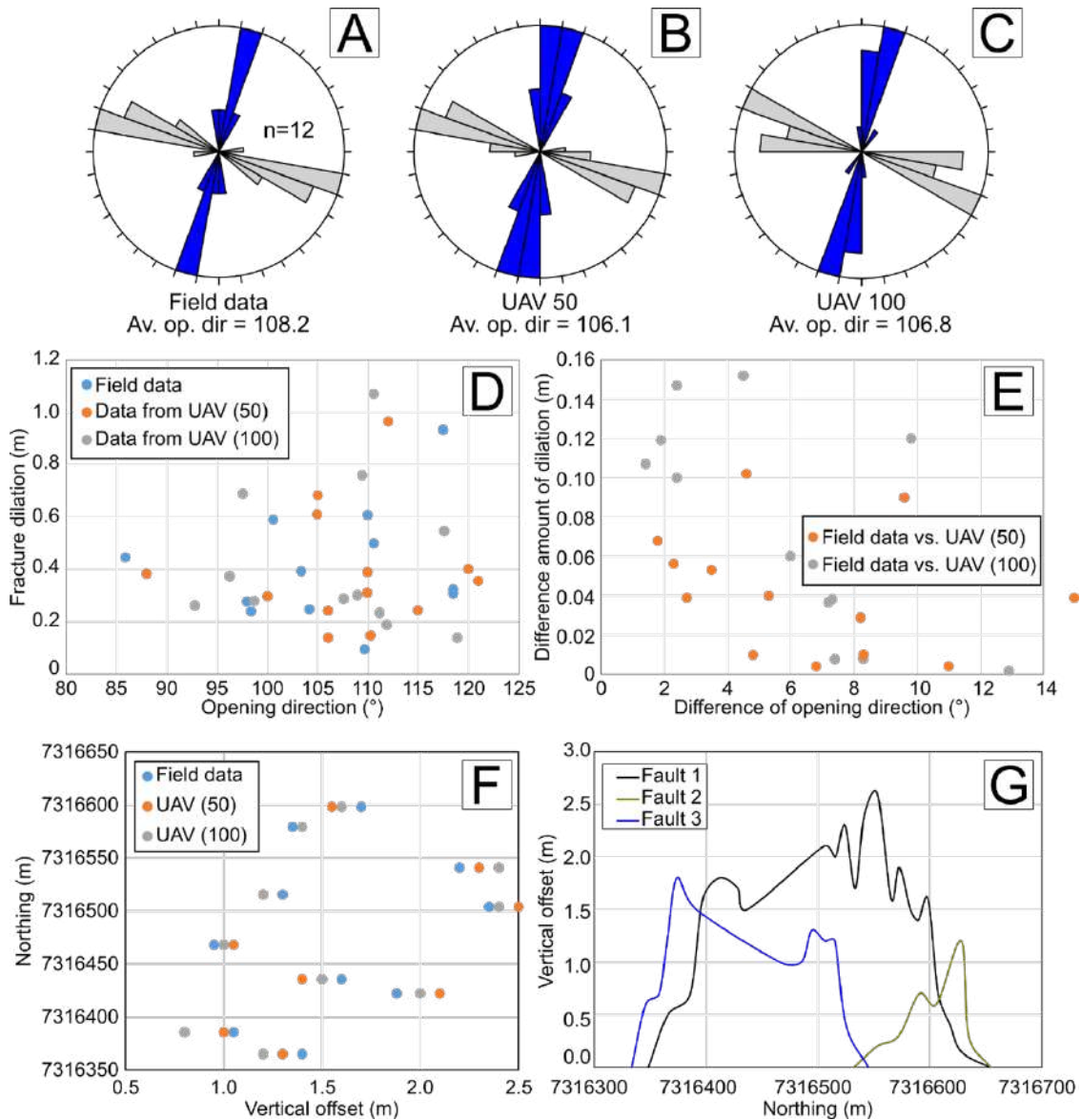


Figure 17 Rose diagrams showing azimuth (blue) and opening direction (grey) of extension fractures measured in the field (A), and on Orthomosaics by UAV surveys at a flight height of 50 m (B) and 100 m (C), (D) Opening direction vs. fracture dilation for field data and SfM by UAV surveys at both flight heights, (E) Difference in opening direction vs. difference in amount of dilation between field-acquired data and flight surveys at both heights, (F) Vertical offsets measured in the field and by SfM by UAV surveys at both flight heights, (G) Slip profiles of fault scarps located within the graben in

Key area 1 (location in Fig. 28): vertical offsets have been remotely measured on the DSMs (modified after Bonali et al., 2019a).

By comparing field data with UAV data, a good match both regarding fault vertical offsets and fracture dilation/opening directions has been found.

The Orthomosaics and DSMs of Key area 2 (location shown in Fig. 28) resulting from UAV surveys at flight heights of 50 meters and 100 meters, with a resolution of 2 cm and 8 cm respectively, are shown in Figure 18. At a general level, the area is characterized by NNE-SSW-striking extension fractures that affect 8-10 ka old lava units (Fig. 10).

The level of detail of surveys at each flight height can be appreciated from the insets in the lower right corner of Figs. 18A-B, which represent the same area. In particular, the blue inset in each of the latter figures shows a zoomed view of an example of extension fracture, where piercing points are clearly visible. The altitude of the area is lower to the south and to the north than in the central part, as confirmed by field observations (Figs. 18C-D). Furthermore, the topographic profile A-A' shown in Figures 18C-D highlights the presence of a roughly-2-m bulge, in correspondence of the extension fractures, possibly related to the presence of a dyke underneath (review in Tibaldi, 2015). The lighter colour that can be seen inside the extension fractures in Fig. 18D, which is related to the 50-m-flight height survey, reveals that the lower the flight height of the survey, the higher the possibility of reaching deeper levels within fractures. Since the good match between field and UAV data, regarding the opening direction and dilation, has already been demonstrated for Key area 1, here we focus on a different aspect.

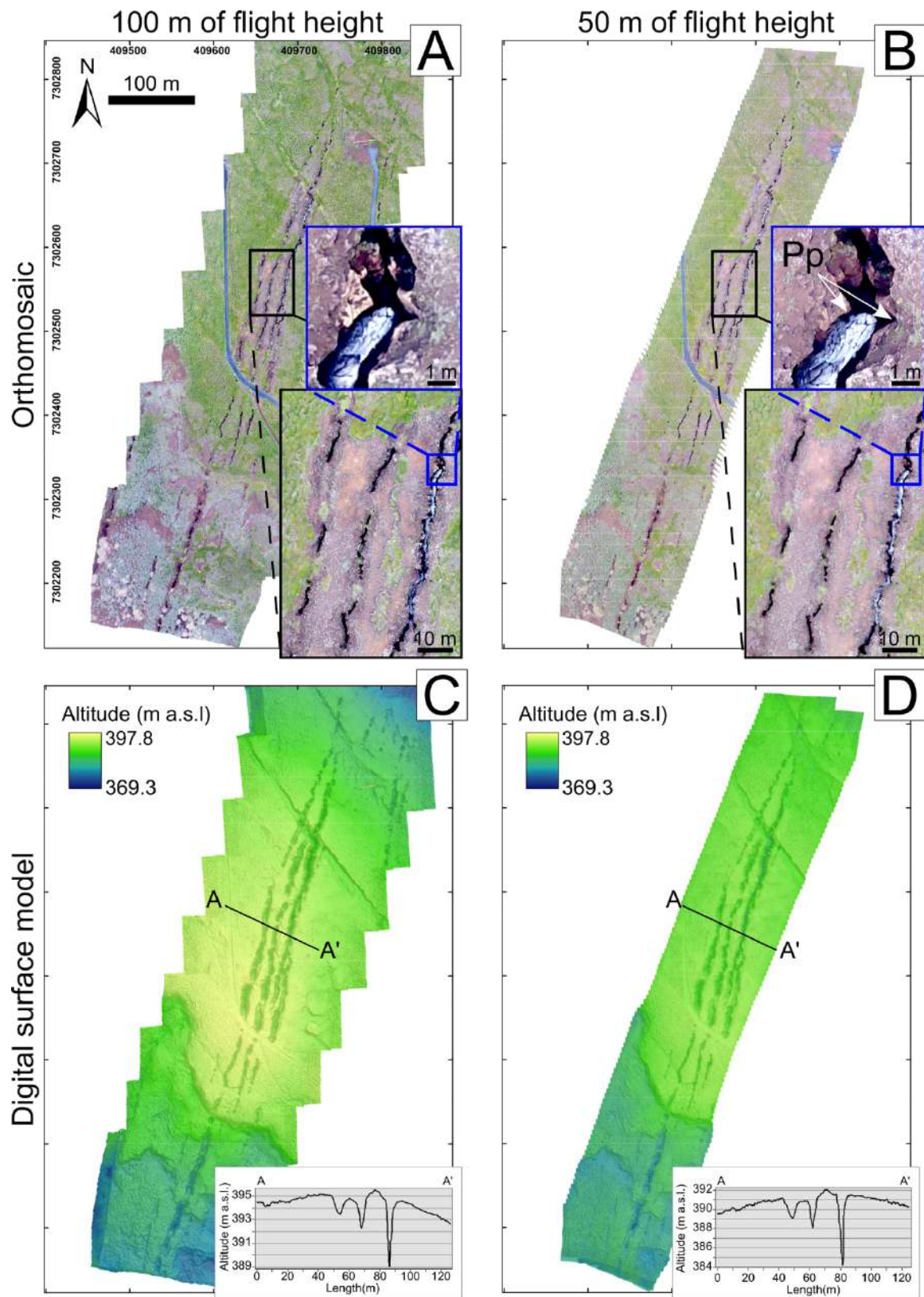


Figure 18 Orthomosaics (A-B) and Digital Surface Models (C-D) of Key area 2 (location in Fig. 28) from UAV surveys at a flight height of 100 m (A-C) and 50 m (B-D), respectively. In the lower right corner of Figures A and B, same detail of fracture field (black inset) and zoomed view of each fracture (blue inset). Piercing points (Pp) are indicated in Figure B. In the lower right corner of Figures C and

D (DSMs), same topographic profile A-A'. Altitudes are shown as a color range (legend in figure) (modified after [Bonali et al., 2019a](#)).

We present a comparison among different Orthomosaics aimed at accurately measuring the amount of opening and opening directions of extension fractures ([Figs. 19A-B-C](#)). Although the resolution of the satellite image ([Fig. 19A](#)) is very high (50 cm – image from Worldview-2 sensor, Catalogue ID 1030050051F92D00), it is not enough to provide accurate quantitative measurements of opening directions, and thus it does not represent a valid alternative to field measurements. Differently, Orthomosaics from UAV surveys at different heights (100 m and 50 m, [Figs. 19B-C](#) respectively) are suitable for tracing the line connecting piercing points along the fracture representing the opening vector, which is characterized by a direction and *modulo*. In both cases of this example, opening vectors have been traced by the same operator and by using the same methodology: on the best-resolution Orthomosaic, associated with 50-m-flight height survey ([Fig. 19C](#)), it has been possible to recognize and measure 7 opening vectors, only one more than in the Orthomosaic in [Figure 19B](#). [Figure 19D](#) represents a scatter plot of opening direction versus fracture dilation measured on the 100-m-flight height (grey dots) and 50-m-flight height (orange dots) Orthomosaics. Regarding the overall Key area 2, 34 opening vectors have been recognized on the Orthomosaic associated with 100-m-flight height survey and 40 opening vectors associated with 50-m-flight height survey. Much more important, the 33 common points of measurements for the two sets of data have been compared ([Figs. 19E-F](#)); the average opening direction is 107.9° and 108.1° for UAV100 and UAV50, respectively. The difference in opening direction is always lower than 12° and the average value is 3.4°. Regarding the dilation, the difference is always lower than 0.15 m with an average value of 0.07 m. Since dilation and opening direction quantifications are almost the same in both Orthomosaics, even though they have different resolutions, we suggest that a flight height of 100 m provides enough and reliable results for studying extension fractures.

Furthermore, UAV images enable distinguishing the area enlarged due to erosion with respect to the original fracture geometry ([Fig. 12F](#)), and thus the view from above allows to quantify more correctly the dilation amount.

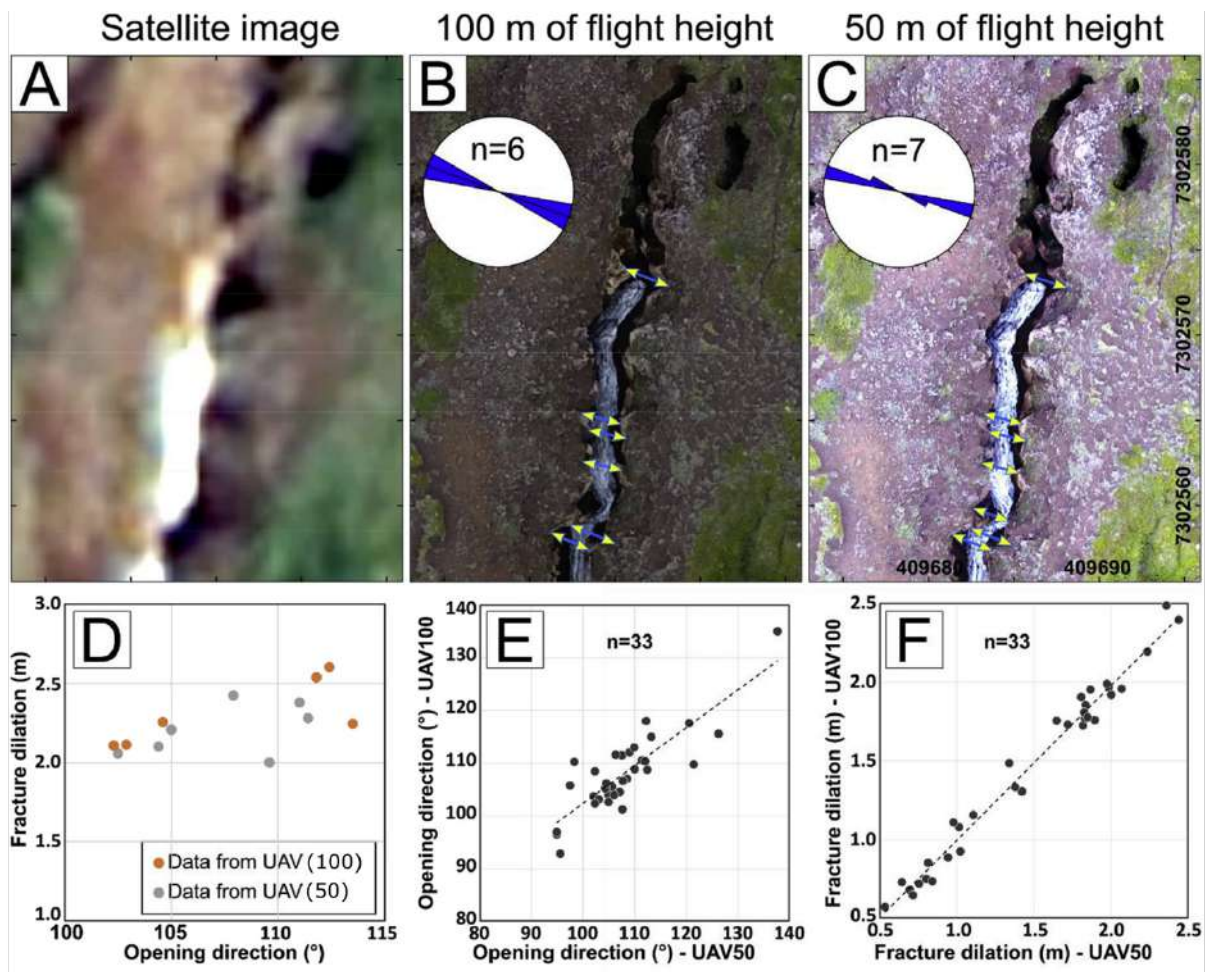


Figure 19 (A) Satellite image (0.5 m resolution) belonging to the Key area 2 characterized by 8-10 ka old lavas. See [Figure 28](#) for location. (B-C) Orthomosaic resulting from UAV survey at a flight height of 100 m and 50 m, respectively, in the same area as [Figure A](#). Rose diagrams of opening directions measured through piercing points of [Figures B](#) and [C](#) are shown. (D) Scatter plot with opening direction vs. fracture dilation, referring to Orthomosaics shown in [Figures B](#) (orange dots) and [C](#) (grey dots), respectively. (E-F) Scatter plots of opening direction/fracture dilation measured on Orthomosaic from flight heights of 100 m (Y-axis) and 50 m (X-axis) respectively (modified after [Bonali et al., 2019a](#)).

This concept is also highlighted in [Figure 20](#), where a comparison of measurements of opening direction between field data and data coming from the two different flight heights is shown. In some cases, the difference between such two kinds of measurements is higher. This occurs in particular when surveying an highly eroded fracture at the surface: in this case, the view from above that can be reached with a drone helps to take a more accurate value of opening direction at deeper levels ([Fig. 12F](#)). Furthermore, these graphs show that the trend lines associated with the measure distribution are almost identical, proving that 100 m is a suitable flight height for surveying

extension fractures and collecting plenty of data. Thus, this flight height has been used in all UAV surveys presented in this research.

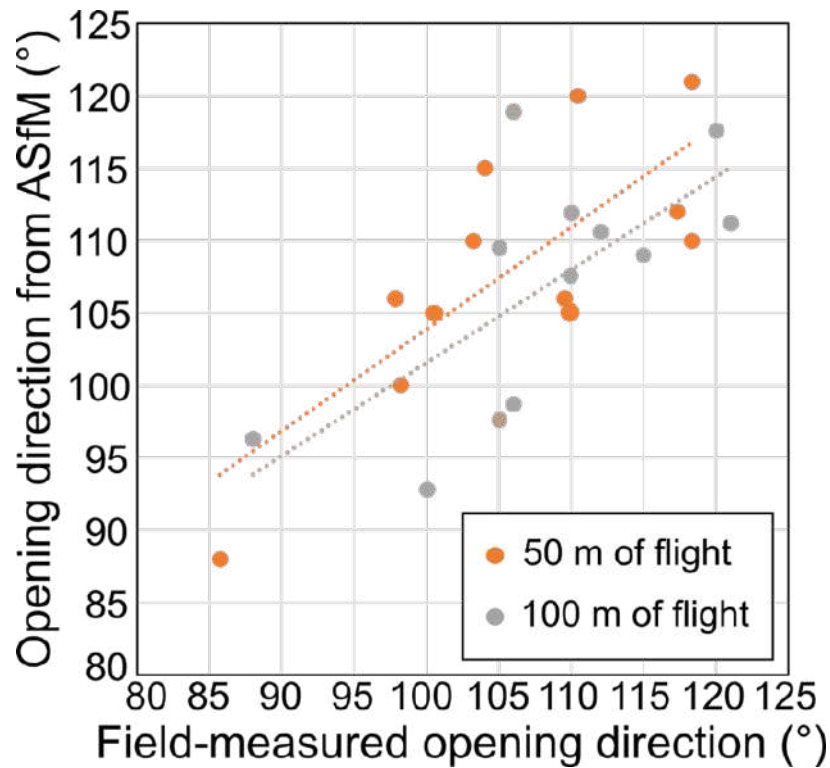


Figure 20 Plot of opening directions measured in the field (x-axis) versus opening directions measured on Orthomosaics derived from UAV surveys (y-axis) both at a flight height of 50 m and 100 m (modified after Bonali et al., 2019a).

3.3 Numerical modeling

Numerical models have been developed through Coulomb 3.3 freeware software, implemented by the USGS and several Universities (www.coulombstress.org; Lin and Stein, 2004; Toda et al., 2011), which allows to investigate magmatic intrusions-induced deformation patterns. Calculations are made in an elastic halfspace with uniform isotropic elastic properties following Okada's formulae (1992). Coulomb 3.3 software allows to calculate static displacements, strains, and stresses at any depth caused by fault slip, magmatic intrusion, or dike expansion/contraction: many evidences show that faults and magmatic systems interact, and that static stress changes influence intrusions and eruptions (e.g. Currenti et al., 2008). Geologic deformation associated with strike-slip faults is also a useful application.

Most importantly, it is possible to calculate static stress changes caused by the displacement of magmatic bodies which can be defined as "source faults" (Figure 21). The shear and normal

(clamping when the stress increases and unclamping when the stress decreases) components of the stress change are resolved on “receiver” fault planes, with specified strike, dip and rake. The position, geometry and slip of the source faults and the position and geometry (also rake) of the receiver fault influence the resulting shear stress increase or decrease, whereas the normal stress change (clamping or unclamping) is independent of the receiver fault rake. This modeling is based on the Coulomb failure criterion,

$$\Delta\sigma_f = \Delta\tau_s + \mu' \Delta\sigma_n,$$

in which failure is hypothesized to be promoted when the Coulomb stress change is positive. Here, $\Delta\sigma_f$ is the change in failure stress on the receiver fault caused by slip on the source fault(s), $\Delta\tau_s$ is the change in shear stress (reckoned positive when sheared in the direction of fault slip), $\Delta\sigma_n$ is change in normal stress (positive if the fault is unclamped), and μ' is the effective coefficient of friction on the fault.

For this research, I focused on the calculation of Coulomb stress change induced by a dyke with a width of 2 meters, located at depths between 0.2 km and 1 km, on right- and left-lateral strike-slip faults of varying orientation (20° strike intervals from NNW-SSE to NNE-SSW). The upper crust has been modelled as an elastic isotropic halfspace characterized by:

- a Young's modulus $E = 40$ GPa, based on [Mithen \(1982\)](#), [Lin and Stein \(2004\)](#) and [Toda et al. \(2005\)](#), which corresponds to the stiffness of the isotropic elastic material;
- a Poisson's ratio $\nu = 0.25$, based on [Lin and Stein \(2004\)](#) and [Toda et al. \(2005\)](#), which corresponds to the ratio of the contraction (perpendicular to the applied load) and the extension or axial strain (in the direction of the applied load), when a material is stretched;
- a friction coefficient $\mu = 0.4$, which is within the range 0.0-1.0, that is considered typical of the crust ([Lin and Stein, 2004](#); [Toda et al., 2005](#)).

The stress field defined as input is based on data from the World Stress Map database ([Heidbach et al., 2008](#)). The grid size has been defined as 0.5 km x 0.5 km.

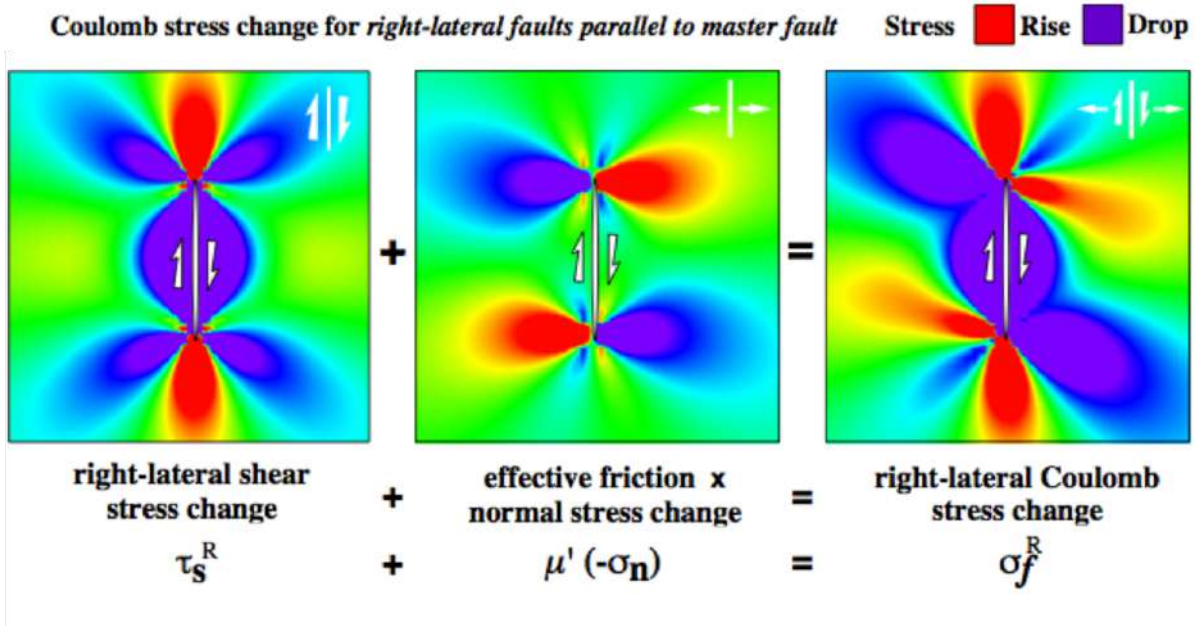


Figure 21 Illustration of the Coulomb stress change (modified after *King et al., 1994*). The panels show a map view of a vertical strike-slip fault embedded in an elastic halfspace, with imposed slip that tapers toward the fault ends. Stress changes are depicted by graded colors; green represents no change in stress.

Chapter 4

Results – Northern Volcanic Zone

In the present chapter, results will be presented separately for the Theistareykir ([Section 4.1](#)) and Krafla Fissure Swarms ([Section 4.2](#)).

4.1 Northern Volcanic Zone: Theistareykir Fissure Swarm

[Section 4.1.1](#) presents a throughout survey of the complete structural architecture and kinematics of the Theistareykir Fissure Swarm (ThFS), comprising 7500 measurements along 6124 post-Late Glacial Maximum (LGM) extension fractures and faults, and 685 pre-LGM structures. Data have been collected in the framework of several campaigns over the past years with BSc and MSc students. [Section 4.1.2](#) focuses on key areas within the central ThFS, where extensive field and UAV surveys have been performed due to the presence of plenty of well exposed Holocene extension fractures and normal faults ([Pasquaré Mariotto et al., 2015](#); [Tibaldi et al., 2016a](#)).

4.1.1 Entire Theistareykir Fissure Swarm

In this section, results of the investigation of the complete structural architecture and kinematics of the Theistareykir Fissure Swarm (ThFS) will be presented. Data have been collected through extensive field surveys and with the aid of drone mapping with centimetric resolution. The goal of this part of the present research has been to define, with an unprecedented detail, the kinematics of the rift, in terms of the geometry, direction and amount of opening of both faults and extension fractures. Measuring several sites along each structure allowed to collect a great amount of data (about 7500 measurements), helpful for assessing the strike-slip components and distinguishing the different roles played by tectonic and magma-induced forces in affecting post-Late Glacial Maximum (LGM) deformation within the ThFS. The focus here is on: *i*) the geometric characterization of all the structures, with special reference to the strike and length of faults and fractures; *ii*) the quantification of the opening directions of extension fractures and the possible presence of shear components; *iii*) the estimation of the strain amount along the rift; *iv*) the assessment of the origin of the structures; and *v*) the evaluation of the overall working of the rift.

4.1.1.1 Geometry of faults and extension fractures

The Theistareykir Fissure Swarm is composed by faults and extension fractures that affect both pre-LGM (Last Glacial Maximum) and post-LGM lithostratigraphic units. Structures affecting pre-LGM units, which are a total of 685 and are divided into 679 normal faults and 6 extension fractures, are concentrated mainly in the western part of the area and strike predominantly from N-S to NNE-SSW, subordinately NE-SW and NW-SE (Figs. 22A and 22C). Normal faults dip mostly E and W, and subordinately SE to S, whereas extension fractures strike NNE-SSW and NW-SE. The structures belonging to the Husavik Flatey Fault, which also affect mostly pre-LGM units, strike mostly NW-SE (Fig. 22B). The orientation of post-LGM structures, that reach a total of 6124, is shown in Figs. 22A and 22D: by considering all the structures together, or separated (4181 extension fractures and 1943 faults), it is possible to notice a preferential NNE-SSW strike, whereas minor sets strike N-S and NE-SW (Figs. 22A-D-E-F).

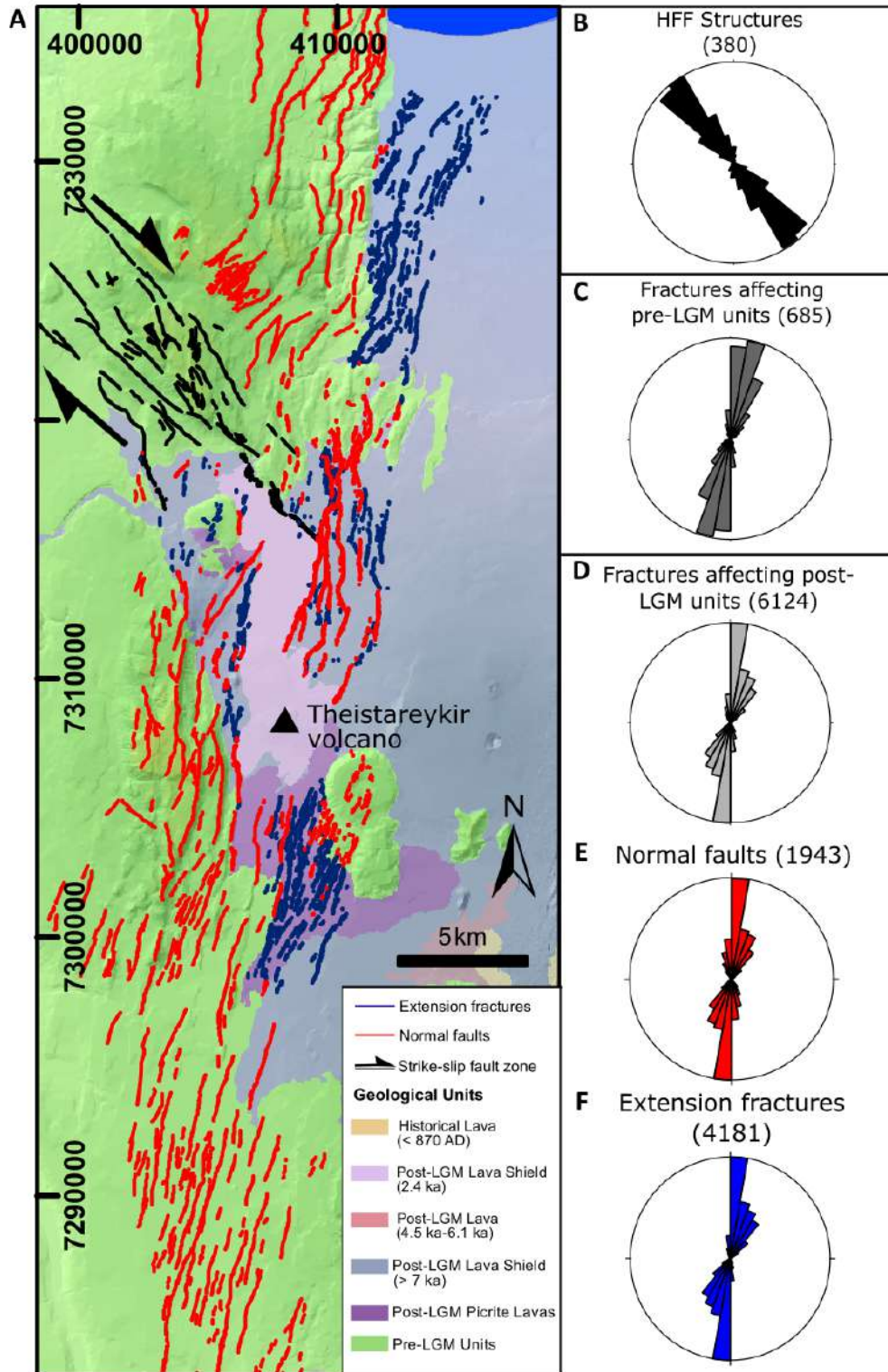


Figure 22 (A) Map of faults (red) and extension fractures (blue) identified in the study area. Rose diagrams show: (B) the strike of all the HFF faults, (C) the strike of all structures affecting pre-LGM units, (D) the strike of all structures affecting post-LGM units, (E) the strike of faults only affecting post-LGM units, and (F) the strike of extension fractures only affecting post-LGM units. Geological

units after *Saemundsson et al. (2012)*. Spatial reference: WGS 84 / UTM zone 38N (*Tibaldi et al., 2020b*). Location shown in *Figure 9*.

As shown in *Figs. 23A-B*, the length of pre-LGM structures is generally longer than the structures affecting post-LGM units: in fact, the longest pre- and post-LGM structures measure 7652 m and 3062 m, respectively, with an average length of 488 m and 39 m. Among post-LGM structures, normal faults present a maximum length of 3062 m and an average length of 45 m (*Fig. 23C*), while extension fractures are 634 m long, with an average length of 36 m (*Fig. 23D*).

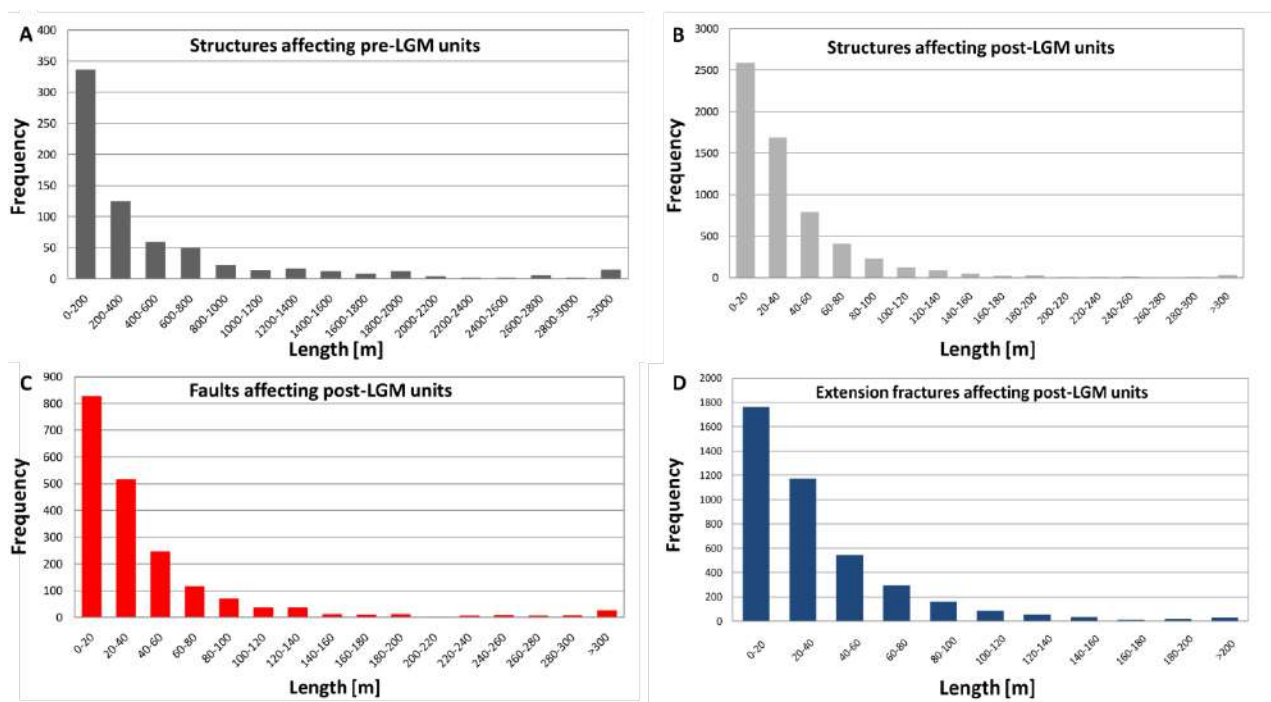


Figure 23 (A) Length distribution of pre-LGM structures, (B) Length distribution of post-LGM structures (C) Length distribution of post-LGM faults, (D) Length distribution of post-LGM extension fractures (*Tibaldi et al., 2020b*).

4.1.1.2 Opening directions

Opening direction values at extension fractures have been surveyed throughout the whole rift zone, totaling 1633 measurements, that show a N27°-174° range, with an average of N111° and a standard deviation of 17° (*Figure 24A*). Such opening directions can be related to Easting (*Fig. 24B*) and Northing (*Fig. 24C*), revealing range variations depending on the location within the rift. In fact, the western part of the rift is characterized by directions mostly in the N80-140° range, whereas they

trend mostly between N100° and N160° in the eastern part. On the other hand, the southern and central sections of the rift show similar ranges, mostly in the order of N80-140°, whereas the northern part shows an increased range mostly of N100-160°. The combination of the two graphs highlights a clockwise rotation from around N60° to N160° of opening directions from the southwestern to the northeastern part of the ThFS. As shown on Fig. 24D, such clockwise rotation corresponds to the clockwise rotation of extension fracture strikes from NW-SE to NE-SW.

Although this indicates that the two are linked together, as will be discussed in the related section, it is worth underscoring the wide data scatter, which may indicate a more complex relation.

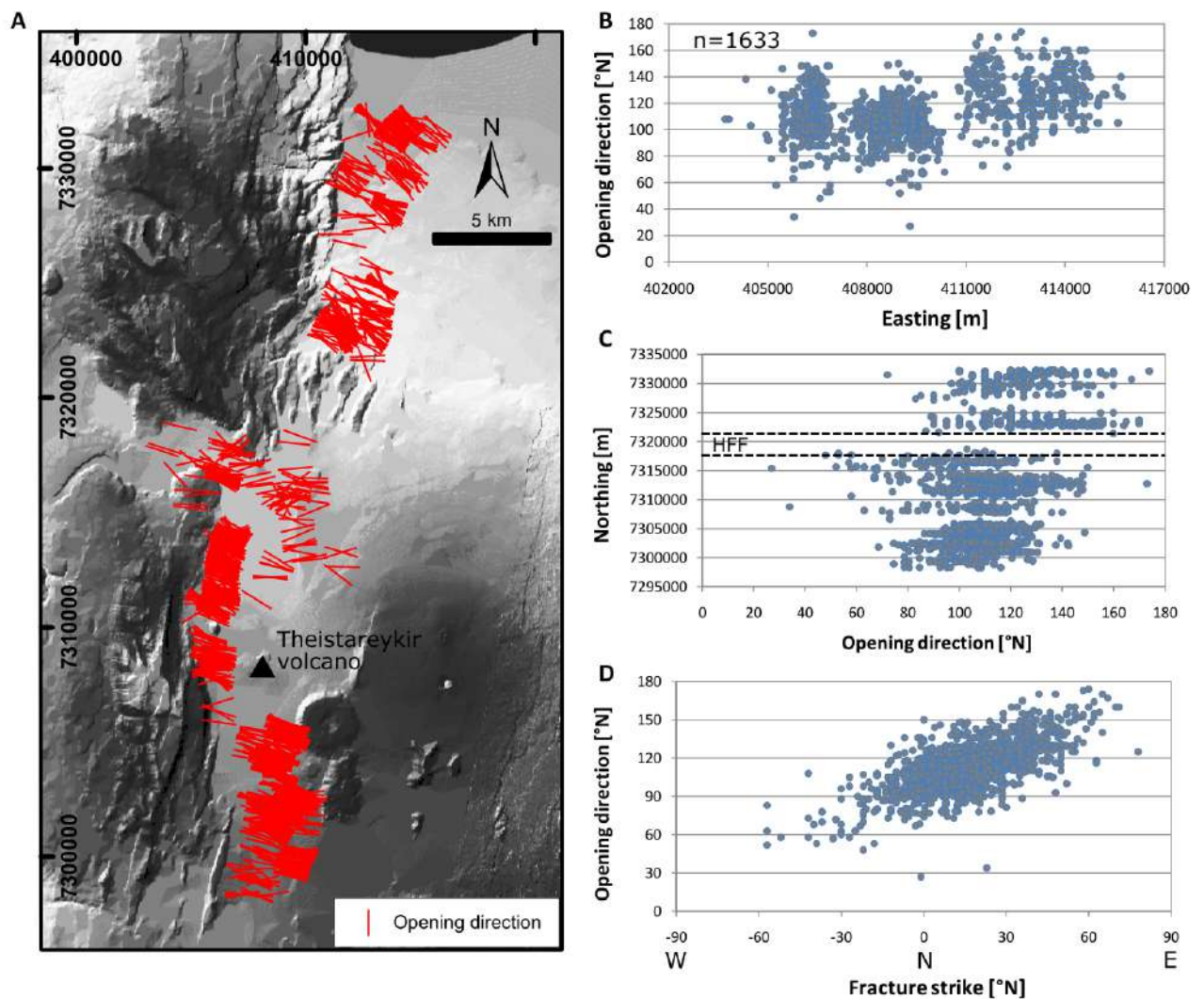


Figure 24 (A) Map of opening directions (lines) obtained along extension fractures, (B) graph of opening directions (Y axis) vs. Easting (X axis), (C) graph of opening directions (X axis) vs. Northing (Y axis), the intersection with the HFF is shown, (D) graph of opening directions (Y axis) vs. extension fracture strikes (X axis). Spatial reference: WGS 84 / UTM zone 38N (Tibaldi et al., 2020b).

4.1.1.3 Strike-slip components

A strike-slip component of motion along extension fractures, which results on opening obliquely to their strike, has been observed at 1129 out of 1633 structural stations (Figure 25). In fact, only 31% of the entire fracture population analyzed here shows pure extension, considering the fact that all fractures with less than 5° of lateral component have been considered as such. In view of the above, out of 1633 total data, 504 are pure extension fractures (31%), 854 fractures show a right-lateral component (52%) and 275 show a left-lateral component (17%). The average value of the strike-slip component is +6.4°, and the standard deviation is 14°, suggesting a predominance of the right-lateral component.

In particular, the structures striking from N60°W to N10°W (Fig. 25A) show only right-lateral components, whereas left-lateral components are present along fractures striking N60-80°. Those striking N10°W to N60° can have both components, although it is possible to notice a gradual shift from right-lateral to left-lateral components, along with the clockwise rotation of fracture strike.

By plotting the opening direction azimuth with respect to the strike-slip component (Fig. 25B), it is possible to note a shift from left-lateral to right-lateral component, along with the clockwise rotation of opening directions. The red stripes indicate how the lateral component is expected to change in case of clockwise variations in fracture strike, according to the plate separation vector. The latter has been obtained as the average value (N109°) out of the available vectors; in the study area, based on geomagnetic data (as far back in time as 2.6 Ma) the long-term spreading vector is N104-106° (DeMets et al., 1994, 2010; Hjartardóttir et al., 2012). Based on GPS data from different time windows (1997-2011, 2006-2010, 2008-2014), the short-term spreading vectors are N109-115-112° (Metzger et al., 2011, 2013; Drouin et al., 2017).

The comparison of the strike-slip component with respect to Easting shows a slightly higher frequency of right-lateral components along the westernmost part of the rift (Fig. 25C). The comparison of the strike-slip component with respect to Northing indicates the more frequent occurrence of right-lateral components northwards (Fig. 25D).

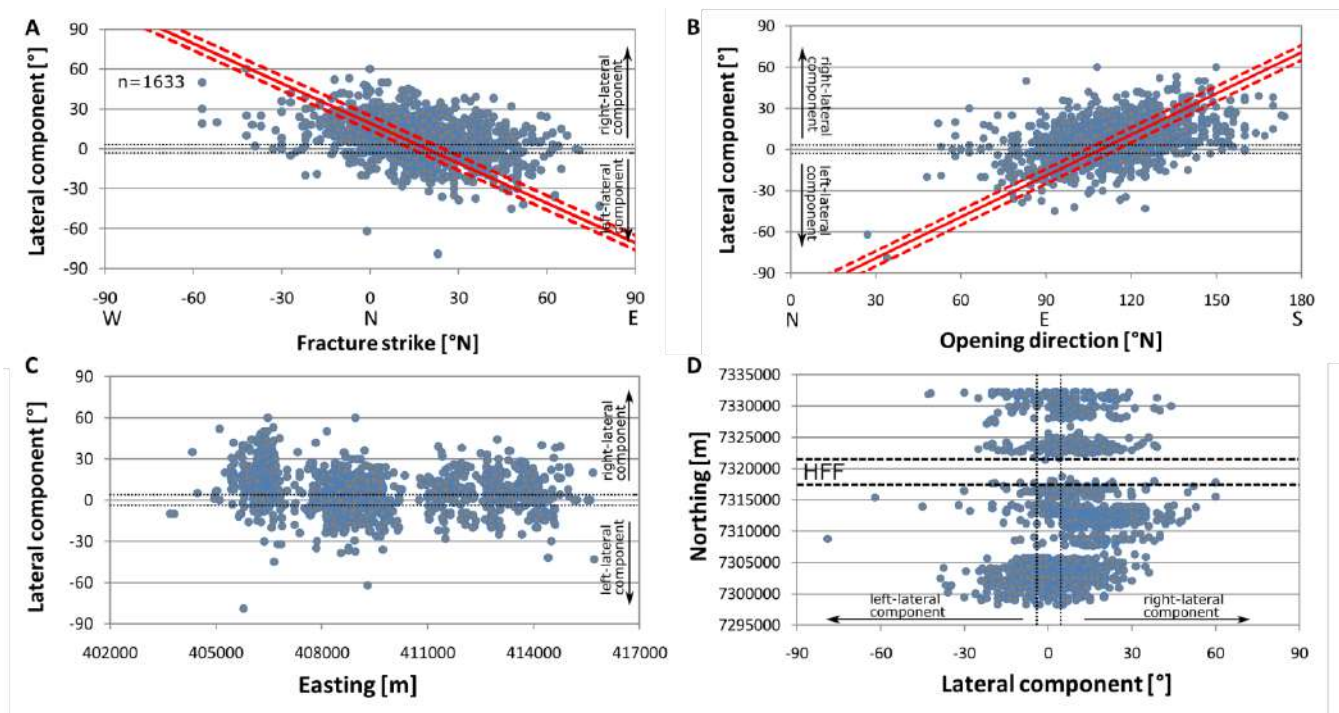


Figure 25 (A) Graph of the lateral component of opening directions (Y axis) with respect to fracture strike (X axis), (B) opening direction (X axis) vs. lateral component (Y axis). In (A) and (B), red stripes indicate how the lateral component is expected to change in case of variations of the values along the X axis, according to plate separation vector range (N104-115°). (C) graph of lateral component (Y axis) vs. Easting (Y axis), (D) graph of lateral component (X axis) vs. Northing (Y axis); the intersection with the HFF is shown. Black dashed lines enclose pure extension fractures, with lateral component values < 5°. Spatial reference: WGS 84 / UTM zone 38N (Tibaldi et al., 2020b).

4.1.1.4 Extensional strain

The extensional strain cumulated between normal faults and extension fractures (Figs. 26A-B) has been measured along N109°-striking paths, each spaced 1000 m in a N-S direction, parallel to the average long-term spreading direction, obtained as explained above. At extension fractures, net opening amounts have been quantified both in the field as well as on UAV-derived high resolution images, totalling 2745 measurements (1698 along extension fractures and 1047 along normal faults).

At normal faults, the horizontal extension has been calculated based on the downdip slip and the dip of the fault plane, averaged at a value of 75° (Forsslund and Gudmundsson, 1991). Extension fracture opening is in the 0.1-10 m range, with an average of 1.2 m, the higher values being in the

south-central part of the rift (Fig. 27A). Horizontal dilation values along normal faults are in the 0.1-9.5 m range, with an average of 1.4 m (Fig. 27B).

In regard to the extensional strain measured along the N109° transects, values have been calculated both considering only fractures affecting Post-LGM units and considering also fractures affecting Pre-LGM units. In the first case, the cumulated dilation is in the range of 3-6 m north of transect 11 (Fig. 27C). A minimum is observed at transect 12, and then a rather steady increase can be noticed southward as far as transect 21, where the cumulated dilation is = 35 m. Further south, the cumulated dilation decreases. If we consider also fractures affecting Pre-LGM units, the cumulated dilation is in the range 5-18 m north of transect 11, a minimum is reached at transect 13, and then an increase is observed up to transect 21. At transects 18-22, values coincide with the ones obtained considering only Post-LGM units. Going southward, dilation decreases between transects 23-27, whereas another peak can be observed at transect 28 (dilation = 34 m). Dilation values remain greater than 24 m between transect 29-31, showing a gradual decrease further south.

Regarding the number of fractures, it ranges mostly around 1-20 in Post-LGM units (Fig. 27D). This range is also valid in the rift section where there is the greatest value of cumulated dilation (i.e. between transect 20 and 22). This means that in this area the same amount of fractures takes up a larger deformation than in the other sections of the rift. Considering also Pre-LGM units, the number of fractures increases showing a range between 4 and 28.

The average fracture spacing is 0.40 km, with a maximum value of 1.35 km if we consider only fractures affecting Post-LGM units, whereas it presents an average value of 0.67 km and a maximum value of 1.52 considering also Pre-LGM units. (Fig. 27E).

In Post-LGM units, the area affected by dilation is wider in correspondence of the central sector of the ThFS (transects 17-19) (Fig. 27F). From here, it slightly increases northward from 0.9 km to 3 km, whereas it decreases southward from 4.5 km to 2 km. In the southernmost sector of the rift, each transect (36-40) intersects only one fracture, setting to 0 km the average spacing between fractures and the area of deformation. Taking into account also the Pre-LGM units, the width of the area affected by dilation stays the same between transects 17-19, whereas it increases going northward up to 11.5 km (transect 1); going southward it remains greater than 6 km up to transect 37, decreasing further south.

The stretch ratio (Fig. 27G) in Post-LGM units, calculated on the basis of the maximum width of the area affected by fractures (as wide as 9.8 km), ranges up to a maximum of 1.0035, with an average of 1.00084. Being generally constant in the northern part, it reaches a peak in the central

part (at transect 21), and it gradually decreases in the southern part. Considering also Pre-LGM units, the maximum width of the area affected by fractures is 11.5 km, which results in a maximum stretch ratio of 1.031, with an average of 1.011. Two peaks are observed at transects 21 and 28, with a decrease in the southern part, whereas in the northernmost part an increase can be noticed.

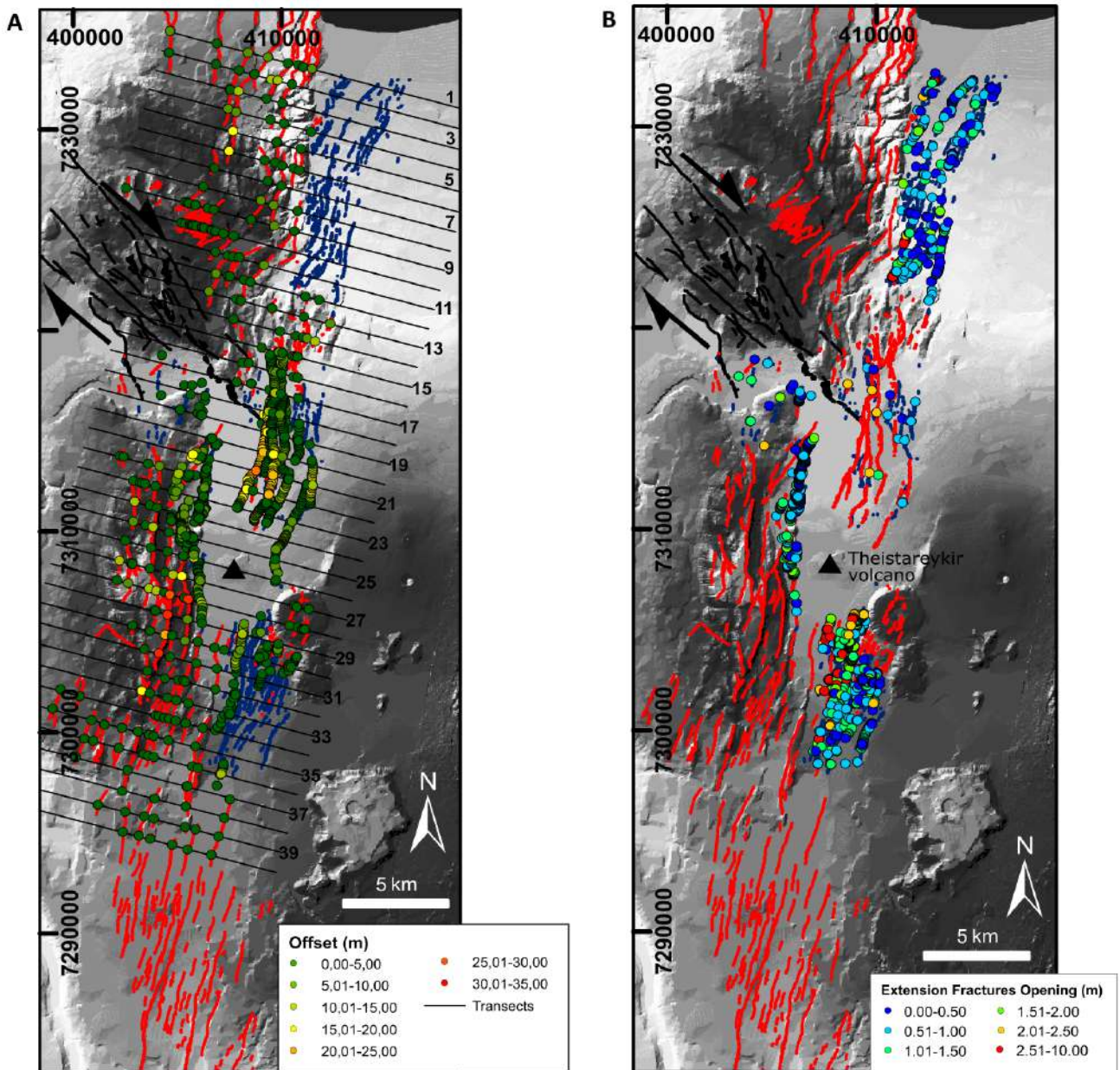


Figure 26 (A) Distribution of measurements of vertical offset values at normal faults and (B) net opening amount values at extension fractures. Black lines show transects along which extension was cumulated. Spatial reference: datum WGS 84/UTM zone 28N (Tibaldi et al., 2020b).

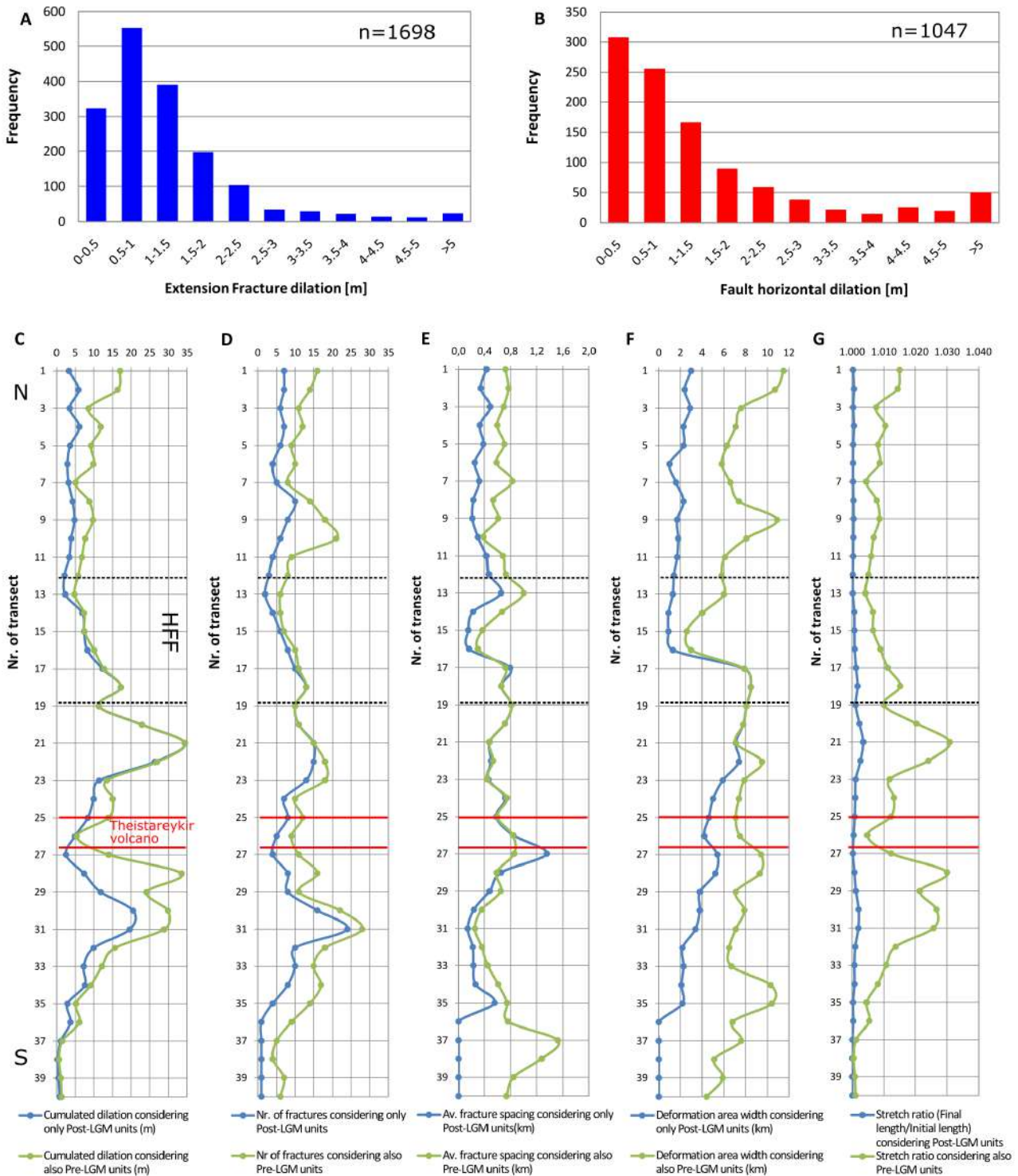


Figure 27 (A) Graph showing the frequency distribution of dilation at extension fractures, (B) Graph showing the frequency distribution of horizontal dilation at normal faults, (C) cumulated dilation and (D) number of fractures, (E) average fracture spacing and (F) deformation zone width, (G) stretch ratio, calculated both considering only Post-LGM units and considering also Pre-LGM units along WNW-ESE transects (shown as thin black lines in Fig. 25A) (Tibaldi et al., 2020b).

4.1.2 Theistareykir Fissure Swarm: focus on the central part of the rift

In this section, a focus on the central part of the rift is presented: data have been collected in order to evaluate the Holocene deformation through mapping of 397 structures, mainly related to extension fractures and subordinately normal faults in the Theistareykir Fissure Swarm, collecting 1098 and 21 structural data, respectively. This allowed to reconstruct the overall spreading direction and the stretch regarding 8-10 ka old lava units and thus to relate deformations in the area, comprising the presence of lateral components of motion, both to dyke intrusions and extensional tectonics.

4.1.2.1 Key areas selection

The key sites selected within the ThFS to perform extensive field and UAV surveys, named as Key areas 1 and 2 in [Fig. 28](#), are characterized by lava flows of different ages (2.4 and 8-10 ka, respectively, [Saemundsson et al., 2012](#)). The most recent lavas, in Key area 1, are affected by extension fractures and normal faults, with very small dilation and vertical offset, whereas older lavas, in Key area 2, are affected by several extension fractures with dilation amounts generally > 40 cm. An example of surveyed extension fractures is shown in [Figure 12](#). Quantitative measurements have been collected both in the field and on SfM-resulting Orthomosaics and Digital Surface Models (DSMs), created as explained in [Section 3.2.2](#). Furthermore, two different flight heights have been tested, 50 m and 100 m respectively, in order to find the best height to maintain to survey this kind of structures ([Section 3.2.3](#)). This approach was then applied to define the Holocene strain field within the Key area 3, characterized by 8-10 ka lava flows affected by hundreds of extension fractures and some normal faults ([Fig. 28](#)).

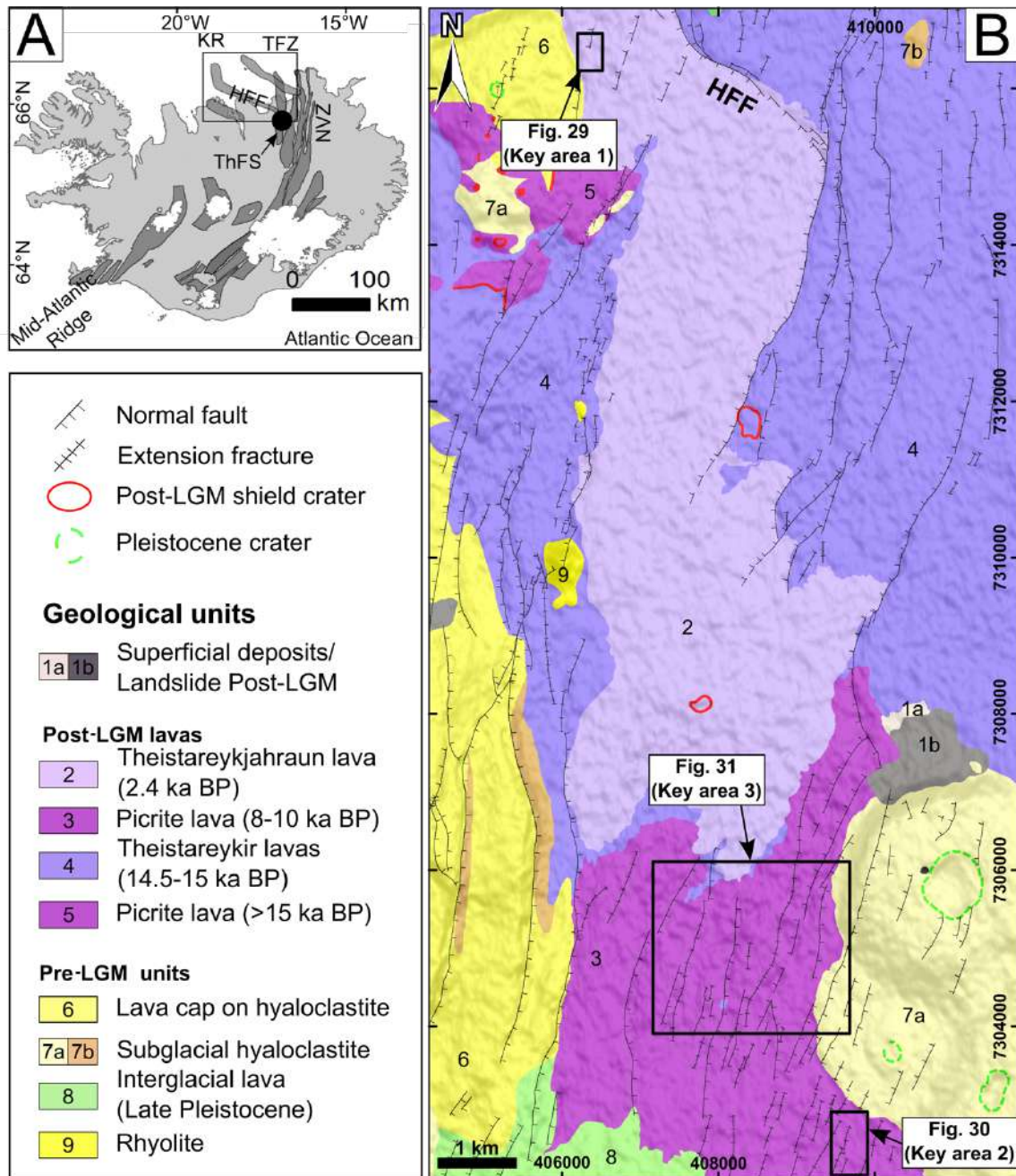


Figure 28 Geological map of the study area based on Saemundsson et al. (2012). Key areas are indicated as black rectangles. Figures 29, 30 and 31 are located. LGM = Last Glacial Maximum (modified after Bonali et al., 2019a). Location shown in Figure 9.

4.1.2.2 Data collection

The survey for Key area 1 (location in Fig. 28) is presented in Figure 29: the overall fracture azimuth in this area is N18.9°, the opening direction is N108.1°, dilation values range from 0.09 m to 1.21 m and the averaged fracture dilation is 0.38 m (Fig. 29A). The whole set of (mostly) N-S striking 69 fractures traced on the Orthomosaic is reported as a sketch in Figure 29B.

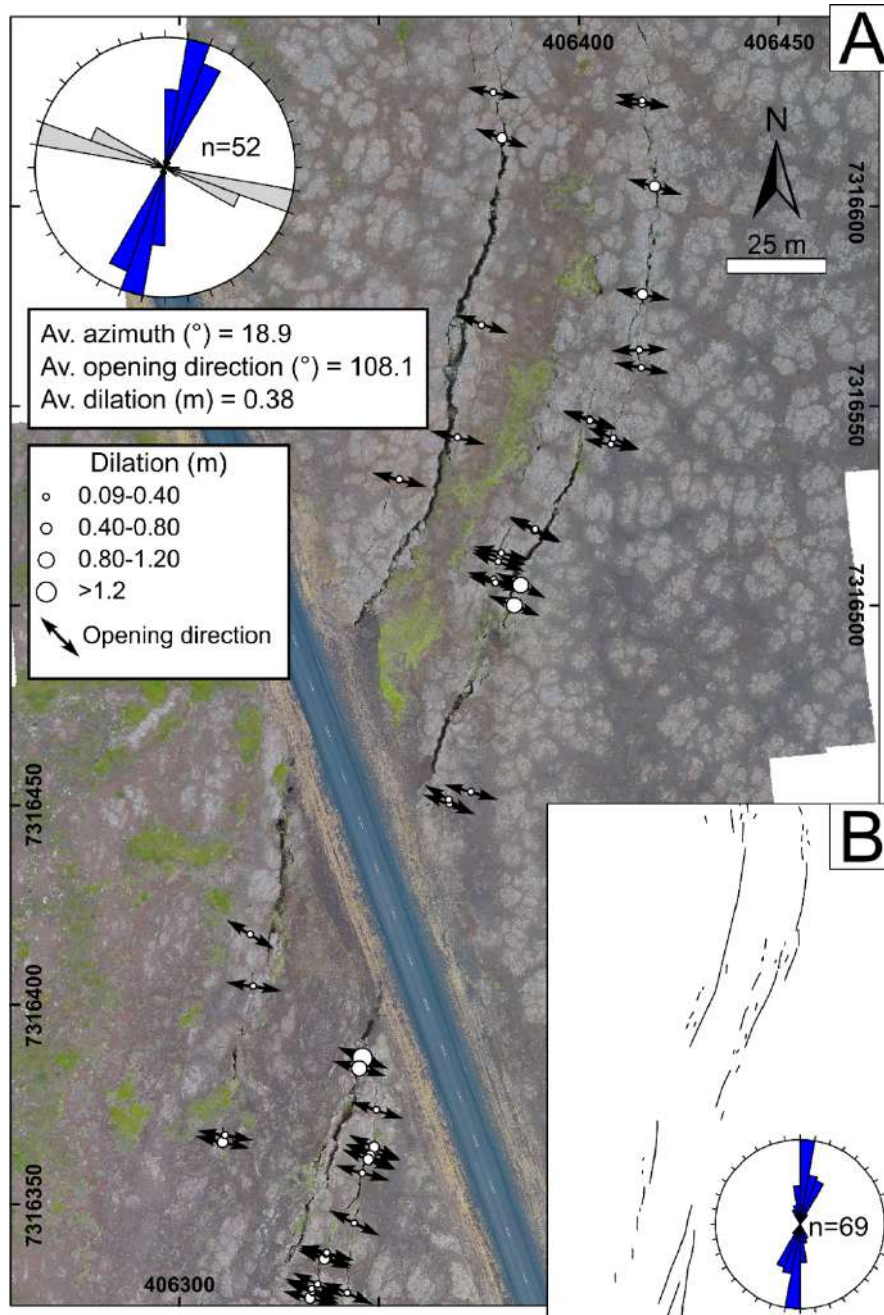


Figure 29 (A) Fracture dilation (in meters) and opening direction measured on the 8-cm-resolution Orthomosaic, related to a UAV survey at 100 m of flight height in Key area 1. A total of 52 measurements have been taken, as shown by the rose diagram in the upper left corner. Fracture azimuth (represented in blue in the rose diagram), opening direction (represented in grey in the rose diagram) and dilation (in meters) are provided, also as averaged values. (B) Sketch of fractures traced on the Orthomosaic. Rose diagram shows azimuth values for the 69 fractures (modified after Bonali et al., 2019a).

Figure 30 shows the survey results for Key area 2 (location in Fig. 28) on the Orthomosaic, resulting in the following: i) fracture dilation values range from 0.5 to 2.5 m; ii) the average azimuth

of fractures is N12.7°; *iii*) the average opening direction is N108°; and *iv*) the average fracture dilation corresponds to 1.44 m. Fractures belonging to this area (total of 68) have also been traced by hand on the 100-m-flight height Orthomosaic (Fig. 30B): according to the rose diagram, their azimuth is in the N-S to NNE-SSW range.

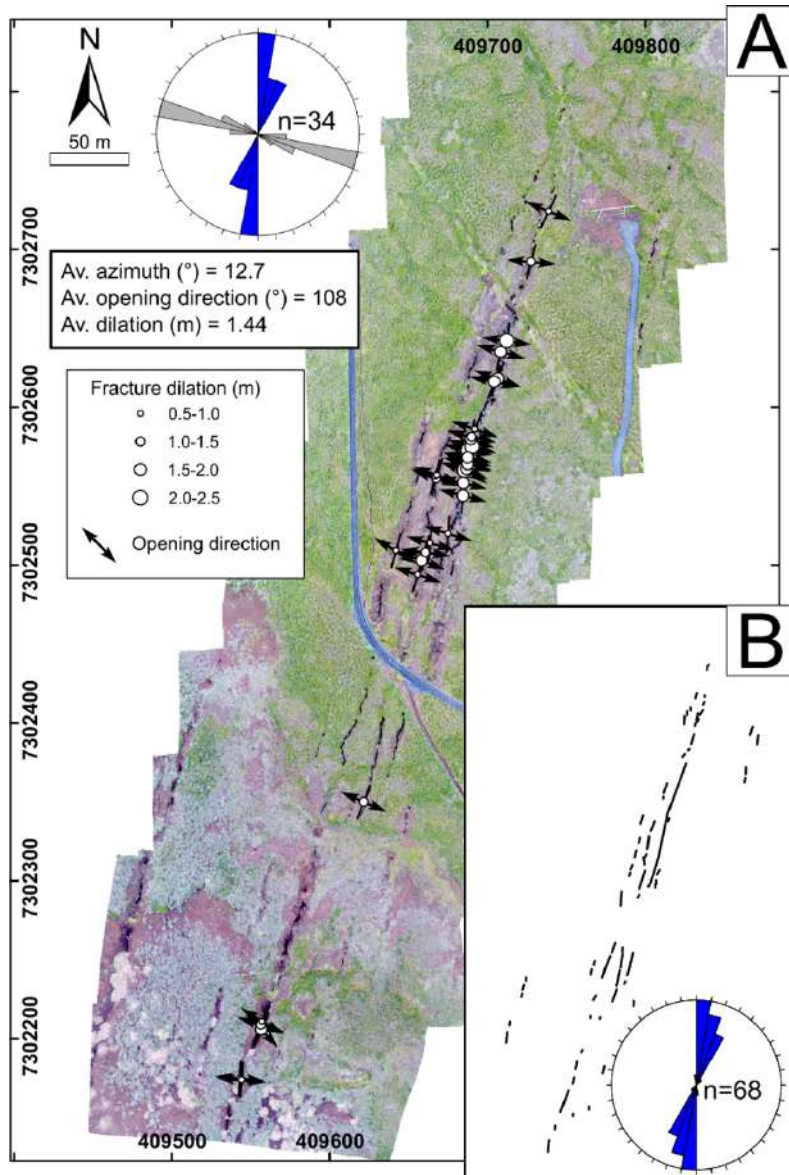


Figure 30 (A) Fracture dilation and opening directions measured on the 8-cm-resolution Orthomosaic, related to Key area 2. A total of 34 measures have been taken, as shown by the rose diagram in the upper left corner. Average fracture azimuth (blue in the rose diagram), average opening direction (grey) and average dilation (meters) are reported. (B) Sketch of fractures remotely traced on the Orthomosaic. Rose diagram shows azimuth values for the 68 fractures (modified after Bonali et al., 2019a).

Key area 3 (location in Fig. 28) has been surveyed for studying rifting processes in the 8-10 ka old lava units and for investigating the presence of strike-slip motions along extension fractures and normal faults. Thanks to the very high level of detail of the SfM-derived Orthomosaic, it has been possible to map each single fracture segment outcropping in the area: a total of 275 fracture azimuths, 275 opening directions and 275 dilation values (totalling 825 structural measurements at 275 single sites) has been collected along 260 fractures over an area of 2.5 km². The Orthomosaic is shown in Figure 31A.

The average opening direction is N108.2°, whereas the average azimuth of fractures corresponds to N13.9° (Fig. 30A) and dilation values range from 0.34 to 6.24 m. Spatial variations of opening direction and azimuth of fractures are shown in Figs. 31B-C-D-E. Figures 31B-D display the relation between opening directions, easting (Fig. 31B) and northing (Fig. 31D): the range increases moving eastward, and the maximum value increases up to N140-150°. The same occurs in relation with northing (Fig. 31D): generally speaking, the range of opening directions is wider and reaches higher values (N132°) with an increase in northing, apart from a higher value (comprised in the interval N140-150°) found towards the south. Figures 31C-E show the relation of azimuth of fractures with easting (Fig. 31C) and northing (Fig. 31E). As for opening direction values, also in this case the azimuth of fractures reaches higher values (up to N42°) going eastward and northward, and the range of possible azimuth values is wider. The total extensional component, measured along the 1.7-km-long white dashed line in Figure 31A, is 24.33 m, corresponding to a stretch of 1.013. Regarding the above calculation, thanks to the Orthomosaic resulting from SfM processing, the real fracture dilation has been collected on extension fractures (as shown in Figure 31F-G); regarding normal faults, the vertical offset, and the corresponding dilatational component, have been measured at a distance from the scarp that is enough to avoid any possible mistake induced by block tilting, erosion or gapping.

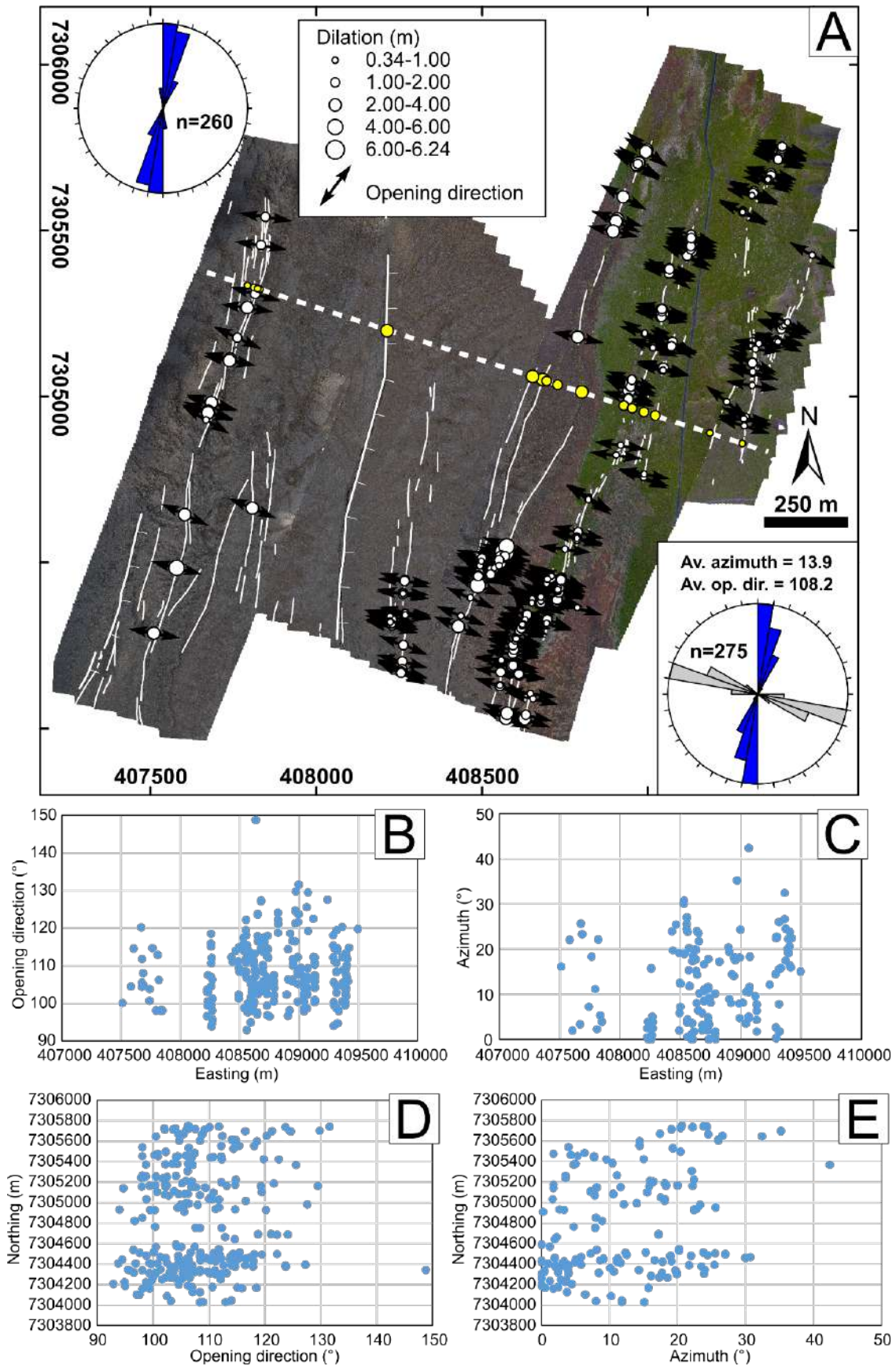


Figure 31 (A) Map of the 260 fractures (azimuth is reported in the upper left rose diagram) of Key area 3 (location in Fig. 28), mapped on the Orthomosaic. The rose diagram in the lower right corner reports fracture azimuth (blue in the rose diagram) and corresponding opening direction (in grey).

Faults and extension fractures are outlined in white, bars indicate downthrown block for normal faults. Graphs show fracture opening direction and azimuth vs. the easting (B-C) and the northing (D-E). Yellow dots represent locations where dilation has been quantified to calculate the stretch along the dashed white line, oriented N108° (modified after [Bonali et al., 2019a](#)).

The mapped 397 extension fractures and normal faults in all three Key areas (located in [Fig. 28](#)) have azimuth between N-S and NE-SW, with the maximum frequency at N-S and NNE-SSW (rose diagram in [Fig. 32A](#)). Left and right-lateral components are also present, with a predominance of the latter ([Figs. 32B-C](#)). In particular: *i*) 148 fractures have a lateral component $< 5^\circ$ (and thus are considered mainly extensional); *ii*) 170 fractures show a right-lateral component $> 5^\circ$ and are mainly in the strike range $N0^\circ$ - $N25^\circ$; and *iii*) just 42 fractures show a left-lateral component $> 5^\circ$ and are in the strike range of $N15^\circ$ - $N30^\circ$ ([Figs. 32B-C](#)).

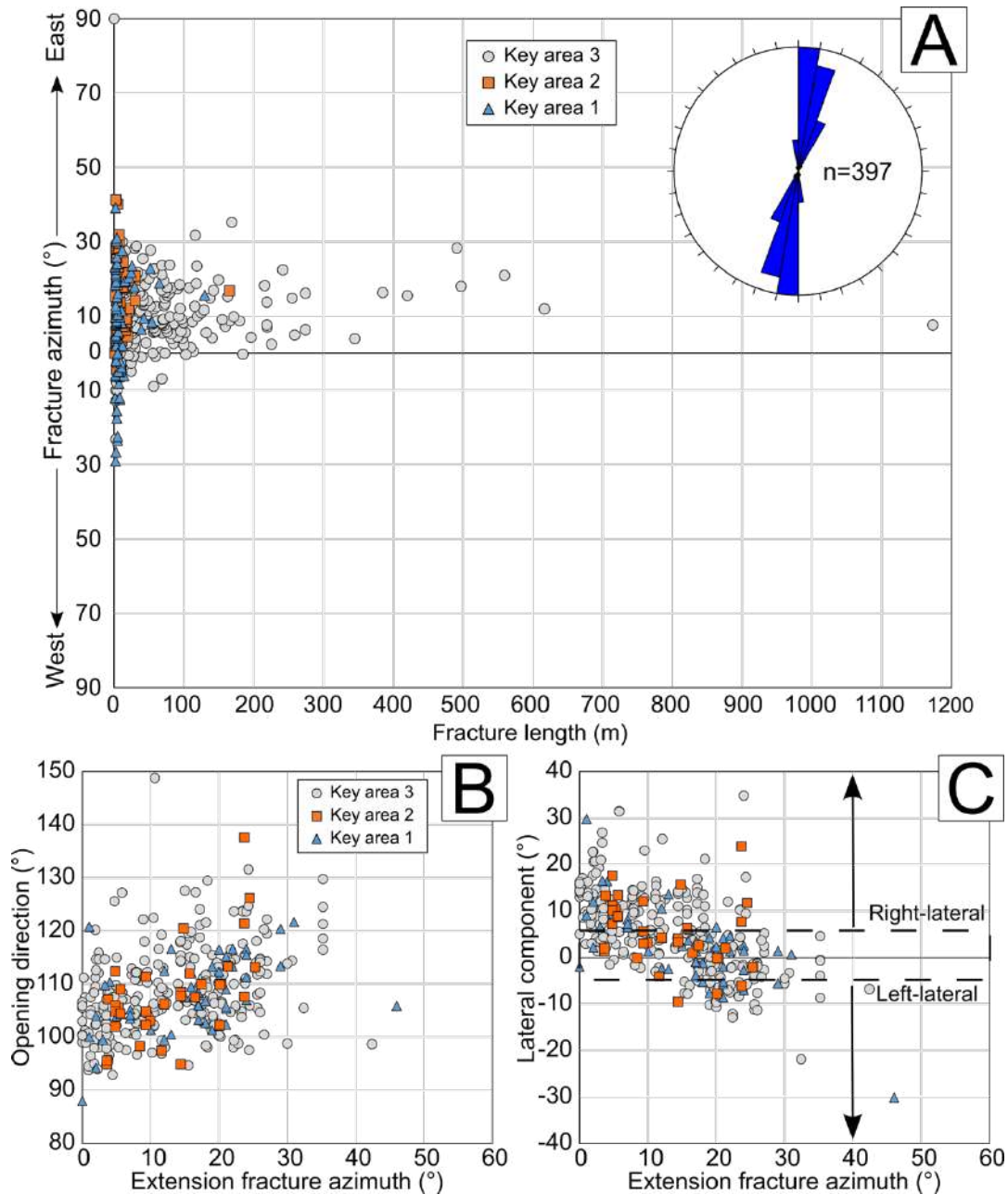


Figure 32 (A) Distribution of fracture length versus azimuth for the three key areas. Rose diagram of overall fracture azimuth is reported. (B-C) Shear components of fractures: (B) Fracture azimuth vs. opening direction, and (C) Fracture azimuth vs. right-lateral and left-lateral component. All three key areas located in Fig. 28 are represented (modified after Bonali et al., 2019a).

4.2 Northern Volcanic Zone: Krafla Fissure Swarm

In this part of the present research, results of a detailed systematic analysis of all the faults and extension fractures of the western part of the Krafla Fissure Swarm (Figure 9) through UAV surveys and field checks are presented (Section 4.2.1). In this area, structures are mostly oriented N to NNE

and have been subject to volcano-tectonic deformation since 100 thousand years ([Angelier et al., 1997](#); [Hjartardóttir et al., 2016c](#)).

The lava flows outcropping in this study area belong to three basaltic, Holocene main sequences: the oldest two sequences are 11-12 ka old, whereas the uppermost lavas belong to the 1975-1984 AD Krafla eruptive period ([Fig. 33](#)).

More in detail, the study area is characterized by the presence of the Hituholar late Pleistocene hyaloclastite ridge ([Figs. 39A-B](#)), which will be discussed more in detail through a 1:5000 lithostratigraphic survey aimed at detecting lateral components of motion in [Section 4.2.2](#). The age of the hyaloclastite deposits can be ascribed to the Weichselian High Glacial, at 29.1-12.1 ka BP. The 2.5-km-long hyaloclastite ridge, elongated N-S, is affected by several N-S to NNE-SSW-striking normal faults and extension fractures, and is surrounded by post-LGM horizontal lavas: also, this deformation zone is marked by a range of features, such as topographic bulging, parallel extension fractures, and narrow grabens affected by local floor uplift, and thus represents a peculiar spot in which to investigate the relation between magmatic intrusions and the occurrence of strike-slip motions.

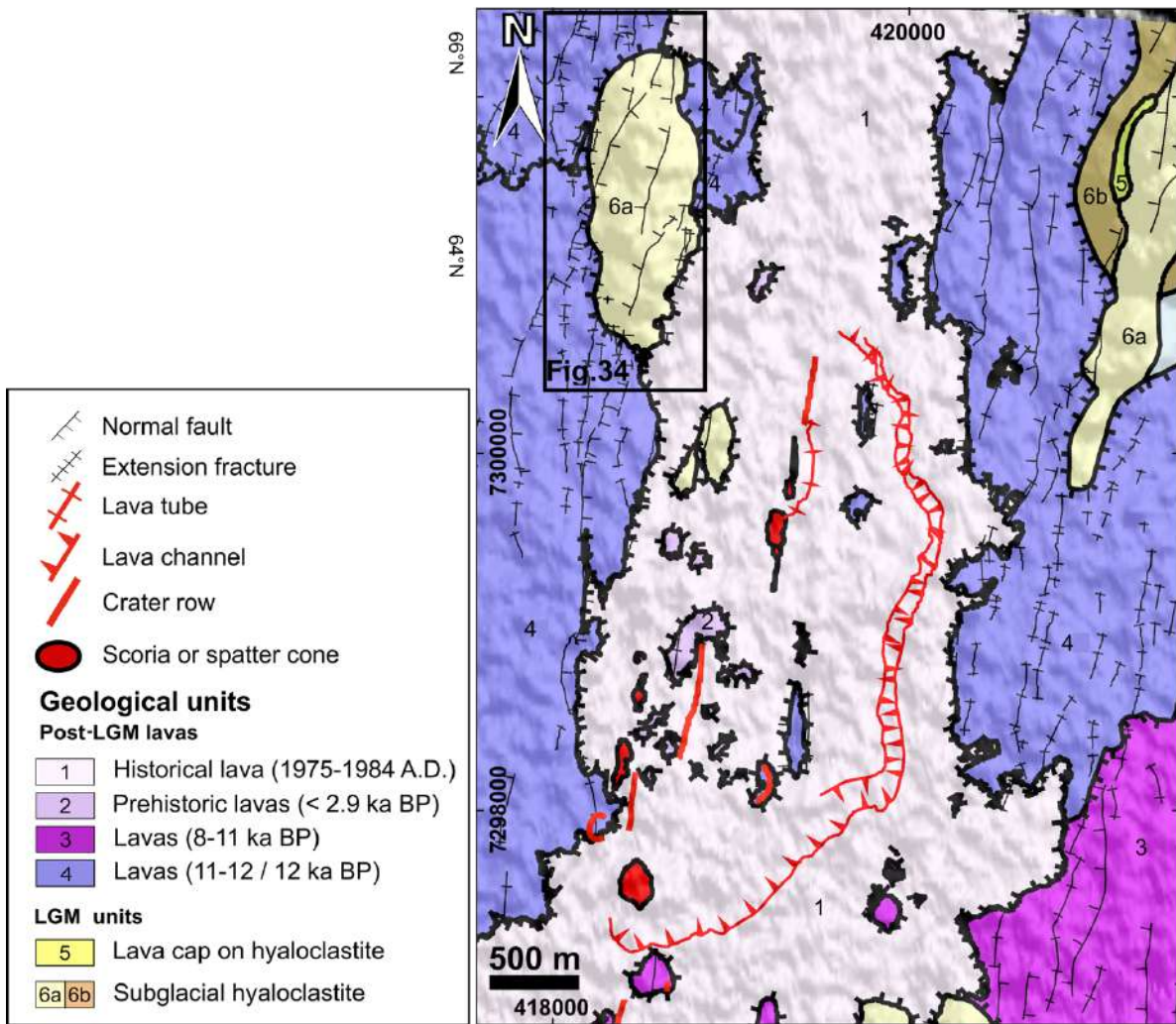


Figure 33 Geological map of a portion of the KFS where the study area is shown as a black rectangle, based on [Saemundsson et al. \(2012\)](#). Reference system: UTM28-WGS84 ([Bonali et al., 2020b](#)). Location shown in [Figure 9](#).

4.2.1 Western part of the Krafla Fissure Swarm

4.2.1.1 High resolution outputs from photogrammetry processing

The areal coverage of the study area is about 2.7 km² divided into 9 different surveys, performed at 80-95 m of height from the ground ([Fig. 34](#)); the surveys were carried out during the summer 2019 campaign, during which we collected a total of 6068 photos during a total flight time of 4.68 hrs. The surveyed sector is characterized by the presence of a hyaloclastite ridge composed of deposits dated, on a stratigraphic basis, to the Weichselian High Glacial (29.1-12.1 ka BP), and a series of lava flows mostly of 11-12 ka BP.

Thanks to the workflow described in [Section 3.2.2](#), such photos were used to reconstruct a high quality Orthomosaic and a DSM ([Fig. 35](#)), respectively characterized by a resolution of 2.59 and

10.40 cm/pixel; the resulting GeoTIFFs have a storage dimension of 15.8 and 1.11 GBs respectively, the Orthomosaic has been converted to JPEG 2000 (JP2) for data collection in GIS. The 3-D Tiled model is characterized by a texture resolution that is identical to the Orthomosaic and a storage dimension of 9.87 GBs.

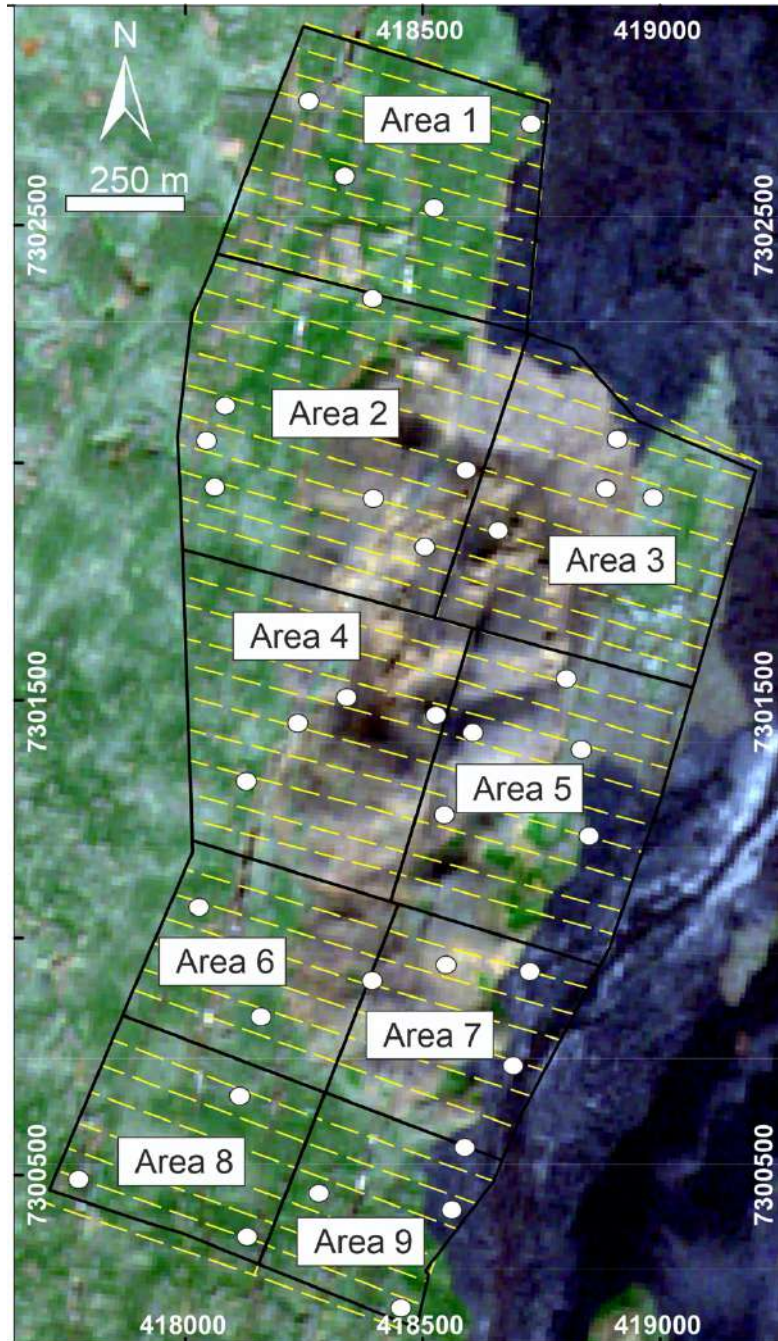


Figure 34 UAV flight paths (yellow line) above the surveyed 9 subareas. White dots indicate the 37 GCPs collected to georeference the model. Satellite image is from Sentinel 2 (European Space Agency - ESA, <https://sentinel.esa.int/web/sentinel/missions/sentinel-2>). Reference system: UTM28-WGS84 (Bonali et al., 2020b).

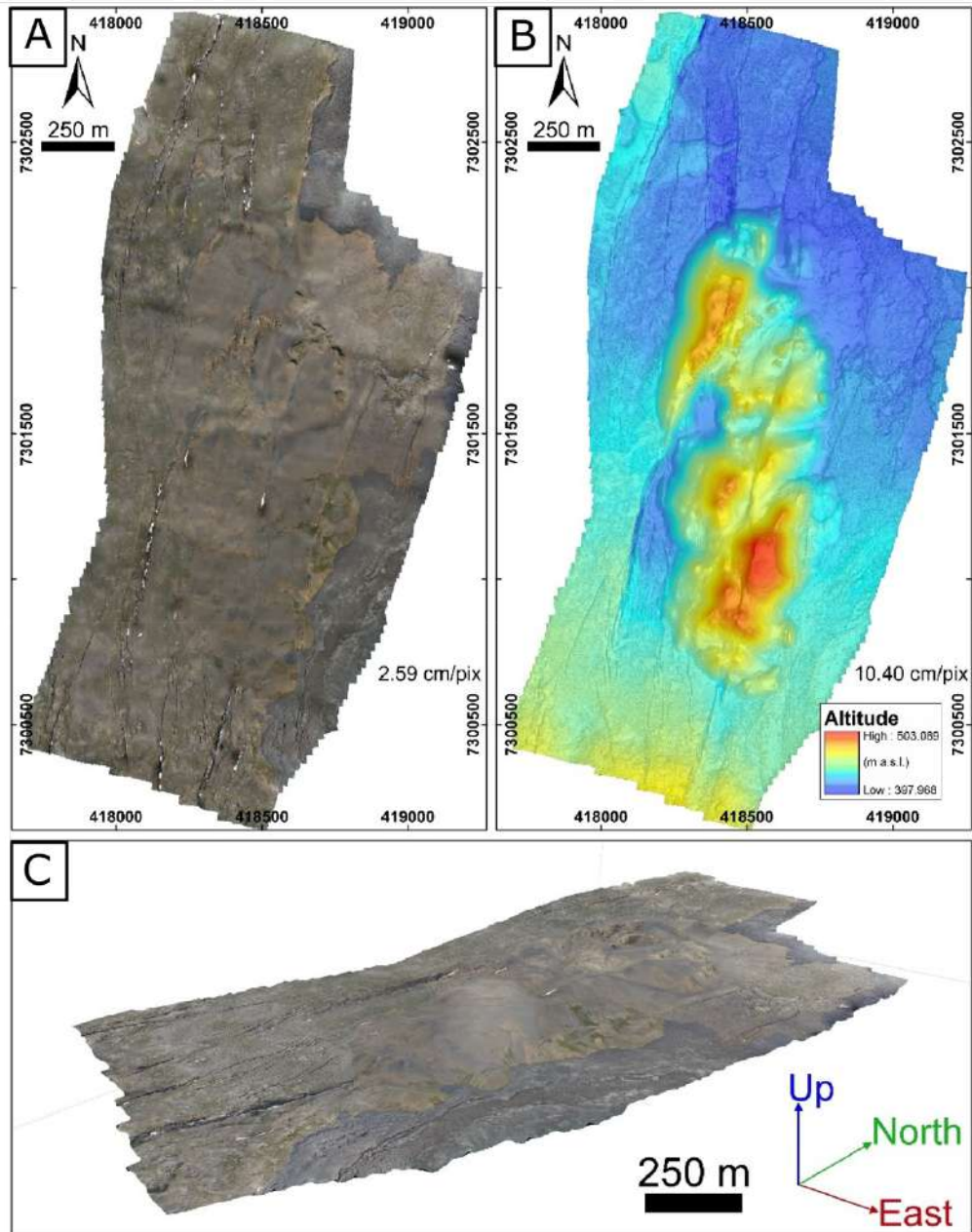


Figure 35 SfM-derived Orthomosaic (A) and DSM (B) of the study area, with corresponding resolution indicated in the lower right corner. Altitudes are shown as a colour range (legend in figure); reference system: UTM28-WGS84. (C) The final 3-D Tiled model (Bonali et al., 2020b).

4.2.1.2 New geological-structural data

A total of 1355 fractures, classified as normal faults (86) and extension fractures (1269), have been mapped: these fractures strike from NNW-SSE to NNE-SSW, they are mostly comprised between

N0°-20°E, whereby the av. strike is N8.2°E and strike values range between N0°-20°E, as shown in the rose diagram in [Figure 36B](#). The longest fracture reaches a length of 1156.1 m, whereas the overall average length is 28.3 m ([Fig. 36E](#)).

Thanks to the high resolution of the new DSM and Orthomosaic, the number of mapped fractures is dramatically greater respect to the 45 main fractures documented on the 1:100,000 scale geological map by [Saemundsson et al. \(2012\)](#) ([Fig. 2B](#)). In addition to the newly mapped fractures mentioned above, the geological map of the area has also been redrawn, tracing with very high detail the geological limits, as shown in [Figure 36A](#).

In regard to normal faults, they mainly strike from N-S to NE-SW, dipping towards WNW and ESE ([Fig. 36C](#)), and show an overall average and maximum length of 167.9 m and 1156.1 m respectively ([Fig. 36E](#)). On the other hand, extension fractures mainly strike from NNW to NNE, with an av. value of N8.1°E ([Fig. 36D](#)), and an overall average and maximum length of 18.8 m and 240.7 m respectively ([Fig. 36E](#)). In order to better define the deformation processes that have been occurring since Pleistocene times, a series of quantitative data have been collected at a total of 852 sites, 284 along normal faults and 568 along extension fractures. Regarding normal faults, 284 values of vertical offsets have been collected, thus obtaining a maximum value of 42 m along faults affecting pre-LGM units and of 19 m along faults affecting post-LGM units ([Figure 37](#)).

Regarding extension fractures, a total of 1704 structural data has been collected in post-LGM units at 568 different sites, focusing on the strike, opening direction and fracture dilation ([Figure 37](#)).

Opening direction values are in the range of N46.3°-142.3°E, with a mean value of N97.7°E and a SD of 13.3°: only 109 values fall within the regional spreading direction range. Furthermore, extension fracture azimuth ranges N48.1°W-N61.5°E, with a mean value of N7.9°E and a SD of 18.5°: only 119 values show an azimuth that is compatible with the spreading direction range. If we consider both the extension fractures opening direction and the extension fractures strike, only 43 out of 568 are compatible with the spreading direction ranges N104-115°E ([Fig. 38A](#)).

Furthermore, the dilation is in the range of 0.1-4.1 m, with a mean value of 0.64 m and a SD of 0.5 m. [Figure 38B](#) shows the relation between fractures strike and amount of opening: we observe that most of extension fractures with a dilation > 1 m have a strike between NNW-SSE and NE-SW, as well as longer fractures are characterized by an opening direction N80-120°E ([Fig. 38C](#)) and a lateral component < (+/-) 20° ([Fig. 38F](#)). The greatest amount of opening (4.1 m) is found in correspondence of opening direction values of N87.8° and a lateral component slightly larger than 0°.

Regarding the presence of lateral components of motion along extension fractures, 358 exceed 5° of lateral component, of which 177 are right-lateral and 181 are left-lateral with an average lateral component of 15° and 16°, respectively; the overall average value is 0.29°.

The relation between such lateral components and opening direction values shows that by increasing the values of opening directions, the calculated lateral component is greater, and becomes mainly positive (right lateral), up to 46.9° (Fig. 38D). On the other hand, by increasing the extension fractures strike, we observe an increase in the opening directions with a sort of clockwise rotation of values (Fig. 38A). In fact, considering N-S to NE-SW fractures, opening direction values range from N73.7° to N142.3°, whereas NW-SE fractures are characterized by opening direction values ranging from N46.4° to N125.5°. On the other hand, by increasing the strike, we notice a decrease in the lateral component, that changes thus from right-lateral to left-lateral (Fig. 38E). Furthermore, N-S to NE-SW fractures are mainly characterized by left-lateral components of motion, whereas NW-SE fractures have mainly a right-lateral component. Finally, values of the amount of opening slightly increase for fractures characterized by a left-lateral component of motion (Fig. 38F).

Also the extensional strain in the area has been measured by cumulating the dilation values obtained at both extension fractures and normal faults, along three N105°E-striking transects, each with a length of 0.62 km, in order to obtain the cumulative dilation, stretch and extension rate in the three outcropping units (Figure 37). To calculate the dilational component at normal faults, we based on the measured vertical offset, considering a dip of the fault plane of 70°. Along the northernmost transect, which cuts structures affecting 11-12 ka BP lavas, we measured a cumulated dilation of 16.6 m, corresponding to a stretch of 1.027; along the central one, which cuts only faults affecting the hyaloclastite, we obtained a cumulated dilation of 29.3 m, corresponding to a stretch value of 1.049; along the southernmost transect, which cuts structures affecting 12 ka lavas, the cumulated dilation has a value of 11.2 m, with a stretch value of 1.018. The overall dilation, calculated in central part of the area along a 1.23 km-long transect and considering all fractures affecting pre and post-LGM units, is 36.4 m, corresponding to a stretch of 1.0304.

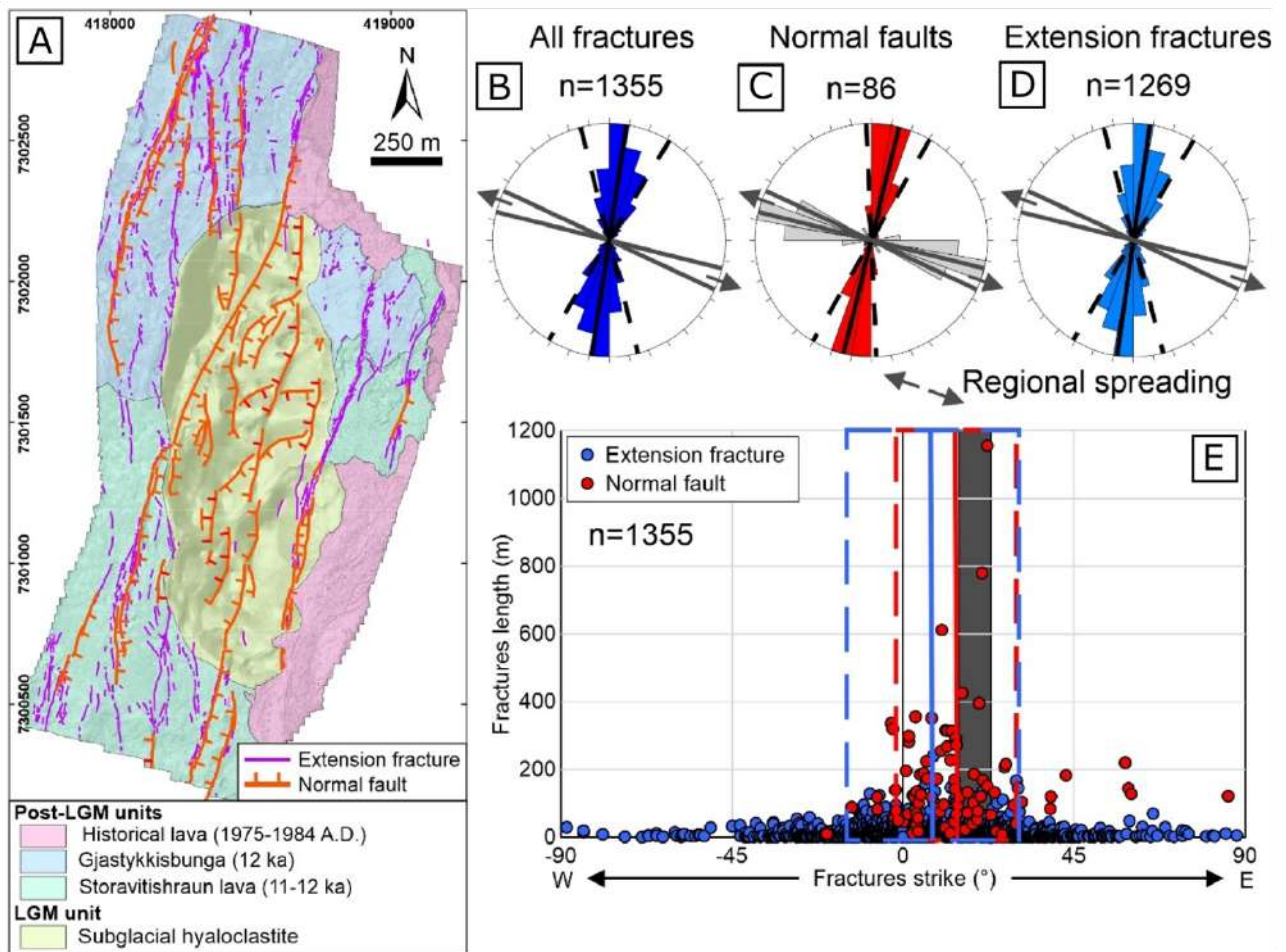


Figure 36 (A) Geological map of the area based on high-resolution outputs from SfM photogrammetry processing and field checks, reference system: UTM28-WGS84. Rose diagrams representing the strike for the whole set of fractures (B), normal faults - including the dip direction of fault scarps - (C) and for extension fractures (D). For each set the average value and standard deviation is represented as continuous and dashed lines respectively, the regional spreading direction range is reported as dark gray lines. (E) Fracture strike vs. length (for both extension fractures and normal faults), average value is reported as continuous line, the SD range is represented as a dashed line (box), and the regional spreading direction range is represented as a dark gray rectangle (Bonali et al., 2020b).

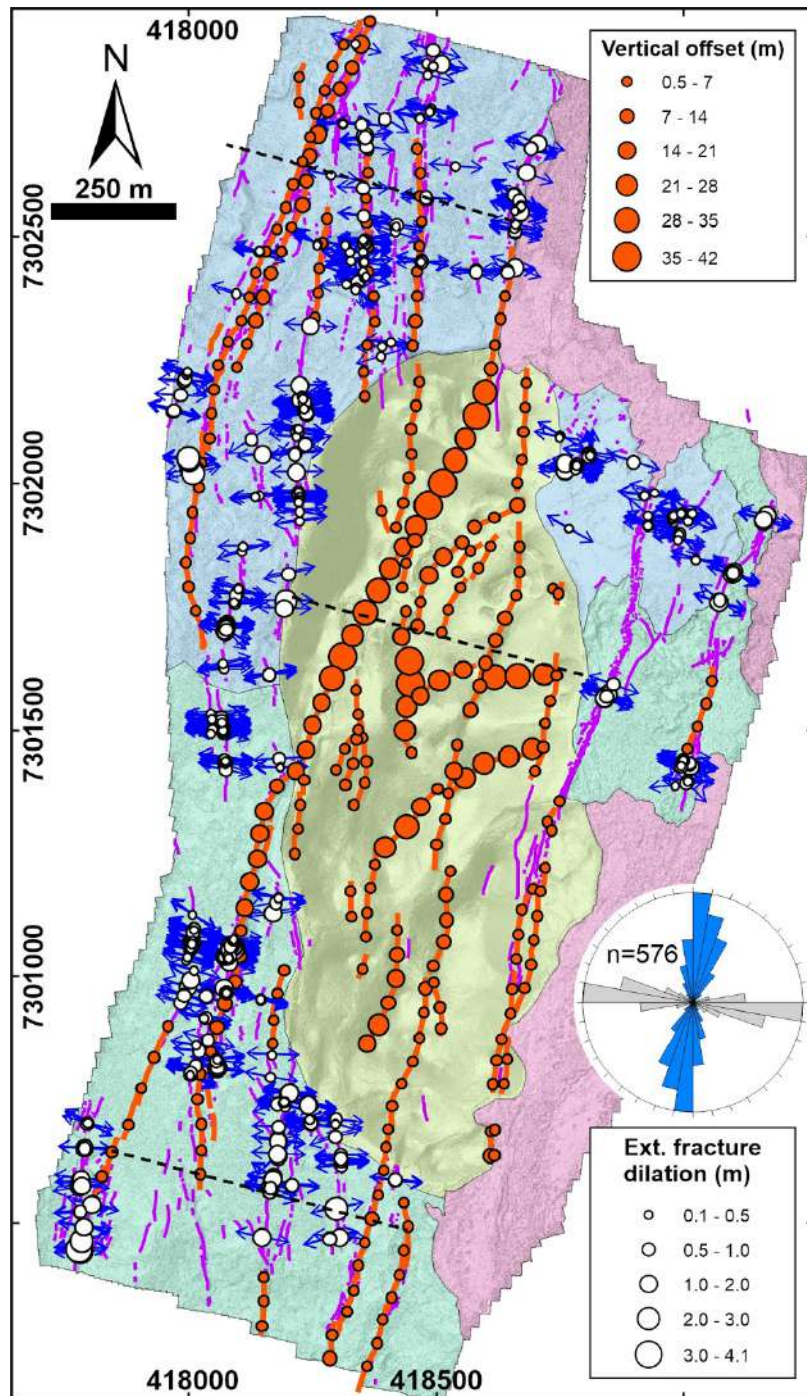


Figure 37 Vertical offset values for normal faults (red lines), opening direction and dilation for the extension fractures (cyan lines) are reported. The legend for the geological units is the same as [Figure 36A](#). The rose diagram shows both extension fracture strikes and opening directions ([Bonali et al.](#),

2020b).

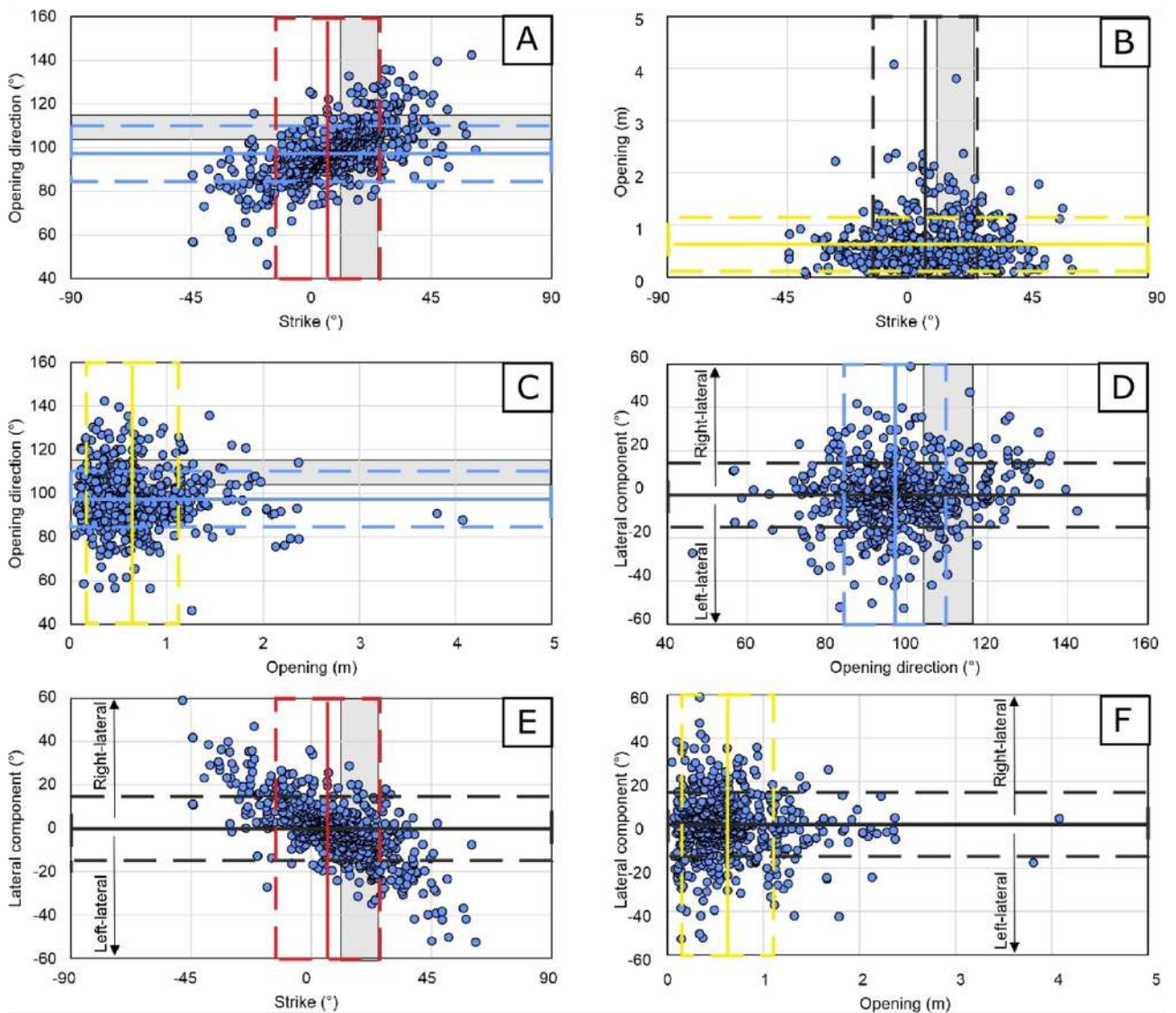


Figure 38 Graphs show (A) fracture azimuth vs. opening direction, (B) fracture azimuth vs. fracture dilation, (C) fracture dilation vs. opening direction, (D) opening direction vs. lateral component of movement, (E) fracture azimuth vs. lateral component of movement, and (F) fracture dilation vs. lateral component of movement. For all data, the mean value (continuous line) and the standard deviation range have been reported (dashed lines box), as well as the gray rectangle represents the expected range of values considering the spreading direction range (N104-115°) (Bonali et al., 2020b).

4.2.2 Focus on the Hituholar graben

4.2.2.1 General geometry of the studied structure

Structures of the Hituholar graben affect all the deposits cropping out in the study area, except the 1975–1984 lava flows (Figs. 39 and 40). This extensional deformation zone strikes from N0° in the south to N25° northward, as can be seen by the strike distribution (Fig. 41), and is composed of 237 extension fractures, most of which strike N20–40° and are in the 2–6 m length range. The longest fracture reaches 134m (Figs. 41A–C), whereas the 10 faults present in the area reach lengths of 10–320 m, and strike mostly N0–20° (Fig. 41D). The features along the sites from 1 to 10 are here described in detail, in order to give a complete picture of the morphology of the studied graben. Starting from the southernmost part of the study area, Site 1 (Fig. 39B) is characterized by a horizontal, flat area, occupied by the 12-ka-old and the 1975–1984 lavas. Here, a N5° trending, 168-m-long extension fracture locally turns into a normal fault, with lava flows onlapping it. At Site 2 (Fig. 39B) the 1975–1984 flows partly cover the structures, which crop out further north and are composed of three rectilinear extension fractures that are marked by a right-stepping geometry to the south and by a left-stepping geometry to the north. The segments strike N5° to N10° and are 75 to 110 m long. Their opening directions are from N90° to N110°, mostly perpendicular to the local fracture strike. The southernmost of these three segments locally shows a limited, eastward-directed offset, the escarpment of which guided the northward flow of the 1975–1984 lavas. Further north, (Site 3 in Figs. 40C and 42A), the deformation zone is covered by the 1975–1984 lavas and turns then in a very narrow, N-S-trending graben, partially infilled with the historic lavas that can be observed in correspondence of the first deposits of the Hituholar hyaloclastite ridge. The east-dipping fault has an about 2-m high scarp, whereas the offset of the opposite, west-dipping fault is poorly measurable due to the presence of the 1975–1984 lavas. This section of the graben is 81 m long and its width ranges from 8 m in the south to 6 m in the north. Further north, at Site 4 (Fig. 40C), the deformation zone is observed affecting the slopes of the hyaloclastite ridge, and is represented by two parallel faults with converging dips. The faults strike from N0° to N13°. Both display pure dip-slip normal displacements and thus define a 115-m-long graben with a width from 17m in the south to 12.5m in the north, and a maximum width of 23m at the top of the hill (Fig. 42B). This graben occurs in correspondence of a N-S elongated hill, with an elevation of 20 m above the surrounding flat area. The scarps of these faults, offsetting pillow lavas, are subvertical (80°–90°), with very limited erosion. The offset is 2.5–3 m along both faults.

At Site 5 (Fig. 40C), the graben's eastern fault is mostly hidden by the 1975–1984 lavas, but its presence is still recognizable owing to the change in attitude of the historic lavas. The graben's western fault crops out for about 40 m, although it is partially onlapped by the historic lavas, with an estimated minimum scarp height of 1.5 m. At Site 6 (Figs. 40C and 42C), the graben crops out entirely once again, still composed of the two parallel faults with converging dips and an about $N0^\circ$ strike. The graben is 9.7 m wide to the south, then it widens as much as 36.5 m in correspondence of the top of the hill, and then it narrows again to 16 m, where it reaches the altitude of the surrounding flat area. The top of the hill is 20–25 m higher than the nearest flat area. This graben section is 245 m long, its bounding faults are from 2.5 to 3.5 m high. Some 0.5-m to 1-m-large fissures can be observed around part of the western fault scarp, but they seem due to gravity effect of the slope.

Further north, at Site 7 (Fig. 40C), in correspondence of another hill, a 196-m-long section of the graben is marked by the coexistence of extension fractures and faults, with scarp height gradually decreasing. The greater number of parallel fractures occurs in correspondence of the hill's top, which is 30 m higher than the surrounding flat area. At Site 8 (Fig. 40A), where the graben structure intersects once again the flat area in correspondence of the contact with the 11–12 ka old lava flows, only two main parallel extension fractures are present, for a total length of 245 m. The main fractures strike $N5^\circ$ to $N27^\circ$, are 3.7 to 7.4 m spaced apart, and show opening directions that are dominantly perpendicular to the fracture strike, i.e. trending $N100$ – 110° . The amount of dilation is greater along the eastern fracture, ranging from 0.5 to 1.2 m. The western fracture, instead, is from 0.2 to 1 m wide. At Site 9 (Fig. 40A), the western fracture gradually fades out, and the deformation tends to concentrate along the main eastern fracture for 86 m, which becomes discontinuous. The eastern fracture is made of several short fracture segments striking from $N0^\circ$ to $N30^\circ$, concentrated in a deformation zone from 6 to 9 m wide. This segmentation coincides with the frontal zone of the 11–12 ka old lava flow and probably is the effect of the blocky structure of the uppermost part of the flow. At Site 10 (Fig. 40A), in the zone of contact between the 11–12 ka old lavas and the 12 ka old lavas, there is a left-stepping en-échelon connection to another, about 12-m-wide deformation zone, where it is possible to notice a main, more continuous fracture striking $N20$ – 29° . The dilation ranges 0.4–1m and its direction is about perpendicular to the fracture strike. Another left-step connects with a $N30^\circ$ -striking final main fracture whose dilation gradually decreases, as far as a point where the fracture disappears. Another offset fracture with a left-stepping arrangement, and with minor opening is present for further 150 m.

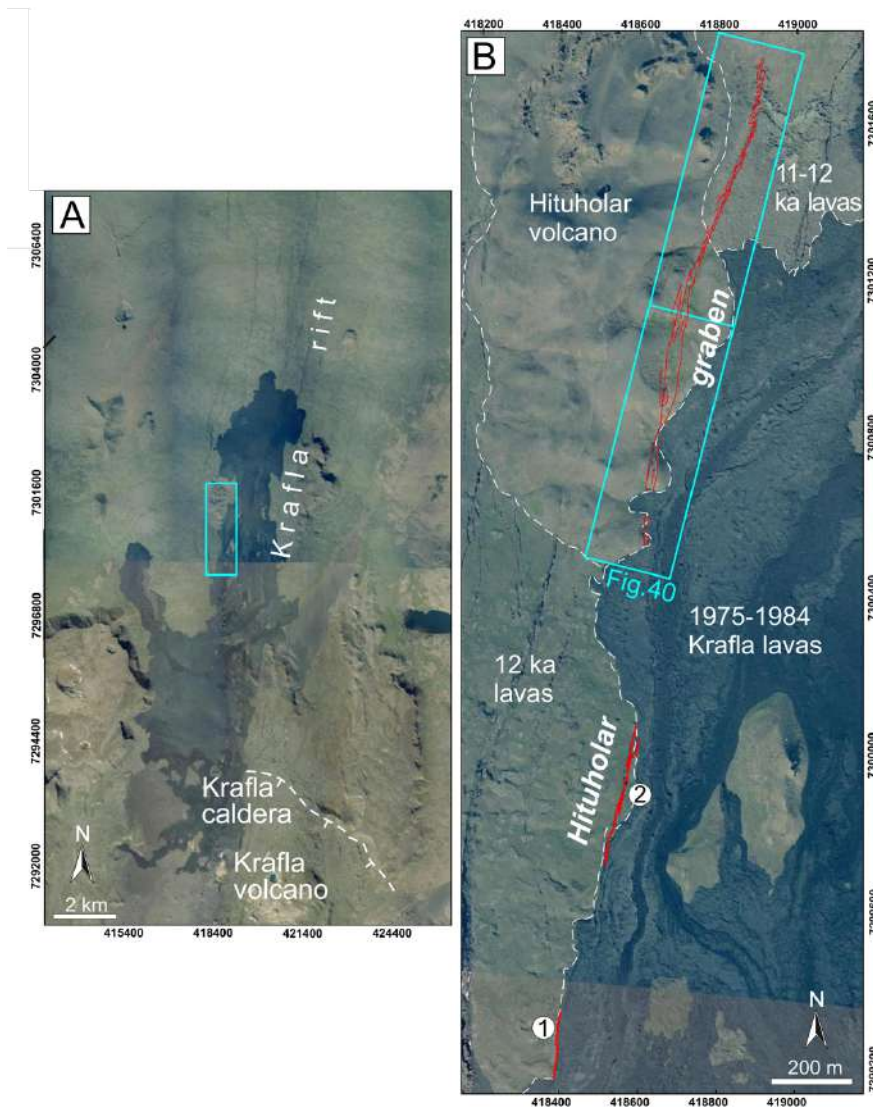


Figure 39 (A) Location of the Krafla volcano, the Krafla caldera (white dashed line) and the NNE-SSW trending Krafla Rift. Box locates **Figure B**. (B) Red lines represent the faults and fractures of the studied Hituholar graben. Dashed white lines delimit the main geological units. Numbers refer to sites discussed in the text. Box locates the area displayed in **Fig. 40** (modified after [Tibaldi et al., 2020a](#)). The study area is located in **Figure 9**.

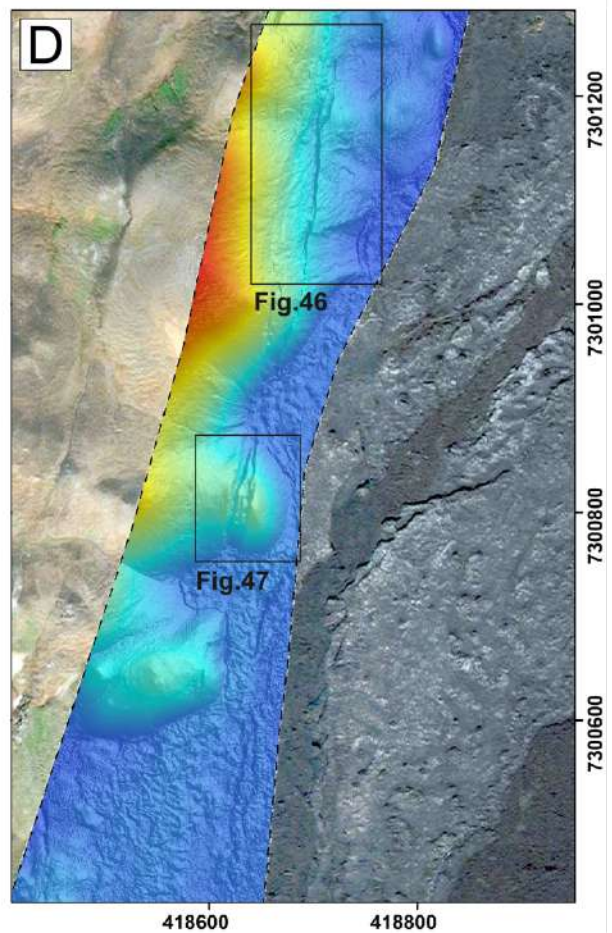
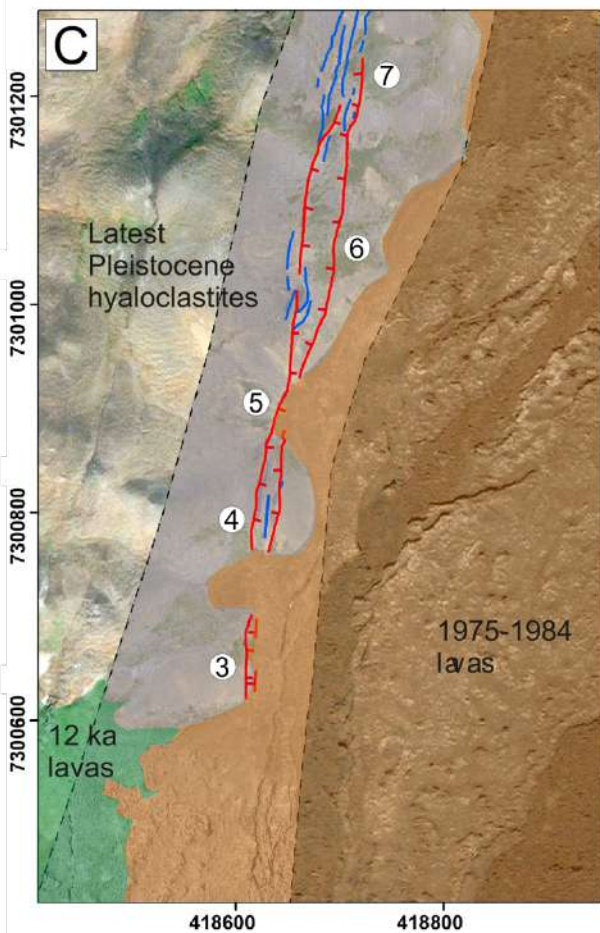
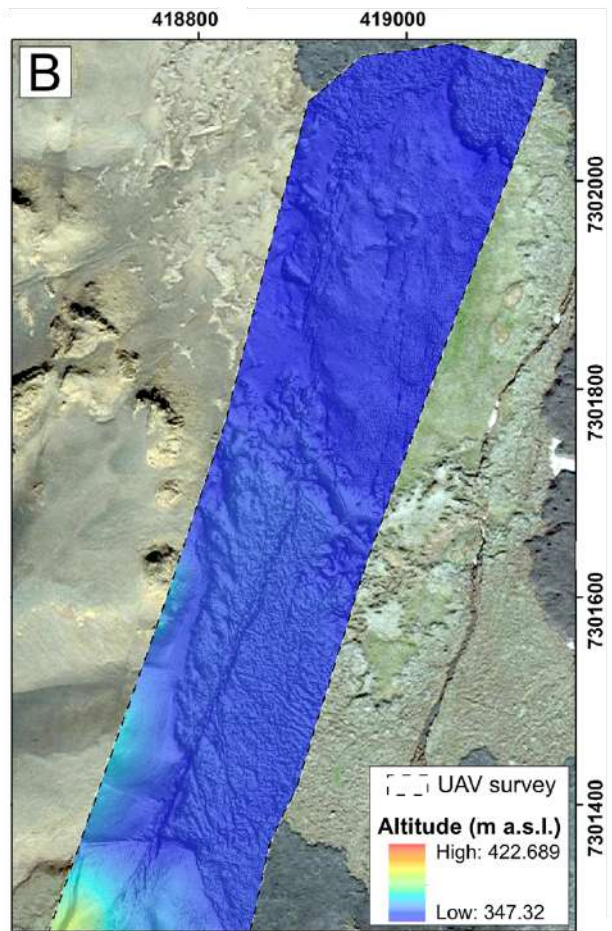
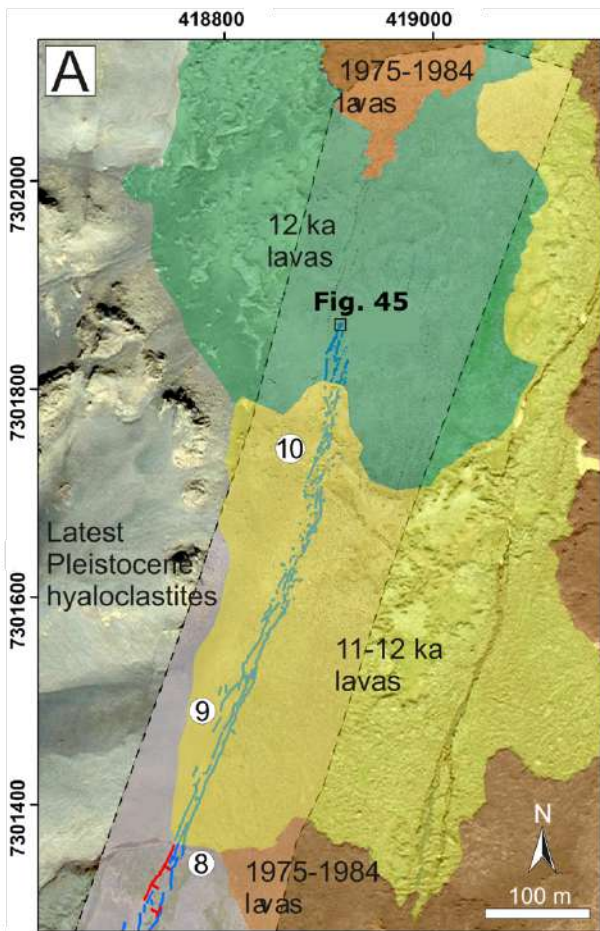


Figure 40 (A) and (C) SfM-derived Orthomosaics of the northern and southern part of the studied zone. Geological stratigraphic units from [Saemundsson et al. \(2012\)](#) and [Tibaldi et al. \(2020\)](#), (B) and (D) SfM-derived DSMs of the northern and southern part of the studied zone; black dots show the location of measurement sites at strike-slip faults, as discussed in the text. Boxes locate [Figs. 46](#) and [47](#) ([Tibaldi et al., 2020a](#)).

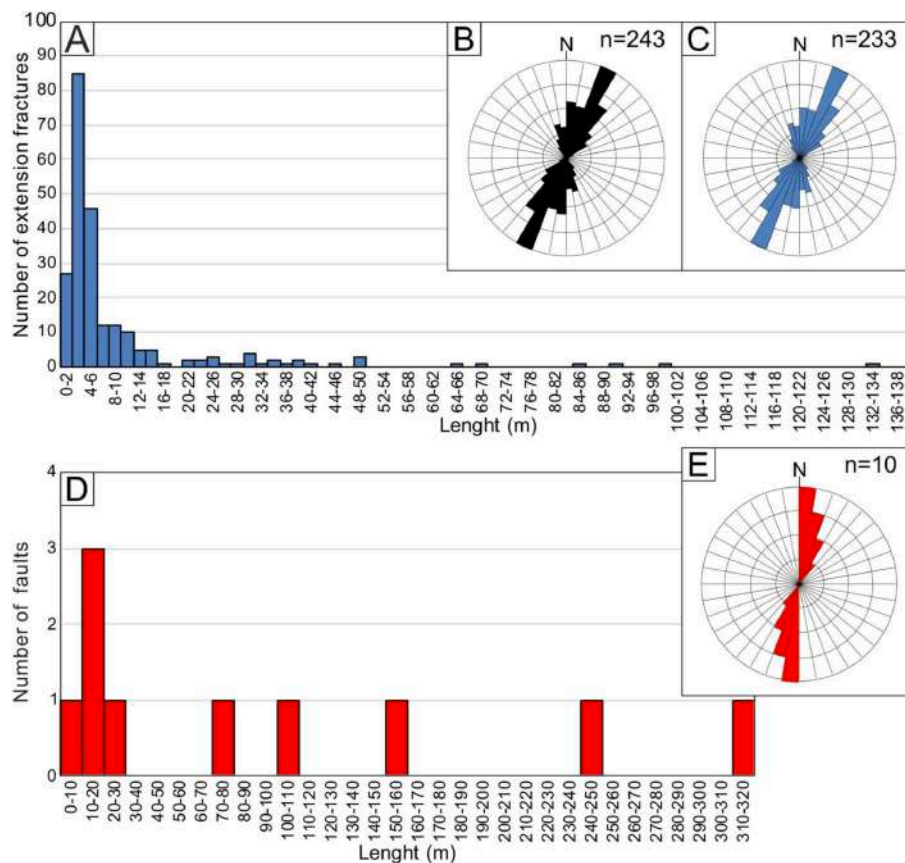


Figure 41 (A) Graph of extension fracture length distribution; length intervals of 2m, (B) Rose diagram with the strike distribution of all measured structures, (C) Rose diagram with the strike distribution of extension fractures, (D) Graph of fault length distribution; length intervals of 10 m, (E) Rose diagram with the strike distribution of faults ([Tibaldi et al., 2020a](#)).

4.2.2.2 Secondary structures

Two different types of secondary structures have been studied along the deformation zone: morphostructures affecting the graben floor ([Fig. 42](#)) and secondary fractures, with offsets ranging from 1 cm to 10-15 cm ([Fig. 43](#)). Such fractures mostly strike N5–25°, being thus parallel to the main fractures and faults ([Fig. 43](#)): they are mostly characterized by pure dilation and thus they can be interpreted as linked with the main processes affecting the main deformation zones, or as resulting

from local gravity collapse towards the main fissures. Additionally, several secondary fractures oblique to the main fracture zone have been found. These fractures have two main orientations: one set is composed of fractures with lengths mostly ranging from 1 to 6 meters rotated in anticlockwise sense to the strike of the main deformation zone, with strikes ranging from NNW-SSE to N-S (N140–180° and N0–5°) (Fig. 43A). The other set is composed of fractures rotated in clockwise manner to the strike of the main deformation zone: they strike NE-SW (N25° to N57°) and their length is mostly ranging from 1 to 9 m (maximum value 17 m). These secondary fractures, oblique to the main rift trend, have different kinematics, as shown in the graph of Fig. 43B. In the Y-axis of the graph, the sense of the strike-slip component is shown, expressed as the angle between the direction perpendicular to the fracture strike and the net direction of dilation; in the X-axis, the fractures strike is provided. The NNW-SSE to N-S fractures recorded motions corresponding to a right-lateral component and a dilatant component (e.g. Fig. 44, right column). The NE-SW secondary fractures show offsets corresponding to a left-lateral component and a dilatant component (e.g. Fig. 44, left column). At each set, the two components of motion are usually of the same magnitude and in the order of a few cm to 15 cm. It is worth pointing out that each of the two sets has a coherent kinematics. A map of the distribution of fractures oblique to the trend of the main deformation zone (here NNE-SSW), based on field data and drone surveys is shown in Fig. 45: these converge towards the main deformation zone and are limited in distance. They are highly segmented, being interrupted by the NNE-SSW-striking fractures and fissures of the main deformation zone. Northwards, where the main N10–20°-striking extension fracture terminates, it is replaced by two N-S and NE-SW-striking fractures, each with offsets in the order of 1 to 10 cm (Fig. 46). The main NNE-SSW-striking fracture shows pure dilation, whereas the N-S secondary fracture is characterized by a right-lateral sense of shear and the NE-SW fracture shows left-lateral displacement. As far as the morphostructures affecting the graben floor are concerned, it is possible to observe that, at most segments, the floor is depressed with respect to the graben shoulders (examples in topographic profiles n. 5, 6 and 7 shown in Fig. 47). At some sites, the graben floor appears uplifted; an example can be seen in a field photograph (Fig. 40B) and in the SfM-derived 3D model (Fig. 48), where the topographic surface in correspondence of the central area of the graben floor is 1.5 m higher than the foot of the surrounding fault scarps, and is 1m lower than the graben shoulders. Another site (Fig. 40D) is characterized by the graben floor uplifted to the same altitude as the graben shoulders, whereas other sites are visible in the topographic profiles n.1 to 4 of Fig. 47. In these cases, the morphology of the uplifted graben floor is elongated parallel to the local orientation

of the bounding faults and presents an upward convex topography. In the southern site (Figs. 40B and 47), in the center of the uplifted zone there is a fissure parallel to the graben faults, whereas two transversal high-angle reverse faults allowed for a differential uplift.

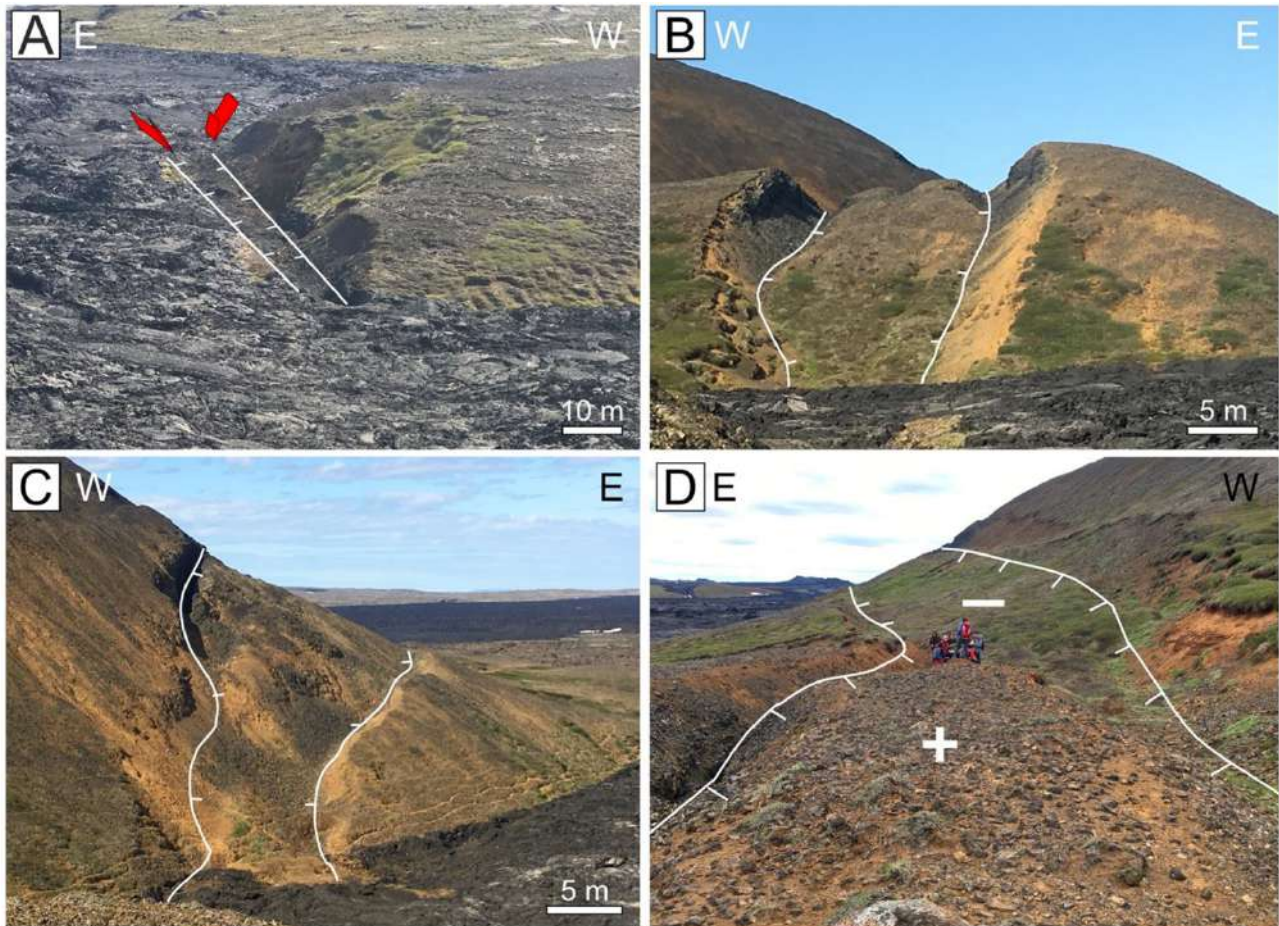


Figure 42 (A) In correspondence of the foothills of the Hituholar hyaloclastite ridge (Site 3, Fig. 40C), the studied deformation zone is made of two parallel normal faults with converging dips, defining a narrow, 6–8m wide graben. (B) A hill belonging to the Hituholar ridge is crossed by a 12.5 to 17m wide graben, which widens up to 23m at the top (Site 4, Fig. 40C). (C) Further north, the graben widens again in correspondence of a 25–30m high hill (Site 6, Fig. 40C). (D) In the background of the image, the two normal faults define a graben with a depressed floor (– sign); in the foreground, the graben floor appears uplifted (+ sign). Persons for scale (100 m north of Site 6, Fig. 40C) (Tibaldi et al., 2020a).

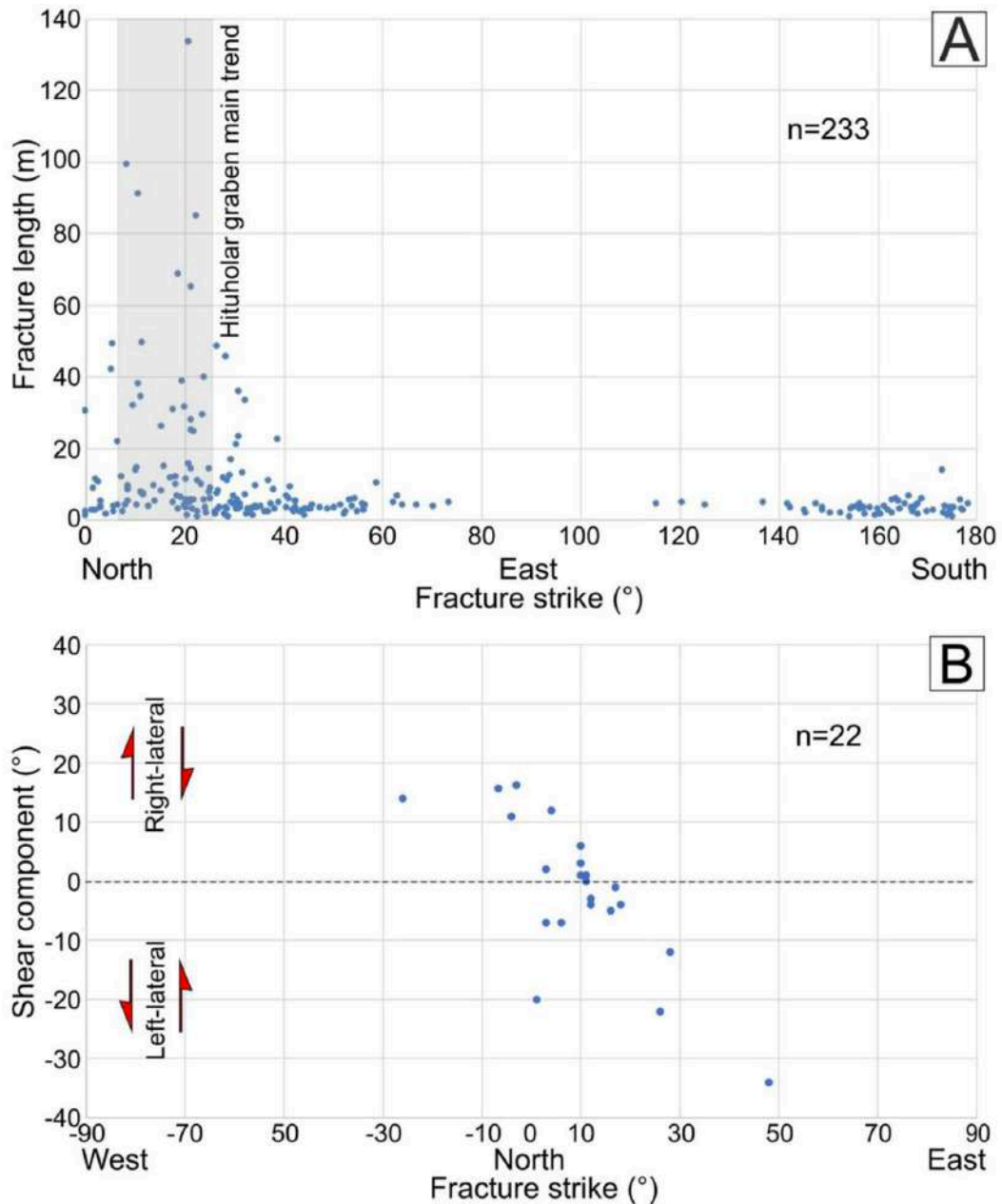


Figure 43 (A) Fracture strike vs. length. Main trend of the Hituholar graben is shown as a grey shaded area. (B) Fracture strike vs. strike-slip component. Above the dashed line, the right-lateral shear component is shown, whereas the left-lateral shear component is displayed below the line. Sites of measurement in Figs. 40B-D (Tibaldi et al., 2020a).

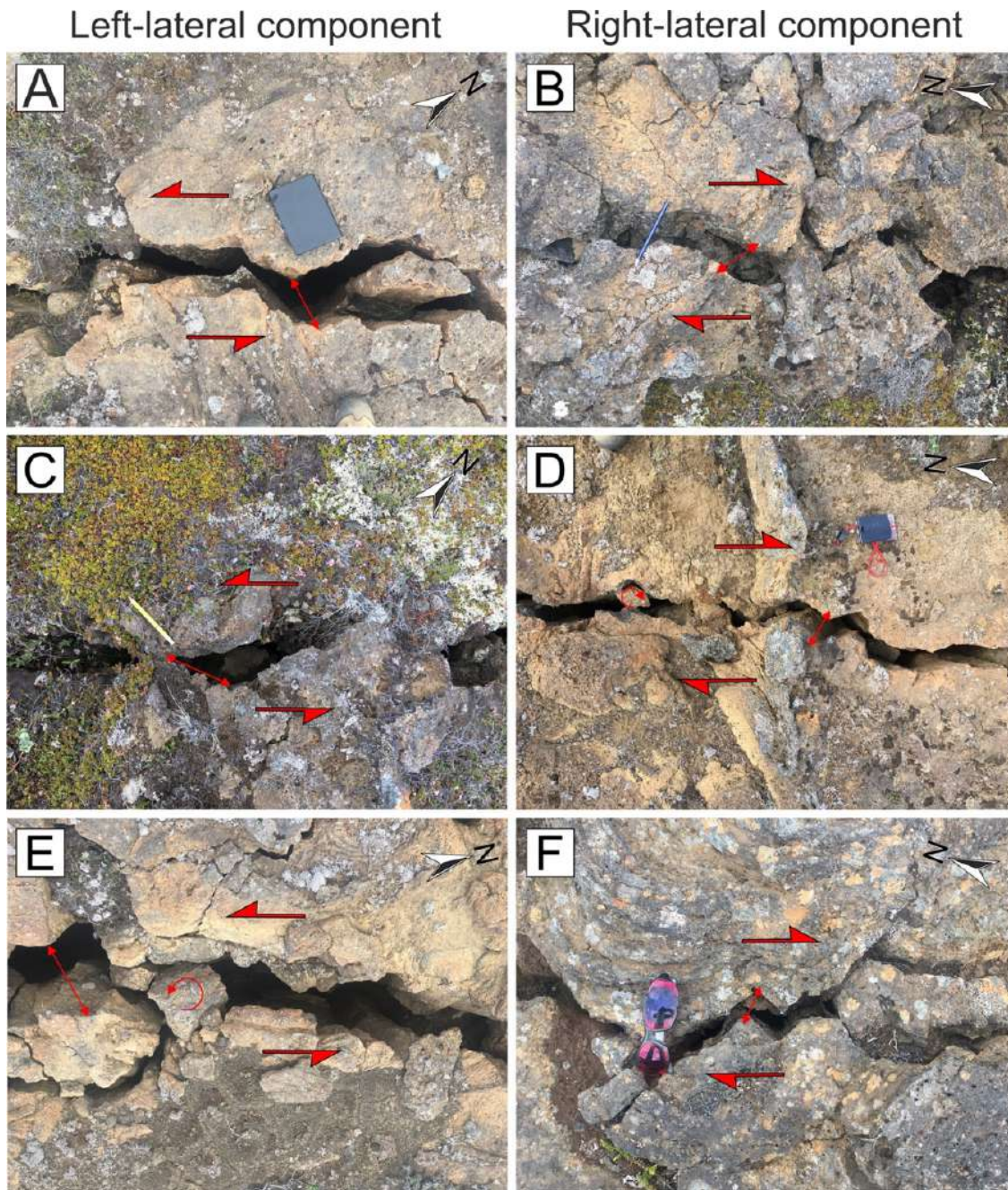


Figure 44 Secondary fractures with oblique strike located in correspondence of the main $N10^{\circ}$ to $N20^{\circ}$ striking extension fractures. Left column (A-C-E): examples of fractures striking NNW-SSE with a left-lateral sense of strike-slip motion. Right column (B-D-F): examples of fractures striking NE-SW with a right-lateral sense of strike-slip motion (Tibaldi et al., 2020a).

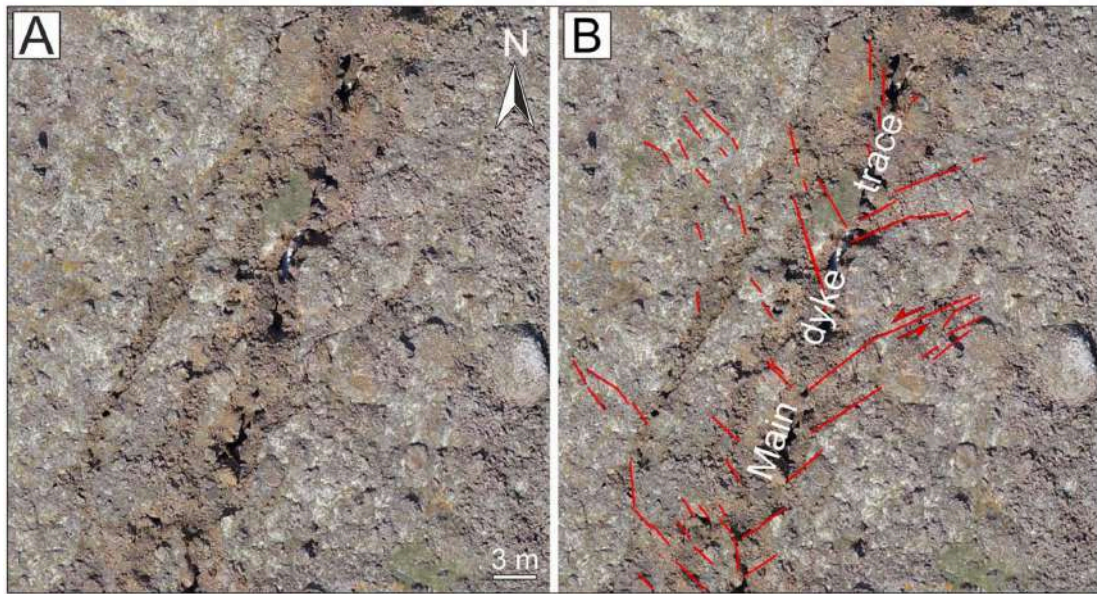


Figure 45 Highly-detailed example of the distribution and characteristics of oblique fractures (modified after [Tibaldi et al., 2020](#)). Only the fractures oblique to the trend of the main deformation zone (here NNE-SSW) were mapped, based on field data and drone surveys. Note that the fractures converge towards the main deformation zone and are limited in distance. Location in [Fig. 40A](#) ([Tibaldi et al., 2020a](#)).

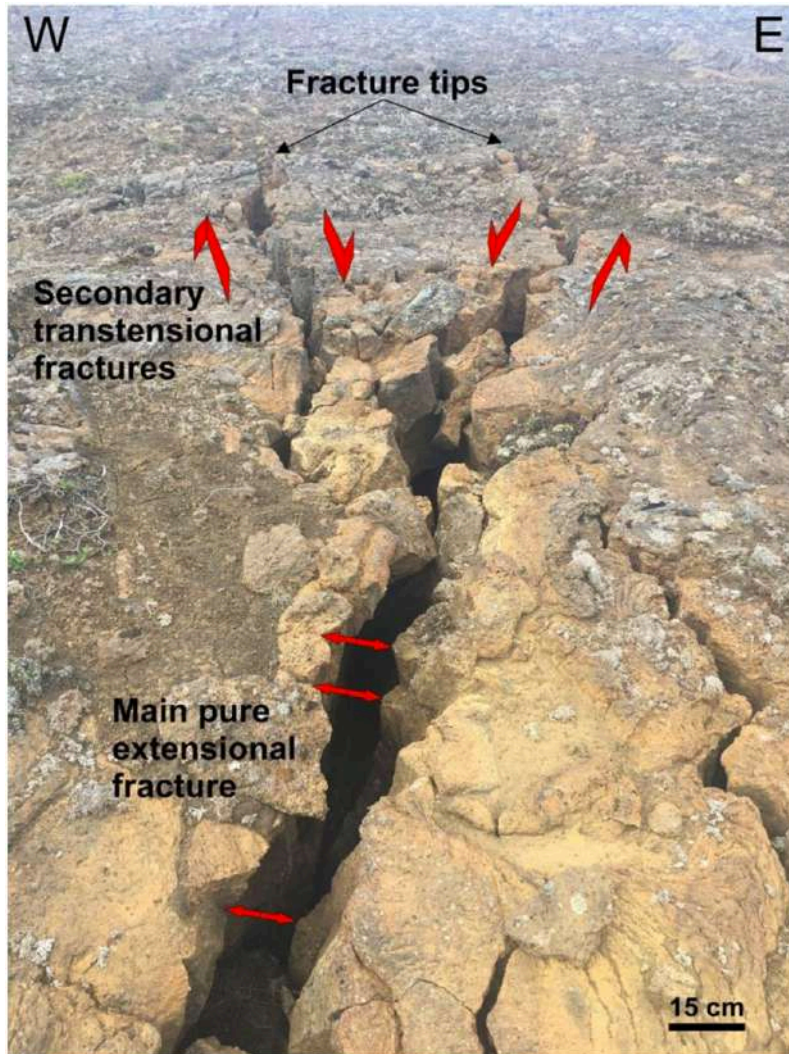


Figure 46 Field view showing the N-S striking right-lateral fissure and the NE-SW left-lateral fissure located at the end of the main N10–20° extension fracture (Tibaldi et al., 2020a). Strike-slip zones are represented with parallel arrows, whereas diverging arrows located on the main extension fracture represent corresponding piercing points. Location in Fig. 40D.

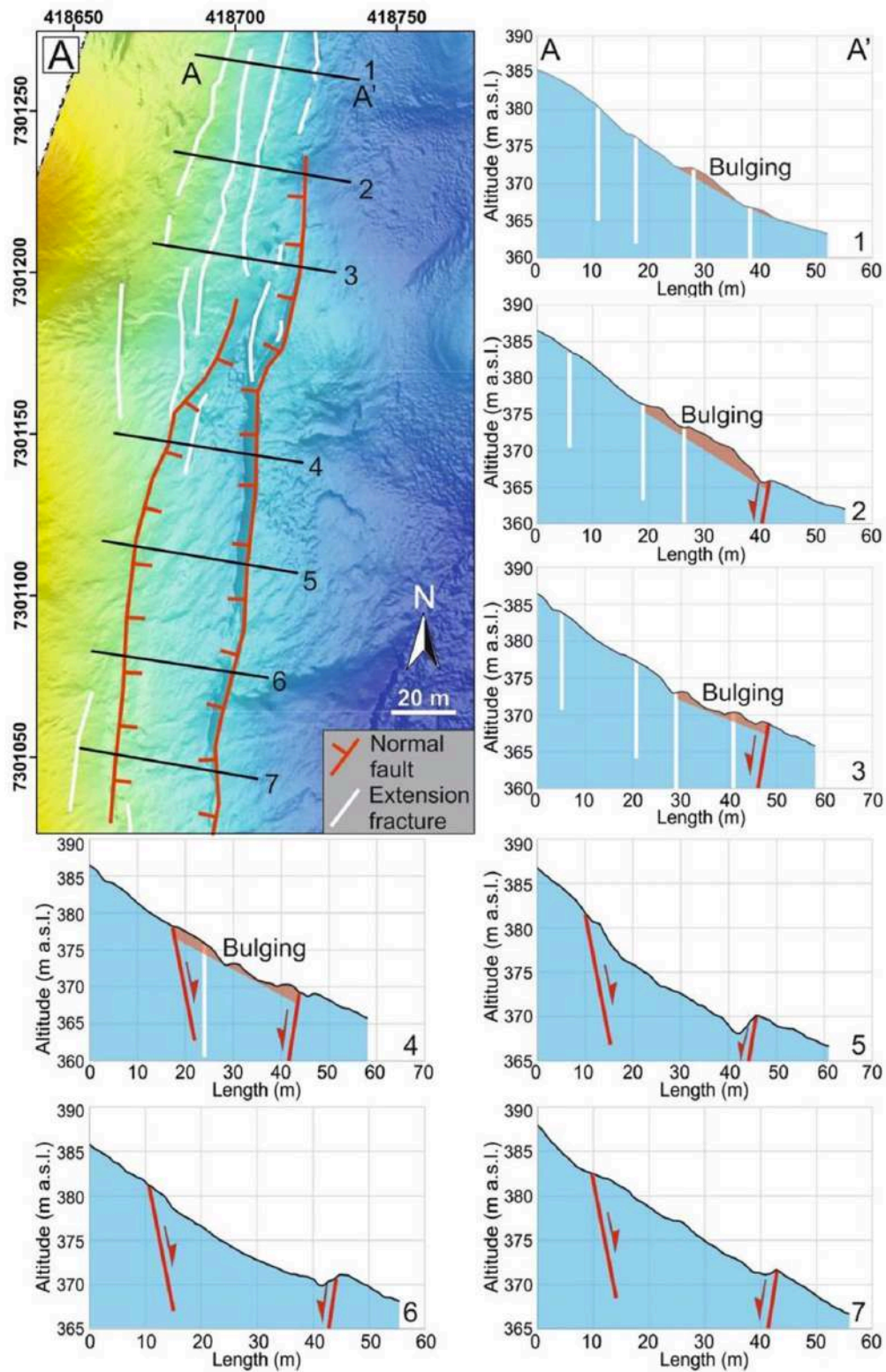


Figure 47 (A) SfM-derived DSM of the central segment of the studied area (Tibaldi et al., 2020a). Black lines are traces of topographic profiles 1–7 all oriented as A-A'. Location of Figure A is shown in Fig. 40D. The uplifted areas of the graben floor have been highlighted in red along the topographic profiles.

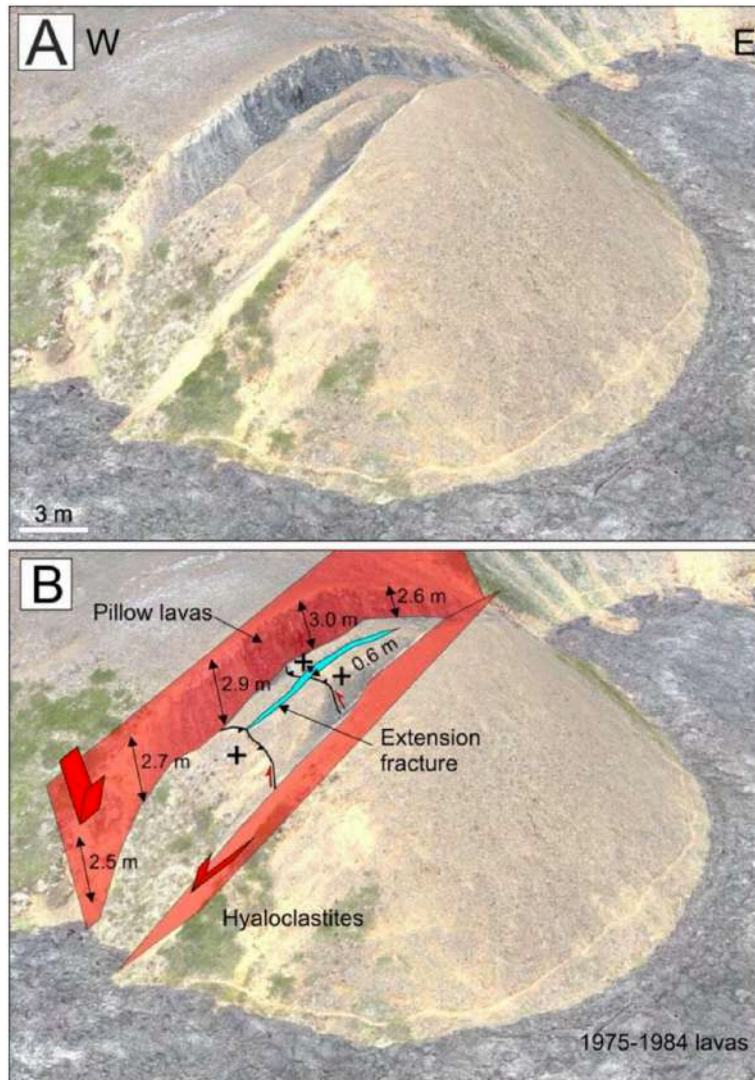


Figure 48 (A) Oblique view of the SfM-derived 3D model for the southern segment of the Hituholar graben (Tibaldi et al., 2020a). (B) Examples of measurements of the western fault scarp and of an extension fracture made on the 3D model. It is worth observing the presence of secondary structures (thin black lines) on the graben floor that allowed for differential uplift (cross symbol). Location in Fig. 40D.

4.3 Numerical modeling: dyke-induced stress change on transcurrent faults

Results of numerical modeling developed through Coulomb 3.3 software are shown in Figs. 49 and 50: the Coulomb stress change exerted by a N-S-striking magmatic dyke considered as a 'source', with a width of 2 meters and a depth comprised between 0.2 km and 1 km, is calculated on faults ('receivers') with right- and left-lateral components of motion that have strike values coherent respect to the ones detected in the field within the Northern Volcanic Zone in the present research. First, the Coulomb stress change on right-lateral transcurrent faults has been calculated (Figure 49). All figures represent horizontal planes of analysis, thus containing calculations of Coulomb stress changes at different depths. Starting from the first row, which describes Coulomb stress changes in the surroundings of the dyke (0.5 km depth), we notice that the presence of NW-SE, NNW-SSE and N-S right-lateral strike-slip faults is favoured in correspondence of the dyke tip, where the Coulomb stress change is positive (red colours) whereas it is inhibited at the sides. The situation is the opposite if considering NE-SW to NNE-SSW right-lateral faults: in such case, their presence is inhibited in correspondence of the dyke tip and favoured along the eastern and western side of the inflating dyke.

Moving towards the surface, at 0.2 km depth, which is the uppermost limit of the dyke, Coulomb stress variations indicate that NW-SE to N-S faults are inhibited both at the sides and at the tip of the dyke, whereas NNE-SSW to NE-SW right-lateral faults are mainly favoured at the sides.

Furthermore, at 0.1 km depth, above the inflating dyke, we find mainly NW-SE to N-S right-lateral strike-slip faults in correspondence of the tip of the dyke and NNE-SSW to NE-SW faults at the eastern and western side of the dyke (Figure 49), similarly to the results obtained at 0.5 km depth.

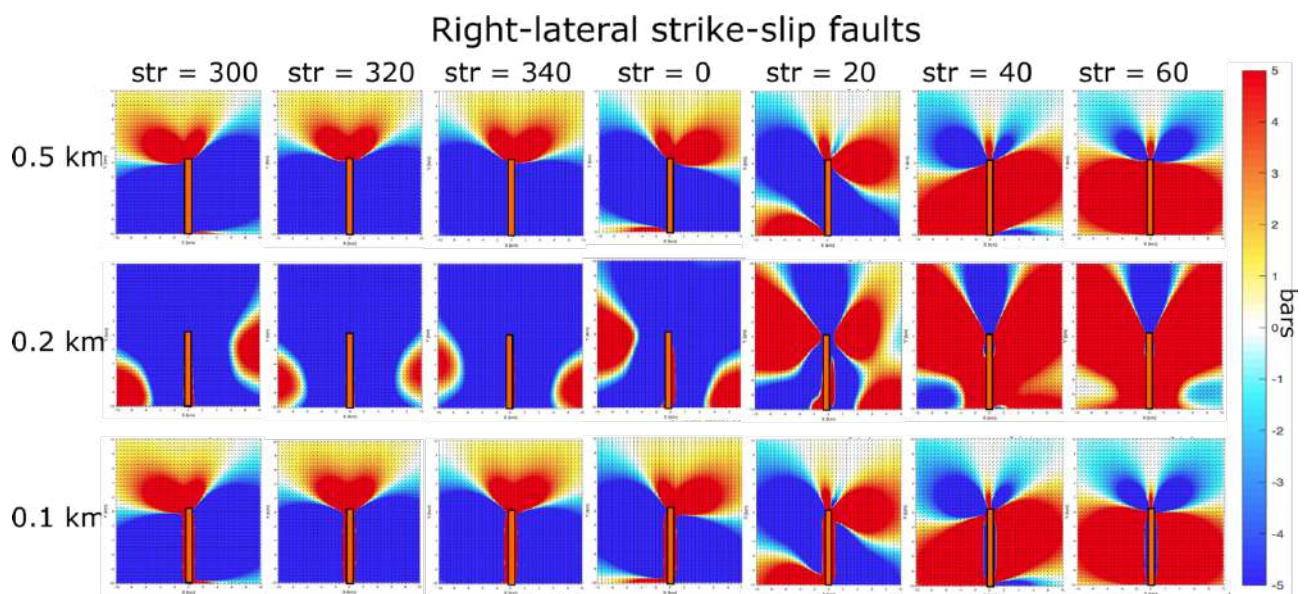


Figure 49 Coulomb stress change exerted by an inflating N-S dyke on right-lateral transcurrent faults with a strike from NNW-SSE to NNE-SSW. Horizontal planes are shown: depth calculations are 0.5 km (within the dyke), 0.2 km (top of the dyke) and 0.1 km (above the dyke). Stress changes are depicted by graded colors (scale on the right). Dyke is represented as an orange rectangle. Width of the dyke not scaled.

As a next step, the Coulomb stress change on left-lateral transcurrent faults has been calculated (Figure 50). By looking at the results, it is easy to notice that the situation is mirrored compared to Figure 49. In fact, starting from the first row, which describes Coulomb stress changes in the surroundings of the dyke (0.5 km depth), we notice that the presence of NW-SE, NNW-SSE and N-S right-lateral strike-slip faults is favoured in correspondence of the dyke sides, where the Coulomb stress change is positive (red colours) whereas it is inhibited at the tip. The situation is the opposite if considering NNE-SSW to NE-SW left-lateral faults: in such case, their presence is inhibited in correspondence of the dyke sides and favoured in front of the tip of the advancing dyke. Moving towards the surface, at 0.2 km depth, which is the uppermost limit of the dyke, Coulomb stress variations indicate that N-S to NE-SW faults are inhibited both at the sides and at the tip of the dyke, whereas NW-SE to NNW-SSE left-lateral faults are mainly favoured at the sides. Furthermore, at 0.1 km depth, above the inflating dyke, we find mainly NW-SE to N-S right-lateral strike-slip faults in correspondence of the dyke sides and NNE-SSW to NE-SW faults at the tip (Figure 50), similarly to the results obtained at 0.5 km depth.

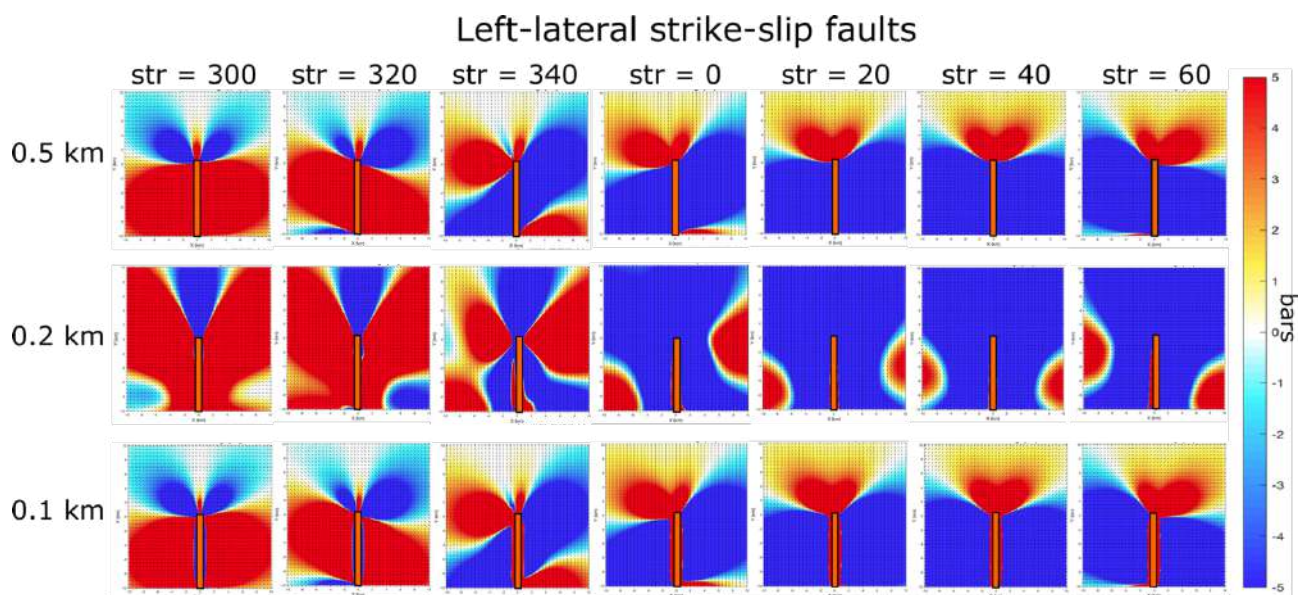


Figure 50 Coulomb stress change exerted by an inflating N-S dyke on left-lateral transcurrent faults with a strike from NNW-SSE to NNE-SSW. Horizontal planes are shown: depth calculations are 0.5 km (within the dyke), 0.2 km (top of the dyke) and 0.1 km (above the dyke). Stress changes are depicted by graded colors (scale on the right). Dyke is represented as an orange rectangle. Width of the dyke not scaled.

Chapter 5

Discussion – Northern Volcanic Zone

5.1 Theistareykir Fissure Swarm

A general discussion of the reconstructed structural architecture, with a main focus on strike-slip kinematics, of the Theistareykir Fissure Swarm is here presented. In fact, the extremely detailed survey of opening directions performed along the entire set of structures has been crucial to study the occurrence and characteristics of lateral components of motion and, most importantly, made it possible to unveil a quite peculiar pattern.

What is the process at the origin of such fractures? From [Figure 24D](#) it can be seen that, as the fracture strike rotates, their opening direction changes as well. This may be claimed to reflect a process that is linked to fracture orientation, and only subordinately to the remote tectonic stresses. If the tectonic least principal stress (σ_3) would dominate, the opening direction should remain quite stable at fractures with different orientations. Nonetheless, the results of this research suggest that the genesis of most extension fractures in the ThFS is linked to a strong local dilatant stress that forces the fracture walls to open along a direction from perpendicular to sub-perpendicular to the fracture strike. This type of stress can be produced by magma migrating in the crust along shallow-depth dykes. In fact, according to a commonly accepted model of dyke emplacement at shallow depth, the upward advancement of a dyke tip line should induce, at the surface, the development of a narrow graben or extension fractures above it ([Pollard and Holzhausen, 1979](#); [Bonafede and Olivieri, 1995](#)). In Iceland, such process has been observed, for example, during dyke emplacement events at Krafla ([Opheim and Gudmundsson, 1989](#)) and Holuhraun ([Hjartardóttir et al., 2016b](#); [Ruch et al., 2016](#)). In particular, [Gudmundsson \(1995b\)](#), thanks to field observations in Iceland, suggested that dyke emplacement does not necessarily lead to graben formation but, instead, results more often in the development of extension fractures above it. Thus, when magma propagates horizontally along a shallow, vertical dyke, it can produce also fractures with strike-slip components as well. This is testified to by the onset of seismic events, contemporaneous to dyke intrusion, with double-couple focal mechanism solutions showing strike-slip components of deformation, as observed in the past at Long Valley caldera ([Savage and Cockerham, 1984](#)), during the 2014 event

(Shelly et al., 2016) at Yellowstone caldera (Russo et al., 2017, 2020), and during the 2014 Bárðarbunga dyking episode in southern Iceland (Ágústsdóttir et al., 2016).

Furthermore, **Figures 24A** and **24B** show that the southern and central sections of the rift display similar opening directions, in the N80-140° range, whereas the northern part shows a systematic clockwise rotation of opening directions, that attain a N100-160° range. This is reflected in both Northing and Easting variation because the rift is oriented NNE-SSW and, therefore, the measurement sites positioned further east correspond also to those located at the northern termination of the rift. This clockwise rotation could be induced by the effect of shear on the northernmost onshore part of the rift, produced by the transtensional right-lateral Grimsey Lineament.

The graphs of **Figures 25A**, **25C** and **25D** demonstrate the predominance of opening directions rotated in a clockwise direction relative to fracture strike, which are expressed as the dominant right-lateral component. From a quantitative point of view, 52% of extension fractures show a right-lateral component, 31% pure extension, and 17% a left-lateral component. **Figure 25A** is particularly insightful, as it shows that the presence of the right-lateral component cannot be accounted for in terms of a rotation of the strike of fractures. The dominant right-lateral component, instead, is systematically observed whatever the orientation of the fractures. The red stripes indicating how the lateral component is expected to change in case of variations in the fracture strike with respect to the plate spreading direction, separates a large amount of values where the right-lateral component is present. The reason for this opening pattern, marked by a widespread right-lateral component, can be found in the model of **Figure 51A**, where oblique rifting is normally found at rifts with structures whose strike is not perpendicular to the direction of plate separation (Fournier and Petit, 2007). Another possibility is that the kinematics of the ThFS rift is also guided by the presence of the nearby Krafla rift and the interposed tectonic block. The latter has a wedge shape with the apex towards the south, where the two rifts come closer. A further complication may arise from different opening directions and/or amount along the Krafla rift.

Figure 51B shows a partitioning of motions at the sides of a rift that is propagating outward from the hotspot center: normal faults develop close to the rift axis, strike-slip faults further away on both sides (Karson, 2017). The predominance of left-lateral strike-slip faults in the western part of the rift is in contrast with field data collected in the present research, which show the predominance of right-lateral motions within the ThFS (**Figure 26**).

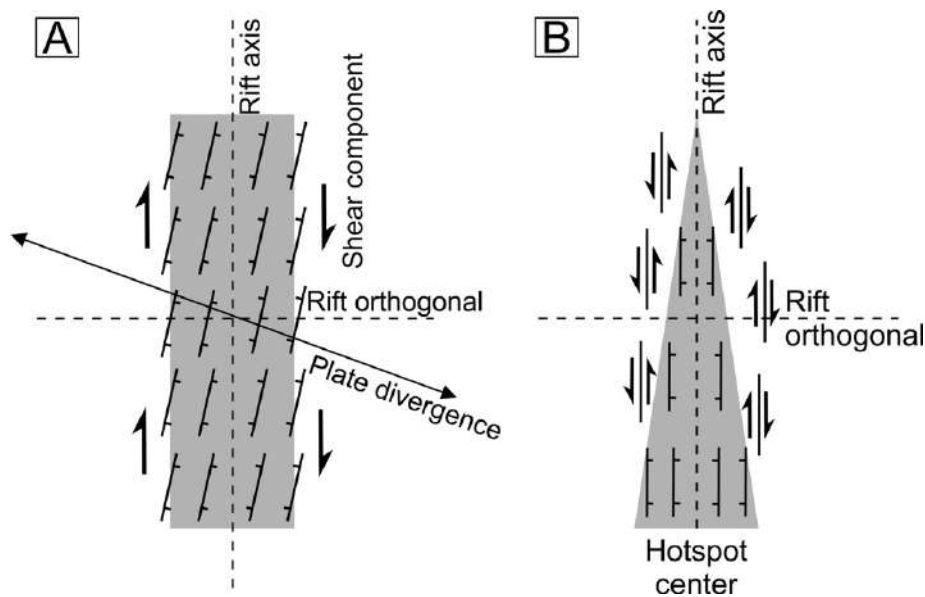


Figure 51 Sketches of rift zones with rift-parallel shear component that takes place through different fault patterns: (A) oblique rifting with en-échelon faults, the strike of which is not perpendicular to plate separation direction (after Fournier and Petit, 2007). (B) Partitioning of motions with strike-slip faults at the sides of a rift that is propagating outward from a hotspot centre (after Karson, 2017 and Tibaldi et al., 2020b).

Drone surveys allowed to collect high-detail measurements along extension fractures in the central part of the rift (location of key areas in Fig. 28).

Here, the mapped 397 structures, comprising both extension fractures and normal faults, have azimuth between N-S and NE-SW, with the maximum frequency at N-S and NNE-SSW (rose diagram in Fig. 32A). The longest continuous fractures, reaching up to 1173 meters in Key area 3, are in the range N4-28° (Figs. 31A and 32A), although most of them are < 300 m. In general, Key areas 1 and 2 are characterized by shorter length of fractures with respect to Key area 3 (Fig. 32A). As shown in Figures 16 and 31, some fractures are associated with a vertical component and are classified as normal faults, when a systematic and continuous vertical offset > 1 m is detected. On the contrary, the fractures without this offset have been classified as extension fractures and quantified through measures of opening direction and dilation (e.g. Figs. 12D-E).

In all three key areas, the opening direction is about N108° (Figs. 29, 30 and 31A): lava deposits in Key areas 2 and 3 have an age of 8-10 ka, whereas rocks in Key area 1 have an age of 2.4 ka, suggesting that the overall spreading direction in the area has been the same for the post-Last Glacial Maximum time interval. The spreading direction in the NVZ is provided as follows, by

different authors and through different methodologies. [Hjartardóttir et al. \(2012\)](#) suggested a spreading vector of N106° calculated from [DeMets et al. \(1994\)](#) who used geomagnetic data (up to 2.6 Ma - long-term data). [DeMets et al. \(2010\)](#) suggested a spreading vector of N104°, considering GPS and geological data (magnetic, bathymetric and earthquake data; up to 3.16 Ma - long-term data). [Drouin et al. \(2017\)](#) indicated a present-day spreading direction of N112° for the 2008-2014 time window, based on GPS data. Other authors who worked in the time intervals 1997-2011 and 2006-2010, found out a spreading direction of N109° and N115°, respectively ([Metzger et al., 2013](#); [Metzger et al., 2011](#)). Data of the present research cover a time interval (Holocene times) that is much longer than GPS data but much shorter than the periods investigated by way of geomagnetic data. Hence, data in the present research indicating N108° are very close to the previous, long-term N106° results ([DeMets et al., 1994](#)).

The overall fracture azimuth is mostly orthogonal to the spreading vector, as also suggested for the active Krafla fissure swarm ([Hjartardóttir et al., 2012](#)), where fractures and eruptive fissures azimuth is usually N to NNE. Local perturbations in opening directions can be related to possible dyke intrusion at a shallow depth, as shown by [Ruch et al. \(2016\)](#) for 2014-2015 Bárðarbunga dyking event. Furthermore, both fracture azimuth and opening direction in these areas do not seem to be influenced by strike-slip movements along the HFF, since they are farther away than 500 m. At a distance < 500 m, [Tibaldi et al. \(2016a\)](#) found a complex fractures geometry due to the interaction between the ThFS and the HFF. Always in regard to the opening direction, rose diagrams show that most opening occurs perpendicular to fracture azimuth ([Figs. 28A, 30 and 31A](#)) although left and right-lateral components are also present, with a predominance of the latter ([Figs. 32B-C](#)). In particular: *i*) 148 fractures have a lateral component < 5° (and thus are considered mainly extensional); *ii*) 170 fractures show a right-lateral component > 5° and are mainly in the strike range N0°-N25°; *iii*) just 42 fractures show a left-lateral component > 5° and are in the strike range of N15°-N30° ([Figs. 32B-C](#)). Based on all the above, we conclude that our spreading direction can represent the summa of multiple incremental events of crustal tectonic stretching under plate spreading, in combination with events of shallow dyking.

The relation between dyke injection and fissure swarms has already been explored in previous studies ([Sæmundsson, 1974](#); [Helgason and Zentilli, 1985](#); [Forslund and Gudmundsson, 1991](#); [Gudmundsson, 1995](#); [Tentler, 2005](#)): fractures at the surface are the result of the emplacement of dyke swarms at depth, such as those in the Tertiary lava-pile of Iceland ([Walker, 1965](#); [Opheim and Gudmundsson, 1989](#); [Tentler, 2005](#)). Furthermore, the formation of a narrow

graben at the surface might be induced by the upward advancement of the tip line of a shallow dyke below it (Pollard and Holzhausen, 1979; Bonafede and Olivieri, 1995).

Fractures in Iceland are seismically and geodetically highly active during rifting periods, which usually occur at time intervals of tens to a few hundred years, whereas they become inactive during inter-rifting stages (Hjartardóttir et al., 2016b). During rifting events, movement along fractures can occur in association with subsiding areas forming graben structures, fracture dilation and sometimes opening eruptive fissures. Such features have been observed both in Iceland rift zones as well as in the Eastern Africa Rift (e.g. Bjornsson et al., 1977; Abdallah et al., 1979; Tryggvason, 1984, 1994; Hamling et al., 2009; Wright et al., 2012). The intense earthquake activity associated with rifting migrates away from a rapidly subsiding volcanic centre (Einarsson, 1991; Einarsson and Brandsdóttir, 1980), suggesting magma migration along dykes that can result in a subaerial eruption, as occurred in the well-documented cases of Krafla and Bardarbunga rifting episodes (Buck et al., 2006; Wright et al., 2012; Hjartardóttir et al., 2012, 2016c; Sigmundsson et al., 2015; Gudmundsson et al., 2016). For example, most faults and extension fractures that originated during the 1975-1984 Krafla rifting episode are the result of rifting events, during which the magma migrated away from the caldera of the volcano toward the north or south along the fissure swarm, as far as 50 km, to form dykes at shallow levels in the crust, as suggested by earthquake distribution and characteristics (Brandsdóttir and Einarsson, 1979; Einarsson and Brandsdóttir, 1980; Wright et al., 2012).

On the other hand, the effect of tectonics has been proved to be crucial, as dyke formation is favoured at divergent plate boundaries as a result of crustal extension (Sigmundsson et al., 2015). For example, Dauteuil et al. (2001) suggested that fissuring and faulting have played a nearly equal role in accommodating the deformation over a period of 10,000 yrs in the northern Krafla fissure swarm. Differently, Hjartardóttir et al. (2012) observed a clear predominance of the regional tectonic stress field on the origin of extension, shown by the fact that eruptive fissures within Krafla central volcano are parallel to the rift fracture swarm. The prevailing role of tectonics in controlling the formation of extension fractures, which thus can originate before dykes are injected, is also stated by Paquet et al. (2007), who noticed that eruptive fissures usually occur within the first ten of kilometres from the volcanic centres, whereas rarely-erupting fissures can form farther away. To lead to an eruptive episode, a dyke might also intersect at depth pre-existing open faults (Gudmundsson, 1992) or fissures. An example of the above process is shown by the most recent 2014 Bardarbunga rifting event, where a propagating dyke has been captured by the plate-

spreading field when it was sufficiently far from the Bardarbunga central volcano, which is located west of the central axis of plate spreading (Sigmundsson et al., 2015).

5.2 Krafla Fissure Swarm

The focus of this section is to describe the main outcomes of the research conducted in the western part of the Krafla Fissure Swarm, followed by an in-depth focus on the dyke-induced Hituholar graben.

The studied rift segment is located along the northwestern part of the KFS and is characterised by the presence of grabens arranged en-échelon with a left-stepping geometry. Although the whole Krafla rift has an about N-S elongation, once you define the structures in detail it emerges that several single faults have a bimodal strike given mostly by N-S and NNE-SSW segments, with a curvilinear trace in plan view. In the study area, two main grabens are present: one, to the north, affects the Holocene lavas only, and interrupts in correspondence of the other graben. This second graben is located more to the south and mostly affects the hyaloclastic ridge and, to a lesser extent, it prolongs into the surrounding Holocene lava succession.

Focusing on the kinematics of surveyed extension fractures in the area (Fig. 32), the collected data suggest an average spreading direction of N97.7°E, with a range of N46.3-142.3°E for the Holocene times (Figure 36). This average value is lower than those given in the literature (e.g. DeMets et al., 1994; Metzger et al., 2011, 2013; Hjartardottir et al., 2012; Drouin et al., 2017; Bonali et al., 2019b, 2020): it is closer to those previously calculated based on geological data that cover a larger time window with respect to only GPS data, suggesting a slight overall anticlockwise rotation of the spreading direction in the NW part of the Krafla rift.

The overall fracture azimuth is suggested to be orthogonal to the spreading vector range discussed above: in fact, longer and more developed fractures show an azimuth N-S to NNE-SSW, as suggested for the active Krafla fissure swarm (Hjartardottir et al., 2012).

By paying attention to the presence of strike-slip components along extension fractures, it can be seen that the average value suggests an overall very low left-lateral component, even though the majority of data are characterized by values with right-lateral component (Figs. 38E-F). This component is the result of local perturbations by dyking at shallow depths, as shown for the 2014-2015 Bárðarbunga dyking event (Ruch et al., 2016) and as suggested in the ThFS (Bonali et al.,

2019a,b). In support of this hypothesis, the area has been subjected to recent historical rifting events characterized by N-propagating dykes (Hofton et al., 1996), and Tibaldi et al. (2020b) described textbook examples of dyke-induced deformation at the surface in the eastern part of the area presented in this study.

The Hituholar graben (location in Fig. 32) has been chosen for a more in detail study on the occurrence of lateral components of motion based on its dyke-induced origin: in fact, graben structures can be mainly originated by “high topography” stresses (Tibaldi and Bonali, 2018, and references therein), volcano spreading (Borgia, 1994), remote tectonic stresses (Bott, 1982; Acocella, 2014) and shallow dykes (review in Tibaldi, 2015). Since the studied area is flat and of very low altitude, the first two hypotheses can be disregarded. Both tectonic stresses and shallow dyking can produce surface faulting and fissuring. In the North Volcanic Zone of Iceland, as discussed above, the active tectonic stress field is characterised by horizontal σ_3 and σ_2 , which trend WNW-ESE and NNE-SSW respectively (Ziegler et al., 2016). More in detail, in the studied area the σ_3 trends N90-100° and can be responsible, in theory, of the formation of the extensional structures that strike N-S to NNE-SSW.

Anyway, in volcanotectonic rift zones like Krafla, a possible explanation for faults and extension fractures can also be related to the magmatic stresses originated from shallow dyking. In fact, the hydraulic pressure build-up in a magma chamber cannot be compensated by elastic dilation of the surrounding host rock, and fractures propagate from the walls of the chamber and accommodate all the magma necessary to relieve pressure in the source region (Delaney and Pollard, 1981). Once a fracture advances, magma propagates further away from the magma chamber along the fracture plane. The advancing dyke and related stresses are capable of inducing extension fractures and normal faults at the surface once the magma intrusion reaches up to a few km from the surface. The pressurized dyke produces two tensile stress concentrations at the surface to either side of the upward projection of the dyke, resulting in the possible generation of a graben (Pollard et al., 1983). This process is testified, for example, by the formation of dyke-induced grabens with a width from a few tens of meters up to 1.5 km at the Hawaiian volcanotectonic rifts (Jackson et al., 1975); at Medicine Lake Highland Volcano (California), dyke-induced grabens are from 150 to 250 m wide (Fink and Pollard, 1983); at Inyo Craters, Long Valley (California), a dyke-induced graben fracture zone is tens of meters to 400 m wide (Mastin and Pollard, 1988); in Iceland, during the Bárðarbunga dyke intrusion, a 0.5-0.8 km wide graben formed (Ruch et al., 2016), similar to the width of the Sveinar graben (Tentler and Mazzoli, 2005), and the Sveinagja graben prior to the 1875

eruption ([Gudmundsson and Bäckström, 1991](#)). All these data indicate that dyke-induced grabens are typically narrow, frequently in the order of few tens of meters. This is related to the fact that only shallow dykes can produce enough stress to offset the surface, and since the graben width is about equal to twice the depth to the dike top ([Pollard et al., 1983](#)), as a consequence there is a limit to the resulting graben width.

These observations support the hypothesis that the Hituholar graben structures had been originated by a shallow dyke. This interpretation is further, strongly supported by four other considerations.

1) The graben is located in a zone prone to shallow dyke intrusion. In the past and recent history of this volcano, tens of dykes propagated northwards and southwards from the magma chamber ([Tryggvason, 1978](#); [Bjornsson et al., 1979](#)). This was triggered by magma pressure build up in the magma chamber and favored by regional tectonic plate separation. Brittle deformation of the magma chamber walls is testified by earthquakes in the interior of the Krafla caldera structure that successively propagated northward or southward along the volcanotectonic rift. This has been interpreted as evidence of magma horizontal migration up to 40 km from the magma chamber, along vertical, propagating fractures ([Brandsdottir and Einarsson, 1979](#); [Hofton and Foulger, 1996](#)). The studied Hituholar graben crops out from 8 to 11 km from the Krafla caldera, a distance that is fully compatible with a dyke propagated from this volcano.

2) As already demonstrated by our data and as shown in [Figures 47](#) and [48](#), the presence of local uplift of the graben floor is a diagnostic characteristic typical of dyke-induced surface structures ([Fink and Pollard, 1983](#)).

3) Similarly, our data indicate local arching of the topography along the studied structure, which is also a typical evidence of shallow dyking ([Fink and Pollard, 1983](#)).

4) Finally, also width variations along strike of a dyke-induced graben in relation to altitude differences, is a diagnostic criterion. In order to fully evaluate this relation, in [Figure 52](#) the values of 266 measurements of the width of the zone of deformation measured systematically along strike are plotted, respect to their absolute altitude. [Figure 52A](#) shows the amount of measurements done respect to northing, which is to say respect to graben strike, testifying to the completeness and systematic of values. [Figure 52B](#) shows the plot of width values versus altitude: these data indicate frequent variations of the graben width in strict correlation with differences in altitude, as it is typical of dyke-induced structures.

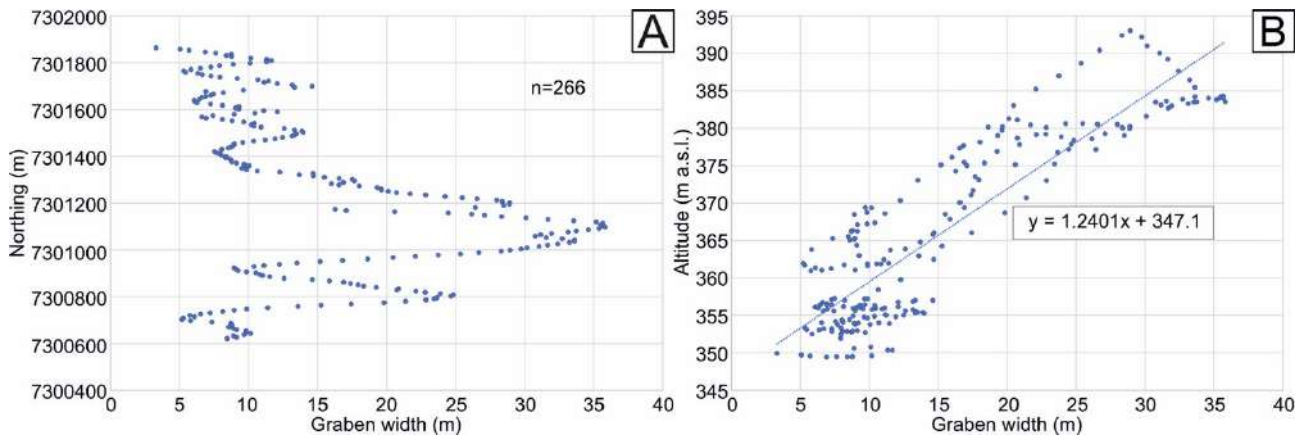


Figure 52 (A) Graph showing the amount and distribution of measurements of deformation zone width (X-axis) respect to Northing (Y-axis), which is to say respect to graben strike. (B) Graph plotting deformation zone width values (X-axis) versus altitude (Y-axis), which shows a good correlation typical of dyke-induced structures. Regression line and related equation are shown (Tibaldi *et al.*, 2020a).

The along-strike characteristics of the studied deformation zone change not only in correspondence of topographic variations, but also of geological differences. South and north of the Hituholar volcano, the deformation zone is composed by extension fractures, whereas approaching the volcano, the fractures change into faults (Figure 40). Such lithological change is clearly reflected in a change of the rheological properties of the deposits: lavas have a much higher stiffness than hyaloclastites.

According to the location of the Krafla magma chamber respect to the studied zone and the typical intrusion processes along the Krafla rift (Tryggvason, 1978; Brandsdottir and Einarsson, 1979; Bjornsson *et al.*, 1979; Hofton and Foulger, 1996), the dyke responsible of the formation of Hituholar graben structures propagated northward. Although field observations indicate that the main structures have been produced by pure extension, in the form of dip-slip normal motions along faults or pure dilation across extension fractures, a series of secondary fractures have been detected, that show strike-slip components of motion. The right-lateral shear at fractures rotated anticlockwise respect to the main deformation zone, and left-lateral shear at fractures rotated clockwise, are coherent with the meaningful outcrops found along the Hituholar deformation zone (e.g. Fig. 45) and at its tip (Fig. 46).

These field data can be compared with analytical models; the stress surrounding a dyke tip produces shear concentration until rock failure is reached along planes suitably oriented. The stress capable of inducing rock failure is composed by the superposition of the ambient stress with the stress

perturbation produced by the dyke overpressure. The pressure variations in the dyke may be neglected when assessing the effects on inelastic deformation of rock volumes at distances approaching the dyke height or length, whereas pressure variations are effective on outcrop-scale deformations occurring up to several meters from the dyke tip (Rubin, 1992; Rubin and Gillard, 1998). The dyke overpressure produces maximum shear along planes, oriented at about 30° respect to the dyke plane, which can be located at a few meters from the dyke tip without intersecting the dyke, or can depart nearby the dyke tip, or from the dyke wall behind the magma front (Rubin and Gillard, 1998). Field data indicate that all the left-lateral and right-lateral fractures behind the termination of the fracture zone, are now exposed at the side of the main fracture zone and are interrupted by the main NNE-SSW extension fractures. This observation, together with the presence of fractures oblique to the main trend also in the interior of the main deformation zone, suggest that the secondary strike-slip zones preceded the formation of the NNE-SSW main extension fractures at the surface.

Chapter 6

Methodology – Yellowstone volcanic plateau

Regarding the Yellowstone volcanic plateau, the analysis has been focused on the elaboration of seismic data regarding both earthquakes of magmatic and tectonic origin. Seismic data elaboration allowed to evaluate the location, geometry and kinematics of rift-parallel structures both at the near surface and within the upper crust.

6.1 Yellowstone volcanic plateau: seismic data and processing

The seismic data analyzed in this study have been provided by the University of Utah Seismograph Stations (UUSS), which operates the Yellowstone seismic permanent network, consisting of up to 47 short-period, vertical and three-component seismic stations, to record and document earthquakes, locate epicenters and provide public information and data for scientific research (Figure 53). The Yellowstone earthquake catalog is based mainly on data from a telemetered seismic network in the Yellowstone region. On September 2006, the network consisted of 26 stations: six broadband 3-component digital telemetry stations, three 3-component short-period stations and 17 vertical-component short-period stations. An upgrade to the network was introduced in the time period between 2009 and 2011 from the ARRA (American Recovery and Reinvestments Act) by USGS and NPS funding that included installation of two vertical short-period, seven three-component short period, 11 broadband seismometers and seven accelerometers.

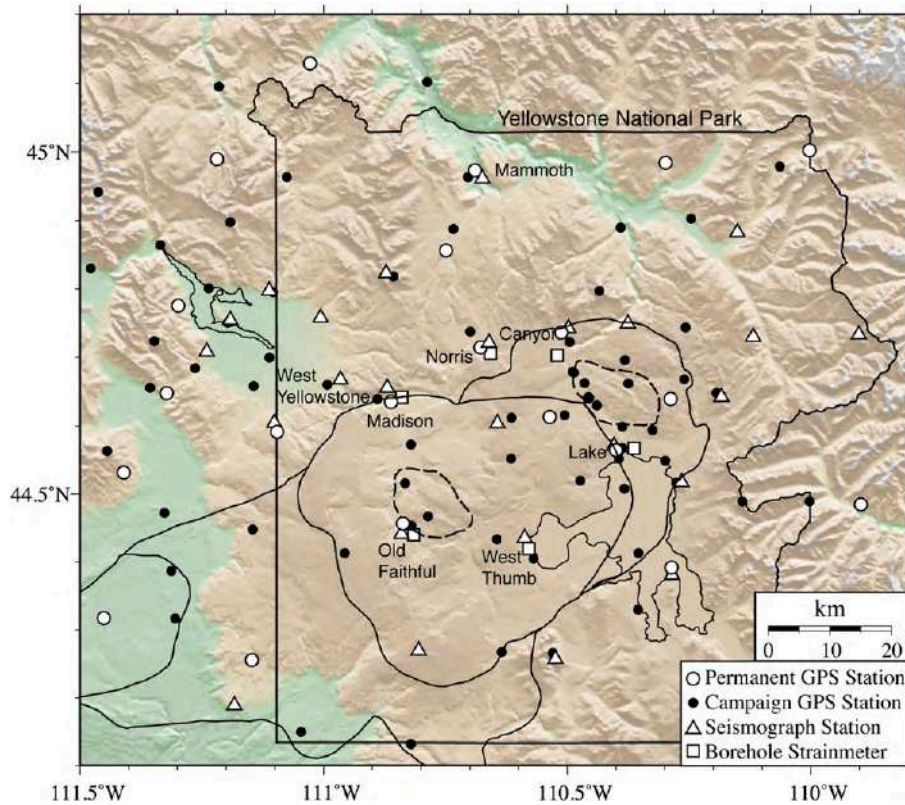


Figure 53 Station map of Yellowstone National Park and surrounding area showing regional seismograph, GPS, and borehole strainmeter networks. Seismic stations consist of broadband and short-period seismometers operated by the University of Utah and the Yellowstone Volcano Observatory. GPS sites include 26 permanent and 90 temporarily occupied (campaign) sites operated by the University of Utah and EarthScope PBO (Smith et al., 2009).

The area that contains all epicentres that have been processed, which is shown in Figure 56A, is comprised between 470000 and 580000 easting (X axis) values (WGS84/UTM coordinate system), and between 4850000 and 5000000 northing values (Y axis).

The elaboration of the raw seismic data was performed in five steps. It consisted in: *i*) hypocenters relocation; *ii*) best quality seismic events selection; *iii*) focal mechanism solutions (FMS) calculation; *iv*) pressure and tension (P- and T) axes evaluation; and *v*) state of stress estimation.

6.2 Seismic data elaboration: hypocenters relocation and earthquakes selection

The elaboration of seismic data consisted in hypocenters relocation with high detail, selection of best quality seismic events, calculation of focal mechanism solutions (FMS), of the corresponding pressure and tension (P- and T-) axes and of the state of stress.

The first step that has been made was to relocate hypocenters in order to create an homogeneous dataset in order to calculate take off angles aimed at determining focal mechanism solutions, as it has been done in previous studies in the Yellowstone area (e.g. [Husen and Smith, 2004](#); [Pang et al., 2019](#)). In the present research, a non-linear relocation approach known as NonLinLoc ([Lomax et al., 2000](#)) has been used, and a three-dimensional velocity model computed with local earthquake tomography ([Farrell et al., 2014](#)). This relocation approach assures the high-quality location and uncertainty parameters for each earthquake. NonLinLoc follows the probabilistic formulation of nonlinear inverse problems by [Tarantola and Valette \(1982\)](#). The formulation relies on the use of normalized and unnormalized probability density functions to express knowledge about the values of parameters. If the probability density functions giving a priori information on the model parameters and on observations are independent, and the theoretical relationship relating a vector of observed data and unknown parameters can be expressed as a conditional density function, then a complete, probabilistic solution can be expressed as a posteriori probability density function ([Tarantola and Valette, 1982](#)). In earthquake location, the unknown parameters are the hypocentral coordinates and the origin time. The observed data are arrival times measured at seismograph stations and the theoretical relation gives predicted or theoretical travel times. In NonLinLoc, the probability density function can be computed in different ways ([Lomax et al., 2000](#)): using a grid-search algorithm with successively finer, nested grids, with a Metropolis-Gibbs sampling algorithm performing a directed random walk within a special volume to obtain a set of samples that follow the probability density function, and with an Oct-Tree Importance sampling algorithm, which gives accurate, efficient and complete mapping of the probability density function of the earthquake location problem ([Lomax and Curtis, 2001](#)). It uses recursive subdivisions and sampling of cells in three dimensions to generate a cascade of sampled cells, where the number of sampled cells follows the values of the probability density function at the cell center, leading to a higher density of cells in areas of higher probability density function. Multiple minima in the function are reliably detected by the grid-search algorithm and the Oct-Tree algorithm but are missed by a factor of 100 in computing time. This algorithm may not detect narrow, local minima in the density function.

As a next step, a selection of a subset of earthquakes has been performed, with the aim of identifying the best-quality earthquake locations for FMS computation and stress-field inversion according to [Yang et al. \(2012\)](#). Firstly, only the earthquakes with a minimum number of observations at seismic stations of 10 have been taken into account. In fact, increasing numbers of arrival-time observations generally result in improved earthquake locations. The maximum ratio of minimum distance from the closest stations and depth was imposed to be 1.50. Another parameter that has been considered was the difference between the maximum likelihood and expectation hypocenter locations. Large differences between the maximum likelihood and the expectation hypocenter locations can result from an ill-conditioned location problem ([Lomax et al, 2000](#)). In this case, Gaussian location estimates, for example the confidence ellipsoid, are not adequate uncertainty estimates anymore because location uncertainties can be irregular or show multiple minima. For this research, the higher difference was imposed to be equal to 500 meters. The azimuthal gap, which is the largest distance between azimuthally adjacent stations, was imposed to be lower than 180 degrees. In general, the smaller this number, the more reliable is the calculated horizontal position of the earthquake.

Furthermore, the average error, which is the average length of the three axes of the 68% ellipsoid, had to be lower than 2000 m. The root-mean-square (RMS) travel time residual, measured in seconds, provides a measure of the fit of the observed arrival times to the predicted arrival times for this location and has been imposed to be less than 0.5 seconds. Smaller numbers reflect a better fit of the data. This value depends on the accuracy of the velocity model used to compute the earthquake location, the quality weights assigned to the arrival time data and the procedure used to locate the earthquake.

6.3 Focal mechanism solutions

The calculation of focal mechanism solutions (FMS) is a key point for the structural-geological-seismological analysis of the key sites of this research. The focal mechanism of an earthquake sums up the slip motion of the rocks underground and the orientation of the fault that the slip occurred on. Focal mechanisms are important in particular for determining fault orientation and slip direction for an earthquake magnitude less than 5 or 6, when the ground surface is not ruptured to produce a visible fault scarp. Furthermore, apart from preliminary informations such as the precise hypocentral location and the fault kinematics, an advanced elaboration of focal mechanisms allows to calculate compression P and tension T axes, a crucial information to reconstruct the stress field

at the origin of each seismogenetic structure. Also, the spatial distribution of hypocenters at depth, shown by plots of focal mechanisms, is useful to determine planes of movement that generated earthquakes, which can be compared and correlated to field surficial evidences of active faults, such as geometry and kinematic indicators. Also, by subdividing focal mechanisms into temporal and spatial windows according to phases of surficial deformation (either uplift or subsidence) and magmatic intrusions, it has been possible to evaluate variations in the stress field and to relate these changes with movement and emplacement of magmatic fluids.

The determination of new double-couple FMS out of the selected earthquakes has been performed through the FORTRAN program HASH (Hardebeck and Shearer, 2002), which fits P-wave first motion polarity to the double-couple focal mechanisms. The HASH method uses a grid-search over possible combinations of nodal planes, generates a set of acceptable mechanisms for each event given the sources of uncertainty, and returns the most likely mechanism. Mechanism quality is assigned based on the solution stability with respect to model uncertainty, represented by the spread of the acceptable mechanisms, which take into account the uncertainty in polarity measurements, event location and take-off angle. The most probable solution is computed together with some estimates of the quality of the solution. The preferred solution is the average of the acceptable fault plane solutions after outliers have been removed. The RMS difference between the acceptable nodal planes and the preferred planes is computed. The final step is to find the data misfit for the preferred mechanism. The inputs for both the subroutines are the set of polarity (and amplitude ratio) observations for the stations, the azimuth, the takeoff angle to each station and the preferred mechanism. The outputs are the weighted fraction of misfit polarities and the station distribution ratio.

Four parameters have been used to define the quality of resulting solutions (Table 1): average misfit, Root Mean Square of the fault plane uncertainty, station distribution ratio, and mechanism probability (Hardebeck and Shearer, 2002). Kilb and Hardebeck (2006) found that the single best discriminator of solution quality was the RMS fault plane uncertainty.

Quality	Average misfit	RMS fault plane uncertainty	Station distribution ratio	Mechanism probability
A	≤ 0.15	$\leq 25^\circ$	≥ 0.5	≥ 0.8
B	≤ 0.20	$\leq 35^\circ$	≥ 0.4	≥ 0.6
C	≤ 0.30	$\leq 45^\circ$	≥ 0.3	≥ 0.7
D	maximum azimuthal gap $\leq 90^\circ$, maximum takeoff angle gap $\leq 60^\circ$			
E	maximum azimuthal gap $> 90^\circ$, maximum takeoff angle gap $> 60^\circ$			
F	fewer than 8 polarities			

Table 1: Focal mechanism quality determination (modified after [Hardebeck and Shearer, 2002](#)).

6.4 Calculation of the state of stress from FMS

Earthquakes are passive markers of deviatoric stress and individually determined FMS have been used to estimate the best uniform stress field within limited space-time windows through different procedures ([Angelier, 1984](#); [Gephart and Forsyth, 1984](#); [Michael, 1987](#); [Rivera and Cisternas, 1990](#); [Horiuchi et al., 1995](#); [Robinson and McGinty, 2000](#); [Abers and Gephart, 2001](#); [Hardebeck and Shearer, 2003](#); [Hardebeck, 2006](#)). For this research, a new iterative stress inversion method, known as STRESSINVERSE, that has been proven to perform better than the standard linear inversion, has been used. This modifies Michael's method ([Michael, 1987](#)) and inverts jointly for stress, which is calculated in iterations, and fault orientations, which are determined by applying the fault instability constraint ([Vavrycuk, 2014](#)). Also the overall friction on faults is determined. The method has been exemplified on real data from central Crete and from the West- Bohemia swarm area of the Czech Republic.

6.5 Seismic catalogue declustering and swarm identification

Seismicity declustering allows to separate earthquakes into two parts: *i*) independent earthquakes, which are not triggered by previous earthquakes but instead by tectonic loading or, in case of seismic swarms, by stress transients; and *ii*) dependent earthquakes, triggered by mechanical processes at least partly controlled by previous earthquakes, for example aftershocks, foreshocks, or multiplets. The declustering process consists into the removal of dependent events, which is

useful to model processes based on event independent from each other. Regarding dependent earthquakes, foreshocks and aftershocks are both temporally and spatially dependent on the mainshock. Aftershocks can be distinguished based on spatio-temporal proximity to previous earthquakes or by a greater rate respect to the averaged seismicity rate over long periods. In order to relate an aftershock to a mainshock it is thus necessary to define a measure of space-time distance between the two: to achieve these goals, several algorithms are available ([Gardner and Knopoff, 1974](#); [Reasenber, 1985](#); [Zhuang et al., 2002](#); [Hainzl et al., 2006](#); [Zaliapin and Ben-Zion, 2013](#)). The best algorithm must account for tectonic differences and estimate the background rate without removing all earthquakes within a temporal and spatial window.

6.6 Numerical modeling

In the case of the Yellowstone volcanic plateau, Coulomb 3.3 freeware software allowed to investigate the deformation patterns in the upper crust resulting from the inflation of a horizontal magmatic body.

In fact, I focused on the calculation of crustal dilatation resulting from the inflation of a sill below the 0.63 Ma Yellowstone caldera, proposed by [Chang et al. \(2007, 2010\)](#) ([Figure 54](#)), located at depths between 9 km and 11 km. The upper crust has been modelled as an elastic isotropic halfspace characterized by:

- a Young's modulus $E = 80$ GPa, based on [Mithen \(1982\)](#), [Lin and Stein \(2004\)](#) and [Toda et al. \(2005\)](#), which corresponds to the stiffness of the isotropic elastic material;
- a Poisson's ratio $\nu = 0.25$, based on [Lin and Stein \(2004\)](#) and [Toda et al. \(2005\)](#), which corresponds to the ratio of the contraction (perpendicular to the applied load) and the extension or axial strain (in the direction of the applied load), when a material is stretched;
- a friction coefficient $\mu = 0.4$, which is within the range 0.0-1.0, that is considered typical of the crust ([Lin and Stein, 2004](#); [Toda et al., 2005](#)).

The stress field defined as input is based on data from the World Stress Map database ([Heidbach et al., 2008](#)). Crustal dilatation values have been calculated at depth intervals of 2 km from a depth of 8 km to the surface, according to the location of the sill ([Chang et al., 2007, 2010](#)).

The grid size has been defined as 4 km x 4 km.

The inflating sill has been divided in 30 patches, which have been defined through their coordinates (longitude, latitude, depth), the strike, dip, and horizontal and dip lengths (in km), and the opening (in meters) ([Figure 52](#)). The strike and dip slips have been set to zero for a pure sill inflation.

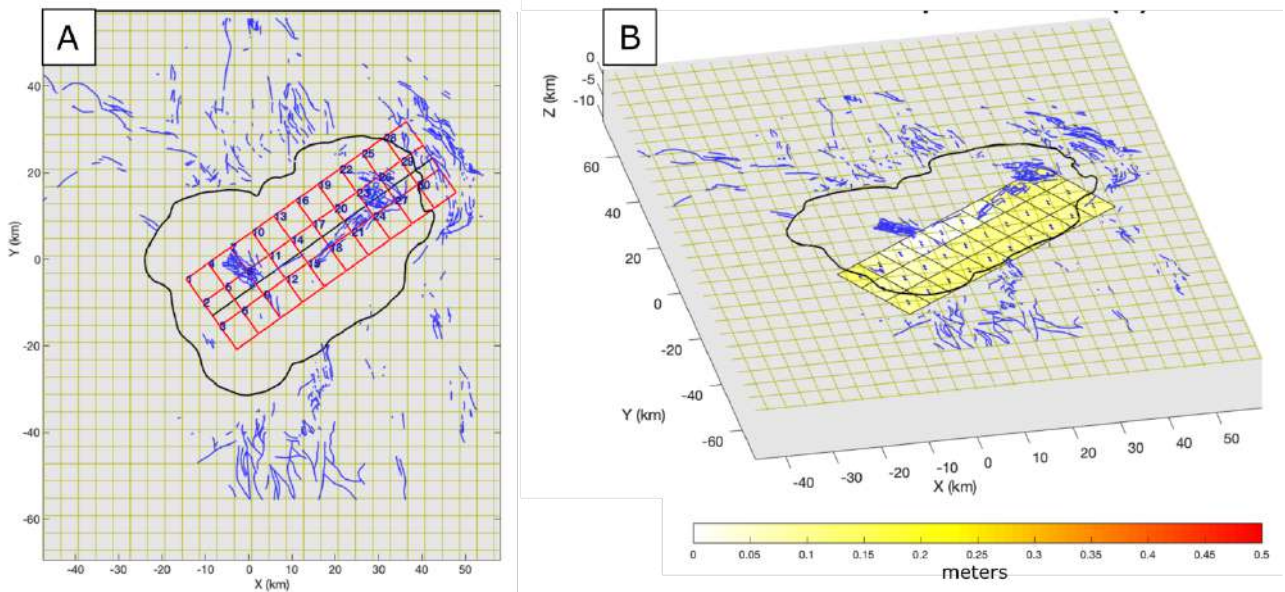


Figure 54 (A) Two-dimensional and (B) three-dimensional outline of the modeled sill (from [Chang et al., 2007, 2010](#)), divided in 30 patches (red squares) on Coulomb 3.3 software. The 0.63 Ma Yellowstone caldera is shown as a black line, Quaternary faults from [Christiansen \(2001\)](#) are shown in blue. Color scale represents the opening values of each patch of the sill.

Chapter 7

Results – Yellowstone volcanic plateau

Over the next sections, the focus will be on the results of a fully-integrated evaluation of seismicity, fault kinematics, and stress field at Yellowstone volcanic plateau, through the analysis of a rich seismic catalogue and related focal mechanism solutions. The earthquake catalog has been analyzed in terms of location, time, and kinematics according to the phases of surficial deformation documented by GPS data in order to identify systematic patterns of deformation and has been compared to the 1988-2009 seismicity. The questions addressed here are: *i)* Are there systematic patterns of deformation that can be identified by grouping earthquake source mechanisms in terms of space and time? *ii)* What is the influence of past sill intrusions on the most recent stress field? *iii)* Which process causes the concurrence of normal and strike-slip kinematics? *iv)* What are the relationships between fault kinematics, stress changes and magmatic processes? *v)* What magmatic processes (fluid properties, dimensions, and dynamics) might have been occurring?

7.1 Faulting system

As a first step, I analyzed the 3097 Quaternary faults that have been mapped by [Christiansen \(2001\)](#), who distinguished them between certain and concealed, based on the reliability of the location of the structures ([Figure 55A](#)): the latter structures have a poorly defined trace in the field and are inferred on the basis of topography, whereas certain faults have been mapped by photogrammetry on a topographic basemap at a scale of at least 1:250,000 ([Machette, 2001](#)). The orientation of such faults is preferentially N-S, as shown in the rose diagrams in [Figure 55B](#), with subordinate ENE-WSW and WNW-ESE orientation of faults located within the 0.63 Ma Yellowstone caldera and out of the northeastern caldera rim.

Furthermore, the relation between fault length and azimuth is shown in the graph in [Figure 55C](#). The maximum fault length reaches 10.4 km, whereas the majority of faults have lengths comprised between 0.1 and 2 km.

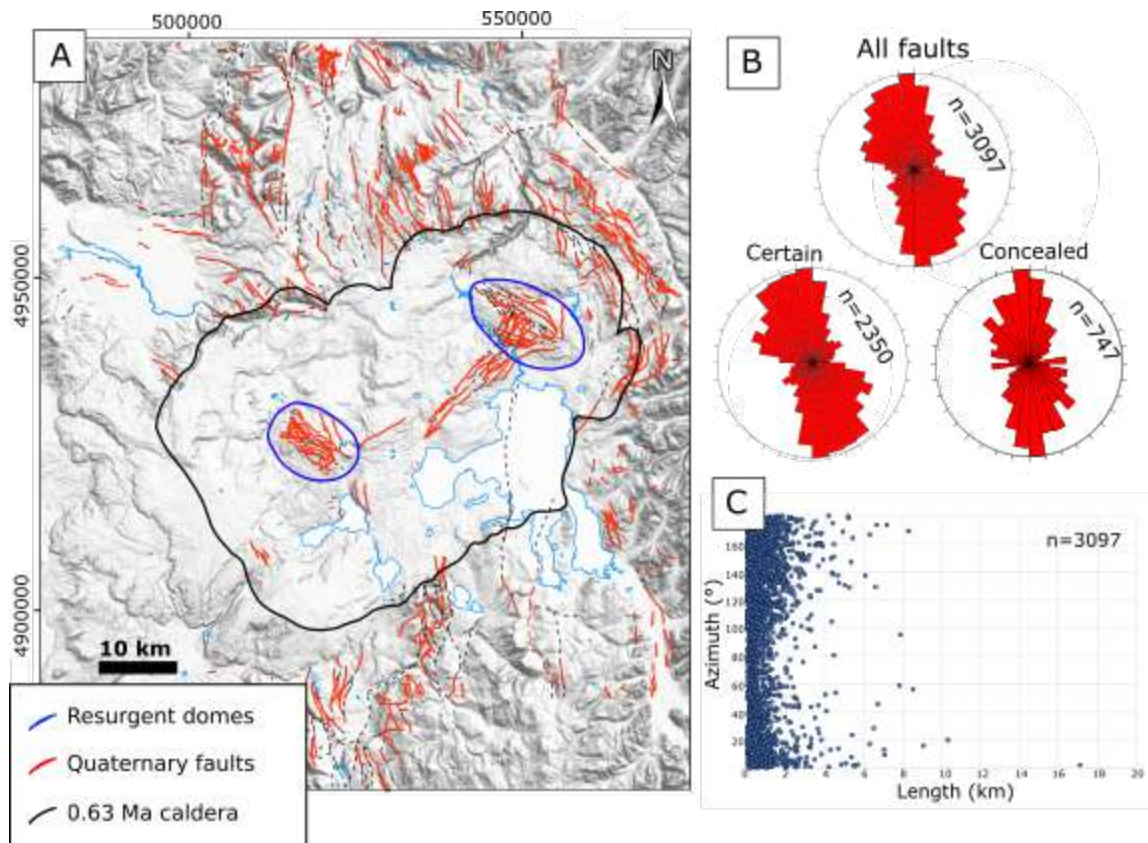


Figure 55 (A) Yellowstone Quaternary faults after [Christiansen \(2001\)](#). Dashed lines indicate concealed faults. Shaded view of the Digital Elevation Model (DEM) provided by the USGS National Elevation Dataset. Coordinate system: WGS84/UTM zone 12N. Coordinates are expressed in meters. (B) Rose diagrams showing strike of Quaternary faults (after [Christiansen, 2001](#)), divided between ‘certain’ and ‘concealed’. (C) Plot of the relation between length and azimuth of all faults (certain and concealed) ([Russo et al., 2020](#)).

7.2 Earthquake relocations

We relocated a total of 10,201 earthquakes from the UUSS catalog ([Figure 56A](#)) using a nonlinear relocation approach known as NonLinLoc ([Lomax et al., 2000](#)) and a three-dimensional velocity model computed with local earthquake tomography ([Farrell et al., 2014](#)). The 10,201 relocated earthquakes are distributed throughout the Yellowstone volcanic plateau and the areas of especially concentrated seismicity are shown with black rectangles in [Fig. 56A](#). One E-W-trending cluster northwest of the 0.63 Ma Yellowstone caldera lies between Norris Geyser Basin and the 1959 Hebgen Lake earthquake epicenter: such area of seismicity has been identified also in previous studies and is known as Norris-Hebgen seismic belt ([White et al., 1988](#); [Waite and Smith, 2004](#)). A second region of concentrated seismicity occupies the NW caldera, north of the Mallard Lake resurgent dome and includes the 2010 Madison Plateau swarm ([Shelly et al., 2013](#)). Elsewhere,

smaller clusters of seismicity are found within and adjacent to the 0.63-Ma caldera, especially near the southern margin and within Yellowstone Lake. Most of the seismic swarms that have occurred since seismic recording at Yellowstone began in 1973 are within the area of these two main clusters of concentrated seismicity (Figure 56B; Waite and Smith, 2002; Farrell et al., 2010; Shelly et al., 2013). These swarms, common in volcanic settings and associated with changes in crustal deformation from uplift to subsidence, have been attributed to stress changes induced by the movement of magmatic fluids in the subsurface (Chang et al., 2010). In particular, 1352 earthquakes of our new database (65%) were part of the 2010 Madison Plateau seismic swarm that occurred over a one-month period near the northwest boundary of the caldera (Massin et al., 2013; Shelly et al., 2013). This swarm, like the 2008-2009 swarm beneath Yellowstone Lake (Farrell et al., 2010) and the 1985 swarm in the northwestern part of the caldera (Waite and Smith, 2002), was driven by the release of magmatic fluids from the crustal reservoir to the surrounding area along pre-existing NNW-striking rupture zones (Shelly et al., 2013). Our database also contains 80 selected earthquakes from another earthquake swarm that occurred near the Norris Geyser Basin between September 2013 and June 2014, associated with the M_w 4.8 earthquake (Farrell et al., 2014; Stovall et al., 2014). As mentioned before, the deformation in the Norris area reversed from uplift to rapid subsidence shortly after this earthquake (Figure 5).

7.3 Analysis of relocated seismicity

Preliminary analysis of the relocated seismic data are shown in Figure 57: the relation between time and depth of the earthquakes (Fig. 57A) reveals greater depths of hypocenters since late 2012, when earthquakes extend down to 20 km depth instead of 15 km. Furthermore, in 2010, we notice the presence of a main cluster of hypocenters between 5 and 8 km depth, which corresponds to the 2010 Madison Plateau seismic swarm.

The histogram in Figure 57B shows the depth distribution of the whole set of relocated hypocenters: most of the earthquakes in the relocated catalog are shallower than 12 km, with the greatest concentration of seismic events located at depths between 2 and 4 km. Furthermore, Figure 57C shows the relation between magnitude values (M_w) and temporal occurrence of seismic events: magnitudes range from 0.1 to 4.8, the latter being associated with the March 2014 earthquake that was part of the Norris seismic swarm (Farrell et al., 2014; Stovall et al., 2014).

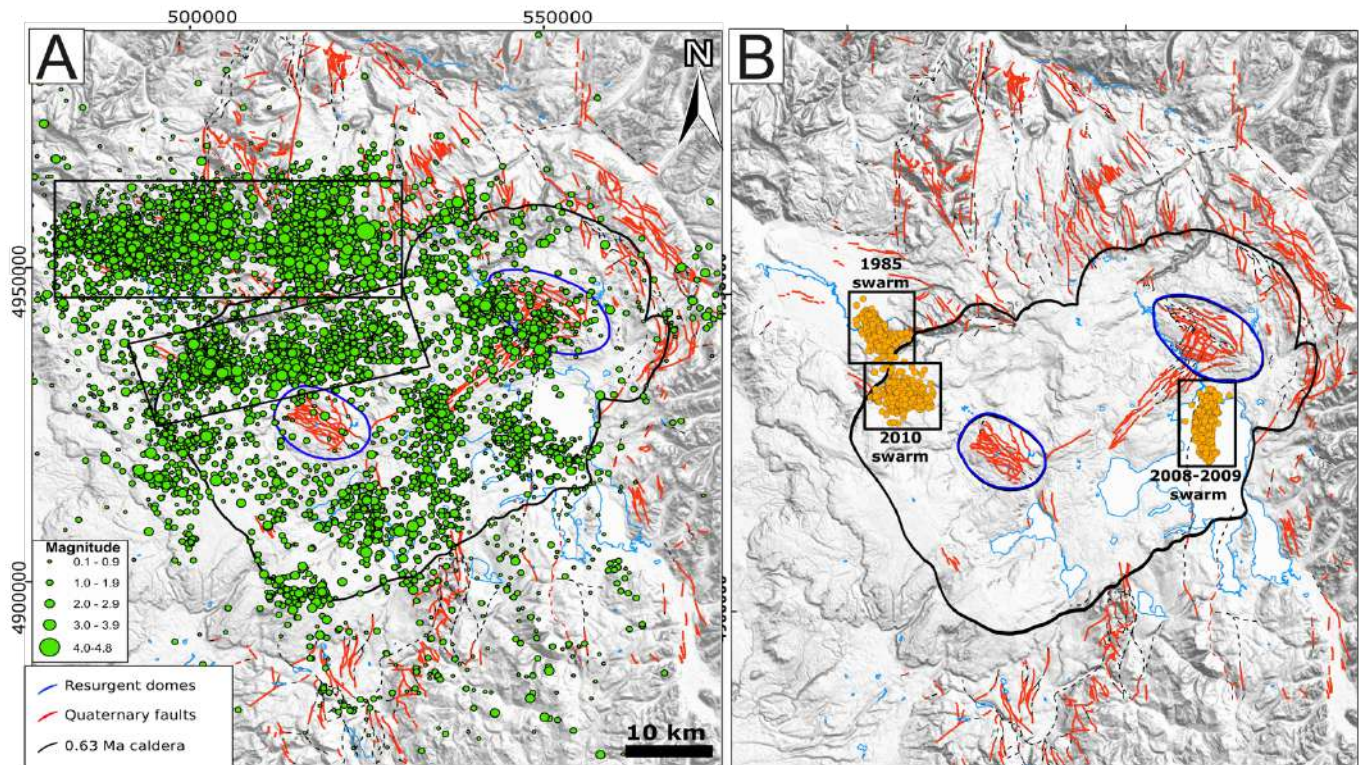


Figure 55 (A) Total of 10,201 relocated earthquakes from 2010 to 2016. Fault data, represented in red, after [Christiansen \(2001\)](#). (B) Main seismic swarms in the Yellowstone volcanic plateau. The 0.63-Ma-old Yellowstone caldera rim is outlined in black, the resurgent domes in blue. Black rectangles indicate main clusters of seismic activity. Dashed lines indicate concealed faults. Shaded view of the Digital Elevation Model (DEM) provided by the USGS National Elevation Dataset. Coordinate system: WGS84/ UTM zone 12N (modified after [Russo et al., 2020](#)).

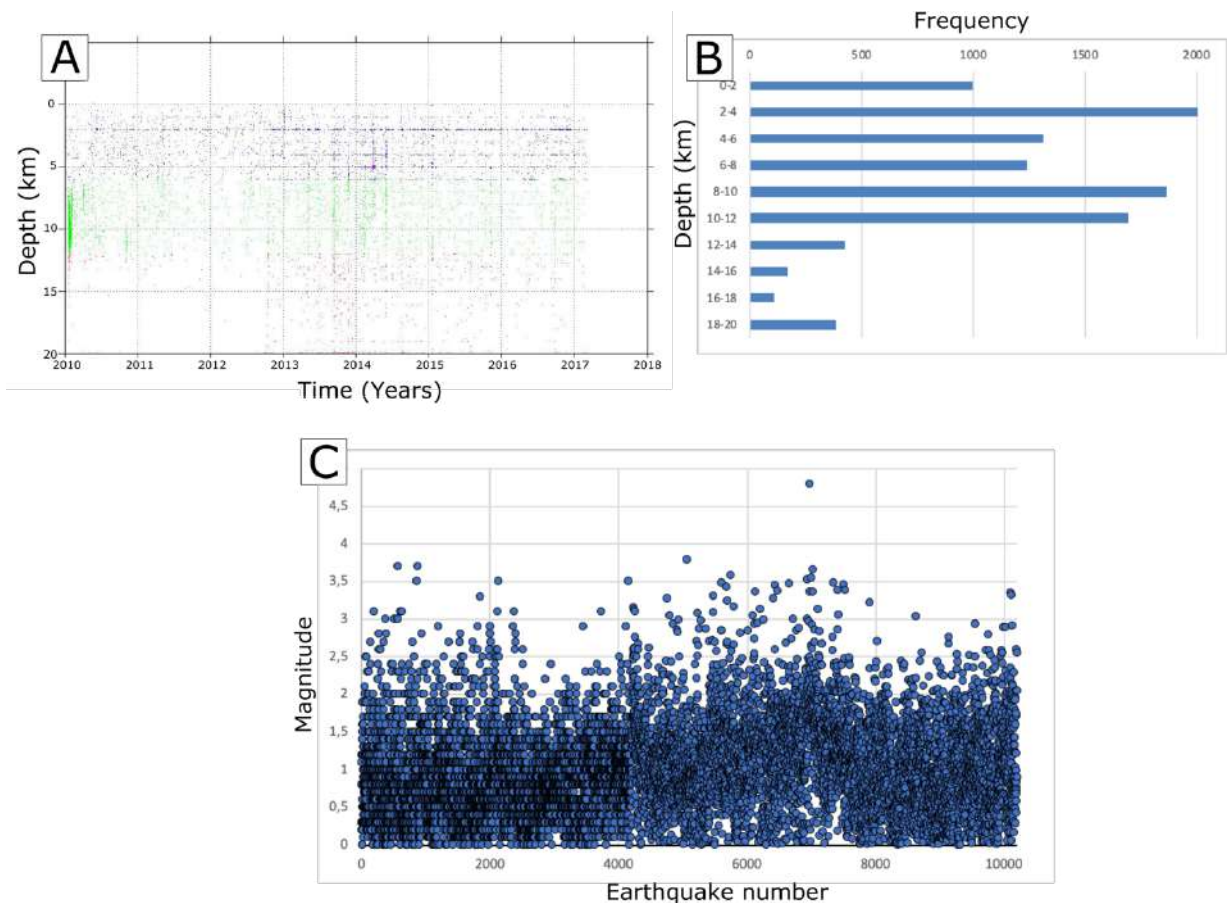


Figure 57 (A) Distribution of depths depending on year of occurrence of the 10'201 relocated earthquakes, (B) Depth distribution of the whole set of hypocenters, (C) Relation between magnitude values and year of occurrence of the 10'201 relocated earthquakes.

Figure 58 shows the results of the identification of temporal phases of seismicity between 2010 and 2016: thanks to the calculation of the cumulative number of earthquakes, shown as a yellow line in **Fig. 58A**, it has been possible to distinguish five time-progressive phases, which are shown in **Figs. 58B-F**. Furthermore, the frequency histogram of earthquakes shown in **Fig. 58A** shows a peak of more than 9,000 events in early 2010 due to the Madison Plateau seismic swarm: this is also shown in **Fig. 56B**, where most seismic events are concentrated in correspondence of the above cited swarm. This part of the analysis allowed to identify temporal migrations of seismic activity over time: for example, the transition from Phase 4 (**Fig. 58E**) and Phase 5 (**Fig. 58F**) is characterized by a westward migration of earthquakes. Also, the activity in an east-west trending zone located north of the 0.63 Yellowstone caldera border increases in Phases 3 to 5 (**Figs. 58D-F**) respect to the first two phases.

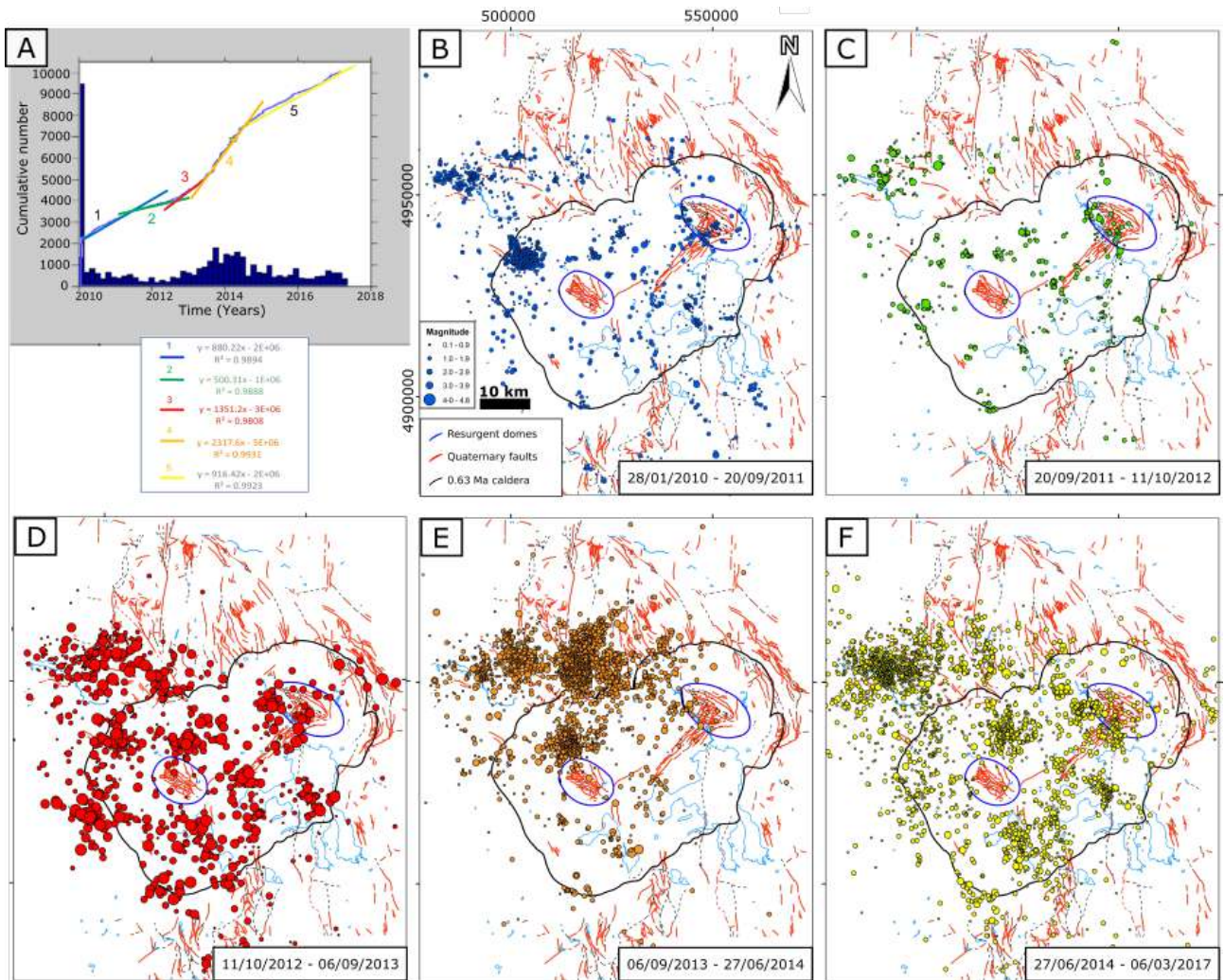


Figure 58 Temporal phases of seismicity at Yellowstone. (A) Cumulative distribution of earthquakes between 2010 and 2016, shown as a yellow line, and identification of temporal phases, represented with different colors. Lines equations and corresponding R values are represented. Histogram of frequency of earthquakes over two months intervals is shown as a background of the image. (B-F) Plots of epicentres corresponding to each temporal phase represented in Figure A. Each temporal window is indicated in the lower right corner in a white box. Earthquakes symbols have been scaled according to corresponding magnitude values. Quaternary faults, represented as red lines, are modified after Christiansen (2001).

Results of earthquake catalog declustering are shown in Figure 59, where both catalogues (declustered and clustered) are shown.

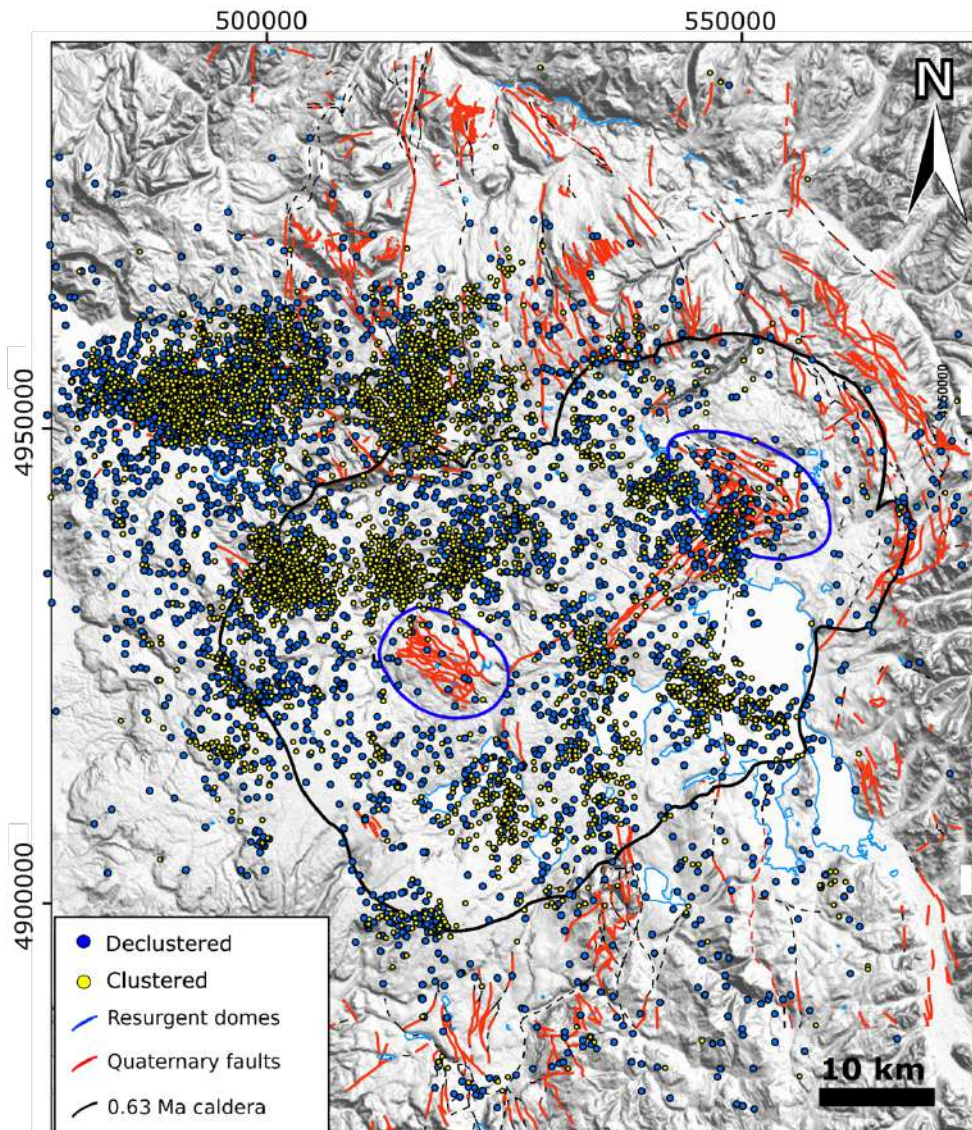


Figure 59 Declustered seismic catalogue, represented as blue circles, and clustered, represented as yellow circles, at Yellowstone volcanic plateau. Fault data, represented in red, after [Christiansen \(2001\)](#). The 0.63-Ma-old Yellowstone caldera rim is outlined in black, the resurgent domes in blue.

Six seismic swarms have been identified, which are shown in [Fig. 60](#) along with depth histograms: such swarms are all located in the northwestern part of the study area. Seismic swarms n. 2, 3 and 4, all located outside the Yellowstone caldera within the Norris Geyser Basin, are characterized by predominant depths between 5 and 7 km in the first and second case and between 3 and 6 km in the third. Differently, according to its depth histogram, the 2010 Madison Plateau seismic swarm (n.1), which is within the caldera close to the northwestern margin, is located at greater depth, mainly between 9 and 11 km.

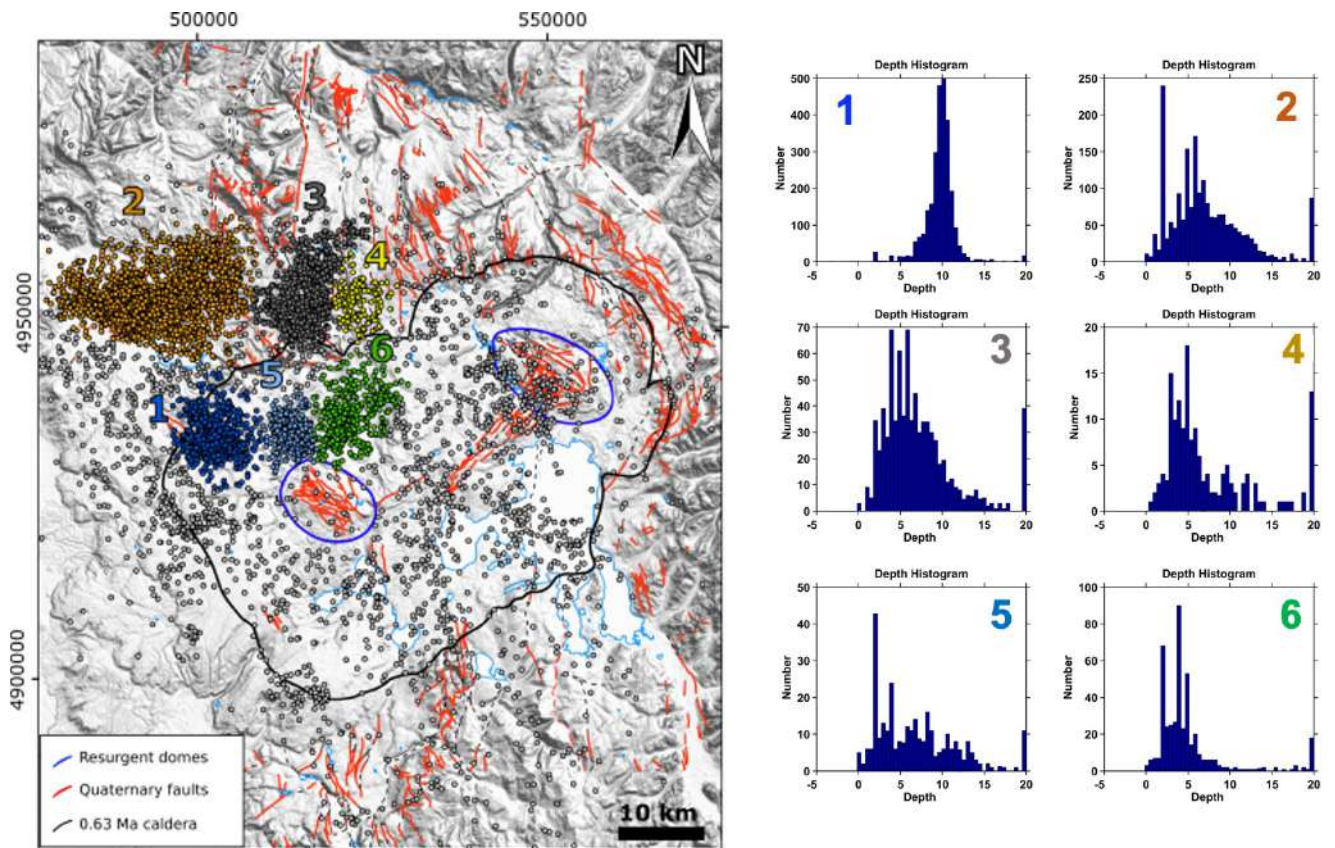


Figure 60 Seismic swarms identified at Yellowstone and corresponding depth histograms. Fault data, represented in red, after [Christiansen \(2001\)](#). The 0.63-Ma-old Yellowstone caldera rim is outlined in black, the resurgent domes in blue.

7.4 Quality selection

As a next step, a subset of earthquakes has been selected with the aim of identifying the best-quality earthquake locations for FMS computation and stress-field inversion according to [Yang et al. \(2012\)](#). The following criteria have been imposed, as described in [Section 6.2](#): *i)* 10 or more first-motion observations; *ii)* the ratio of the nearest station distance to hypocentral depth must be lower than 1.50; *iii)* the azimuthal gap must not exceed 180°; *iv)* the euclidian distance between the maximum likelihood and the center of the uncertainty ellipsoid (being fitted over the location PDF) given by the nonlinear location procedure must not exceed 500 m (larger differences can result from an ill-conditioned location problem, [Lomax et al., 2000](#)); and *v)* the Root Mean Square residual must be lower than 0.5 seconds and *vi)* the average of location uncertainties less than 2 km.

About 20% of the relocated events met all six criteria, yielding 2167 earthquakes for FMS analysis ([Figure 61](#)).

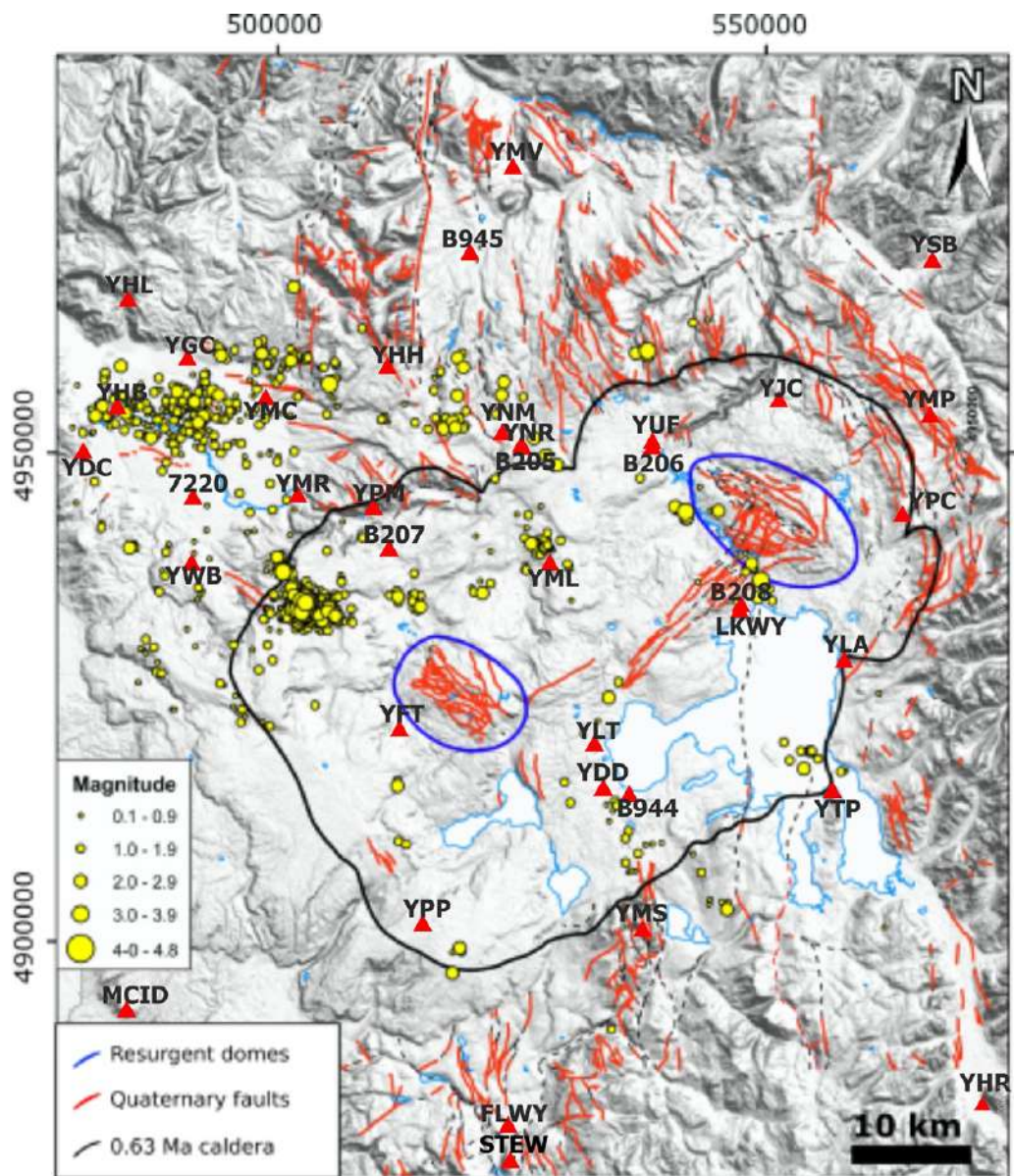


Figure 61 Total of the 2080 selected earthquakes. Fault data, represented in red, after [Christiansen \(2001\)](#). The 0.63-Ma-old Yellowstone caldera rim is outlined in black, the resurgent domes in blue. Grey dashed lines indicate concealed faults. Seismic stations of the Yellowstone network are indicated as red triangles. Shaded view of the Digital Elevation Model (DEM) provided by the USGS National Elevation Dataset. Coordinate system: WGS84/ UTM zone 12N ([Russo et al., 2020](#)).

7.5 Focal mechanisms and kinematics

224 new double-couple FMS have been determined out of 2080 selected earthquakes from 2010-2016 by using the program HASH ([Hardebeck and Shearer, 2002](#)), which fits P-wave first motion polarity to the double-couple focal mechanisms. Two non-double couple FMS that were robustly

constrained in Yellowstone were interpreted to have been triggered by pressurized hydrothermal fluids in the upper crustal magma system (Taira et al., 2010). Nevertheless, while fluid-driven earthquakes, which occur in active volcanic areas, may produce non-double-couple events, allowing non-double-couple events in the analysis of the present study would increase the ambiguity.

Four parameters were used to define the quality of resulting solutions (Table 1 in Section 6.3): average misfit, Root Mean Square of the fault plane uncertainty, station distribution ratio, and mechanism probability (Hardebeck and Shearer, 2002). The majority of our data (96%, 216 FMS) is characterized by D quality, whereas no solutions are characterized by quality A, 2 have quality B, and 6 quality C. Qualities E and F have been discarded, due to their likely inaccuracy.

Kilb and Hardebeck (2006) found that the single best discriminator of solution quality was the RMS fault plane uncertainty. The majority of the solutions are rather low quality D which have no specific classification based on this parameter, but we found that 58% have a value between 35° and 45°, consistent with quality C.

The lack of highest-quality solutions is due in part to the fact that the solution quality scheme was developed for California, where station density of the network is higher than in the Yellowstone volcanic field.

Figure 62 shows the new set of 224 double-couple FMS computed for the time period 2010-2016. Of the 224 FMS, 154 FMS show a strike-slip faulting mechanism, 23 FMS are normal, 30 are normal-oblique, and 3 have a reverse-faulting mechanism. The strike-slip events are mostly associated with the 2010 Madison Plateau seismic swarm; in fact, a total of 146 earthquakes of our database (out of 224) are part of that seismic swarm.

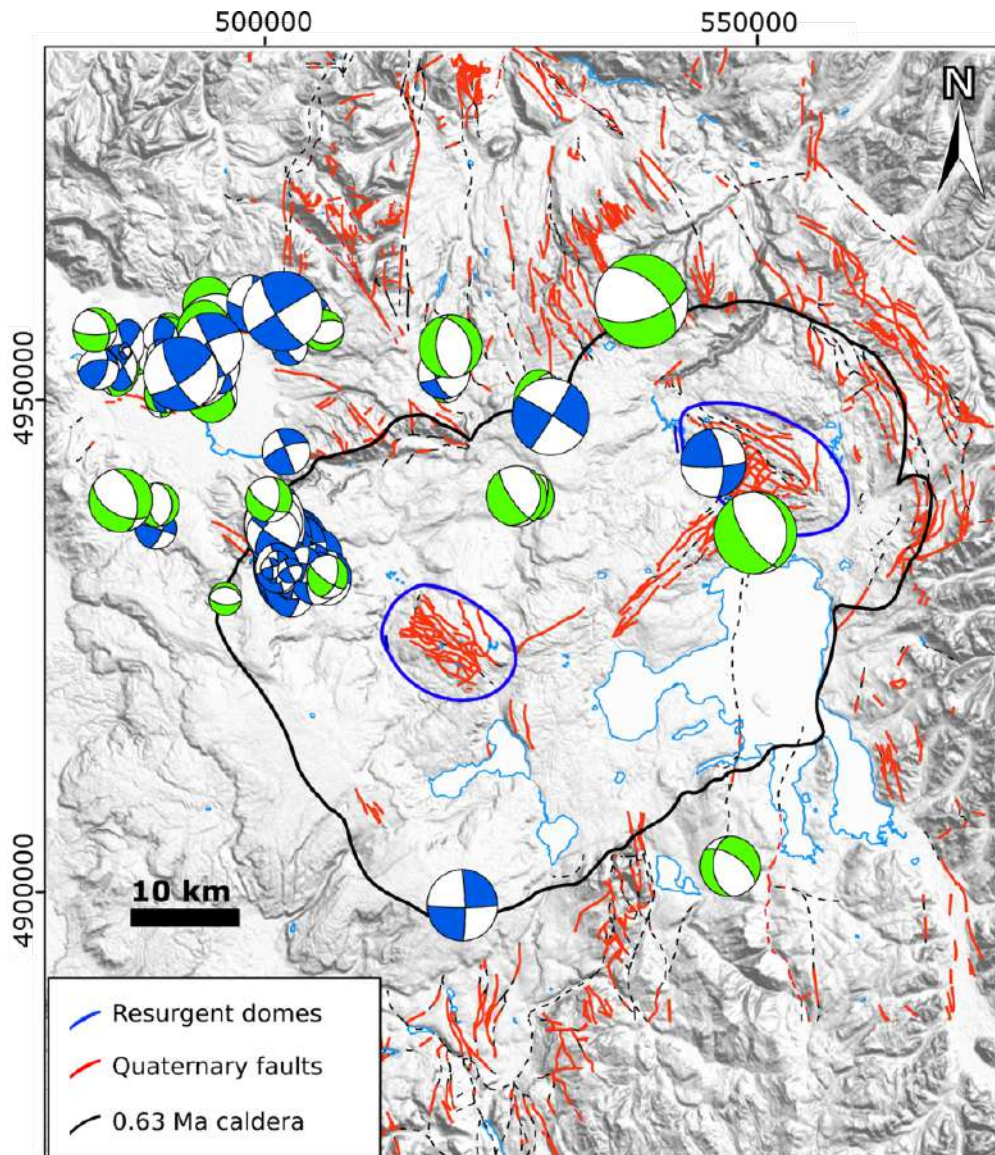


Figure 62 Complete set of 224 new double-couple focal mechanism solutions computed for the time period 2010-2016, scaled according to magnitude values. Earthquakes are divided by kinematics: blue beach balls represent strike-slip faulting, green beach balls represent normal to normal-oblique faulting. The black line is the 0.63 Ma Yellowstone caldera boundary, blue lines are the resurgent domes. Shaded view of the Digital Elevation Model (DEM) provided by the USGS National Elevation Dataset. Fault data, represented in red, after [Christiansen \(2001\)](#). Dashed lines indicate concealed faults. Coordinate system: WGS84/UTM zone 12N ([Russo et al., 2020](#)).

The presence of normal and normal-oblique kinematics is expected given that the location of the Yellowstone volcanic plateau is within the Basin and Range Province ([Fig. 2](#)), a region of NE-SW tectonic extension characterized by many listric and planar normal faults with opposing dip that produce a “horst and graben” geometry ([Christiansen, 2001](#)). As also shown by past studies of FMS

(e.g., [Waite and Smith, 2002](#); [Russo et al., 2017](#)), the majority of FMS are consistent with this regional trend.

7.6 Calculation of the stress field and relation with surficial deformation

Earthquakes are passive markers of deviatoric stress and individually determined FMS have been used to estimate the best uniform stress field within limited space-time windows through different procedures ([Angelier, 1984](#); [Gephart and Forsyth, 1984](#); [Michael, 1987](#); [Rivera and Cisternas, 1990](#); [Horiuchi et al., 1995](#); [Robinson and McGinty, 2000](#); [Abers and Gephart, 2001](#); [Hardebeck and Shearer, 2003](#); [Hardebeck, 2006](#)). In the present study, a new iterative stress inversion method has been used, known as STRESSINVERSE, that modifies Michael's method ([Michael, 1987](#)) and inverts jointly for stress and fault orientations ([Vavrycuk, 2014](#)).

FMS have been divided into temporal, spatial, and depth windows with an iterative, trial-and-error approach, in order to identify variations of the stress field within the Yellowstone region ([Figs. 63-64-65](#)). The upwarping and downwarping episodes of surficial deformation documented by GPS data ([Fig. 5](#)), have been correlated with the focal mechanism inversions of the coeval seismicity, in order to delineate the stress field associated with the deformation episodes. The WLWY and NRWY GPS stations have been chosen from among the Yellowstone network according to previous studies (e.g. [Chang et al., 2010](#)) as the most representative of surficial deformation within the Yellowstone caldera and the Norris Geyser Basin, respectively.

Regarding the spatial windows of analysis, the stress field of the inner 0.63 Ma Yellowstone caldera and the Norris Geyser Basin has been calculated separately. Furthermore, data was divided into 2 km depth intervals in order to analyze the variations of the stress field from the upper to the lower crust. This depth interval is slightly less than the estimated uncertainty of the earthquake locations; the average of the longest uncertainty ellipse axis, usually close to vertical, is 2.6 km, whereas the average of the shortest is 0.95 km. We interpret only the depth windows containing at least 6 events.

Focal mechanism solutions have also been divided according to their kinematics prior to stress field calculation, in order to perform a detailed investigation on temporal and spatial variations of faulting and related orientation of principal stress axes.

[Figure 63](#) shows the results of focal mechanism inversions and related stress field of the inner part of the 0.63 Ma Yellowstone caldera divided into kinematics, depth, and temporal windows, according to phases of surficial deformation recorded at WLWY GPS station between 2010

and 2016. Strike-slip kinematics, occurring between the surface and 10 km, appear to be shallower than normal and normal oblique, which both extend down to 14 km depth, and in particular all the normal oblique faults are deeper than 6 km. According to the results, the stress field associated with the 2010 Madison Plateau seismic swarm, being characterized by normal oblique and strike-slip kinematics, is characterized by a nearly horizontal greatest principal stress (σ_1) with a NW-SE direction in the case of strike-slip faulting and NNW-SSE in the case of normal oblique faulting. By extending the temporal window of analysis to the subsidence stage up to 2014, we observe that: *i*) regarding normal-oblique faults, the extension direction has a NNE-SSW direction between 8 km and 12 km depth; *ii*) in the case of strike-slip faulting, by looking at the least principal stress (σ_3) directions, we notice a slight rotation from a NE-SW orientation to NNE-SSW between the 6-8 km and 8-10 km depth windows. A single normal oblique FMS during the stasis between late 2014 and late 2015 hints at the presence of normal oblique faults at the shallow levels (2-4 km). The smaller number of selected earthquakes during uplift is due to a lower quality of raw seismic data, which has been then discarded.

In [Figure 64](#), the results of focal mechanism inversions and related stress field of the outer part of the 0.63 Ma Yellowstone caldera are presented, specifically in the Norris Geyser Basin, divided into kinematics, depth, and temporal windows, according to phases of surficial deformation recorded at NRWY GPS station between 2010 and 2013, during a period of low-rate subsidence. The deformation pattern associated with this phase is very heterogeneous, being characterized by normal, normal-oblique, strike-slip, and subordinate reverse faults, all of them located at depths > 4 km. By taking into account strike-slip faults, which represent the predominant kinematics and are characterized by depth windows with at least 6 events between 6 km and 12 km, we observe a clear clockwise rotation of both the σ_3 and σ_1 directions, differently from the case of the inner part of the Yellowstone caldera ([Figure 63](#)), where only a slight rotation of σ_3 is observed.

Focal mechanisms inversion in the Norris Geyser Basin from 2013 on ([Figure 65](#)) has not been performed due to the fact that all depth windows contain less than 6 seismic events and thus are not considered reliable.

Figure 63 Seismic events of the inner part of the 0.63 Ma Yellowstone caldera (119 selected earthquakes) divided into kinematics, depth and temporal windows, according to phases of surficial deformation recorded at WLWY GPS station between 2010 and 2016. P and T axes are represented as red circles and blue crosses respectively, the orientation of principal stress axis (when calculated) is indicated as red circles for σ_1 , green triangles for σ_2 and blue squares for σ_3 . Diverging white arrows indicate direction of extension (σ_3), converging black arrows direction of compression (σ_1). Earthquake occurrence rate, considering relocated hypocenters of our database, divided per quarter of year, is shown in the graph (Russo et al., 2020).

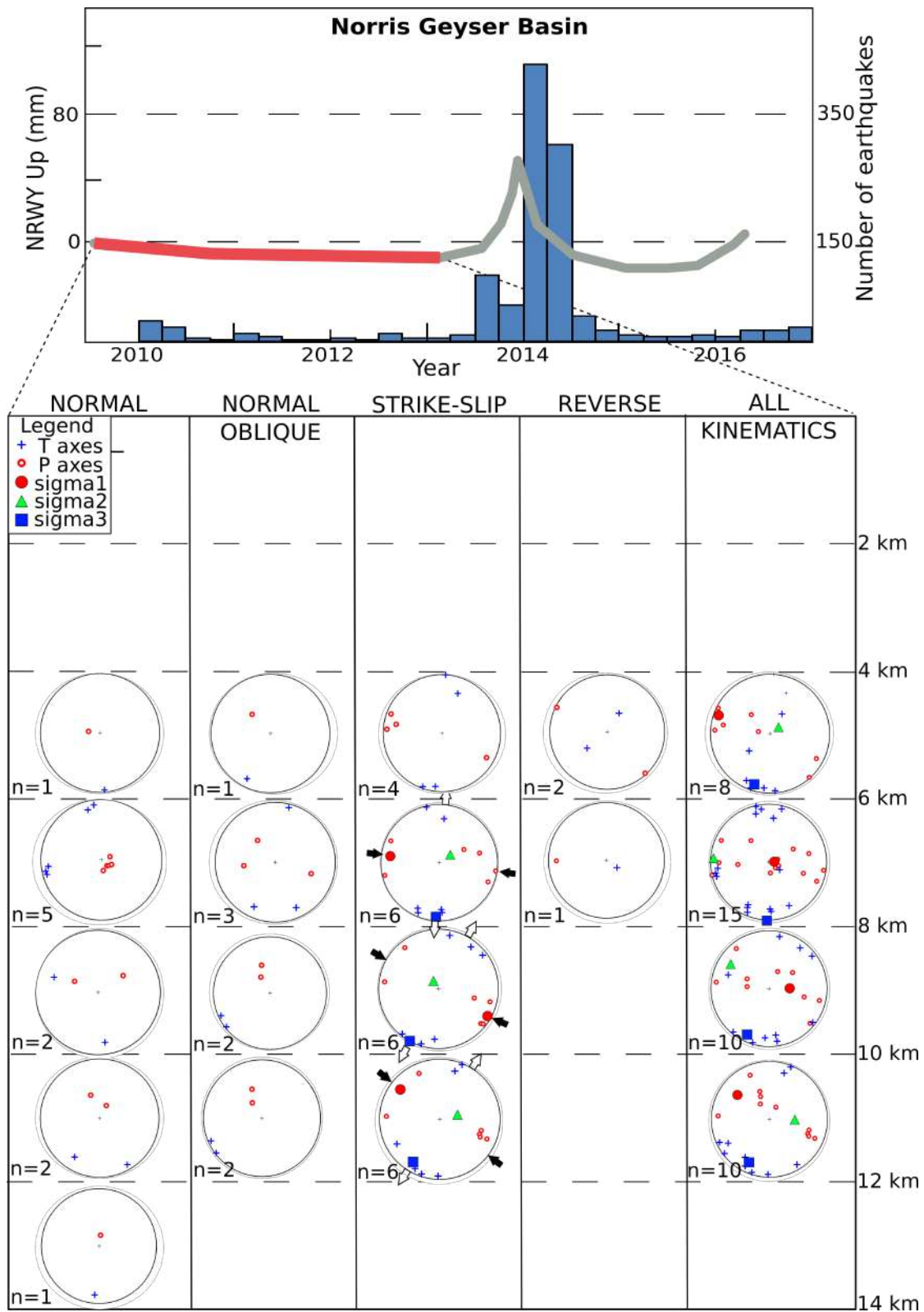


Figure 64 Seismic events of the outer part of the 0.63 Ma Yellowstone caldera, in the Norris Geyser Basin area (44 selected earthquakes), divided into kinematics, depth and temporal windows, according to phases of surficial deformation recorded at NRWY GPS station between 2010 and 2013. P and T axes are represented as red circles and blue crosses respectively, the orientation of principal stress axis (when calculated) is indicated as red circles for σ_1 , green triangles for σ_2 and blue squares

for σ_3 . Diverging white arrows indicate direction of extension (σ_3), converging black arrows direction of compression (σ_1). Earthquake occurrence rate, considering relocated hypocenters of our database, divided per quarter of year is shown in the graph (Russo et al., 2020).

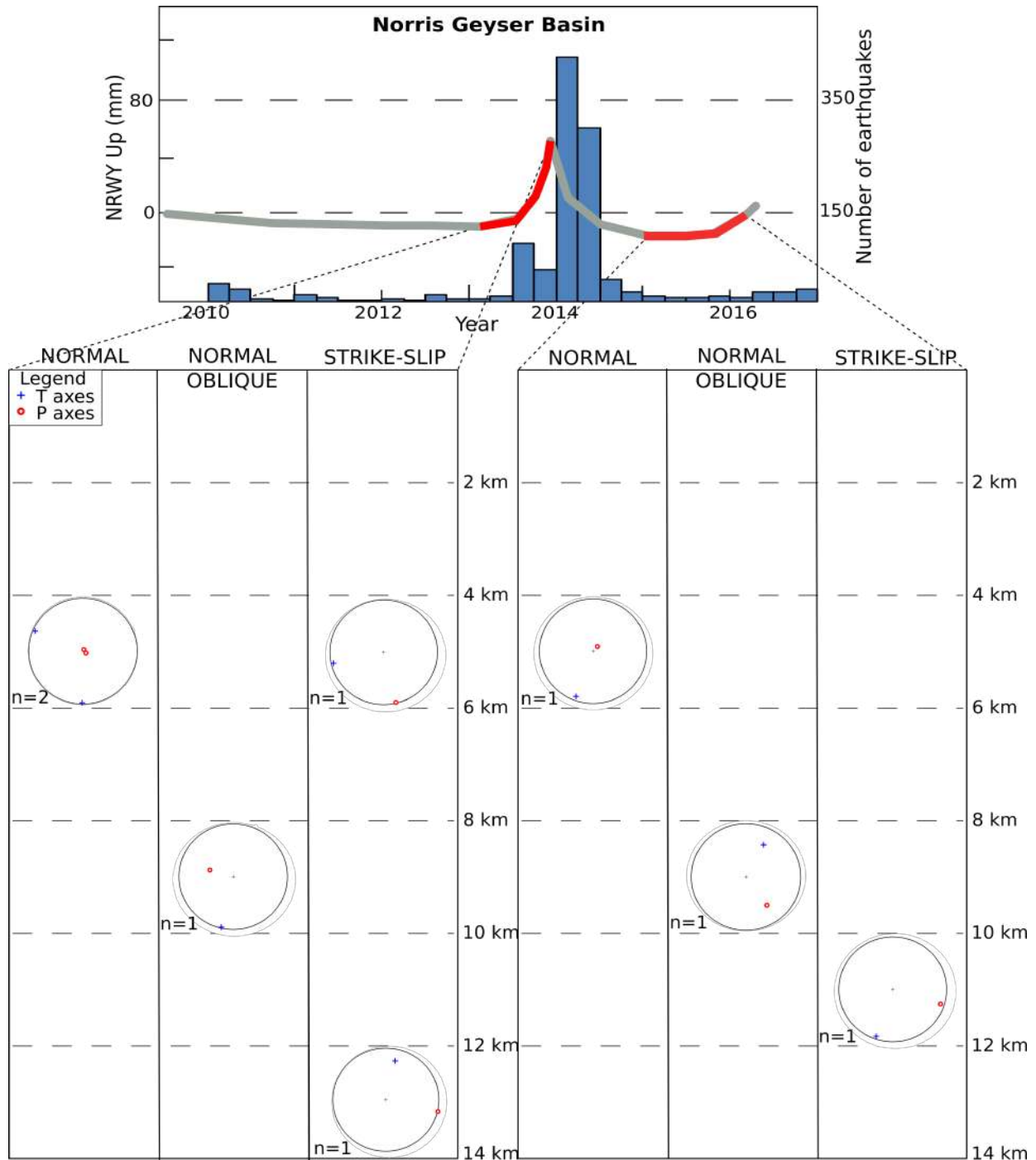


Figure 65 P and T axes calculations of the outer part of the 0.63 Ma Yellowstone caldera, in the Norris Geyser Basin area (7 selected earthquakes), divided into kinematic, depth and temporal windows, according to phases of surficial deformation recorded at NRWY GPS station between 2013 and 2014,

and 2015 and 2016. *P* and *T* axes are represented as red circles and blue cross respectively. Earthquake occurrence rate, considering relocated hypocenters of our database, divided per quarter of year is shown in the graph (Russo et al., 2020).

7.7 Numerical modeling

This section presents the results of numerical modeling of upper crustal dilatation that occurs within the 0.63 Ma Yellowstone caldera in response to the inflation of a sill that has been related to an accelerated uplift stage (at a rate of 7 cm/yr) detected between 2004 and 2010 by GPS measurements (Chang et al., 2007; 2010). In fact, recent researches have enlightened the relations between surficial deformations, movement of magmatic fluids at depth and seismic activity (Waite and Smith, 2002, 2004; Shelly et al., 2013; Russo et al., 2017). Dilatation values at the surface and at 2 km depth (Figs. 66A-B) are positive (orange to red colours) on top of the sill and negative (light blue) outside its margins: more in detail, at the surface (Fig. 66A) the greatest values of dilatation are found along the northeastern side of the sill, in correspondence of the Sour Creek resurgent dome (Fig. 4), where values range between 0.6×10^{-5} and 0.8×10^{-5} bars. Around the sill, negative values of dilatation range between 0 and -0.2×10^{-5} bars. At 2 km depth, the positive range of crustal dilatation values on top of the sill decreases to $0-0.3 \times 10^{-5}$ bars (Fig. 66B).

Moving towards the sill, at 4 km depth, we observe positive values of dilatation between 0.1 and 0.2×10^{-5} bars along the northern edge of the sill, and negative values around -1×10^{-5} bars between patches n.1 and n.4, in the southwestern part above the sill (Fig. 66C).

Furthermore, at 6 km and 8 km depth (Figs. 66D-E), we observe negative values of crustal dilatation on top of the sill and positive values outside its margins: more in detail, the greatest positive values are observed at 8 km depth (Fig. 66E) in correspondence of patches n. 1, 4, 22, 28, which are located along the northern edge of the sill and are comprised between -0.9 and -1×10^{-5} bars. Positive values around the margins of the sill are comprised between 0.2 and 0.4×10^{-5} bars.

At a general level, focusing on the top of the sill, the calculation of crustal dilatation showed that the strain is positive at depths comprised between the surface and 4 km, whereas it becomes negative from 4 km depth to the top of the inflating sill, the latter being a zone under compression, where strike-slip movements might occur (Figure 66).

Crustal dilatation

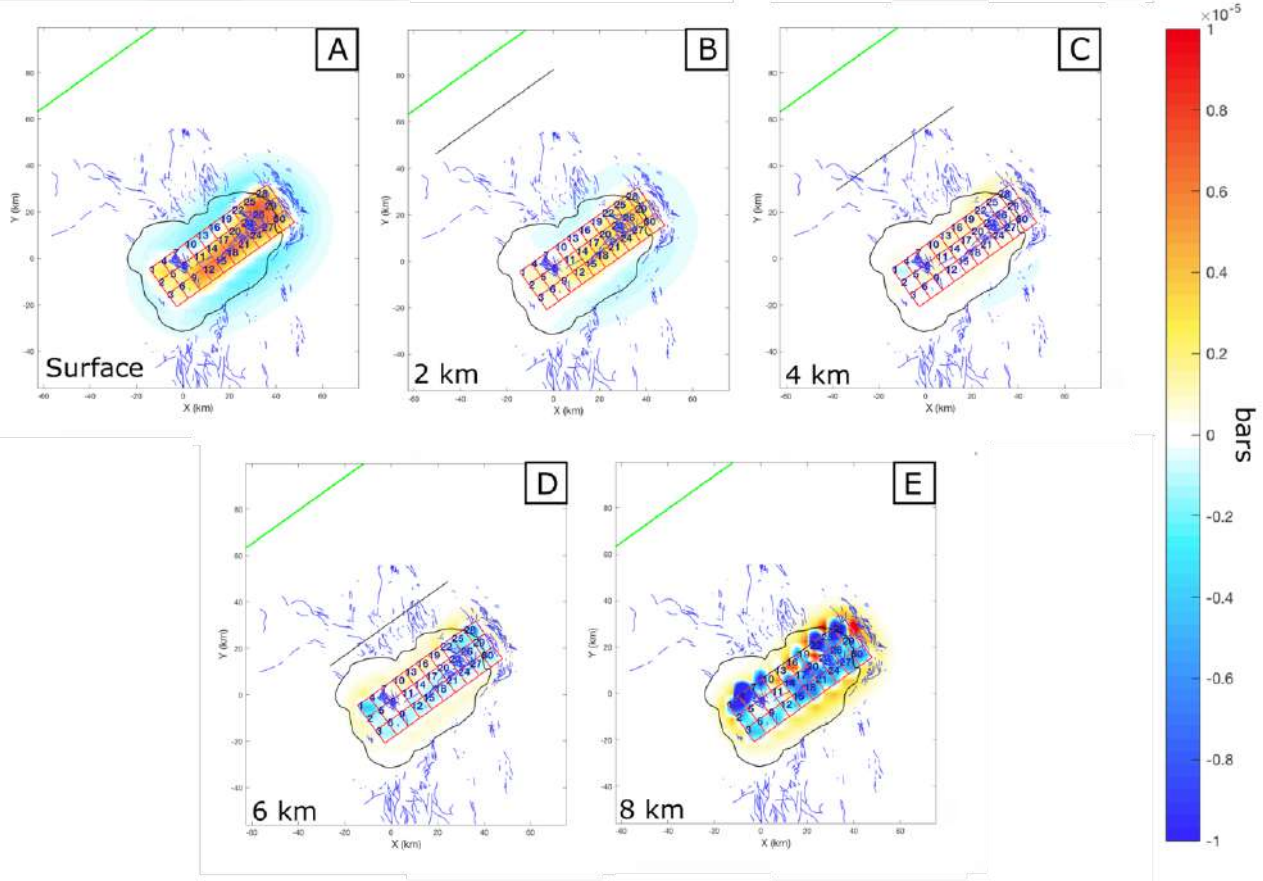


Figure 66 Crustal dilatation caused by the inflating sill proposed by [Chang et al. \(2007, 2010\)](#) at the surface (A), at 2 km (B), 4 km (C), 6 km (D) and 8 km depth (E). The 0.63 Ma Yellowstone caldera is shown as a black line, Quaternary faults from [Christiansen \(2001\)](#) are shown in blue.

Chapter 8

Discussion – Yellowstone volcanic plateau

8.1 Seismic swarms and relation with strike-slip faulting mechanisms

The distribution of the 10,201 Yellowstone caldera relocated epicenters of the present research, consisting of both clusters and more scattered events, indicates a complexity of fault slip with the predominance of lateral components of motion during clustered seismic swarms, and subordinate normal motions. Such seismic swarms (Figs. 56B and 60) are common in the Yellowstone plateau volcanic history (Waite and Smith, 2002; Farrell et al., 2010; Shelly et al., 2013), as well as in volcanic settings in general, and are frequently attributed to the movement of magmatic fluids in the subsurface. Fluid propagation can be accompanied by enlargement of pre-existing fractures and/or the development of new fractures and small faults. At Yellowstone, the 1985 and 2010 seismic swarms occurred in concomitance with or at the beginning of a period of caldera subsidence, suggesting that fluid escape along the coseismic fractures may have originated a decrease of pressure beneath the caldera floor and the consequent downsagging.

In map view, the relocated epicenters of the present research tend to focus in two main groups (black rectangles in Fig. 56A): *i*) one located north of the Mallard Lake dome, which coincides with the 2010 Madison Plateau and 1985 seismic swarm locations (Fig. 56B) (Massin et al., 2013; Shelly et al., 2013), and *ii*) another group more to the north, in the Norris Geyser Basin area. At a higher detail, north of the caldera rim there is a wide cluster in the western part, with no clear elongation, whereas in the eastern part there is another N-S-elongated cluster (seismic swarm n.3 in Fig. 60). This orientation is similar to the NNW-SSE elongation of smaller clusters at the southern margin of the 0.63-Ma caldera and to the N-S elongation of the 2008-2009 Yellowstone Lake swarm (Fig. 56B). The NNW-SSE to N-S range coincides with the dominant strike of the Quaternary normal faults present in the whole area (e.g. Fig. 55). This is also consistent with the FMS obtained in the present research that have slip planes that mostly strike NW-SE to NNW-SSE, perpendicular to the regional σ_3 orientation (Zoback, 1992). The stress orientation based on the performed seismic analyses, typically horizontal NE-SW σ_3 especially during the uplift phases at the Yellowstone caldera, is also consistent with the regional σ_3 direction of the Basin and Range Province: thus, the orientation of dominant coseismic faulting may be influenced by regional tectonics, irrespective of magmatic or tectonic origin of fault slips.

Such complexity is being interpreted both considering the possible control of regional tectonics on preferential orientation of faults, and the relation with seismic swarms, sill emplacement and deflation phases. In fact, calculation of focal mechanism solutions performed in the present research revealed the concomitance of normal and strike-slip motions during the 2010 Madison Plateau seismic swarm: in order to explain this phenomenon, we adopt the model represented in [Figure 67](#), which is based on the concept developed by [Ágústsdóttir et al. \(2016\)](#) and [Ruch et al. \(2016\)](#) for the 2014 Bárðarbunga-Holuhraun dyke intrusion, and on the strike-slip components measured along volcano-tectonic fractures in north Iceland described in the present research. This model suggests that overpressurized fluids can start to escape from the main magmatic body following a suitably-oriented vertical fracture. At the advancing fluid tip, a new fracture can develop at an oblique angle in response to stress concentration ([Pollard and Holzhausen, 1979](#); [Bonafede and Olivieri, 1995](#)). If the fluid plane propagates upward, normal faults with converging dips may form ([Fig. 67A](#)), followed by upward fluid flow. If the vertical fluid plane propagates horizontally, left-lateral or right-lateral strike-slip faults might form at oblique angles ([Fig. 67B](#)), followed by horizontal fluid flow. These faults have left-lateral motions if oriented clockwise with respect to the strike of the main fluid plane, and right-lateral if rotated anticlockwise. After the faults are formed, the fluid may advance by intruding into one of the two faults, thus inducing opening of the fault plane.

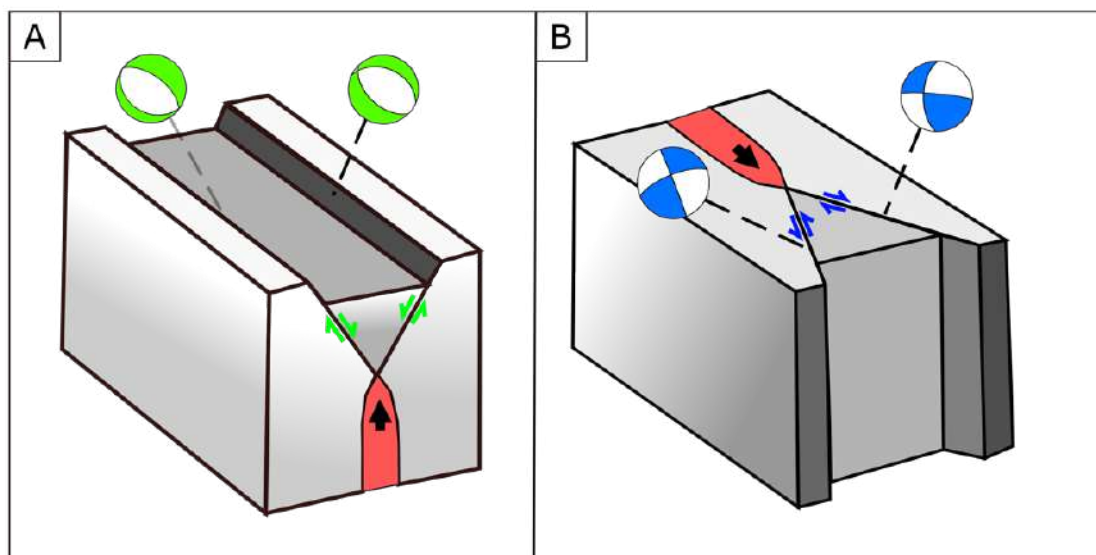


Figure 67 Geomechanical model of brittle deformations resulting from the stress field linked to the propagation of fluids in different directions: (A) refers to upward propagation of magma, and (B) to horizontal magma propagation along vertical planes. The beach balls give the typical kinematics:

green = normal faulting, blue = strike-slip faulting. The red zone gives the plane from which magmatic fluids propagate and the black arrow shows the fluid flow direction (Russo et al., 2020).

8.2 Association between strike-slip faulting and deformation: a comparison with previous data

A comparison between the new FMS catalog of the present research with the 1988-2009 data by Russo et al. (2017), where the same kind of analysis has been conducted, has been performed in order to more fully interpret the association between faulting kinematics and deformation. In the 1988-2009 period analyzed by Russo et al. (2017), the majority of earthquakes (58%) are associated with a normal faulting mechanism, followed by 40% associated with strike-slip faulting and subordinate reverse faulting. Normal faults occurred mostly (93%) between the near-surface and a depth of 10 km, thus indicating that brittle deformation has developed also at the shallowest level under extension. These authors found no relation between the orientation of fault planes revealed by FMS and the GPS-measured phases of surficial deformation. Nevertheless, they found that strike-slip faults were present along the peripheral uplifting zone (Fig. 68B), which has been related to the inflation of a sill between 2004 and 2009 within the 0.63 Ma caldera (Chang et al., 2007, 2010). These faults were the result of a secondary, widespread adjustment of the shallow crust as block-faulting, showing that the rocks surrounding an inflating sill may accommodate deformation by transcurrent faulting. These results complement the classical model of extensional fracturing at the tip of an intruding horizontal magma sheet (Malthe-Sørenssen et al., 2004; Kavanagh et al., 2006). Normal motions instead, can be attributed to the extension that takes place in the extrados zone of an upwarping fold-like structure under the pressure of the inflating sill (Fig. 68A).

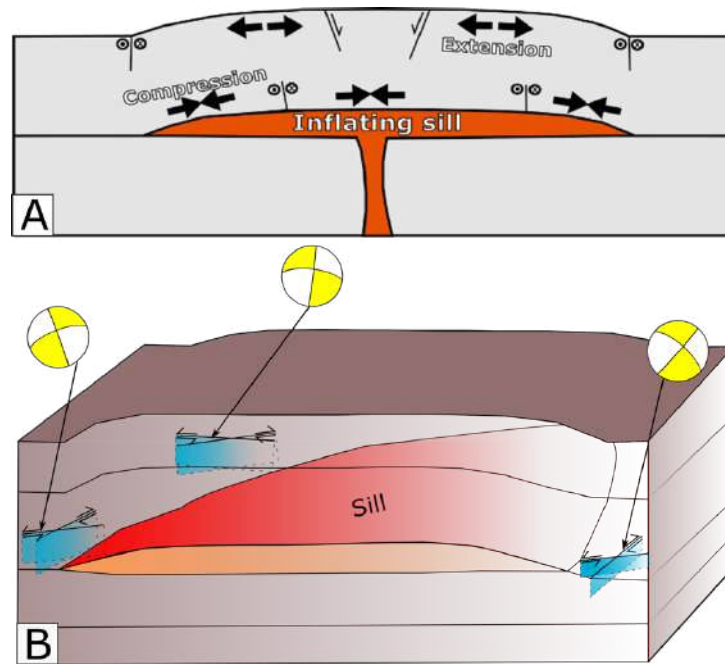


Figure 68 (A) Geomechanical model of brittle deformation above an inflating sill and in the surroundings. Circles define motion of strike-slip faults. Diverging arrows show extension in the extrados zone of the upwarping overburden, converging arrows show compression in the intrados zone (Russo et al., 2020). (B) 3D view of the same inflating sill and the related strike-slip motions.

The rarer occurrence of normal motions in the 2010-2016 period with respect to the previous time window, can be explained by the change in the surficial deformation shown by GPS data, which reveals a switch between uplift (pre-2010) and subsidence (2010-2016) (Figure 5). In 2010, in fact, the sill inflation ended causing a continuous contraction of the overburden. This contraction has been accommodated by structural adjustment in the form of strike-slip motions on a multitude of small fault planes, thus providing a further explanation on the occurrence of strike-slip kinematics apart from the model of seismic swarm development of Figure 67B. The distribution of deformation at several small faults is consistent again with the low magnitudes of the seismic events (Fig. 69B).

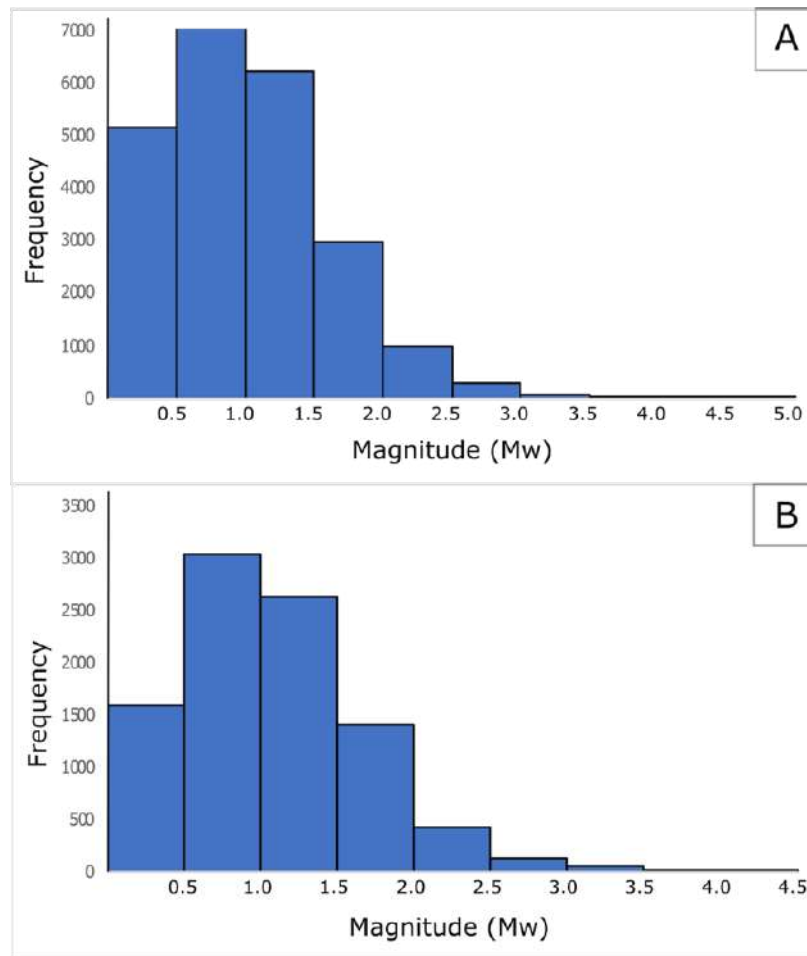


Figure 69 Graph showing magnitude of seismic events vs. frequency for the period 1988-2009 (A) and 2010-2016 (B) (Russo et al., 2020).

Multiplets could be defined as groups of earthquakes produced by re-activation of a self-similar seismic source: for example, [Massin et al. \(2013\)](#) showed that they preferentially occur during crustal subsidence episodes, and interpreted this as due to the preferential re-activation of pre-existing structures rather than the creation of new faults. This is consistent with the data of this research, where scattered strike-slip motions may be the effect of reactivation of already existing fractures under contraction.

Chapter 9

Discussion – Origin of rift-parallel transcurrent faults in extensional volcano-tectonic settings

The Northern Volcanic Zone in Iceland and the Yellowstone volcanic plateau in the United States both represent an excellent natural laboratory to study the interaction between magmatic activity and an active extensional tectonics at least since Pliocene times, being both located above an active hot-spot and a divergent plate margin (Paquet et al., 2007). These areas share further common geological characteristics, consisting in complex volcano-tectonic structures and multiple episodes of magma intrusions. The origin of rift-parallel structures with strike-slip motions, which have been detected in previous researches both in Iceland and at Yellowstone (e.g. Christiansen, 2001; Waite and Smith, 2002, 2004; Khodayar and Einarsson, 2002; Nanfity, 2011; Proett, 2015; Runnals, 2015; Karson et al., 2015, 2018; Ruch et al., 2016; Tibaldi et al., 2016a,b; Ágústsdóttir et al., 2016; Hjartardóttir et al., 2016a; Russo et al., 2017, 2020; Karson, 2017; Horst et al., 2018; Bonali et al., 2019a,b), represents a scientific question of great international interest. The present research confirms the occurrence of such structures in both rift zones, through field and UAV data in the case of the Northern Volcanic Zone and the analysis of seismic data in the case of the Yellowstone volcanic plateau: their complex geometry and distribution is interpreted both considering the possible control of regional tectonics on the orientation of faults and the relation with seismic swarms, sill emplacement, that could cause the enlargement of pre-existing fractures or the development of new fractures and small faults, and deflation phases.

More in depth, the occurrence of strike-slip motions and in particular its predominance during the 2010 Madison Plateau seismic swarm at Yellowstone revealed by the FMS calculated in the present research, lead to the geomechanical model shown in Figure 67, based on the concept developed by Ágústsdóttir et al. (2016) and Ruch et al. (2016) for the 2014 Bárðarbunga-Holuhraun dyke intrusion: here I focus in particular on Fig. 67B, which shows that, when the fluid plane is propagating horizontally, left- (if oriented clockwise respect to the fluid plane strike) or right-lateral (if oriented anticlockwise) strike-slip faults can form at oblique angles, in response to stress concentration at the advancing fluid tip (Pollard and Holzhausen, 1979; Bonafede and Olivieri, 1995). Also, the FMS calculated in the present research, especially those related to seismic swarms, and the numerical models developed to investigate horizontal dyke propagation show that such fractures with transcurrent motions (both right- and left-lateral) can be found at the sides of the advancing

magmatic body and be parallel or sub-parallel to its strike. The kinematic of such structures depends on the depth: if they occur at the depth of the dyke, they can show a strike-slip component of motion, but, if they occur above the dyke, they have a normal kinematics.

Furthermore, field data collected through classical methods and high-resolution quantitative measurements on Orthomosaics created through UAV surveys within the Theistareykir and Krafla Fissure Swarm allowed to convalidate such geomechanical model. In fact, [Figure 24D](#) shows that, as the strike of extension fractures rotates, also the opening direction changes, but, if the tectonic least principal stress (σ_3) would dominate, the opening direction should remain quite stable at fractures with different orientations. This confirms the genesis of structures with oblique components of motion as related to a strong local dilatant stress that forces the fracture walls to open along a direction from perpendicular to sub-perpendicular to the fracture strike. This type of stress can be produced by magma migrating in the crust along shallow-depth dykes ([Figure 67](#)). Furthermore, past researches conducted in Iceland revealed strike-slip components of deformation contemporaneous to dyke intrusion, through the analysis of double-couple focal mechanism solutions ([Shelly et al., 2016](#); [Ruch et al., 2016](#); [Ágústsdóttir et al., 2016](#)).

Combining all the aforementioned observations, the following evolutionary model could be presented to explain the genesis and evolution of such faults and fractures with lateral components of motion both at the tip and at the sides of an horizontally advancing dyke. Although the classical scheme of dyke tip propagation assumes that a vertical dyke tip line can propagate horizontally by a new fracture parallel to the main dyke plane, here I suggest that one or two strike-slip planes can form at oblique angle respect to a propagating dyke tip ([Fig. 70A](#)), following the idea of [Ágústsdóttir et al. \(2016\)](#). In fact, the dyke overpressure produces maximum shear along planes, oriented at about 30° respect to the dyke plane, which can be located at a few meters from the dyke tip without intersecting the dyke, or can depart nearby the dyke tip, or from the dyke wall behind the magma front ([Rubin and Gillard, 1998](#)). Field data collected in the Northern Volcanic Zone indicate that all the left-lateral and right-lateral fractures behind the termination of the fracture zone, are now exposed at the side of the main fracture zone and are interrupted by the main NNE-SSW extension fractures. The coloured sectors in [Figure 70A](#) correspond to the range of field data collected in the present research. Based on this model, magma can penetrate one of the two planes and thus the resulting dyke changes its orientation ([Fig. 70B](#)); the other strike-slip zone is abandoned on the side of the advancing magma front. The dyke gradually thickens in the newly occupied fracture, and extension fractures propagate to the surface offsetting the abandoned strike-slip zone. Then the

process starts again with the formation of other strike-slip zones at the dyke tip (Fig. 70C). Their orientation is rotated (clockwise in this example), but consistent with the range of our field data (coloured sectors). The successive intrusion propagation in theory might exploit both strike-slip faults, but the ambient stress should favour magma propagation through the more suitably oriented fault. In this example, magma propagation should be favoured along the N-S fault, being oriented more perpendicularly respect to the regional σ_3 of this part of Iceland.

Another possibility is represented by the formation of a fracture parallel to the dyke plane that bisects the angle between the two strike-slip fracture zones (Fig. 70D). Magma can intrude the dyke-parallel fracture, with consequent abandoning of the strike-slip fractures. In this case, dyke thickening will be accompanied by the formation at the surface of the extension fractures at the sides of the dyke tip, which will offset the abandoned strike-slip fractures (Fig. 70E). The formation of strike-slip fracture zones only, of dyke-parallel fracture only, or of all sets, can depend upon a series of co-causes that comprehend the pre-existence of fractures suitably oriented respect to the local stress field, which facilitate shear or pure extension due to zero cohesion, the stress perturbation due to magma overpressure, the influence of the tectonic stress field, and the rheological properties of the host rock. The latter argument is supported by the fact that the strike-slip faults, oblique to the dyke trend, have been found only where the dyke crossed the lava succession, whereas in the hyaloclastite zone only faults parallel to the dyke have been found. The possibility that the strike-slip faults reach the surface depends also on a sufficiently shallow location of the dyke.

In regards to the orientation of the strike-slip planes, data of the present research indicate that a large range may occur, spanning from 5° to 40° respect to the main dyke trend. This is different from previous findings of [Ágústsdóttir et al. \(2016\)](#) who found that the typical angle between the strike-slip fractures and the dyke plane was of 13° at the Bárðarbunga dyking event. This wide distribution of angle values may be the effect of a combination of different rock coefficient of friction, fluid pressure, and pre-existence of fractures also in the form of cooling structures.

The model presented above can have applications elsewhere. For example, at the same Krafla rift, the dyke event of 1977 was accompanied by the formation at the surface of dominant normal faults and extension fractures, and some, small strike-slip faults ([Brandsdóttir and Einarsson, 1979](#)). Moreover, the 1977 seismological data showed the occurrence of dominant first-motion pattern consistent with normal faulting, but also several other events that were more compatible with strike-slip faulting. At Long Valley caldera, in the US, [Savage and Cockerham \(1984\)](#) reported that

the 1982–1983 deformations have been induced by a dyke, whose emplacement was accompanied by strike-slip motions. At the Yellowstone caldera, [Russo et al. \(2017\)](#) have found diffuse earthquakes with strike-slip double-couple solutions during intrusive phases. During the 2014 Bárðarbunga dyking event (Iceland), focal mechanism solutions show exclusively left-lateral strike-slip faulting subparallel to the advancing dike tip at the magma front, and both left-lateral and right-lateral strike-slip earthquakes behind the magma front ([Ágústsdóttir et al., 2016](#)). These seismological data have been interpreted, by the same authors, as due to failure of the rock along shear fractures oblique to the dyke plane. Other field examples come from the Theistareykir Fissure Swarm, NE Iceland, where [Bonali et al. \(2019b\)](#) found widespread strike-slip components of motion along volcanotectonic fractures. Dominant strike-slip focal mechanisms have also been found during fluid propagation along dyke-like structures, as at the Long Valley Caldera in 2014 ([Shelly et al., 2016](#)), and at Yellowstone caldera in 2010 ([Russo et al., 2020](#)). These earthquake swarms may have been linked to evolving fluid pressure transient of a low-viscosity fluid, mainly composed of water and CO₂ exsolved from underlying magma.

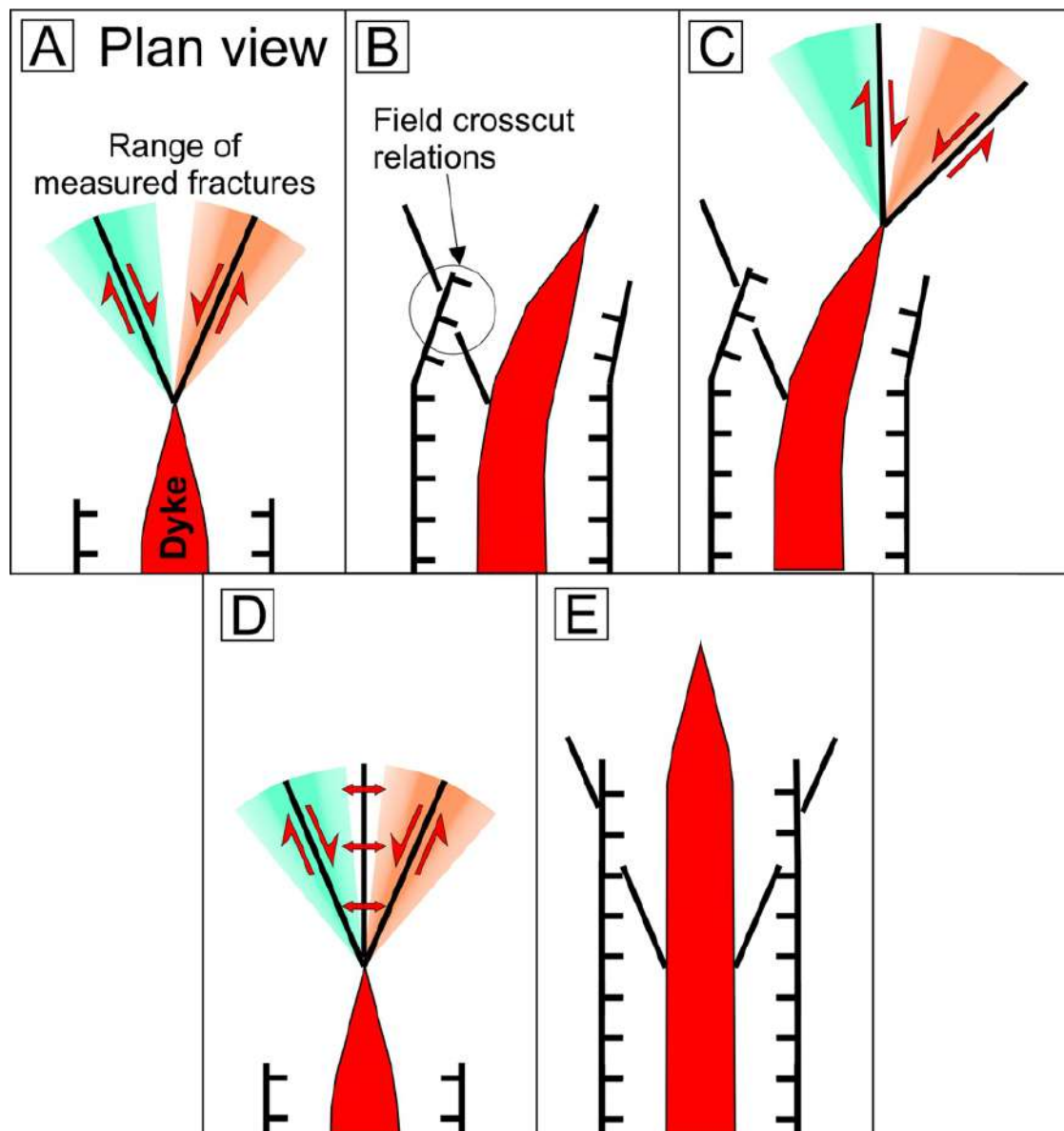
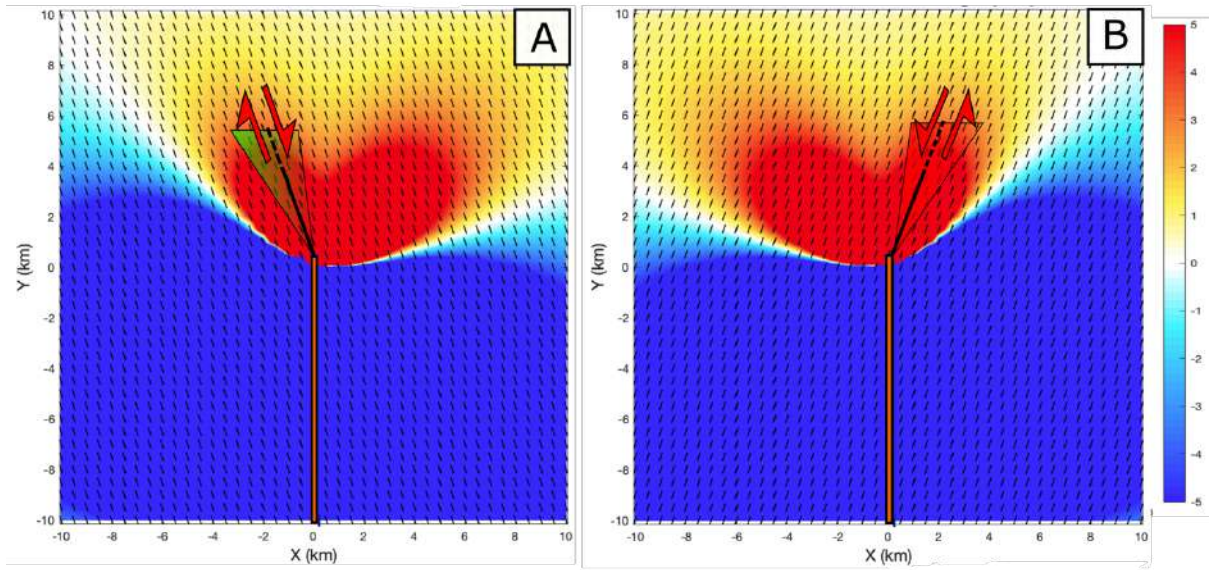


Figure 70 Evolutionary model, in plan view, of dyke propagation and surface deformation based on field data. (A) One or two strike-slip planes can form at oblique angle respect to a propagating dyke tip. (B) Magma can penetrate one of the two planes resulting in a change of dyke strike, the other strike-slip zone being abandoned. The dyke gradually thickens in the newly occupied fracture, and extension fractures propagate to the surface offsetting the abandoned strike-slip zone. (C) The process starts again with the formation of other strike-slip zones at the dyke tip whose orientation is rotated but consistent with the range of our field data (coloured sectors). (D) A fracture parallel to the dyke plane can also form guiding dyke advancement. (E) Both strike-slip zones are abandoned by dyke propagation, while dyke thickening induces formation of surface extension fractures at the sides of the dyke tip, which offset the strike-slip zones (Tibaldi et al., 2020a).

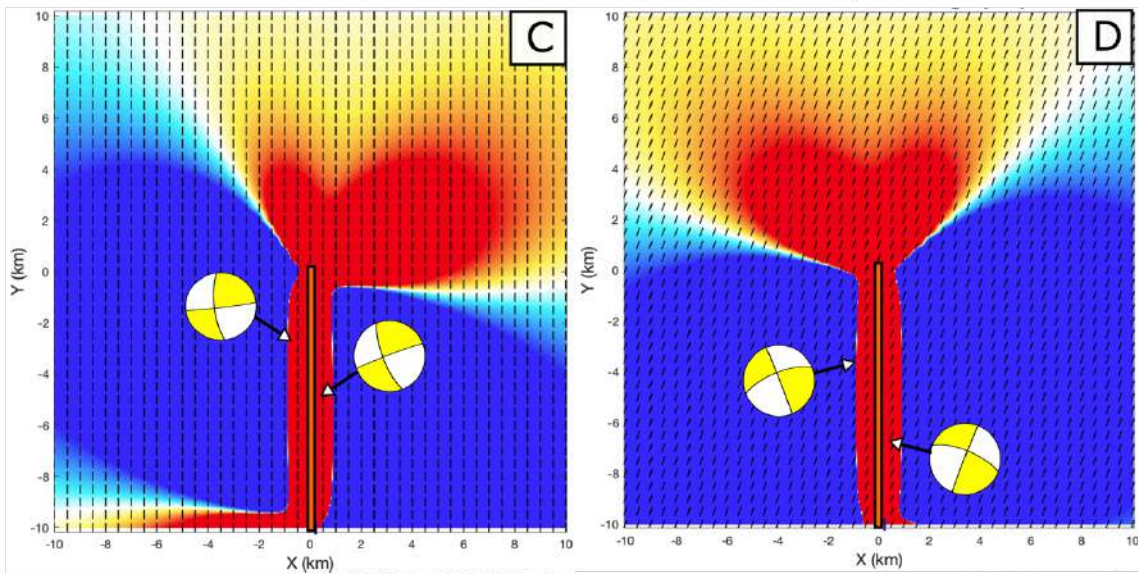
Numerical models developed in the present research confirmed that structures with right- and left-lateral (Figs. 71A-B and Figs. 49-50) components of motion can form at the tip of a dyke in response to its horizontal propagation. In fact, in areas coherent with the range of strike values of oblique fractures detected in the field within the Northern Volcanic Zone (which are shown in Figs. 71A-B as shaded green and red areas respectively), the Coulomb stress change is positive (values around +5 bars) and thus motion along strike-slip fractures with planes in this strike interval is favoured. Furthermore, additional numerical models confirm the presence of fractures with lateral components of motion (either right- or left- lateral) not only at the tip, but also at the sides of the propagating dyke (Figs. 71C-D and Figs. 49-50), as confirmed by collected field data described in Chapter 4. This latter observation is confirmed by the plot of nodal planes of focal mechanism solutions that indicate transcurrent faulting associated with the 2010 Madison Plateau seismic swarm that occurred at Yellowstone, with the corresponding rose diagram (Fig. 71E): in fact, data indicate that the majority of nodal planes has a N-S strike and subordinately NNE-SSW and NNW-SSE, accordingly with the direction of propagation of the Madison Plateau swarm and its related dyke (Fig. 62). The direction of regional extension (σ_3) at Yellowstone, which is ENE-WSW (Figure 4), is greater than 90° respect to the direction of nodal planes shown in Fig. 71E: this might explain the occurrence of transcurrent/transensional motions in the study area, as also demonstrated by the predominance of left-lateral transcurrent motions during such seismic swarm (Figure 62). On the other hand, the direction of σ_1 could be imposed by magmatic processes, such as in this case the multi-directional propagation of a dyke.

Northern Volcanic Zone

Development of strike-slip motions at dyke tip



Development of strike-slip motions at dyke sides



Yellowstone

Strike-slip nodal planes from 2010 MP seismic swarm

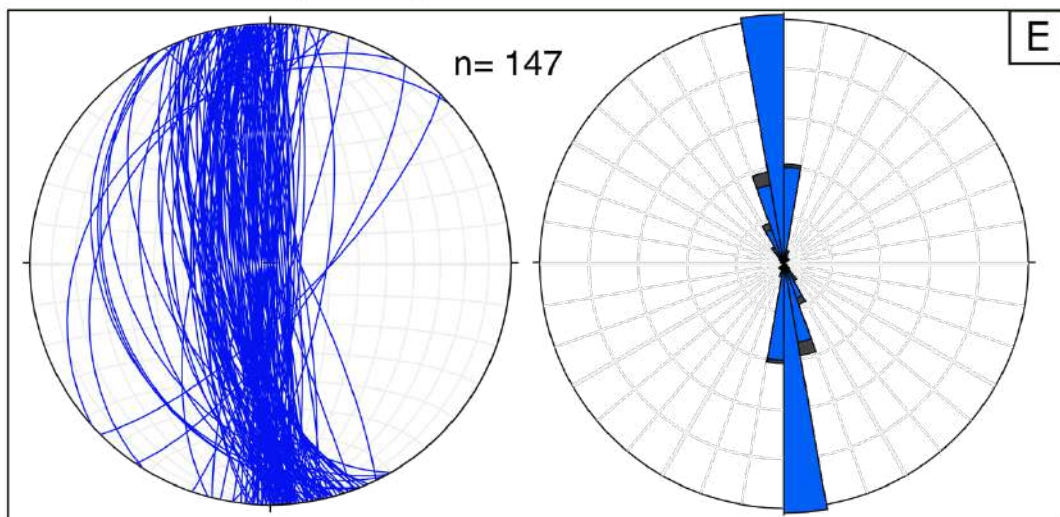


Figure 71 Results of Coulomb stress change calculated in the present research exerted by an inflating dyke (represented as an orange rectangle) on (A) left-lateral transcurrent faults with a NNW-SSE strike and on (B) right-lateral transcurrent faults with a NNE-SSW strike, both located at the dyke tip. Green and red shaded areas represent range of field data collected in the present research within the Northern Volcanic Zone (as in [Figs. 70A-C-D](#)). (C) Right-lateral and (D) left-lateral strike-slip motions that develop at the dyke sides, parallel or sub-parallel to the dyke itself. (E) Plot of nodal planes of strike-slip FMS of the 2010 Madison Plateau seismic swarm at Yellowstone, and corresponding rose diagram.

Chapter 10

Conclusions

- The present PhD project has been devoted to understanding the nature and origin of fractures with transcurrent and oblique components of motion of Holocene age, parallel and coeval to rift zones, which are incompatible with the general stress field associated with extensional settings;
- Case studies are the Yellowstone volcanic plateau, in the western United States, and the Theistareykir and Krafla Fissure Swarms, the westernmost rifts of the Northern Volcanic Zone, in northeast Iceland;
- Main aim has been to: i) define the partition of fault motions at planes with different kinematics; ii) study the temporal relations between faults with strike-slip components and normal faults; iii) evaluate the relations between such transcurrent/transensional faults and magmatic intrusions; and iv) analyze the variations of fault kinematics with depth.
- A multidisciplinary approach has been adopted, that consists in the integration of: i) new geological-structural field data acquired through classical methods; ii) quantitative data collected on Orthomosaics and on Digital Surface Models (DSM) elaborated through Structure from Motion techniques (SfM) applied to Unmanned Aerial Vehicles (UAVs) surveys; iii) seismic data regarding both earthquakes of magmatic and tectonic origin; and iv) numerical models on sill and dyke-induced deformations. The integration of such methodologies allowed to create a three-dimensional scenario describing the occurrence and origin of transcurrent structures;
- The complex geometry and distribution of rift-parallel faults with strike-slip components is interpreted both considering the possible control of regional tectonics on the orientation of faults and the relation with seismic swarms, sill emplacement, that could cause the enlargement of pre-existing fractures or the development of new fractures and small faults, and deflation phases.
- An evolutionary model on the genesis and evolution of faults and fractures with left- or right-lateral kinematics both at the tip and at the sides of an horizontally migrating dyke (the latter being parallel or sub-parallel to the dyke itself) has been developed, particularly focusing on the formation of multiple strike-slip planes at an oblique angle respect to the dyke propagation direction.

- The formation of strike-slip fracture zones only, of dyke-parallel fracture only, or of all sets, can depend upon a series of co-causes that comprehend the pre-existence of fractures suitably oriented respect to the local stress field, which facilitate shear or pure extension due to zero cohesion, the stress perturbation due to magma overpressure, the influence of the tectonic stress field, and the rheological properties of the host rock.
- This geomechanical model is coherent with the predominance of strike-slip motions revealed by focal mechanism solutions during the 2010 Madison Plateau seismic swarm at Yellowstone, with field data collected through classical methods and UAV surveys conducted in Iceland and with the numerical models developed to investigate horizontal dyke propagation.

Appendix 1

Extensional fractures at Theistareykir Fissure Swarm

X (m)	Y (m)	Strike	Opening direction	Amount of opening (m)
412244	7331465	173	72	2,15
412328	7327336	12	83	1,25
412276	7327901	15	85	0,60
412663	7321804	2	87	0,60
411405	7324303	4	89	4,00
411890	7327962	175	90	0,25
412373	7324198	15	90	0,19
412998	7322984	18	90	1,10
412634	7323658	14	90	0,80
411300	7327143	22	90	2,00
412657	7321619	178	92	0,63
413013	7323368	25	95	0,40
413060	7327590	26	95	0,60
410874	7322698	171	95	1,00
412825	7323597	174	95	0,75
412230	7329986	4	97	1,30
413634	7328400	3	98	1,00
413094	7324002	30	100	1,90
413649	7328607	0	100	0,40
413638	7328473	3	100	0,50
412223	7329987	4	100	1,40
413063	7323770	17	100	1,20
414613	7332245	28	100	0,30
413017	7323101	35	100	1,70
414415	7332021	52	100	0,85
413654	7328548	174	100	0,70
410972	7322797	179	100	1,50
412289	7330243	22	101	0,70
412697	7329009	10	102	0,32
411866	7326710	4	102	0,25
413653	7328541	178	102	0,40
412222	7329968	8	103	1,20
411020	7322927	24	104	1,00
412223	7329984	4	104	1,70
411027	7322961	18	104	1,20
415600	7331545	15	105	0,65
412697	7329009	10	105	0,90
413037	7325626	15	105	0,10
412660	7322317	2	105	0,14
412647	7325055	4	105	0,70
414987	7331101	7	105	0,14
415015	7331190	12	105	1,00
414563	7329556	27	105	0,60
414186	7329743	28	105	1,00
411978	7323205	28	109	0,45
410759	7322487	20	110	1,20
413574	7330617	28	110	0,21
414506	7332123	50	110	0,55
413675	7331228	25	110	0,40
412368	7324724	2	110	0,80
414721	7331103	4	110	0,85
412593	7324650	7	110	2,00
412665	7323769	12	110	0,69

412276	7327901	15	110	0,40
411382	7324245	16	110	4,50
413020	7323476	16	110	0,55
411002	7322906	18	110	0,60
412936	7329795	19	110	1,20
413258	7324791	19	110	1,10
412972	7322875	20	110	0,65
413250	7324765	20	110	1,00
413063	7323926	22	110	0,90
413099	7324033	22	110	2,00
414317	7329961	28	110	0,60
414247	7329872	34	110	0,55
412075	7328912	38	110	0,30
414065	7331732	40	110	0,65
413654	7328544	178	110	0,42
411102	7323169	30	111	3,70
411052	7323035	36	112	2,90
413648	7328598	0	112	0,50
413086	7323993	17	112	1,95
411581	7329102	19	112	0,70
413285	7324880	19	112	0,80
411017	7322947	20	112	0,90
412285	7330235	21	112	3,00
411786	7325304	13	113	0,75
412011	7329709	15	113	0,70
412235	7330102	15	114	1,00
411595	7329098	19	114	1,50
414259	7329903	19	114	0,80
413471	7328020	30	115	0,35
412723	7328965	10	115	0,65
413612	7330756	30	115	0,58
413677	7331247	50	115	1,03
413014	7323376	40	115	0,60
413634	7331091	0	115	0,50
412219	7329985	1	115	0,70
412782	7325005	7	115	0,50
413010	7323023	12	115	1,80
413633	7328387	13	115	0,80
413020	7323476	16	115	0,45
413620	7328351	16	115	0,55
413506	7328109	21	115	0,30
414198	7329776	25	115	0,70
414234	7329850	29	115	0,60
413912	7331551	36	115	1,10
412076	7328912	38	115	0,35
411480	7329096	35	116	0,60
411085	7323106	35	116	0,72
411944	7322909	40	116	1,10
411502	7323632	48	116	1,90
411631	7329156	21	117	0,60

412028	7329769	24	117	1,20
415004	7331075	6	118	1,10
411435	7324529	25	118	7,80
411283	7322422	27	119	1,00
411452	7322898	46	120	0,40
412162	7324255	20	120	0,30
414110	7331761	50	120	1,20
413026	7323072	24	120	1,50
413032	7323521	45	120	0,60
412810	7332236	50	120	1,90
412810	7332236	40	120	2,00
413011	7323058	5	120	1,80
414998	7331125	6	120	1,20
413637	7328414	6	120	0,80
413056	7323706	8	120	0,90
413225	7324433	10	120	0,40
412660	7323737	11	120	1,00
413022	7323440	15	120	0,50
412651	7322261	17	120	0,15
413552	7328204	18	120	0,60
413613	7328334	18	120	0,35
413046	7325746	19	120	1,70
413260	7324796	19	120	1,00
412985	7322890	21	120	0,60
413330	7324948	22	120	1,30
412028	7329769	24	120	0,32
414219	7329816	25	120	1,00
413071	7323961	26	120	1,80
413507	7328118	26	120	0,37
413530	7328156	26	120	0,35
414180	7329739	28	120	1,20
413650	7331216	28	120	0,50
413302	7324919	29	120	0,60
413266	7324816	30	120	1,30
412761	7332191	31	120	3,00
413029	7323122	33	120	1,80
413762	7331374	34	120	1,20
412803	7332259	37	120	1,90
414009	7331669	39	120	1,10
414316	7331940	45	120	0,85
414586	7332174	46	120	0,70
415018	7331194	12	122	0,28
412327	7330325	29	122	0,60
412778	7332203	50	123	2,90
412984	7322923	25	123	0,55
411830	7329451	26	123	1,00
411046	7323030	28	123	2,10

414320	7329970	28	123	1,00
415027	7331270	12	124	0,26
411599	7323009	20	124	1,10
411819	7329471	27	124	0,40
413648	7328491	23	125	0,57
413281	7330538	38	125	0,44
413636	7331155	20	125	0,11
413684	7331256	30	125	1,00
412897	7322677	45	125	1,30
412917	7322698	20	125	0,90
412810	7332236	50	125	0,70
412810	7332236	55	125	0,70
414732	7331090	11	125	1,50
412939	7322720	17	125	0,55
413061	7323913	19	125	1,50
413654	7331216	28	125	0,50
413268	7324818	30	125	1,40
414753	7330107	31	125	0,64
413316	7324957	32	125	1,10
414550	7332170	33	125	0,64
412810	7332236	36	125	0,50
414282	7331901	45	125	0,75
414517	7332103	45	125	0,70
412853	7327631	54	125	0,28
415728	7331830	78	125	0,40
415231	7331666	36	126	0,70
414228	7329829	21	126	2,00
411731	7323178	38	126	0,70
415606	7331574	37	127	0,35
415152	7331547	37	127	0,73
411699	7329240	23	127	0,62
411784	7329413	26	127	1,00
411087	7323080	34	127	0,55
411935	7322898	40	127	1,20
413610	7330754	30	128	0,65
413674	7331247	25	128	1,40
412097	7329815	47	128	0,60
410816	7322539	28	129	2,10
411422	7322619	52	129	0,95
412106	7323427	15	130	0,50
414451	7332052	50	130	1,00
413868	7331495	55	130	0,75
413705	7331322	35	130	0,85
413007	7322948	10	130	1,40
412708	7323863	18	130	1,10
413254	7324746	21	130	1,50
412989	7322963	29	130	1,10

412799	7332239	30	130	3,50
412761	7332191	31	130	3,00
411435	7324553	34	130	1,90
412896	7322652	37	130	1,80
412803	7332259	37	130	3,40
412803	7332259	37	130	2,00
413446	7328013	40	130	0,70
412779	7332217	41	130	6,50
414151	7331812	43	130	1,00
413738	7331342	43	130	0,55
413731	7331333	44	130	1,10
414583	7332174	46	130	0,75
414614	7332218	47	130	0,50
414056	7331718	48	130	1,15
414271	7331918	50	130	0,65
414184	7331838	51	130	1,30
414416	7332021	52	130	1,05
414086	7331741	54	130	0,81
411944	7329623	32	131	1,00
413969	7329408	37	131	0,80
411277	7323327	38	131	3,30
411594	7323033	40	131	1,10
411641	7322788	50	131	0,87
415543	7331416	42	132	0,23
413000	7322941	21	132	0,50
410780	7322480	26	132	2,60
414121	7329652	30	132	1,00
412065	7329793	36	132	0,85
412766	7332208	37	132	3,55
414150	7331808	43	132	1,10
414528	7330451	35	133	0,84
413669	7331238	40	133	0,40
411344	7324159	30	134	4,20
411782	7322987	31	134	1,00
411612	7323639	40	135	1,00
411438	7324559	45	135	2,40
411640	7322789	56	135	0,80
412685	7323797	12	135	0,40
413504	7328104	21	135	0,40
412713	7323888	22	135	0,80
413539	7328166	22	135	0,60
414310	7329942	28	135	0,40
412769	7332204	30	135	2,70
412888	7322644	34	135	1,50
413106	7328103	38	135	1,15
414042	7331708	39	135	1,40
412793	7332235	39	135	3,40

414042	7329542	41	135	0,50
411172	7323240	43	135	2,10
414314	7331940	45	135	0,74
411244	7323314	49	136	2,10
411713	7322869	28	136	0,41
411060	7323065	30	136	2,10
412836	7332277	40	136	1,85
413996	7329493	41	136	0,60
412807	7332259	37	137	3,40
411934	7323152	38	137	1,20
411286	7323343	40	137	1,90
411311	7323382	35	138	3,00
413446	7328013	40	138	0,40
414109	7331762	51	138	0,50
411277	7323332	35	139	1,90
411130	7323208	44	139	1,84
415690	7331729	30	140	0,10
413746	7328179	48	140	0,35
412106	7324731	50	140	0,40
413865	7331509	40	140	0,25
413858	7331481	65	140	0,70
412810	7332236	45	140	0,60
414768	7331317	11	140	0,55
412506	7324170	16	140	0,30
413295	7324870	21	140	1,50
413621	7328359	22	140	0,50
412875	7322619	28	140	1,00
414782	7329842	34	140	0,70
412764	7332199	35	140	3,10
413912	7331551	36	140	1,00
413719	7331322	36	140	0,67
412809	7332252	37	140	3,90
414316	7331940	45	140	0,73
414571	7332197	47	140	0,70
412772	7332213	48	140	2,70
413964	7331619	49	140	1,10
413743	7331345	49	140	1,15
413946	7331597	52	140	0,75
411127	7323215	46	141	1,72
411902	7323112	25	141	0,72
411566	7322714	49	141	0,95
411759	7323043	50	142	0,58
413877	7331532	46	142	1,92
411058	7323139	38	142	0,90
411243	7323306	59	143	2,50
411437	7322636	47	143	1,00
411235	7323286	47	143	1,40

411594	7322748	49	144	1,20
411210	7323282	45	145	1,50
414229	7329256	15	145	0,60
412860	7322608	40	145	0,45
412978	7329976	11	145	1,05
413699	7331298	27	145	0,50
413812	7331426	32	145	0,85
414506	7332121	33	145	0,40
413931	7331578	33	145	1,05
412885	7322635	34	145	1,20
413912	7331551	36	145	0,95
412906	7322671	37	145	1,10
412917	7322694	37	145	0,60
411021	7323103	38	145	1,10
414689	7329767	38	145	0,85
414046	7331703	39	145	1,30
413868	7331502	39	145	0,50
413747	7331352	45	145	1,10
411570	7323000	43	146	1,50
411552	7322971	47	146	0,63
411869	7329544	35	147	0,70
412058	7329794	37	147	1,08
411853	7322820	38	147	0,80
411503	7323619	36	148	1,82
411922	7323139	36	148	0,40
411268	7322730	61	148	0,62
411895	7323103	35	149	0,76
413739	7328177	45	150	0,40
414581	7329612	29	150	0,75
413991	7331640	37	150	1,00
413849	7331464	40	150	0,70
414024	7331681	41	150	1,21
414315	7331940	45	150	0,71
414047	7331718	46	150	1,18
411406	7322603	50	150	0,82
414224	7331867	55	150	0,90
412031	7323248	44	151	0,55
411422	7323546	62	152	1,80
411372	7322577	49	152	0,83
414099	7329581	56	152	0,80
411537	7322694	57	152	1,00
411680	7322632	58	153	0,18
411615	7322763	46	153	0,51
411217	7323294	58	154	2,00
411954	7323178	37	154	1,16
411747	7322918	38	154	0,74
411423	7323543	52	154	1,10

414145	7331792	55	155	0,90
413304	7324927	29	155	0,50
412690	7332123	36	155	1,00
413473	7328029	39	155	0,60
411510	7322675	52	155	1,00
412923	7322731	62	155	0,50
411575	7323643	64	156	1,68
411617	7323049	42	156	0,66
411445	7323549	46	156	1,55
413766	7331378	40	157	0,50
414451	7332052	70	160	0,65
414082	7331733	60	160	1,20
413974	7331620	55	160	0,90
414612	7329644	32	160	1,10
413333	7324977	34	160	0,90
411804	7323002	53	160	0,60
412563	7321396	71	160	0,85
411326	7322756	62	164	0,78
411301	7323424	36	165	1,00
413384	7330689	67	167	0,50
412494	7323137	65	170	0,30
411968	7323742	42	170	0,40
411416	7323563	48	170	1,20
412659	7332107	60	174	1,10
408257	7304184	16	99	1,81
408256	7304181	16	105	2,02
408253	7304171	16	101	1,35
408252	7304165	175	102	1,34
408252	7304163	20	94	1,06
408252	7304162	20	95	0,90
408337	7303640	4	106	2,80
408336	7303644	4	110	3,41
408339	7303650	42	110	3,04
408344	7303657	42	107	2,66
408362	7303700	20	97	2,39
408361	7303701	20	100	2,30
408381	7303733	35	106	4,67
408380	7303748	14	104	4,74
408381	7303745	167	103	5,22
408381	7303743	167	105	5,13
408381	7303750	14	101	4,82
408384	7303766	2	98	4,11
408385	7303762	14	102	4,02
408394	7303876	10	95	4,21
408391	7304135	13	86	6,68
408614	7303970	16	106	1,44
408615	7303971	16	111	1,57

408619	7303985	1	91	2,78
408625	7304009	6	101	1,54
408627	7304038	21	93	2,25
408630	7304049	11	98	1,49
408633	7304066	6	101	1,23
408634	7304070	12	96	2,46
408646	7304113	175	100	0,46
408646	7304114	175	101	0,67
408554	7304138	6	97	0,92
407924	7304342	16	104	0,65
407925	7304345	16	111	0,49
408646	7304113	175	99	0,64
408596	7304087	12	111	1,25
408600	7304097	10	99	1,71
408336	7303649	4	115	3,75
407925	7304345	16	125	0,60
408255	7304178	16	101	1,58
408145	7303910	12	112	3,14
408384	7303761	14	105	4,20
408554	7304136	6	93	0,92
408557	7304177	175	99	1,50
408136	7302306	176	99	2,25
408148	7302377	179	97	2,48
408146	7302380	179	95	2,41
408147	7302383	179	101	2,06
408147	7302384	179	95	2,07
408146	7302387	179	93	2,53
408146	7302391	170	93	3,06
408146	7302393	170	93	2,70
408145	7302396	170	90	2,06
408142	7302415	21	89	3,21
408146	7302416	21	89	3,69
408145	7302433	3	97	2,76
408148	7302472	14	89	1,84
408148	7302485	0	81	1,61
408151	7302489	0	91	1,53
408150	7302513	165	87	2,19
408333	7303630	8	110	1,97
408340	7303648	27	118	3,00
408363	7303699	19	100	2,35
408266	7303589	23	111	2,21
408266	7303590	23	117	1,81
407750	7302479	178	111	6,71
407754	7302470	178	98	7,06
407753	7302482	178	115	6,70
407752	7302490	13	102	8,21
407754	7302494	13	104	7,79

407758	7302504	13	95	9,56
407757	7302502	13	97	8,95
408154	7302579	175	90	3,81
408145	7302436	3	105	2,58
408148	7302471	14	85	2,44
408149	7302548	7	94	2,32
408136	7302618	13	103	4,83
408138	7302626	13	99	5,63
408609	7303875	8	101	1,45
408609	7303874	8	99	1,34
408609	7303875	8	97	0,77
408625	7304009	16	105	1,56
408624	7304008	16	104	1,47
408642	7304101	8	99	1,10
408643	7304101	8	100	1,17
408643	7304102	8	111	0,82
408645	7304113	0	96	0,55
408646	7304113	0	99	0,62
408930	7304050	6	98	0,94
408946	7304119	25	95	0,96
408947	7304123	12	90	0,79
408953	7304144	8	102	0,62
408615	7303971	19	97	1,63
408630	7304049	7	105	1,13
408608	7303871	8	101	1,75
408619	7303988	2	106	1,70
408631	7304054	24	91	2,15
408952	7304139	36	88	1,52
408611	7304170	5	101	1,62
408612	7304169	175	101	2,05
408567	7302544	22	102	1,96
408509	7302304	5	102	0,38
408508	7302305	5	101	0,46
408510	7302199	16	96	1,16
408509	7302195	3	100	0,98
408509	7302197	3	97	1,33
408417	7302265	20	108	0,98
408766	7303030	22	106	1,37
408768	7303031	22	112	1,63
408765	7303026	22	114	1,45
408767	7303028	22	105	1,61
409286	7302409	25	116	1,61
409303	7302437	35	142	1,89
409303	7302436	35	131	1,05
409303	7302435	35	118	1,12
409353	7302522	27	130	1,14
409357	7302529	5	119	0,41

409411	7303048	16	123	1,26
409411	7303045	16	118	1,44
409224	7302776	13	112	1,14
409224	7302777	13	114	1,04
409223	7302779	13	103	0,92
409222	7302774	13	99	1,02
409218	7302760	15	111	0,90
409136	7302945	37	109	0,86
409156	7302998	9	104	0,65
409156	7302997	9	105	0,78
408421	7302271	14	106	1,24
408411	7302246	7	90	1,59
408413	7302248	7	95	0,80
408606	7302416	11	99	0,54
408607	7302417	11	101	0,67
408566	7302546	22	101	1,41
408580	7302584	19	114	1,86
409274	7302386	24	119	1,95
409276	7302390	24	116	2,73
409278	7302394	24	111	2,34
409279	7302396	24	117	1,42
409279	7302396	24	117	2,04
409323	7302467	32	111	1,19
409027	7301971	20	114	1,48
409039	7301997	29	103	1,31
409480	7302735	13	110	2,36
409209	7303393	13	139	0,59
408740	7303025	10	104	2,37
408744	7303041	10	98	1,92
408582	7302499	178	90	1,79
408509	7302199	16	97	1,11
408473	7302105	180	90	1,59
408472	7302107	180	92	1,89
408491	7302169	15	99	2,14
408543	7302477	30	82	5,03
408677	7303132	26	95	1,99
408773	7303061	16	103	1,67
409169	7303051	19	104	2,82
409139	7302951	37	114	0,78
409413	7303051	28	110	1,09
408981	7302155	22	118	0,63
408857	7303405	13	95	1,57
408859	7303425	3	100	1,45
408858	7303420	3	101	1,34
408858	7303427	3	95	1,68
408858	7303429	3	110	1,85
408861	7303435	177	98	1,91

408861	7303438	177	104	1,69
408860	7303439	177	105	2,12
408865	7303451	25	115	2,95
408868	7303467	6	113	2,19
408868	7303468	6	109	1,68
408868	7303471	179	104	1,81
408868	7303472	179	104	1,95
408879	7303497	27	111	1,72
408893	7303511	47	126	1,15
408903	7303537	34	110	2,01
408922	7303587	41	128	1,60
408927	7303598	21	117	1,82
408933	7303622	45	106	1,72
408937	7303625	45	117	1,75
407815	7298300	2	95	1,05
407841	7298283	13	108	1,55
407841	7298284	13	107	1,35
407846	7298305	23	116	1,44
408563	7301034	32	122	3,52
408596	7301046	18	120	0,98
408533	7300994	18	115	1,08
408533	7300994	18	121	0,94
408533	7300996	18	112	1,24
408570	7301045	39	114	3,08
408573	7301050	39	126	3,49
408572	7301050	39	122	3,39
408597	7301048	18	112	1,78
408588	7301083	38	119	1,64
408534	7300996	18	107	1,18
408338	7302074	8	79	0,65
408340	7302081	18	103	0,77
408338	7302073	8	84	0,67
408339	7302076	8	85	0,67
408338	7302077	8	89	0,90
408341	7302083	9	117	0,61
408344	7302093	33	99	0,81
408347	7302115	167	96	0,74
408346	7302115	167	94	0,73
408393	7302093	11	105	0,65
408655	7301867	17	118	1,13
408654	7301866	17	118	1,32
408629	7301766	15	99	0,90
408629	7301765	15	105	0,67
408650	7301836	3	95	1,03
408649	7301835	3	97	0,82
408646	7301826	9	104	0,91
408655	7301868	17	114	1,21

408673	7301932	2	85	0,58
408641	7301815	22	111	0,96
408650	7301843	3	109	1,18
408510	7300952	32	111	1,52
408488	7300901	26	123	2,33
408490	7300903	26	128	2,35
408491	7300944	25	127	0,84
408491	7300944	25	127	0,98
408492	7300945	25	127	0,95
408489	7300938	25	124	0,65
408493	7300946	25	117	1,03
408493	7300946	25	122	0,91
408478	7300920	32	130	0,38
408489	7300939	25	121	1,02
408492	7300945	25	124	0,88
408520	7300936	13	128	1,24
408519	7300935	13	125	0,90
408685	7301254	40	122	5,26
408676	7301234	26	114	4,92
408629	7301149	28	114	1,80
408654	7301195	28	97	3,18
408660	7301200	28	103	3,44
408677	7301239	26	107	5,08
408716	7301316	36	123	4,65
408716	7301318	36	120	4,13
408718	7301319	36	114	4,40
408726	7301332	36	122	3,28
408733	7301339	29	113	3,98
408756	7301390	35	114	4,23
408756	7301392	35	116	4,49
408762	7301393	63	118	3,99
408732	7301344	29	117	4,58
408759	7301392	63	116	3,75
408759	7301393	63	116	4,59
408744	7301361	29	115	5,57
408754	7301388	35	116	4,88
408752	7301385	35	108	4,52
408769	7301413	33	118	3,42
408772	7301422	33	113	4,13
408777	7301424	33	112	4,21
408777	7301426	33	118	4,47
408768	7301409	33	120	3,73
408767	7301408	33	122	3,49
408772	7301418	33	110	3,64
408793	7301455	23	102	3,21
410045	7301881	179	99	0,70
410045	7301881	179	99	0,70

409935	7301486	9	99	0,70
409935	7301486	9	99	0,60
409935	7301486	19	94	1,00
409925	7301402	4	89	0,70
409825	7301123	9	94	0,70
409608	7300062	179	99	1,20
409600	7300014	9	109	1,00
409577	7299943	9	104	1,50
409442	7299727	9	109	1,30
409436	7299695	179	109	1,10
409435	7299659	9	109	1,20
409388	7299519	4	106	1,50
409380	7299464	4	99	0,75
409374	7299421	4	109	0,50
409370	7299392	4	101	1,00
409366	7299368	9	109	1,50
409325	7299205	19	94	1,50
409312	7299176	19	104	1,60
409297	7299140	19	109	1,20
409292	7299106	14	104	1,20
409649	7301787	179	89	0,60
409393	7301772	19	109	0,45
409376	7301770	29	119	0,45
409066	7301777	179	89	0,50
409091	7301784	14	109	0,25
408781	7301485	179	89	0,50
408400	7300807	9	109	0,60
408470	7301284	29	99	0,58
408468	7301287	19	109	0,45
408468	7301287	19	109	0,45
408397	7301339	19	104	0,48
408482	7301485	14	109	0,80
408485	7301486	19	109	0,80
408548	7301649	24	109	0,83
408566	7301698	7	110	1,40
408564	7301694	14	109	1,25
408626	7301779	9	109	0,78
408664	7301927	19	109	1,16
408341	7302114	9	106	0,70
408347	7302118	9	94	1,00
408379	7302071	9	111	1,02
408461	7302061	5	101	1,17
408402	7301909	19	119	1,13
408325	7301700	19	109	1,79
408313	7301658	17	89	1,50
408285	7301488	9	94	0,63
408258	7301431	12	99	1,20

408221	7301273	177	84	1,10
408221	7301273	9	104	1,10
408134	7300619	16	104	0,86
407856	7300265	19	104	2,36
407821	7300226	19	114	2,30
407810	7300199	19	113	2,30
407863	7299465	19	129	1,20
407863	7299465	29	89	0,50
407373	7299183	13	79	1,26
407767	7298849	19	114	1,10
407767	7298849	9	106	1,40
407767	7298849	14	104	1,20
407767	7298849	9	104	0,97
407808	7298940	9	109	1,30
408117	7298925	9	94	1,00
408117	7298925	9	94	1,00
408117	7298925	4	109	1,15
408595	7301062	19	123	1,00
408208	7301152	29	109	0,60
407990	7301405	5	109	1,10
407990	7301404	4	114	1,20
407998	7301461	13	101	1,50
408005	7301758	172	79	1,50
408050	7301819	174	104	0,60
408079	7302062	4	119	1,80
407838	7301948	5	113	1,70
408550	7298325	174	81	0,60
409909	7301395	19	96	1,20
409861	7301204	7	115	1,00
409839	7300971	13	95	0,30
409666	7300119	19	112	0,30
409541	7299925	17	107	1,00
409543	7299914	21	85	1,10
409484	7299789	19	109	0,80
409498	7299813	23	97	1,20
409462	7299746	19	107	1,00
409460	7299751	21	104	1,20
409422	7299637	13	89	0,80
409400	7299570	4	95	1,30
409398	7299460	8	103	0,45
409399	7299472	15	99	1,10
409371	7299396	9	101	0,90
409360	7299360	8	81	1,10
409364	7299315	13	91	0,52
409358	7299301	17	95	0,61
408139	7302481	175	75	1,40
408150	7302490	171	95	2,00

408116	7302216	174	77	8,30
409679	7301848	179	69	1,50
409679	7301848	19	99	1,00
408068	7302026	5	113	1,70
407976	7301422	5	109	1,10
408200	7301146	174	81	0,60
407226	7298337	11	97	0,70
407227	7298337	7	79	0,62
407227	7298338	11	93	1,23
407227	7298339	3	85	0,73
407232	7299328	10	111	1,65
407257	7299563	12	100	3,79
407899	7300815	14	110	1,43
407897	7300837	29	113	0,75
407930	7300966	11	114	1,33
407847	7301192	29	84	0,67
408245	7301091	29	109	0,60
408593	7301027	19	123	1,00
407450	7299103	19	114	1,10
407377	7299178	13	79	1,26
408120	7298944	9	75	1,30
408123	7298961	17	95	0,91
407996	7299725	11	103	1,10
408161	7299967	33	121	1,00
408288	7300143	27	115	0,88
408515	7300157	11	113	1,34
408594	7300449	19	107	1,18
409073	7301319	177	85	1,42
409094	7301470	7	117	0,65
409089	7301667	173	89	0,63
409546	7301536	13	97	0,82
409335	7301386	19	119	0,50
408844	7300105	19	97	1,26
408696	7299834	21	105	1,20
408666	7299785	21	105	1,45
408591	7299712	17	109	1,09
408589	7299696	23	127	1,43
408577	7299684	23	127	1,36
409330	7299202	21	103	0,70
409334	7299225	23	99	1,00
409330	7299272	21	93	1,00
409347	7299282	21	89	0,40
409784	7300335	29	97	0,80
409770	7300301	29	105	0,50
409754	7300279	25	97	1,20
409730	7300210	25	79	1,00
409705	7300168	25	109	1,00

409700	7300176	21	101	0,70
409687	7300125	25	97	1,30
409672	7300098	29	93	0,60
410151	7302350	19	87	0,70
410186	7302448	13	83	0,50
409768	7302125	17	104	1,00
409687	7301870	11	91	2,00
410062	7302791	13	85	0,50
410035	7302775	17	127	0,30
410021	7302762	16	98	1,00
409968	7302612	14	101	2,00
409927	7302462	11	97	1,00
409897	7302286	11	97	0,30
409821	7302479	9	92	0,30
409824	7302203	1	79	0,40
409808	7302192	12	101	0,50
409784	7302192	11	101	0,50
409776	7302120	19	93	1,50
409732	7302010	15	94	2,00
409469	7301969	15	107	1,20
409490	7302046	17	111	0,70
409567	7302271	14	109	1,00
409613	7302402	14	124	0,60
409646	7302401	11	125	0,60
409653	7302474	8	112	0,50
409698	7302627	11	119	1,20
409688	7302623	5	101	0,60
409720	7302742	7	107	0,80
409808	7302721	11	125	0,50
409475	7302282	7	105	0,70
409358	7301996	12	79	0,70
409338	7301934	179	93	0,50
409004	7301931	11	121	0,60
409094	7302063	23	143	1,00
409172	7302229	25	109	1,26
409202	7302251	15	105	0,40
409308	7302440	29	117	1,90
409325	7302465	29	109	1,47
409354	7302524	24	107	1,00
409593	7302907	39	124	0,40
409865	7302324	14	101	0,10
409733	7301986	14	102	1,00
408412	7312177	177	97	
408412	7312177	177	87	
408412	7312177	177	94	
408695	7312629	7	107	
408695	7312629	7	104	

408695	7312629	7	105
408724	7312754	22	117
408857	7312946	32	122
409350	7314695	12	112
409467	7315673	177	87
409446	7315730	177	97
409446	7315730	177	102
409455	7315986	22	102
409544	7316362	147	57
409627	7316538	22	112
409304	7315400	-1	27
409326	7315377	157	67
410136	7312989	2	77
409700	7312979	172	77
409712	7313276	2	101
409718	7313595	177	77
409718	7313595	177	67
409718	7313595	177	87
409662	7313996	157	67
409639	7314321	7	77
409555	7314689	2	92
411396	7312290	2	127
411609	7312616	177	92
411511	7313268	9	107
411503	7313226	11	73
410162	7312940	177	85
406878	7317710	153	58
406878	7317710	162	53
406763	7317946	141	53
407317	7317212	163	108
407832	7311226	170	122
406350	7316880	7	98
406576	7317663	158	48
406585	7317854	0	113
406611	7317911	0	107
406580	7317985	10	138
406463	7318007	8	106
407013	7317495	163	80
407013	7317495	163	90
407013	7317495	163	95
406472	7317819	138	108
406472	7317667	0	100
407371	7317106	163	90
407371	7317106	163	80
407371	7317106	163	93
405449	7317219	6	110
405101	7317202	168	78

405101	7317202	168	130
408577	7315961	143	78
407756	7317061	158	70
408856	7315743	158	85
408856	7315743	158	98
408993	7315616	123	63
408993	7315616	123	52
409140	7315555	150	63
409140	7315555	150	68
409328	7315413	138	58
409328	7315413	138	58
409328	7315413	138	58
409221	7315271	176	93
409271	7315271	176	103
408953	7315545	0	150
408147	7316189	123	83
406480	7316762	8	118
406480	7316762	8	122
406480	7316762	8	120
406506	7316645	0	108
406506	7316645	0	88
406637	7316614	0	88
405923	7317236	58	132
404331	7316643	13	138
403821	7317780	28	108
403707	7317690	28	108
404481	7318734	8	103
406176	7316775	28	103
406176	7316775	28	118
406223	7316727	18	108
406223	7316727	18	108
406223	7316727	18	128
410352	7315084	140	68
410205	7315494	0	98
410281	7315920	0	98
410210	7316113	0	98
410205	7316189	0	98
410200	7316316	0	90
410200	7316346	0	90
410190	7316483	0	92
408700	7315715	150	60
409460	7315745	12	115
409690	7316290	5	92
409535	7316895	178	85
409555	7316390	22	118
407740	7316620	162	78
407930	7316370	158	75

407810	7316240	170	85	
409420	7318020	5	96	
409730	7318320	12	110	
405460	7315790	178	85	
404990	7315340	176	92	
404960	7315190	5	96	
405030	7315960	175	92	
406323	7316290	29	113	0,79
406326	7316296	31	122	0,60
406333	7316327	7	104	0,41
406333	7316329	20	111	0,26
406333	7316328	20	112	0,32
406335	7316330	21	115	0,26
406342	7316328	22	113	0,31
406337	7316337	21	105	0,57
406336	7316336	21	109	0,50
406337	7316338	21	106	0,30
406337	7316338	21	102	0,38
406344	7316345	20	117	0,24
406346	7316358	17	106	0,38
406347	7316361	24	111	0,43
406349	7316363	24	107	0,63
406348	7316362	24	117	0,48
406349	7316364	24	116	0,52
406350	7316374	15	108	0,19
406346	7316387	12	113	1,21
406345	7316384	12	106	0,97
406304	7316320	18	107	0,28
406312	7316367	12	100	0,25
406311	7316366	18	103	0,43
406319	7316405	3	100	0,27
406318	7316418	1	121	0,19
406368	7316450	4	110	0,16
406368	7316451	29	120	0,13
406373	7316453	46	106	0,14
406379	7316506	7	105	0,37
406379	7316506	7	104	0,27
406381	7316513	17	103	0,28
406380	7316512	17	106	0,36
406380	7316511	17	110	0,33
406389	7316519	22	117	0,11
406389	7316519	22	117	0,15
406355	7316531	5	104	0,10
406370	7316542	10	104	0,24
406379	7316628	10	101	0,34
406403	7316546	17	108	0,16
406403	7316547	17	108	0,24

406408	7316540	19	101	0,26
406409	7316542	19	113	0,20
406386	7316505	13	117	0,80
406416	7316578	13	101	0,70
406419	7316605	177	106	0,56
406416	7316626	2	94	0,36
406416	7316626	2	104	0,21
409544	7302174	4	95	0,80
409543	7302175	4	96	0,82
409557	7302206	24	138	1,82
409557	7302211	24	121	0,70
409557	7302209	24	108	1,42
409642	7302509	15	121	0,54
409656	7302494	17	108	0,72
409661	7302508	12	98	1,38
409664	7302514	5	106	0,93
409675	7302520	4	107	0,98
409668	7302555	14	109	1,02
409667	7302556	14	108	0,94
409668	7302557	17	110	0,84
409687	7302561	25	126	1,83
409687	7302565	5	112	1,98
409688	7302568	5	102	1,73
409690	7302575	9	105	2,23
409692	7302586	20	110	0,84
409690	7302581	10	103	1,11
409690	7302580	9	111	1,97
409688	7302573	9	102	2,36
409688	7302567	5	106	1,83
409688	7302564	5	105	1,82
409685	7302560	6	109	2,44
409685	7302552	6	104	1,89
409704	7302616	20	102	1,53
409707	7302618	20	110	2,00
409708	7302635	12	106	1,65
409712	7302642	8	98	2,07
409728	7302692	14	95	1,34
409739	7302724	25	113	0,65
409622	7302350	21	113	1,32
409658	7302503	16	112	1,85
409685	7302544	6	105	1,70
405933	7316964	173	95	0,05
405988	7316911	178	103	0,04
406030	7317150	13	113	0,11
405441	7316518	174	98	1,75
406200	7305855	153	98	1,00
406212	7306275	179	120	1,50

406208	7306297	178	108	0,35
406115	7306682	138	73	1,10
406062	7307639	8	114	1,40
406077	7307698	14	118	1,20
406052	7307702	2	108	0,30
406040	7307716	167	73	0,23
406082	7307722	13	116	1,30
406103	7307757	22	136	0,80
406092	7307759	22	118	0,20
406030	7307767	179	113	1,00
406052	7307775	22	118	0,60
406100	7307779	18	128	1,00
406101	7307801	10	106	1,00
406115	7307801	32	140	1,70
406115	7307838	168	93	1,20
406106	7307848	6	111	1,40
406005	7307897	17	119	2,00
405782	7308032	169	98	0,50
405780	7308063	157	84	0,40
405784	7308067	143	70	0,30
405775	7308103	159	80	0,30
405780	7308115	158	78	0,60
405768	7308153	155	63	1,00
405977	7308212	168	87	1,50
405975	7308245	176	97	0,60
405959	7308327	165	99	1,30
405951	7308338	179	110	0,52
405954	7308402	170	104	1,00
405953	7308449	167	115	1,50
405924	7308483	168	103	1,80
405645	7308519	28	106	1,70
406197	7308567	28	127	0,50
406205	7308581	173	117	0,60
406192	7308583	10	118	0,30
406173	7308598	7	106	0,80
405719	7308608	26	106	2,00
406191	7308643	2	119	0,30
405685	7308658	26	106	0,90
406204	7308661	178	118	1,20
406195	7308683	176	115	1,30
405771	7308710	178	102	1,00
406206	7308724	8	119	0,40
405734	7308728	178	98	1,50
406212	7308750	19	128	1,20
405783	7308775	178	113	1,20
405784	7308780	23	34	0,70
406216	7308787	0	110	0,40

406225	7308824	8	122	0,50
405779	7308824	169	105	1,00
406232	7308845	3	112	1,00
406232	7308874	179	109	0,50
406236	7308907	8	104	0,70
405802	7308948	16	108	1,10
405748	7309038	160	88	1,80
405803	7309053	175	80	0,80
405821	7309060	170	86	0,25
406190	7309064	170	99	0,36
405756	7309067	168	118	0,50
405748	7309068	150	96	1,70
406212	7309109	176	92	0,22
405793	7309255	2	108	0,90
405798	7309306	6	108	0,70
405813	7309415	176	126	1,00
405816	7309445	11	106	1,00
405819	7309500	10	108	0,80
405525	7309512	176	113	1,00
405803	7309564	1	108	2,10
405646	7309589	1	124	1,30
405817	7309616	179	108	2,40
405745	7309617	8	129	1,10
405946	7310334	14	113	1,10
405925	7310466	6	114	0,70
405882	7310519	20	121	0,65
405881	7310524	168	96	1,20
405915	7310576	179	109	0,50
405915	7310595	0	103	0,80
405257	7310604	128	58	0,80
405921	7310636	17	114	1,50
405897	7310637	8	119	0,30
405907	7310657	3	110	0,51
405920	7310719	17	114	2,00
405965	7310756	24	120	2,10
405935	7310785	17	114	0,45
406207	7310817	17	116	0,40
405980	7310839	12	138	0,40
406004	7310862	24	120	1,80
406018	7310934	24	120	1,50
405428	7310949	20	126	0,30
406321	7310958	8	105	1,20
406321	7310965	172	108	1,00
405445	7310974	25	146	0,90
405431	7310986	4	118	1,00
405437	7311018	172	90	1,50
406079	7311038	169	97	1,00

405449	7311038	0	103	1,80
406367	7311050	22	128	0,70
405483	7311086	0	103	0,45
406065	7311121	178	108	1,00
406078	7311147	169	97	0,50
405492	7311147	18	118	1,30
405494	7311153	171	123	0,20
406366	7311162	176	108	1,00
405490	7311168	176	106	1,00
405506	7311172	15	113	1,70
406351	7311176	3	103	0,50
406059	7311183	8	99	0,40
406087	7311188	26	112	1,00
406072	7311202	8	103	0,70
406056	7311214	8	99	2,00
406363	7311248	168	99	0,67
406063	7311251	8	99	1,00
405532	7311253	18	126	0,46
405535	7311255	9	116	0,50
406063	7311260	8	90	0,50
406376	7311267	2	120	0,80
406063	7311274	166	93	1,00
405533	7311276	169	94	1,30
406354	7311318	12	109	0,40
406377	7311324	170	100	0,40
406277	7311347	8	114	0,16
406284	7311355	0	74	0,55
406346	7311377	0	115	0,40
406269	7311395	167	105	2,20
406366	7311405	179	136	0,80
406258	7311415	161	96	0,36
406268	7311433	167	105	2,00
406371	7311437	18	118	0,70
406384	7311442	19	129	1,20
406388	7311457	178	95	0,60
406379	7311459	10	108	0,30
406259	7311469	163	106	0,50
406283	7311477	8	110	1,00
406267	7311480	168	102	1,50
406272	7311482	167	105	1,20
406265	7311487	168	102	1,00
406254	7311505	172	89	0,30
406190	7311517	153	105	0,60
406174	7311536	0	112	0,40
406175	7311541	160	101	0,80
406259	7311548	166	96	0,37
406275	7311549	173	111	0,40

406181	7311550	0	112	0,50
406290	7311565	170	109	0,32
406284	7311572	168	98	1,00
406175	7311578	175	113	0,90
406389	7311579	3	118	0,40
406283	7311581	168	98	0,70
406182	7311586	0	112	0,50
406291	7311595	173	93	0,20
406249	7311599	166	87	0,55
406277	7311601	174	109	0,58
406182	7311614	14	118	1,00
406388	7311619	3	118	0,40
406167	7311620	11	124	0,50
406163	7311633	24	126	0,23
406260	7311645	150	88	0,70
406256	7311649	178	136	0,65
406390	7311650	3	118	0,45
406160	7311652	7	116	1,50
406259	7311653	178	108	0,25
406252	7311655	173	92	0,20
406260	7311656	168	105	0,65
406260	7311660	156	90	0,10
406257	7311663	174	118	0,11
406162	7311668	17	135	0,90
406160	7311668	20	118	0,40
406192	7311673	178	88	0,40
406188	7311677	16	148	0,22
406183	7311681	28	118	0,90
406298	7311689	158	107	1,00
406164	7311698	13	120	0,45
406192	7311712	179	103	0,30
406161	7311722	3	115	0,50
406190	7311724	8	110	0,60
406169	7311724	0	134	1,00
406166	7311735	3	115	0,37
406196	7311742	48	128	1,00
406161	7311747	3	115	0,70
406403	7311866	168	88	0,50
406378	7311919	176	110	1,00
406295	7312072	173	124	0,40
406222	7312079	38	147	0,70
406222	7312080	23	143	0,45
406318	7312085	6	120	1,00
406316	7312106	8	110	0,60
406324	7312133	3	117	0,20
406207	7312141	23	118	1,20
406333	7312146	18	124	0,20

406329	7312179	8	113	0,40
406334	7312274	7	117	0,50
406343	7312370	179	114	0,30
406344	7312421	18	127	0,40
406341	7312430	3	106	0,50
406361	7312435	20	138	0,60
406350	7312438	16	140	0,40
406357	7312440	23	138	0,40
406350	7312463	3	128	1,20
406363	7312476	4	144	0,35
406360	7312478	16	118	0,35
406361	7312493	13	118	0,30
406356	7312494	8	130	0,40
406352	7312497	23	130	0,30
406345	7312504	3	99	0,20
406305	7312513	16	111	0,60
406300	7312522	8	110	0,40
406329	7312602	4	110	0,80
406339	7312602	18	130	0,12
406344	7312603	26	140	0,50
406339	7312604	4	108	0,22
406351	7312605	3	136	0,25
406356	7312607	10	105	0,50
406360	7312610	179	129	0,32
406366	7312642	176	108	0,30
406406	7312673	18	129	0,40
406420	7312682	179	133	0,20
406401	7312684	16	100	0,20
406342	7312718	176	103	1,30
406390	7312723	16	131	0,70
406195	7312724	168	98	0,70
406338	7312727	16	108	0,50
406337	7312729	18	106	0,60
406396	7312730	12	125	0,50
406353	7312748	58	173	0,80
406500	7312753	12	108	0,70
406336	7312755	7	100	0,70
406359	7312758	18	116	0,60
406362	7312758	19	136	0,90
406008	7312785	14	148	1,00
406378	7312789	23	128	0,50
406313	7312789	8	119	1,50
406389	7312796	173	104	0,40
406404	7312808	13	128	1,00
406356	7312811	177	104	1,00
406369	7312814	20	136	0,60
406365	7312822	13	117	0,40

406387	7312857	17	116	0,30
406378	7312862	22	134	0,24
406411	7312869	34	128	0,70
406413	7312876	28	127	0,15
406441	7312897	12	141	0,40
406400	7312898	10	118	0,20
406422	7312901	13	124	0,40
406444	7312916	10	120	0,30
406379	7312934	2	103	0,70
406386	7312938	8	100	0,70
406382	7312942	19	128	0,20
406413	7312948	26	128	0,15
406419	7312949	18	136	1,30
406395	7312962	18	128	0,40
406418	7313003	6	114	0,50
406430	7313033	3	123	0,90
406418	7313039	18	114	0,40
406450	7313045	16	118	0,40
406437	7313065	23	123	1,40
406440	7313097	11	123	1,60
406478	7313109	12	129	0,50
406451	7313134	3	128	0,70
406503	7313158	13	118	1,00
406458	7313159	6	146	0,50
406503	7313272	19	143	2,20
406608	7313273	19	118	0,20
406614	7313294	28	138	0,50
406619	7313314	10	118	0,60
406498	7313318	8	114	2,00
406542	7313322	8	110	0,60
406491	7313335	3	111	1,20
406635	7313344	23	116	0,40
406615	7313346	28	120	0,19
406624	7313350	24	140	0,40
406625	7313352	43	118	0,08
406540	7313354	2	107	0,70
406543	7313382	1	126	0,32
406602	7313402	18	128	0,40
406519	7313406	1	114	0,30
406616	7313410	179	108	0,20
406616	7313420	173	98	0,30
406543	7313428	176	98	0,30
406519	7313450	13	98	1,00
406555	7313452	177	112	0,25
406543	7313453	168	80	0,80
406555	7313481	10	106	0,60
406515	7313512	3	126	0,30

406525	7313536	16	109	0,80
406507	7313542	20	118	1,00
406509	7313557	3	104	0,50
406485	7313561	4	126	0,40
406536	7313568	9	106	0,70
406510	7313627	8	109	0,20
406509	7313635	6	111	0,30
406518	7313637	7	108	0,40
406506	7313640	13	118	0,30
406530	7313641	12	108	0,60
406505	7313643	3	98	0,40
406532	7313644	170	109	0,30
406500	7313654	6	123	0,25
406539	7313662	31	120	0,30
406531	7313710	35	139	1,00
406547	7313721	16	107	0,20
406559	7313731	8	118	0,60
406543	7313733	8	110	0,30
406593	7313736	14	113	0,09
406572	7313757	5	107	0,40
406611	7313784	7	108	0,30
406616	7313805	11	111	0,40
406300	7313806	13	104	0,37
406618	7313823	14	93	0,80
406608	7313824	6	127	0,40
406595	7313827	4	109	0,80
406638	7313836	11	127	1,00
406623	7313839	173	136	0,70
406625	7313845	10	120	0,45
406611	7313845	9	108	0,70
406614	7313851	173	108	0,80
406638	7313863	8	126	1,20
406655	7313871	14	117	0,40
406655	7313871	14	117	0,75
406640	7313875	178	119	0,50
406655	7313876	3	99	0,70
406646	7313876	15	138	0,40
406633	7313878	0	133	0,30
406660	7313887	43	137	0,50
406642	7313891	3	127	0,39
406645	7313892	18	108	0,20
406635	7313893	8	99	0,60
406635	7313895	0	114	0,40
406684	7313900	13	109	0,55
406652	7313902	8	130	0,40
406633	7313904	178	89	0,48
406687	7313908	3	104	0,40

406171	7313914	13	117	0,50
406649	7313920	48	93	1,00
406668	7313924	9	98	0,30
406651	7313930	16	108	0,30
406649	7313931	23	120	1,00
406659	7313936	13	108	0,10
406677	7313999	11	127	1,10
406704	7314000	13	128	0,50
406677	7314001	178	118	1,50
406720	7314003	13	106	0,70
406754	7314033	158	88	0,40
406753	7314034	3	96	0,35
406765	7314094	18	116	0,26
406759	7314106	31	126	0,28
406757	7314135	20	78	0,30
406804	7314136	13	148	0,90
406843	7314161	29	116	0,32
406848	7314164	179	76	0,14
406806	7314169	16	103	0,91
406851	7314172	47	105	0,30
406853	7314174	23	108	0,15
406853	7314175	53	148	0,07
406781	7314183	41	136	0,20
406787	7314185	148	72	0,20
406790	7314199	173	88	0,34
406815	7314215	179	103	0,40
406818	7314234	27	110	0,50
406877	7314249	26	103	0,50
406820	7314277	8	100	0,09
406822	7314279	10	98	0,21
406816	7314280	11	107	0,15
406958	7314385	31	118	0,98
406962	7314385	31	118	1,25
408259	7304177	2	111	1,43
408256	7304165	16	116	1,17
408257	7304170	16	119	1,20
408258	7304172	16	115	1,63
408259	7304175	2	107	1,85
408263	7304250	3	112	1,25
408259	7304201	0	105	1,44
408230	7304304	0	103	0,99
408229	7304310	4	101	1,02
408230	7304311	4	99	0,90
408224	7304319	2	97	0,37
408224	7304322	2	103	0,58
408223	7304337	0	104	0,83
408230	7304324	0	108	1,23

408269	7304349	2	101	0,91
408268	7304340	4	98	0,71
408269	7304341	4	96	0,76
408269	7304348	2	96	0,78
408262	7304404	1	100	0,86
408262	7304405	1	101	1,04
408262	7304406	1	94	1,09
408267	7304443	5	95	1,16
408267	7304445	5	106	1,30
408494	7304489	13	115	0,95
408498	7304503	7	108	0,91
408574	7304547	20	112	5,03
408568	7304528	20	112	6,24
408569	7304517	15	100	1,40
408559	7304511	24	107	3,59
408559	7304514	24	116	3,43
408559	7304514	24	116	3,54
408552	7304505	26	111	1,10
408554	7304497	27	118	3,34
408553	7304498	27	122	4,06
408554	7304500	27	114	2,75
408551	7304493	27	120	2,99
408552	7304489	24	112	0,53
408568	7304512	15	98	1,49
408529	7304468	31	117	1,40
408527	7304463	30	114	1,12
408536	7304476	19	114	1,36
408525	7304460	30	116	1,18
408538	7304483	19	99	0,61
408489	7304460	2	102	1,09
408490	7304461	2	110	1,52
408489	7304457	2	102	1,09
408488	7304429	19	111	5,81
408429	7304306	24	112	2,68
408437	7304338	20	111	0,89
408465	7304393	25	114	0,63
408576	7304044	12	114	2,07
408572	7304029	12	113	2,51
408629	7304028	15	109	2,37
408629	7304027	15	108	2,21
408632	7304039	8	103	1,22
408654	7304088	10	103	0,40
408647	7304104	6	97	0,70
408646	7304104	6	98	0,65
408555	7304128	4	107	0,90
408555	7304126	4	108	1,05
408612	7304159	2	98	1,88

408612	7304162	2	99	1,21
408593	7304187	0	95	2,11
408594	7304188	0	106	1,14
408557	7304168	1	99	1,16
408558	7304204	4	99	0,88
408558	7304207	4	93	0,92
408593	7304223	4	99	1,80
408593	7304223	4	95	1,61
408596	7304236	1	100	1,44
408595	7304251	4	105	1,45
408594	7304249	4	102	1,31
408601	7304262	0	104	0,47
408603	7304268	19	107	0,39
408600	7304272	17	102	0,89
408599	7304269	17	103	1,16
408599	7304271	17	105	1,14
408614	7304293	18	106	1,53
408619	7304300	20	111	1,43
408621	7304307	20	110	0,87
408623	7304312	20	100	0,48
408626	7304313	18	113	0,66
408630	7304323	20	107	0,73
408630	7304325	20	108	0,68
408638	7304341	14	108	1,02
408650	7304375	24	118	0,77
408651	7304377	24	124	0,29
408650	7304376	24	124	0,58
408709	7304457	11	118	0,93
408709	7304452	11	117	1,05
408695	7304436	9	109	0,46
408677	7304375	2	103	1,58
408678	7304376	2	115	1,45
408726	7304386	2	106	1,57
408726	7304387	2	113	1,58
408725	7304379	2	104	2,00
408729	7304412	12	103	0,56
408729	7304411	12	105	0,69
408728	7304410	12	99	0,74
408733	7304407	3	97	1,53
408732	7304415	3	105	1,82
408735	7304430	0	106	1,57
408735	7304431	0	106	1,57
408736	7304434	0	106	1,57
408734	7304421	0	106	1,13
408788	7304362	10	106	0,44
408696	7304315	8	105	0,93
408259	7304177	2	111	1,43

407763	7305176	18	115	1,85
407793	7305265	11	98	2,23
407817	7305307	22	106	1,17
407833	7305454	5	98	1,92
407848	7305540	4	98	1,60
407510	7304285	16	100	2,13
407581	7304481	22	105	4,79
407605	7304643	2	115	3,95
407668	7304928	3	120	0,82
407674	7304950	26	104	2,13
407675	7304954	26	112	2,22
407674	7304954	26	106	2,20
407685	7304979	23	108	2,47
407685	7304978	23	105	2,74
407741	7305110	7	104	3,69
407739	7305106	7	101	2,21
407807	7304662	2	113	2,69
409291	7304931	3	94	0,50
409292	7304928	22	100	0,79
409293	7304928	22	100	0,86
409295	7304933	22	115	1,02
409291	7304910	0	106	0,72
409297	7304937	23	111	0,80
409316	7305032	2	99	0,58
409317	7305073	8	108	0,69
409317	7305068	8	103	0,99
409316	7305099	16	111	1,36
409315	7305101	16	120	1,51
409324	7305141	2	95	0,50
409334	7305157	16	98	0,29
409392	7305163	22	113	0,63
409387	7305165	20	99	0,75
409389	7305172	20	100	0,92
409389	7305170	20	103	0,76
409403	7305201	16	112	1,20
409405	7305208	16	107	0,99
409422	7305223	22	115	0,54
409413	7305212	16	106	0,55
409496	7305424	15	120	0,56
409238	7304983	12	128	0,57
408918	7304851	8	98	0,31
408905	7304822	9	97	0,44
408821	7304688	17	122	0,68
408822	7304689	17	124	0,74
408822	7304692	17	119	0,75
408823	7304694	17	121	0,83
408790	7304591	0	104	1,46

408787	7304570	1	101	0,91
408787	7304569	1	105	1,04
408786	7304573	1	104	1,27
408787	7304571	1	108	1,18
408751	7304539	8	97	0,80
408740	7304454	9	112	1,32
408739	7304450	9	114	1,09
408738	7304447	9	105	1,07
408735	7304427	3	118	1,64
408729	7304420	11	115	0,83
408731	7304423	18	105	0,55
408728	7304416	5	105	0,48
408697	7304327	11	110	1,67
408634	7304343	24	149	1,69
408651	7304387	22	124	0,57
408652	7304389	22	117	0,53
408653	7304390	22	105	0,52
408679	7304385	3	114	1,49
408679	7304383	3	105	0,96
408698	7304449	11	106	0,44
408697	7304448	11	114	0,53
408695	7304436	17	110	0,87
408679	7304395	6	127	0,95
408679	7304395	6	127	0,95
408728	7304390	4	107	1,91
408531	7304478	19	108	1,26
408491	7304468	6	101	1,21
408500	7304512	12	109	1,00
408942	7304991	14	106	1,57
408943	7304994	14	106	1,94
408947	7305034	18	110	2,08
408949	7305029	18	112	1,91
408951	7305036	18	111	2,27
408944	7305016	18	117	2,18
408952	7305049	18	110	1,80
409047	7305085	11	106	1,24
409045	7305081	11	105	1,38
409046	7305083	11	106	1,29
409046	7305077	11	102	0,71
409072	7305152	12	102	1,21
409073	7305153	12	107	1,23
409071	7305149	12	109	1,09
409075	7305163	18	119	1,47
409074	7305163	18	130	1,13
409015	7305144	8	109	0,64
409017	7305151	8	108	0,81
408991	7305189	18	105	0,62

408991	7305187	18	122	0,83
409042	7305247	4	98	2,10
409041	7305250	4	103	2,25
409043	7305255	4	101	1,68
409042	7305258	4	99	2,41
409042	7305261	4	104	1,51
409040	7305242	4	98	2,22
409041	7305238	4	102	1,81
409066	7305370	5	107	1,45
409065	7305369	42	126	1,38
409066	7305373	5	99	1,71
409064	7305379	5	104	1,93
409064	7305380	5	104	1,53
409066	7305374	5	102	1,97
409065	7305384	10	104	1,62
409066	7305382	10	106	1,27
409120	7305422	10	123	2,00
409120	7305422	10	112	1,85
409130	7305438	8	110	2,03
409131	7305443	8	107	1,79
409130	7305446	8	111	2,33
409132	7305447	8	104	2,65
409131	7305451	8	107	1,70
409132	7305452	8	112	2,51
409131	7305453	8	101	2,28
409132	7305455	180	104	2,21
409131	7305460	180	106	2,23
409131	7305465	4	100	1,71
409131	7305485	6	108	1,73
409132	7305476	2	101	1,31
408988	7304753	8	108	0,75
408989	7304765	5	100	0,44
408987	7304755	8	108	0,79
408987	7304752	8	112	0,94
409288	7305555	14	112	1,18
409287	7305556	14	115	0,85
409287	7305554	14	118	0,69
409316	7305608	26	114	1,24
409318	7305611	26	115	1,22
409320	7305614	26	115	1,49
409320	7305616	26	114	1,46
409314	7305603	26	108	0,72
409314	7305603	26	105	0,56
409363	7305650	27	112	1,17
409363	7305651	27	120	0,88
409362	7305646	32	101	0,91
409371	7305671	17	106	1,62

409372	7305671	17	105	1,85
409371	7305664	25	109	1,54
409394	7305713	19	106	1,67
409393	7305713	19	102	1,64
409394	7305714	19	104	1,71
409397	7305718	19	108	2,65
409398	7305725	20	104	2,13
409393	7305712	19	109	1,40
409400	7305726	20	102	1,94
409400	7305728	20	107	2,21
409405	7305751	21	106	1,43
409406	7305744	24	112	1,54
409403	7305739	22	110	1,83
409401	7305734	22	110	2,01
408995	7305736	24	124	2,08
408996	7305741	24	132	2,31
408968	7305695	35	125	3,04
408967	7305697	35	117	2,36
408969	7305699	35	121	2,59
408970	7305699	35	125	1,87
408973	7305702	35	130	2,25
408926	7305599	14	119	2,41
408905	7305527	19	114	3,70
408907	7305533	19	106	3,89
408896	7305496	20	102	2,83
408790	7305177	2	102	2,36

Appendix 2

Extensional fractures at Krafla Fissure Swarm

X (m)	Y (m)	Opening direction	Amount of opening (m)	Strike
418179,949	7300636,338	46	1,26	343
418125,998	7302088,477	57	0,82	316
418230,275	7302173,687	57	0,46	316
418065,915	7301514,572	57	0,29	340
418325,689	7302467,555	59	0,13	330
418229,268	7302176,546	61	0,44	345
418247,467	7300704,100	62	0,58	330
418247,440	7300704,714	65	0,66	335
418979,522	7301927,470	66	0,32	353
418233,134	7302151,071	72	0,30	336
418388,594	7302256,370	72	0,39	340
418234,982	7302078,505	73	0,57	353
418296,513	7300675,241	73	0,92	320
418234,961	7302159,616	74	0,82	344
418234,452	7302163,635	74	0,61	341
418107,845	7301862,703	74	0,40	1
418179,348	7300742,508	74	0,62	336
418327,405	7302450,320	74	0,46	3
418233,042	7302150,653	74	0,31	337
418065,692	7301525,152	75	0,54	4
417782,233	7300464,285	76	2,13	10
418235,077	7302159,927	76	0,90	344
418284,708	7300468,946	76	0,87	345
418162,896	7301611,783	76	0,76	17
418229,845	7302174,265	76	0,41	336
418327,695	7302450,920	76	0,43	356
418007,564	7302019,689	76	2,22	333
418355,190	7302420,016	77	0,23	343
418285,423	7300468,390	77	0,71	344
418175,607	7301149,535	77	0,83	354
418355,235	7302489,550	78	0,37	23
418069,588	7301634,873	78	0,21	346
418065,907	7301524,974	78	0,66	4
418162,794	7301611,495	78	0,75	8
418201,821	7301815,893	79	0,57	357
418298,547	7300530,183	79	2,37	356
418224,459	7301971,812	79	0,35	346
418006,230	7302027,193	79	2,28	353
418162,890	7301610,440	79	0,79	345
418351,822	7302493,553	80	0,22	344
417777,619	7300575,174	80	1,47	358
418246,604	7300706,005	80	0,76	330
418070,154	7301626,597	81	0,39	334
418760,881	7302040,062	81	1,08	24
418358,183	7302418,738	81	0,05	322
418070,022	7301626,121	81	0,42	343

418068,958	7301504,211	81	0,64	341
418246,953	7300705,846	82	0,72	328
418233,983	7302147,781	82	0,79	356
418355,945	7302702,325	82	1,30	349
418068,354	7301509,952	82	0,62	350
418355,446	7302420,008	82	0,19	343
418220,395	7302167,527	83	0,73	326
418356,525	7302699,966	83	0,54	332
418057,091	7300832,472	83	0,31	357
418134,628	7301972,219	83	0,10	14
418224,038	7301922,985	83	0,43	4
418230,505	7302171,372	83	0,34	355
418246,710	7300706,370	83	0,78	330
418170,278	7301128,267	83	1,66	18
418215,365	7302060,333	83	0,78	358
418785,281	7302034,229	83	0,37	45
418246,906	7300705,354	83	0,64	337
418308,983	7300619,798	83	0,92	351
418068,820	7301501,306	84	0,58	334
418645,294	7302426,680	84	0,73	359
418581,018	7302427,737	84	0,52	356
418783,392	7302036,901	84	0,45	350
418238,546	7302138,531	84	0,74	13
417781,325	7300586,798	84	1,43	3
418068,693	7301501,935	84	0,51	346
418214,691	7302058,579	84	0,77	7
418352,524	7302467,932	84	0,39	355
418220,382	7302167,672	85	0,72	326
418984,309	7301386,312	85	0,42	356
418311,034	7302728,459	85	0,14	354
418783,582	7302036,775	85	0,50	351
418080,051	7301035,185	85	0,28	354
418223,592	7301974,203	85	0,53	1
418784,075	7302035,363	85	0,62	340
418784,148	7302035,482	85	0,62	340
418056,877	7300832,663	85	0,47	9
418090,079	7301072,323	85	0,13	359
418192,001	7300745,732	85	0,41	26
418224,044	7301943,381	85	0,42	1
418309,078	7300617,935	85	0,81	344
418352,850	7302426,756	86	0,20	353
418092,432	7301758,659	86	0,64	14
418220,509	7302167,775	86	0,74	325
418148,497	7302057,460	86	1,14	355
417780,238	7300523,406	86	0,94	11
418068,815	7301507,163	86	0,77	356
418354,617	7302447,883	86	0,12	0

417779,649	7300522,507	86	0,98	359
418134,656	7301971,764	86	0,24	340
419000,235	7301437,701	86	0,49	349
418182,862	7301441,104	86	0,52	0
418076,774	7301712,631	87	0,92	13
418163,042	7301611,154	87	0,66	358
418784,393	7302034,879	87	0,51	349
418223,166	7301965,085	87	0,35	39
418390,784	7302277,426	87	0,28	350
418224,317	7301973,105	87	0,38	341
418223,339	7301965,853	87	0,34	12
418044,531	7301533,173	87	0,46	337
418073,184	7301437,127	87	0,35	316
418352,632	7302468,352	87	0,44	2
418066,073	7301517,949	87	0,53	12
418068,619	7301507,894	88	0,74	351
418068,420	7301502,403	88	0,65	359
418070,837	7301623,935	88	0,26	352
418142,237	7301974,401	88	0,33	359
418066,285	7301517,646	88	0,54	358
417778,793	7300444,415	88	4,08	355
418070,683	7301494,236	88	0,55	2
418317,773	7302402,574	88	0,11	348
418979,369	7301930,720	88	0,25	352
418191,651	7300744,766	88	0,22	356
418325,616	7302467,805	88	0,12	360
418073,565	7301435,920	88	0,60	342
418760,823	7302024,103	89	1,22	352
418245,449	7300710,348	89	0,47	6
418073,397	7301436,507	89	0,53	331
418224,347	7302197,240	89	1,06	23
418307,385	7300637,578	89	0,85	354
418245,627	7300710,256	89	0,34	8
418352,607	7302467,123	89	0,35	0
418470,547	7302447,290	89	0,50	5
418076,512	7301712,869	89	1,13	12
418224,151	7301970,063	89	0,36	0
418068,275	7301508,878	89	0,62	349
418076,242	7301711,496	89	1,05	27
418216,969	7302022,003	89	1,10	1
418068,429	7301509,164	89	0,76	349
418237,928	7302147,515	89	0,96	10
418245,407	7300710,522	89	0,42	7
418075,984	7301711,694	90	1,15	27
418784,039	7302038,179	90	0,49	23
418784,013	7302032,343	90	0,89	0
418181,490	7300695,997	90	0,72	358

418070,397	7301494,712	90	0,47	337
418069,281	7301499,962	90	0,50	345
418046,908	7301518,518	90	0,39	358
418075,197	7301709,805	90	0,75	4
418184,841	7301423,652	90	0,45	0
418184,954	7301423,493	90	0,44	11
418109,876	7301871,237	90	0,19	330
418222,825	7301961,923	90	0,26	346
418220,871	7301979,670	90	0,58	3
418221,218	7301979,115	90	0,52	349
418221,740	7301982,171	90	0,36	18
418311,168	7302728,653	90	0,18	343
418311,194	7302728,105	90	0,10	142
418311,374	7302727,947	90	0,11	165
418352,891	7302466,845	90	0,27	1
418354,187	7302451,463	90	0,24	8
417999,936	7302047,371	90	2,09	6
418644,844	7302430,540	90	0,84	359
418196,128	7301760,692	91	2,12	2
418223,194	7301965,358	91	0,37	7
418352,009	7302493,752	91	0,28	342
418223,301	7301965,656	91	0,30	15
417778,079	7300447,749	91	3,81	18
418005,522	7301069,643	91	1,08	350
418481,491	7302575,431	91	0,89	0
419008,728	7301396,148	91	0,83	1
418222,051	7301982,743	91	0,41	13
418057,222	7300833,401	91	0,48	359
418193,090	7300744,958	91	0,34	51
418203,548	7300765,081	91	1,27	23
418208,029	7300576,387	91	0,71	1
418194,974	7300745,593	91	0,47	2
418142,426	7302469,370	91	0,07	16
418070,291	7301493,924	92	0,40	14
418192,306	7300746,876	92	0,24	357
418192,722	7301744,971	92	1,14	25
418168,628	7300840,828	92	0,46	347
418201,736	7300761,787	92	1,83	5
417999,404	7302048,328	92	2,18	6
418307,967	7300625,132	92	0,70	4
418979,490	7301927,950	92	0,25	0
417788,043	7300651,976	92	0,98	9
418351,844	7302596,869	92	0,98	0
418980,814	7301919,438	92	0,49	0
418005,891	7301069,214	92	0,98	348
417788,403	7300651,339	92	0,77	2
418096,907	7301775,542	92	0,62	25

418093,372	7301754,841	92	0,46	24
417990,460	7302206,189	92	0,77	6
418356,174	7302491,021	92	0,60	1
418092,769	7301758,151	92	0,44	359
418307,744	7300631,376	92	0,59	357
418355,186	7302485,046	92	0,65	9
418075,818	7301710,222	92	1,07	12
418075,660	7301710,407	92	1,05	12
418043,898	7301493,550	92	0,17	359
418179,303	7300641,006	92	1,10	356
418074,771	7301431,555	92	0,41	353
417999,732	7302051,069	92	2,03	6
418785,597	7302034,664	92	0,25	26
418142,566	7302469,706	92	0,07	359
418782,981	7302026,818	92	0,30	22
418353,169	7302426,514	93	0,17	326
418181,956	7300695,108	93	0,93	0
418191,743	7300745,173	93	0,29	20
418355,078	7302485,689	93	0,52	12
418008,780	7301080,466	93	0,82	356
418245,157	7300710,843	93	0,48	8
417982,608	7302177,733	93	0,52	5
418000,050	7302050,339	93	2,03	7
417999,574	7302049,333	93	2,35	6
418304,760	7300470,765	93	1,23	14
418046,047	7301520,002	93	0,29	0
418090,247	7301073,057	93	0,14	24
418355,014	7302484,988	93	0,60	9
418580,843	7302429,459	93	0,66	2
418191,750	7300745,408	94	0,32	34
418089,964	7301072,039	94	0,16	358
418193,391	7300745,411	94	0,20	44
418245,477	7302317,986	94	1,35	16
418219,806	7302109,915	94	0,26	2
418080,214	7301035,073	94	0,34	338
418409,992	7302285,743	94	0,34	355
418297,769	7300709,832	94	0,75	2
418356,137	7302490,582	94	0,60	8
418216,707	7302094,416	94	0,45	356
418355,225	7302485,280	94	0,67	356
418356,061	7302490,698	94	0,59	7
418193,397	7300745,213	94	0,19	20
418539,704	7302642,467	94	0,22	3
418068,624	7301503,068	94	0,44	21
418046,616	7301500,551	94	0,36	10
418353,907	7302541,673	94	0,57	3
418047,579	7301501,643	94	0,18	6

418164,518	7300574,045	94	1,42	2
418311,379	7302727,746	94	0,13	181
418014,318	7300819,231	94	0,53	359
418141,819	7302467,164	94	0,13	22
417788,281	7300652,707	95	1,21	34
418073,779	7301436,198	95	0,40	329
418418,352	7300588,243	95	0,53	6
418075,527	7301707,490	95	0,97	1
418020,244	7300849,387	95	0,78	2
418047,172	7301501,325	95	0,31	20
419014,916	7301425,398	95	1,06	351
418317,503	7302480,621	95	0,09	5
418308,199	7300625,491	95	0,70	5
418046,285	7301520,439	95	0,35	18
417782,076	7300589,836	95	1,40	348
418480,076	7302577,845	95	0,86	350
418194,429	7300735,618	95	0,46	347
418245,075	7300709,656	95	0,34	6
418488,773	7302753,589	95	0,17	22
417787,631	7300492,431	95	1,38	0
418929,921	7301914,565	96	0,10	18
418979,389	7301929,795	96	0,21	0
418239,004	7302137,546	96	0,77	344
419026,376	7301844,656	96	0,16	354
418979,361	7301928,230	96	0,29	3
418659,745	7302515,100	96	0,49	13
418238,328	7302142,046	96	0,79	336
418311,219	7302728,325	96	0,16	168
418075,970	7301710,824	96	1,04	26
418075,299	7300967,064	96	0,41	32
418349,539	7302726,235	96	0,65	356
418090,569	7301073,672	96	0,15	15
418761,513	7302025,596	96	1,21	351
417783,158	7300575,916	96	1,21	20
418921,304	7301975,074	96	0,15	30
418043,957	7301495,580	96	0,44	6
418237,643	7302144,774	96	0,81	7
418072,523	7301040,612	96	0,73	16
418989,605	7301885,038	96	0,22	12
418242,089	7300740,966	96	1,24	8
418180,383	7300666,342	96	1,15	353
418998,153	7301940,950	96	0,27	22
418071,048	7301442,537	96	0,41	1
418810,136	7302060,729	96	0,92	24
418142,555	7302469,151	96	0,11	4
418080,224	7301034,862	96	0,32	11

418180,675	7301159,410	97	0,12	8
418047,585	7301502,569	97	0,23	3
418069,158	7301498,687	97	0,47	2
418179,960	7300667,898	97	1,62	10
418033,749	7300916,871	97	0,71	357
418202,344	7300762,952	97	1,79	49
418237,772	7302142,905	97	0,78	346
418921,081	7301975,002	97	0,20	10
419009,119	7301395,792	97	0,50	0
418998,279	7301940,678	97	0,25	5
418008,007	7301089,962	97	0,55	3
418056,083	7300830,389	97	0,52	35
419000,483	7301437,223	97	0,58	350
418998,408	7301941,335	97	0,16	2
418247,223	7300701,068	97	0,77	357
418071,183	7301442,254	97	0,38	3
418202,133	7300762,396	97	1,68	16
418237,907	7302144,888	97	0,78	7
418075,818	7301711,122	97	0,92	24
418194,498	7300735,904	97	0,49	47
419000,339	7301437,947	97	0,45	338
418075,771	7301710,932	97	0,85	22
418784,164	7302031,411	98	0,71	359
418071,638	7300977,263	98	1,16	9
418075,665	7300967,381	98	0,32	12
418043,752	7301495,382	98	0,44	13
418047,384	7301501,021	98	0,39	4
418354,164	7302541,234	98	0,54	15
418417,685	7300587,407	98	0,77	14
418979,442	7301928,473	98	0,23	12
418056,896	7300815,107	98	1,07	356
418080,358	7301036,471	98	0,38	3
418784,765	7302041,402	98	0,46	8
418359,151	7302681,518	98	0,95	359
418144,601	7300952,068	98	0,30	13
418056,632	7300813,265	98	1,35	2
418420,157	7302522,935	98	0,78	13
418783,312	7302027,099	98	0,32	2
418056,875	7300814,429	98	0,73	5
418003,678	7300806,213	98	0,59	1
418014,244	7300860,395	99	0,32	13
418208,974	7300577,316	99	0,64	0
418352,992	7302427,098	99	0,12	35
418671,281	7302559,143	99	0,22	19
418659,778	7302509,859	99	0,63	4
418223,847	7301974,508	99	0,39	329
418080,484	7301036,590	99	0,26	3

418221,845	7302110,443	99	0,10	33
418180,769	7301158,873	99	0,11	2
418072,325	7301039,731	99	1,01	14
418997,455	7301939,584	99	0,15	62
418662,099	7302523,544	99	0,29	7
418164,420	7300796,882	99	0,40	350
418470,785	7302447,936	99	0,60	345
418169,588	7300587,052	99	1,33	25
418488,856	7302752,345	99	0,12	6
418004,041	7301057,570	100	0,38	21
418082,463	7301040,759	100	0,58	5
418488,906	7302752,982	100	0,19	5
418005,799	7301065,853	100	0,32	354
418749,938	7302093,038	100	0,41	12
418218,628	7302102,386	100	0,55	12
418419,334	7302519,069	100	0,40	6
418203,826	7300764,460	100	1,21	14
418288,095	7302623,161	100	0,38	10
418046,428	7301521,705	100	0,23	9
418467,626	7302739,556	100	0,38	8
418082,824	7301041,725	100	0,71	36
417989,981	7300961,636	100	0,71	27
418470,579	7302448,629	100	0,59	8
418659,597	7302509,422	100	0,63	10
418082,433	7301041,150	100	0,62	15
418494,955	7302844,402	100	0,32	15
418749,831	7302093,201	100	0,44	12
418997,681	7301429,984	101	0,47	15
419013,323	7301430,750	101	0,94	339
418997,443	7301939,433	101	0,14	49
417787,439	7300493,063	101	1,63	8
418242,759	7300740,117	101	1,29	4
418056,611	7300816,260	101	1,14	10
418224,021	7301941,793	101	0,39	0
418146,021	7300956,417	101	0,28	352
418490,159	7302757,654	101	0,34	312
418081,818	7301039,221	101	0,63	18
418352,512	7302446,173	101	0,32	16
417997,743	7301039,876	101	0,35	22
418810,203	7302059,556	101	0,89	357
418082,889	7301041,415	101	0,80	23
418467,442	7302738,879	101	0,39	30
418081,706	7301039,096	101	0,61	20
418219,300	7302105,242	101	0,53	13
418056,971	7300816,684	101	1,27	0
418148,030	7300471,630	102	1,38	349
418218,770	7302103,473	102	0,55	6

418470,902	7302450,090	102	0,63	42
418072,563	7301039,278	102	0,86	17
418511,459	7302849,033	102	1,09	5
418467,621	7302739,086	102	0,35	17
418495,075	7302845,154	102	0,28	337
418074,493	7301418,680	102	0,54	359
418077,460	7301051,899	102	0,68	13
418659,452	7302509,673	102	0,66	16
419163,176	7301926,199	102	1,15	25
418145,337	7300953,957	102	0,25	18
418999,791	7301438,359	102	0,62	337
418997,269	7301939,399	102	0,11	33
418099,923	7301784,358	103	0,49	19
418081,782	7301039,354	103	0,67	18
418180,784	7301160,082	103	0,15	15
418480,595	7302850,097	103	0,45	10
418242,071	7300739,191	103	1,08	21
418467,768	7302740,158	103	0,36	12
418090,418	7301073,977	103	0,11	2
418144,940	7300952,222	103	0,33	14
418083,177	7301042,039	103	0,58	13
418086,906	7301066,457	103	0,62	16
418221,967	7302110,465	103	0,08	34
418089,485	7301060,906	103	1,84	15
419013,059	7301430,617	104	0,93	338
418692,182	7302679,034	104	0,64	25
417983,774	7300947,285	104	0,95	10
417969,484	7302146,593	104	0,53	36
418081,537	7301038,494	104	0,50	14
417803,170	7300537,774	104	1,72	12
418238,619	7302141,718	104	0,74	5
418989,427	7301884,978	104	0,22	23
418671,357	7302559,331	104	0,16	24
417995,164	7302220,034	104	0,49	11
419099,805	7301815,776	104	1,66	38
418071,565	7301697,092	104	0,98	21
418002,915	7301053,469	104	0,65	8
418354,300	7302415,889	104	0,27	354
418164,328	7300570,870	105	0,59	12
419168,965	7301934,273	105	1,46	21
418168,942	7300586,702	105	1,25	26
417970,045	7302146,842	105	0,62	38
417995,679	7301031,786	105	0,41	19
418145,443	7300954,232	105	0,36	21
417968,405	7302144,662	105	0,60	15
418089,619	7301058,380	105	1,97	8
419072,686	7301758,072	105	1,14	24

418489,683	7302758,009	105	0,26	349
418075,404	7300966,578	105	0,56	10
418942,525	7301980,045	105	0,42	19
419026,358	7301844,930	105	0,21	7
418493,728	7302876,919	105	1,00	16
418030,343	7300916,058	105	0,25	9
418483,813	7302826,719	106	0,30	14
418097,222	7302383,734	106	0,30	31
417997,941	7301038,461	106	0,44	12
418354,545	7302415,763	106	0,26	355
417794,539	7300702,114	106	0,58	26
418841,558	7301562,975	106	1,32	58
418038,322	7300871,527	106	0,55	8
418145,442	7300954,030	106	0,29	18
417998,805	7300978,639	106	1,38	18
418008,953	7301091,926	106	0,66	25
418692,190	7302678,823	106	0,62	26
418090,553	7301073,319	106	0,14	8
418046,638	7301521,800	106	0,14	8
418295,859	7300701,788	106	0,49	352
418030,375	7300915,369	107	0,19	0
418010,475	7301012,315	107	0,37	31
419072,372	7301759,060	107	1,14	23
419009,089	7301921,956	107	0,16	22
418003,236	7301054,022	107	0,50	27
417968,807	7302144,815	107	0,59	23
418706,146	7302687,475	107	1,30	19
419162,509	7301923,689	107	1,88	25
418899,582	7302041,926	107	0,64	29
418238,401	7302141,265	107	0,71	5
418095,351	7301772,113	107	0,57	22
418932,066	7301916,873	107	0,15	47
418009,535	7301093,329	108	0,69	20
417997,402	7302225,626	108	0,42	22
418090,183	7301062,017	108	1,92	15
418932,084	7301916,695	108	0,16	46
418002,155	7301051,524	108	0,43	37
419026,464	7301844,785	108	0,14	357
418086,529	7301066,306	108	0,73	32
418010,422	7301096,232	108	0,56	23
418660,193	7302551,333	108	0,10	22
418009,469	7301094,618	108	0,64	357
417990,045	7300962,327	108	0,87	36
419012,122	7301432,406	108	0,91	353
419163,025	7301922,815	108	1,42	25
417997,439	7301038,216	108	0,42	18
418005,256	7301060,297	108	0,58	17

417997,053	7302224,308	108	0,45	8
418845,368	7301568,612	109	1,12	39
418163,714	7300562,858	109	0,65	13
418141,958	7302467,416	109	0,10	40
419072,388	7301758,727	109	1,14	23
418007,450	7301074,457	109	0,69	11
418417,649	7302508,573	110	0,44	18
418858,943	7301591,978	110	0,55	45
418099,971	7301786,496	110	0,50	0
418847,551	7301570,779	110	1,11	57
418005,621	7301063,519	110	0,67	17
418672,159	7302562,190	110	0,24	15
418336,691	7302889,351	110	0,13	29
418260,030	7302483,685	110	0,32	13
418008,887	7301092,151	110	0,76	25
418003,200	7301054,217	110	0,49	28
418848,492	7301572,313	111	1,20	18
418659,389	7302509,174	111	0,64	1
418145,351	7300953,762	111	0,19	27
418074,176	7301429,991	111	0,63	16
418163,714	7300562,466	111	0,66	14
418660,344	7302551,923	111	0,11	24
418683,754	7302628,864	111	1,58	21
418845,281	7301567,977	111	0,92	38
418084,490	7301064,257	111	1,13	38
418005,907	7301063,821	111	0,67	17
418671,646	7302549,379	112	1,55	28
418929,346	7301912,145	112	0,17	25
418069,540	7301498,977	112	0,34	359
418260,192	7302484,518	112	0,30	20
418080,378	7301035,902	112	0,42	30
418996,388	7301427,480	112	0,35	26
418660,215	7302436,022	112	1,01	32
418009,926	7301095,591	112	0,56	38
418002,866	7300801,179	113	0,37	30
418998,029	7301430,232	113	0,48	15
418003,496	7300802,058	113	0,53	1
418086,437	7301065,869	113	0,53	42
418692,011	7302677,799	113	0,57	8
418007,268	7301073,921	113	0,48	17
418081,510	7301028,972	113	1,27	17
418671,221	7302558,683	113	0,17	17
419101,636	7301817,882	114	0,63	38
418035,682	7300960,120	114	0,63	12
418083,389	7301062,059	114	0,50	24
418089,064	7301056,794	114	2,37	21
418085,884	7301065,760	115	0,64	28

418010,005	7301094,155	116	0,34	339
418260,059	7302484,050	116	0,35	6
417795,453	7300703,200	117	0,39	32
418030,092	7300915,987	117	0,22	51
418086,631	7301072,163	118	0,27	6
419102,889	7301818,388	118	0,96	39
417795,505	7300702,842	118	0,45	24
418036,085	7300961,119	118	0,74	30
418002,845	7300801,484	119	0,46	29
418841,625	7301564,991	119	1,09	10
418657,826	7302584,235	119	0,67	33
418768,520	7301908,065	120	0,18	22
418658,524	7302585,810	120	0,75	30
418036,198	7300960,453	120	0,64	22
418002,747	7300801,150	120	0,34	28
418751,720	7302097,066	120	0,48	31
418848,218	7301571,200	120	1,17	32
418003,833	7300804,840	120	0,52	20
417992,501	7302211,223	120	0,52	24
418930,516	7301915,489	120	0,12	33
418007,198	7301124,573	121	0,36	20
418003,962	7300993,204	121	1,17	33
418930,503	7301915,363	121	0,10	45
418658,282	7302584,651	121	0,70	17
418171,705	7300592,132	121	1,82	17
418171,313	7300593,338	122	1,67	7
418396,747	7302737,671	123	0,68	36
418004,346	7300993,469	123	1,14	31
419019,634	7301939,151	124	0,18	46
419019,560	7301938,848	124	0,21	42
418006,157	7301065,980	125	0,15	0
418075,567	7301703,316	125	0,72	27
418992,801	7301894,989	125	0,40	15
418658,174	7302584,970	125	0,81	17
418669,182	7302572,766	125	0,52	19
418335,899	7302390,515	125	0,16	359
419103,111	7301819,108	126	1,12	39
418170,657	7300589,623	126	1,12	27
418006,995	7301124,577	127	0,32	36
418078,579	7301054,122	127	0,66	24
419073,533	7301762,313	128	0,93	23
418259,327	7302480,910	128	0,39	18
418996,024	7301425,709	129	0,56	26
418337,866	7302394,869	129	0,26	28
418077,441	7301052,914	130	0,96	33
418928,253	7301934,661	130	0,23	33
418078,627	7301054,487	131	0,61	27

418259,383	7302480,478	133	0,29	14
417992,858	7302213,251	133	0,75	38
419007,278	7301392,585	135	0,59	30
418074,092	7301700,360	136	1,44	28
418992,812	7301895,699	139	0,50	47
418338,229	7302395,409	142	0,35	60

Appendix 3

Examples of relocated earthquakes of the Yellowstone volcanic plateau

<i>Yr</i>	<i>Mo</i>	<i>Day</i>	<i>Hr</i>	<i>Mn</i>	<i>Sec</i>	<i>Lat</i>	<i>Lon</i>	<i>Mag</i>	<i>Depth</i>	<i>RMS</i>	<i>Nphs</i>	<i>Gap</i>	<i>Dist</i>
2010	1	1	4	6	14.27	44.893429	-110.849606	0.8	5.832031	0.073	10	173	15.4745
2010	1	1	6	24	21.74	44.671747	-110.45918	1.2	2.304688	0.171	17	71	6.17187
2010	1	1	7	30	52.10	44.751864	-111.174718	0.8	7.917969	0.169	13	114	1.69696
2010	1	2	12	3	48.59	44.719584	-110.960447	0.3	-0.220703	0.053	6	132	5.66983
2010	1	2	12	4	1.57	44.707138	-111.008303	0.2	5.826172	0.165	11	87	5.46709
2010	1	2	23	37	56.97	44.657357	-110.454152	0.3	0.998047	0.167	10	100	7.66254
2010	1	2	23	38	13.80	44.65269	-110.464375	1.1	1.232422	0.163	15	76	7.65686
2010	1	3	13	8	7.93	44.650357	-111.006481	1.2	5.498047	0.156	15	53	3.86335
2010	1	6	14	33	4.68	44.723862	-111.106959	0.3	2.996094	0.088	7	115	7.63853
2010	1	7	7	3	49.87	44.76742	-111.001891	1.6	3.394531	0.180	16	116	1.03184
2010	1	8	4	39	12.95	44.692749	-110.010793	1.4	11.667969	0.178	11	155	8.21171
2010	1	8	11	49	36.19	44.748364	-111.171156	1.5	6.248047	0.231	16	109	1.99115
2010	1	8	12	16	24.64	44.745641	-111.163671	0.0	4.121094	0.163	7	116	2.62543
2010	1	8	17	29	30.29	44.757698	-110.970017	0.5	8.169922	0.158	13	111	2.9071
2010	1	10	2	57	26.77	44.56674	-110.151838	0.6	5.386719	0.183	9	164	9.6064
2010	1	10	14	50	36.92	44.565573	-110.724097	1.4	2.392578	0.158	15	86	7.60942
2010	1	10	14	52	57.45	44.564795	-110.73193	1.9	2.826172	0.176	25	65	8.17887
2010	1	11	22	50	21.13	44.744474	-111.15384	0.3	1.994141	0.144	8	111	3.4104
2010	1	12	10	55	20.52	44.748752	-111.32872	0.2	3.886719	0.143	10	149	8.06467
2010	1	13	6	55	4.92	44.747586	-111.197868	0.0	6.751953	0.081	10	102	0.38572
2010	1	13	17	10	36.56	44.335335	-110.471387	1.0	6.775391	0.179	10	142	8.35274
2010	1	13	17	11	6.53	44.334946	-110.458515	0.1	5.574219	0.113	8	150	9.11878
2010	1	13	17	14	0.10	44.332223	-110.466721	0.4	6.810547	0.136	12	147	8.85979
2010	1	13	17	14	18.51	44.342724	-110.461597	0.3	0.933594	0.101	7	142	8.37135
2010	1	15	9	11	33.95	44.572185	-110.926616	1.6	5.820312	0.189	28	79	8.08489
2010	1	15	17	14	15.04	44.56324	-110.932464	0.9	6.669922	0.144	16	154	9.09212
2010	1	16	5	52	37.86	44.574129	-110.935632	1.7	7.560547	0.155	12	80	10.6471
2010	1	16	9	18	3.82	44.56674	-110.930516	1.2	7.730469	0.149	11	138	8.71548
2010	1	16	9	22	22.77	44.566351	-110.92229	0.5	8.111328	0.155	11	135	8.27184
2010	1	16	9	22	44.52	44.567129	-110.927776	1.3	7.361328	0.152	14	136	8.52557
2010	1	16	9	48	53.20	44.562851	-110.939121	0.8	7.273438	0.132	7	199	9.51298
2010	1	16	9	56	6.39	44.563628	-110.92894	1.0	6.699219	0.156	9	139	8.85986
2010	1	16	12	29	23.92	44.568295	-110.922687	0.8	7.730469	0.159	8	134	8.14284
2010	1	16	19	57	44.35	44.563628	-110.935207	0.7	7.378906	0.121	10	167	9.22327
2010	1	16	20	38	51.24	44.571407	-110.896059	1.3	7.472656	0.154	7	122	6.4949
2010	1	16	22	20	8.85	44.566351	-110.926207	1.3	3.904297	0.167	12	108	8.49389
2010	1	17	20	17	56.77	44.543794	-110.962943	1.0	9.822266	0.147	12	166	12.3347
2010	1	17	20	18	33.72	44.538738	-110.975844	0.3	8.457031	0.125	9	192	13.4708
2010	1	17	20	19	43.12	44.548461	-110.962177	0.7	8.767578	0.170	14	96	11.9426
2010	1	17	20	20	40.30	44.549239	-110.960613	0.5	8.802734	0.166	14	96	11.7923
2010	1	17	20	21	8.49	44.543405	-110.975862	0.3	8.738281	0.078	9	190	13.1332
2010	1	17	20	23	12.08	44.546905	-110.962954	1.3	8.380859	0.149	14	97	12.1031
2010	1	17	20	25	58.85	44.550016	-110.955917	0.7	9.025391	0.178	14	94	11.4565
2010	1	17	20	26	30.76	44.550016	-110.960616	0.7	8.767578	0.179	15	95	11.7357
2010	1	17	20	27	1.20	44.551572	-110.962188	0.9	8.744141	0.210	15	95	11.7186
2010	1	17	20	28	5.41	44.544183	-110.957854	1.2	9.335938	0.140	9	164	12.0113
2010	1	17	20	29	6.27	44.546516	-110.971175	0.3	8.339844	0.085	10	119	12.6261
2010	1	17	20	29	20.49	44.550794	-110.958269	0.4	8.568359	0.225	15	94	11.5385
2010	1	17	20	30	42.36	44.543016	-110.963723	0.7	10.080078	0.152	12	167	12.4388
2010	1	17	20	33	23.68	44.544183	-110.954722	0.7	9.382812	0.136	11	163	11.8335
2010	1	17	20	37	32.19	44.549627	-110.963356	0.8	10.683594	0.118	11	162	11.9287
2010	1	17	20	38	1.52	44.55235	-110.963757	2.1	9.189453	0.168	27	95	11.7596
2010	1	17	20	39	2.22	44.548072	-110.966482	0.5	9.863281	0.137	12	165	12.2298
2010	1	17	20	40	0.25	44.546127	-110.962951	0.6	9.001953	0.158	14	97	12.1605
2010	1	17	20	49	50.08	44.557017	-110.959858	0.8	10.443359	0.130	12	92	11.1941
2010	1	17	20	50	17.49	44.551572	-110.963754	1.9	9.142578	0.169	24	95	11.8142
2010	1	17	20	51	7.19	44.546905	-110.967653	0.5	10.197266	0.129	12	166	12.3845
2010	1	17	20	56	36.58	44.552739	-110.964933	2.0	9.230469	0.154	21	95	11.805
2010	1	17	20	58	37.27	44.551572	-110.964537	0.7	8.322266	0.184	16	96	11.8622
2010	1	17	21	1	45.77	44.551183	-110.961795	1.2	8.597656	0.156	14	95	11.7225
2010	1	17	21	4	6.24	44.551183	-110.964928	2.5	9.136719	0.153	24	96	11.9136
2010	1	17	21	9	45.32	44.543794	-110.962943	0.3	8.919922	0.153	12	166	12.3347

<i>Yr</i>	<i>Mo</i>	<i>Day</i>	<i>Hr</i>	<i>Mn</i>	<i>Sec</i>	<i>Lat</i>	<i>Lon</i>	<i>Mag</i>	<i>Depth</i>	<i>RMS</i>	<i>Nphs</i>	<i>Gap</i>	<i>Dist</i>
2010	1	17	21	10	7.02	44.54885	-110.965702	0.9	9.640625	0.184	13	164	12.1267
2010	1	17	21	15	55.69	44.55235	-110.96454	1.5	9.224609	0.157	21	95	11.8078
2010	1	17	21	18	59.75	44.551572	-110.958272	0.5	9.412109	0.136	10	94	11.4819
2010	1	17	21	24	45.61	44.55235	-110.96454	1.1	9.037109	0.164	18	95	11.8078
2010	1	17	21	25	26.93	44.548461	-110.963743	0.9	9.212891	0.166	16	97	12.0364
2010	1	17	21	25	47.75	44.546516	-110.969609	1.0	9.441406	0.129	12	167	12.2812
2010	1	17	21	38	25.45	44.550794	-110.966101	0.8	8.310547	0.192	15	96	12.013
2010	1	17	21	39	1.56	44.541071	-110.966032	0.7	6.007812	0.185	11	178	11.5704
2010	1	17	21	41	40.43	44.549239	-110.962179	0.9	8.908203	0.155	14	96	11.886
2010	1	17	21	55	33.68	44.557406	-110.957118	0.2	9.652344	0.210	7	91	10.9969
2010	1	17	21	55	54.89	44.550794	-110.962185		7.947266	0.154	10	95	11.774
2010	1	17	21	55	58.04	44.550794	-110.965318	2.5	8.943359	0.189	16	96	11.9649
2010	1	17	21	58	14.38	44.545349	-110.965298	0.7	9.306641	0.162	14	166	12.357
2010	1	17	21	58	49.58	44.551183	-110.963361	0.9	9.417969	0.148	12	141	11.8178
2010	1	17	22	0	33.30	44.554683	-110.962199	1.3	10.197266	0.147	17	94	11.5006
2010	1	17	22	1	3.74	44.552739	-110.963367	1.9	8.550781	0.176	22	95	11.7083
2010	1	17	22	5	28.13	44.555461	-110.964552	0.6	9.541016	0.132	14	94	11.5942
2010	1	17	22	5	49.40	44.54885	-110.965702	0.5	9.921875	0.192	14	164	12.1267
2010	1	17	22	6	26.07	44.553128	-110.965326	0.5	9.564453	0.135	16	95	11.8024
2010	1	17	22	6	41.27	44.547683	-110.96374	0.3	10.302734	0.181	12	164	12.0929
2010	1	17	22	8	2.99	44.557017	-110.966124	1.2	9.365234	0.174	20	94	11.5892
2010	1	17	22	8	27.15	44.54496	-110.968037	0.7	9.675781	0.184	14	167	12.4789
2010	1	17	22	15	9.31	44.553128	-110.96611	0.2	9.880859	0.136	14	161	11.8511
2010	1	17	22	16	15.03	44.553906	-110.972378	1.0	9.693359	0.141	16	163	11.6717
2010	1	17	22	16	52.39	44.555461	-110.966118	0.4	8.826172	0.165	13	95	11.6928
2010	1	17	22	18	56.02	44.557795	-110.965344	1.7	9.833984	0.155	26	93	11.488
2010	1	17	22	24	47.19	44.558573	-110.962997	1.2	9.716797	0.136	23	92	11.287
2010	1	17	22	30	32.49	44.557795	-110.967693	1.3	10.408203	0.134	22	94	11.6385
2010	1	17	22	32	37.39	44.558573	-110.96613	1.1	9.681641	0.133	15	93	11.4874
2010	1	17	22	36	18.67	44.557406	-110.963384	0.8	10.097656	0.153	16	93	11.3894
2010	1	17	22	43	32.74	44.552739	-110.968066	2.3	8.832031	0.159	25	96	11.9999
2010	1	17	22	47	49.09	44.560128	-110.963002	0.5	9.271484	0.156	12	92	11.1851
2010	1	17	22	48	2.67	44.54496	-110.964905	1.2	10.027344	0.224	17	98	12.3625
2010	1	17	22	48	37.74	44.55235	-110.954359	0.2	8.205078	0.220	11	93	11.1914
2010	1	17	22	55	5.59	44.556628	-110.964165	0.8	9.195312	0.137	14	94	11.4909
2010	1	17	22	58	9.88	44.557795	-110.962994	2.0	10.021484	0.135	27	93	11.3386
2010	1	17	23	0	54.08	44.549627	-110.949259	0.3	8.644531	0.186	13	92	11.1003
2010	1	17	23	1	15.58	44.550405	-110.961009	1.0	9.101562	0.171	14	95	11.731
2010	1	17	23	5	25.00	44.560517	-110.966529	0.2	9.324219	0.143	14	93	11.3879
2010	1	17	23	6	1.58	44.558573	-110.95908	1.3	9.611328	0.172	22	91	11.0393
2010	1	17	23	6	42.03	44.550405	-110.961009		9.476562	0.120	11	161	11.731
2010	1	17	23	13	8.38	44.558573	-110.959864	0.9	9.623047	0.126	16	92	11.0886
2010	1	17	23	13	42.20	44.554683	-110.961416	0.1	8.966797	0.124	11	94	11.4521
2010	1	17	23	17	42.31	44.558184	-110.962604	1.5	10.34375	0.135	17	92	11.2879
2010	1	17	23	18	3.51	44.553128	-110.970809	0.5	8.041016	0.135	12	142	11.8222
2010	1	17	23	19	38.09	44.556239	-110.968471	0.2	8.955078	0.150	11	117	11.7903
2010	1	17	23	19	52.06	44.55585	-110.972777	0.3	8.761719	0.168	10	118	12.092
2010	1	17	23	29	6.55	44.546905	-110.971568	1.5	8.826172	0.177	17	146	12.1273
2010	1	17	23	29	43.96	44.545349	-110.963731	0.3	9.177734	0.128	12	165	12.2643
2010	1	17	23	31	20.72	44.550794	-110.959052	1.7	9.001953	0.165	22	95	11.5853
2010	1	17	23	35	49.79	44.558573	-110.962997	2.0	9.904297	0.149	28	92	11.287
2010	1	17	23	37	18.02	44.54496	-110.971169	0.3	8.832031	0.127	8	176	12.7371
2010	1	17	23	37	55.57	44.551572	-110.966104	1.7	10.162109	0.137	20	171	11.9586
2010	1	17	23	49	59.15	44.550794	-110.964535	0.4	9.927734	0.101	11	162	11.917
2010	1	17	23	50	31.70	44.541849	-110.952364	1.1	8.433594	0.142	7	218	11.8874
2010	1	18	1	1	45.62	44.551183	-110.963361	1.1	8.363281	0.174	16	96	11.8178
2010	1	18	1	4	23.79	44.556239	-110.963771	2.3	8.287109	0.161	23	94	11.4924
2010	1	18	1	6	19.97	44.551183	-110.964928	0.9	7.660156	0.193	13	96	11.9136
2010	1	18	1	6	40.69	44.55235	-110.966107	1.2	9.412109	0.210	17	96	11.9047
2010	1	18	1	8	6.13	44.549627	-110.961789	0.5	8.433594	0.176	12	96	11.8343
2010	1	18	1	8	42.57	44.551572	-110.971586	0.8	7.408203	0.208	15	98	11.8554
2010	1	18	1	14	31.45	44.553128	-110.968459	1.5	8.380859	0.186	25	96	11.9842

<i>Yr</i>	<i>Mo</i>	<i>Day</i>	<i>Hr</i>	<i>Mn</i>	<i>Sec</i>	<i>Lat</i>	<i>Lon</i>	<i>Mag</i>	<i>Depth</i>	<i>RMS</i>	<i>Nphs</i>	<i>Gap</i>	<i>Dist</i>
2010	1	18	1	36	15.86	44.558573	-110.960647	1.5	10.044922	0.138	18	92	11.138
2010	1	18	1	37	14.05	44.550794	-110.966884	1.1	8.275391	0.219	14	97	12.0612
2010	1	18	1	50	7.28	44.551183	-110.96806	0.8	9.066406	0.122	11	163	12.1067
2010	1	18	1	52	52.60	44.556239	-110.963771	1.2	8.802734	0.177	18	94	11.4924
2010	1	18	1	53	55.63	44.554294	-110.968072	1.0	9.933594	0.126	13	161	11.8946
2010	1	18	1	54	58.85	44.554294	-110.966506	1.5	9.300781	0.137	11	95	11.7961
2010	1	18	1	58	10.19	44.555072	-110.965725	1.8	9.265625	0.180	21	95	11.6943
2010	1	18	2	4	1.70	44.557406	-110.968084	0.3	8.878906	0.139	14	105	11.6889
2010	1	18	2	23	39.03	44.557795	-110.965344	1.2	9.880859	0.147	21	93	11.488
2010	1	18	2	24	20.04	44.554294	-110.96024	1.0	10.144531	0.136	20	93	11.4068
2010	1	18	2	29	19.65	44.55585	-110.966511	1.3	9.699219	0.141	23	94	11.6915
2010	1	18	2	38	0.45	44.556239	-110.968471	2.7	8.720703	0.175	28	95	11.7903
2010	1	18	2	39	19.48	44.560128	-110.966136	1.1	9.259766	0.138	17	93	11.3872
2010	1	18	2	44	15.10	44.549627	-110.964922	0.2	10.378906	0.095	8	171	12.0236
2010	1	18	2	44	36.00	44.551183	-110.963361	2.4	9.113281	0.166	23	96	11.8178
2010	1	18	2	45	32.60	44.549627	-110.963356	1.0	10.308594	0.085	10	162	11.9287
2010	1	18	2	47	9.50	44.553906	-110.959847	0.2	10.525391	0.137	11	94	11.4101
2010	1	18	2	48	55.96	44.558961	-110.971223	0.2	9.464844	0.138	11	94	11.4873
2010	1	18	2	49	11.72	44.560906	-110.969272	0.2	9.576172	0.169	11	93	11.5305
2010	1	18	2	50	18.14	44.548461	-110.964526	0.9	10.080078	0.151	11	163	12.0835
2010	1	18	2	50	46.55	44.546905	-110.969219	0.7	9.599609	0.141	12	167	12.2843
2010	1	18	2	53	12.33	44.544183	-110.964119	1.4	12.617188	0.106	11	166	12.3742
2010	1	18	3	8	16.96	44.562851	-110.967321	0.3	10.320312	0.141	13	92	11.2936
2010	1	18	3	14	9.31	44.543794	-110.955895	0.6	9.705078	0.217	13	163	11.9301
2010	1	18	3	15	16.63	44.551572	-110.962971	1.4	8.837891	0.197	22	95	11.7663
2010	1	18	3	17	48.18	44.554294	-110.969638	0.7	9.511719	0.154	15	96	11.8399
2010	1	18	3	35	12.96	44.556628	-110.97043	0.2	8.867188	0.160	11	95	11.6619
2010	1	18	3	36	59.47	44.55235	-110.959841	0.8	9.681641	0.149	15	94	11.5204
2010	1	18	3	53	0.04	44.546516	-110.966477	0.9	10.800781	0.140	11	166	12.3419
2010	1	18	3	57	58.49	44.55235	-110.959058	1.3	10.326172	0.164	14	94	11.473
2010	1	18	4	4	48.26	44.554683	-110.964549	1.6	9.072266	0.186	19	94	11.647
2010	1	18	4	18	5.80	44.546516	-110.963344	0.7	10.144531	0.164	12	164	12.155
2010	1	18	4	18	37.91	44.546905	-110.96452	0.8	9.775391	0.146	12	165	12.1964
2010	1	18	4	35	15.27	44.552739	-110.960234	1.0	8.785156	0.157	10	94	11.5165
2010	1	18	4	36	18.18	44.550794	-110.960619	0.7	9.681641	0.157	18	95	11.6794
2010	1	18	5	6	37.58	44.558573	-110.970829	0.5	9.013672	0.149	15	95	11.5345
2010	1	18	5	21	17.49	44.55235	-110.958275	0.3	9.470703	0.148	16	94	11.4257
2010	1	18	5	43	36.41	44.557795	-110.96926	1.2	9.529297	0.144	22	94	11.6843
2010	1	18	5	44	34.17	44.558573	-110.970829	0.4	8.943359	0.138	15	95	11.5345
2010	1	18	5	51	56.98	44.553906	-110.95828	1.2	9.646484	0.146	19	93	11.3144
2010	1	18	5	53	8.88	44.557017	-110.964558	0.8	9.189453	0.199	17	93	11.4897
2010	1	18	5	54	53.16	44.555461	-110.964552	0.9	9.001953	0.187	19	94	11.5942
2010	1	18	5	55	4.76	44.553906	-110.959847	1.9	9.353516	0.164	19	94	11.4101
2010	1	18	5	58	17.21	44.553128	-110.96611	1.7	8.158203	0.172	19	95	11.8511
2010	1	18	6	1	30.86	44.550016	-110.962182	1.1	8.521484	0.169	14	96	11.8298
2010	1	18	6	3	19.54	44.554294	-110.971205	1.2	8.457031	0.170	17	96	11.7315
2010	1	18	6	11	39.43	44.559739	-110.967309	0.6	9.664062	0.137	17	93	11.4882
2010	1	18	6	16	8.63	44.55935	-110.965349	0.8	9.751953	0.122	21	93	11.3866
2010	1	18	6	18	28.25	44.55935	-110.965349	0.1	9.693359	0.158	16	93	11.3866
2010	1	18	6	31	35.83	44.557795	-110.96691	0.6	9.787109	0.130	18	94	11.5882
2010	1	18	6	46	44.34	44.559739	-110.970442	1.3	9.523438	0.134	20	94	11.5039
2010	1	18	6	54	7.52	44.561684	-110.970841	0.0	9.142578	0.163	13	93	11.3813
2010	1	18	7	45	29.74	44.550794	-110.966884	0.7	9.365234	0.151	17	97	12.0612
2010	1	18	7	46	32.89	44.56324	-110.968497	0.0	10.033203	0.164	12	92	11.3476
2010	1	18	7	53	8.79	44.554683	-110.966899	0.3	8.955078	0.145	14	95	11.7944
2010	1	18	8	2	50.52	44.553517	-110.967286	1.0	9.523438	0.131	20	96	11.8979
2010	1	18	8	3	20.78	44.552739	-110.968066	0.6	9.300781	0.127	17	96	11.9999
2010	1	18	8	4	34.59	44.554683	-110.967682	2.0	9.623047	0.160	24	95	11.8438
2010	1	18	8	7	41.26	44.560906	-110.961439	0.5	9.681641	0.149	11	91	11.0339
2010	1	18	8	14	30.16	44.55585	-110.963378	0.9	10.167969	0.123	22	94	11.4941
2010	1	18	8	16	52.68	44.557017	-110.961425	0.4	9.939453	0.132	18	93	11.2921
2010	1	18	8	17	24.49	44.557406	-110.968084	0.3	9.464844	0.141	14	94	11.6889

<i>Yr</i>	<i>Mo</i>	<i>Day</i>	<i>Hr</i>	<i>Mn</i>	<i>Sec</i>	<i>Lat</i>	<i>Lon</i>	<i>Mag</i>	<i>Depth</i>	<i>RMS</i>	<i>Nphs</i>	<i>Gap</i>	<i>Dist</i>
2010	1	18	8	21	55.82	44.556239	-110.966904	1.0	9.517578	0.158	20	94	11.6905
2010	1	18	8	23	57.18	44.558573	-110.967696	0.1	9.306641	0.134	15	94	11.5882
2010	1	18	8	25	32.57	44.552739	-110.958668	0.9	10.707031	0.144	11	94	11.4214
2010	1	18	8	26	12.26	44.553517	-110.96102	1.1	8.820312	0.182	17	94	11.5094
2010	1	18	8	26	32.53	44.546127	-110.958253	1.0	8.966797	0.192	15	96	11.8855
2010	1	18	8	32	23.42	44.550405	-110.957876	0.7	10.507812	0.181	12	94	11.5436
2010	1	18	8	32	52.10	44.557017	-110.97004	1.5	9.037109	0.183	21	95	11.6691
2010	1	18	9	13	33.61	44.558573	-110.965347	1.3	9.048828	0.172	22	93	11.4371
2010	1	18	9	18	9.35	44.560128	-110.961436	1.8	10.478516	0.141	25	91	11.0847
2010	1	18	9	20	25.86	44.558573	-110.955164	0.1	10.349609	0.200	14	90	10.7949
2010	1	18	9	55	55.24	44.553906	-110.96063	0.6	9.365234	0.152	12	94	11.4581
2010	1	18	10	10	21.80	44.555461	-110.965335	1.7	9.212891	0.146	17	94	11.6434
2010	1	18	10	10	41.35	44.554294	-110.968072	3.1	8.996094	0.196	23	96	11.8946
2010	1	18	10	11	24.38	44.55585	-110.963378	0.8	9.277344	0.181	20	94	11.4941
2010	1	18	10	15	47.85	44.553906	-110.966112	0.7	8.380859	0.191	15	105	11.7979
2010	1	18	10	15	58.72	44.548072	-110.980579	0.4	7.636719	0.108	10	177	13.1031
2010	1	18	10	24	26.51	44.549239	-110.962179	0.9	8.908203	0.190	15	96	11.886
2010	1	18	10	25	39.67	44.552739	-110.963367	0.9	8.105469	0.209	11	117	11.7083
2010	1	18	10	42	27.62	44.547294	-110.957865	0.8	8.820312	0.220	14	95	11.7747
2010	1	18	10	52	20.64	44.560128	-110.966136	1.1	9.423828	0.138	15	93	11.3872
2010	1	18	10	54	36.30	44.557795	-110.96691	0.6	9.083984	0.125	12	105	11.5882
2010	1	18	10	57	31.73	44.554294	-110.952408	0.3	9.839844	0.171	9	114	10.9323
2010	1	18	11	3	28.41	44.551572	-110.955139	0.7	9.728516	0.138	12	93	11.2951
2010	1	18	11	22	43.83	44.549627	-110.942994	0.9	7.964844	0.196	9	116	13.3273
2010	1	18	11	50	34.88	44.554683	-110.962983	1.2	10.068359	0.127	21	94	11.5493
2010	1	18	11	56	12.33	44.556239	-110.968471	1.9	9.072266	0.144	25	95	11.7903
2010	1	18	11	58	27.03	44.558573	-110.96848	1.0	9.505859	0.152	21	94	11.6388
2010	1	18	12	6	8.04	44.569462	-110.949719	0.6	11.556641	0.271	11	90	9.726
2010	1	18	12	8	41.73	44.55935	-110.96065	0.4	7.830078	0.193	13	92	11.0861
2010	1	18	12	9	9.65	44.558184	-110.950071	0.1	10.71875	0.180	13	92	10.51
2010	1	18	12	29	17.59	44.557795	-110.96691	0.1	9.365234	0.136	15	94	11.5882
2010	1	18	12	29	39.48	44.55935	-110.970049	0.4	9.787109	0.191	15	94	11.5509
2010	1	18	12	53	29.16	44.55585	-110.968078	0.9	8.972656	0.202	24	95	11.791
2010	1	18	12	55	6.14	44.549627	-110.961789	0.8	9.300781	0.137	16	96	11.8343
2010	1	18	12	59	55.18	44.557795	-110.968477	1.5	9.330078	0.150	26	94	11.6889
2010	1	18	13	0	55.09	44.55935	-110.970049	0.6	9.435547	0.149	15	94	11.5509
2010	1	18	13	7	16.44	44.557017	-110.963774	0.7	10.021484	0.150	18	93	11.4401
2010	1	18	13	10	25.38	44.565573	-110.963806	0.2	10.349609	0.112	16	90	10.8943
2010	1	18	13	12	45.50	44.556239	-110.965338	0.3	9.212891	0.158	13	94	11.5912
2010	1	18	13	13	6.42	44.575685	-110.959142	0.1	11.580078	0.129	11	142	9.99748
2010	1	18	13	16	12.44	44.562462	-110.973194	1.2	9.376953	0.140	24	93	11.1762
2010	1	18	13	23	57.19	44.560128	-110.970835	1.4	9.787109	0.142	24	94	11.4569
2010	1	18	13	25	50.90	44.55935	-110.968483	1.2	9.974609	0.124	22	94	11.5892
2010	1	18	13	29	35.46	44.563628	-110.969674	0.5	10.402344	0.096	18	92	11.3746
2010	1	18	13	41	17.77	44.559739	-110.970442	0.5	10.179688	0.122	16	94	11.5039
2010	1	18	14	12	8.66	44.56324	-110.972414		10.103516	0.122	11	93	11.1954
2010	1	18	14	12	14.74	44.536404	-110.97192	0.6	11.046875	0.197	8	172	12.7703
2010	1	18	14	28	0.22	44.571018	-110.964609	0.1	11.041016	0.105	13	99	10.6304
2010	1	18	14	28	10.26	44.575685	-110.96776	0.3	11.298828	0.134	12	96	10.3342
2010	1	18	14	28	45.12	44.564795	-110.963803	0.9	11.064453	0.106	20	90	10.9416
2010	1	18	14	41	16.74	44.566351	-110.961458	0.3	10.888672	0.190	17	89	10.6913
2010	1	18	14	41	52.10	44.562462	-110.963011	0.8	10.736328	0.119	20	91	11.0354
2010	1	18	14	44	15.07	44.558961	-110.966523	1.0	9.699219	0.151	24	93	11.4874
2010	1	18	14	45	15.05	44.55935	-110.969266	0.7	10.220703	0.103	16	94	11.6064
2010	1	18	14	54	9.28	44.561684	-110.961442	0.3	10.970703	0.111	16	91	10.9836
2010	1	18	14	56	51.17	44.568684	-110.966951	0.4	10.853516	0.090	11	116	10.9222
2010	1	18	14	57	8.63	44.560128	-110.959086	1.0	10.455078	0.149	15	91	10.9351
2010	1	18	15	12	40.56	44.565573	-110.970856	0.3	9.904297	0.105	13	91	11.2019
2010	1	18	15	16	24.14	44.566351	-110.971642	0.5	10.021484	0.095	12	91	11.1106
2010	1	18	15	17	3.09	44.56324	-110.97163	1.7	9.775391	0.132	24	93	11.2516
2010	1	18	15	32	15.83	44.55935	-110.967699	1.3	10.091797	0.153	23	93	11.5384
2010	1	18	15	35	0.02	44.565184	-110.955579	0.8	10.238281	0.118	18	88	10.3793

<i>Yr</i>	<i>Mo</i>	<i>Day</i>	<i>Hr</i>	<i>Mn</i>	<i>Sec</i>	<i>Lat</i>	<i>Lon</i>	<i>Mag</i>	<i>Depth</i>	<i>RMS</i>	<i>Nphs</i>	<i>Gap</i>	<i>Dist</i>
2010	1	18	15	38	37.02	44.562462	-110.973194	0.0	9.646484	0.091	12	145	11.1762
2010	1	18	15	39	4.90	44.565573	-110.971639	0.8	9.880859	0.116	16	92	11.145
2010	1	18	15	43	55.25	44.566351	-110.959108	0.1	11.943359	0.106	11	147	10.536
2010	1	18	15	44	7.40	44.56674	-110.958718	0.4	12.347656	0.095	10	147	10.4863
2010	1	18	16	0	13.52	44.557017	-110.967691	2.4	9.318359	0.127	23	94	11.6892
2010	1	18	16	0	56.40	44.55585	-110.964945	1.5	7.707031	0.033	6	245	11.5926
2010	1	18	16	2	32.11	44.557795	-110.970826	0.3	9.400391	0.107	10	148	11.5741
2010	1	18	16	9	2.40	44.557795	-110.966127	1.6	10.642578	0.098	16	94	11.5381
2010	1	18	16	19	3.40	44.564795	-110.963803	1.3	10.513672	0.128	17	90	10.9416
2010	1	18	16	27	4.26	44.562462	-110.965361	1.9	10.935547	0.093	20	91	11.1889
2010	1	18	16	27	41.90	44.557795	-110.962211	0.0	9.611328	0.083	11	125	11.2891
2010	1	18	16	30	4.15	44.555072	-110.965725	1.1	9.453125	0.130	16	95	11.6943
2010	1	18	16	34	33.46	44.558573	-110.96143	1.2	11.146484	0.117	13	139	11.1876
2010	1	18	16	47	21.88	44.564795	-110.964586	2.2	11.099609	0.127	17	103	10.9935
2010	1	18	16	49	54.40	44.564017	-110.974767	0.9	10.044922	0.117	15	93	10.9902
2010	1	18	17	20	0.40	44.563628	-110.96654	1.0	10.707031	0.095	19	91	11.1942
2010	1	18	17	20	27.46	44.558961	-110.968089	0.5	10.261719	0.142	15	94	11.5886
2010	1	18	17	31	37.18	44.56324	-110.966931	1.7	10.021484	0.136	24	91	11.2439
2010	1	18	17	37	22.53	44.563628	-110.968107	0.4	9.769531	0.094	15	92	11.298
2010	1	18	18	3	13.82	44.555461	-110.968468	2.8	9.763672	0.129	23	95	11.8416
2010	1	18	18	6	47.77	44.550794	-110.966101	0.2	9.189453	0.140	13	96	12.013
2010	1	18	18	14	22.23	44.557795	-110.970043	0.2	9.470703	0.143	14	95	11.6292
2010	1	18	18	38	7.66	44.55585	-110.968078	1.3	10.121094	0.098	16	95	11.791
2010	1	18	18	39	48.20	44.558573	-110.966913	0.8	9.927734	0.076	10	149	11.5377
2010	1	18	18	44	34.14	44.556239	-110.968471	1.8	10.326172	0.109	20	95	11.7903
2010	1	18	18	47	45.21	44.556239	-110.970037	2.6	9.517578	0.148	21	95	11.7095
2010	1	18	18	49	27.34	44.553128	-110.966893	1.0	9.611328	0.088	14	96	11.9
2010	1	18	18	50	2.31	44.55935	-110.966133	0.7	10.056641	0.105	13	93	11.4371
2010	1	18	18	51	18.74	44.562073	-110.961835	1.0	10.800781	0.078	10	148	10.9839
2010	1	18	18	53	20.33	44.557795	-110.967693	1.6	10.794922	0.097	17	94	11.6385
2010	1	18	18	55	27.81	44.567906	-110.968515	0.8	10.056641	0.067	10	143	11.073
2010	1	18	18	58	25.76	44.549239	-110.969228	0.9	10.080078	0.097	13	98	12.1481
2010	1	18	18	58	49.04	44.608743	-110.957301	0.2	8.949219	0.139	6	119	6.68444
2010	1	18	19	3	41.82	44.55935	-110.970049	0.9	9.751953	0.065	10	147	11.5509
2010	1	18	19	4	46.50	44.560906	-110.962222	1.9	10.279297	0.118	19	91	11.0843
2010	1	18	19	12	43.86	44.565962	-110.967332	0.8	10.179688	0.105	11	145	11.1063
2010	1	18	19	16	22.26	44.561684	-110.969275	1.9	9.833984	0.125	25	93	11.4934
2010	1	18	19	20	4.05	44.55935	-110.964566	1.4	10.642578	0.097	11	104	11.3362
2010	1	18	19	22	52.12	44.572573	-110.975583	1.1	10.619141	0.078	10	95	10.5652
2010	1	18	19	24	34.02	44.554683	-110.962983	0.6	10.384766	0.109	21	94	11.5493
2010	1	18	19	31	12.35	44.562462	-110.964578	1.3	10.115234	0.147	21	91	11.1376
2010	1	18	19	33	58.46	44.560128	-110.963002	1.5	9.927734	0.132	13	92	11.1851
2010	1	18	19	38	41.55	44.560128	-110.962219	2.6	10.595703	0.135	26	92	11.1348
2010	1	18	19	39	45.19	44.57024	-110.955205	0.9	10.630859	0.139	17	138	10.04
2010	1	18	19	42	18.59	44.558573	-110.964563	1.2	9.224609	0.191	16	93	11.3869
2010	1	18	19	48	21.11	44.569462	-110.965387	0.2	10.162109	0.120	12	143	10.7714
2010	1	18	19	52	0.63	44.560128	-110.963786	0.3	11.169922	0.189	13	104	11.2354
2010	1	18	19	52	17.00	44.564795	-110.963803	0.6	11.181641	0.104	12	146	10.9416
2010	1	18	19	54	50.55	44.553906	-110.968462	0.5	9.716797	0.132	12	96	11.9422
2010	1	18	19	56	7.81	44.54496	-110.986831	0.3	7.027344	0.106	8	170	13.7073
2010	1	18	19	58	29.95	44.575685	-110.977946	0.2	9.763672	0.172	13	88	10.2733
2010	1	18	20	1	5.38	44.564017	-110.964583	0.3	10.525391	0.139	16	90	11.041
2010	1	18	20	1	58.36	44.559739	-110.967309	0.5	10.085938	0.165	19	93	11.4882
2010	1	18	20	2	20.93	44.564017	-110.9591	0.4	10.748047	0.122	14	89	10.6822
2010	1	18	20	5	16.15	44.558573	-110.96613	0.7	10.478516	0.124	18	93	11.4874
2010	1	18	20	8	9.31	44.56324	-110.973197	1.0	9.552734	0.165	23	93	11.1392
2010	1	18	20	10	31.57	44.565184	-110.96968	0.6	10.519531	0.104	17	91	11.3044
2010	1	18	20	12	39.50	44.554683	-110.960633	0.6	9.681641	0.212	20	93	11.4037
2010	1	18	20	17	38.10	44.557795	-110.965344	0.5	11.099609	0.132	12	149	11.488
2010	1	18	20	19	28.59	44.560517	-110.963396	0.4	10.730469	0.107	11	149	11.1851
2010	1	18	20	21	46.93	44.55235	-110.96454	0.7	9.470703	0.117	13	106	11.8078
2010	1	18	20	33	36.30	44.565573	-110.971639	0.8	10.115234	0.075	12	143	11.145

<i>Yr</i>	<i>Mo</i>	<i>Day</i>	<i>Hr</i>	<i>Mn</i>	<i>Sec</i>	<i>Lat</i>	<i>Lon</i>	<i>Mag</i>	<i>Depth</i>	<i>RMS</i>	<i>Nphs</i>	<i>Gap</i>	<i>Dist</i>
2010	1	18	20	40	17.00	44.561684	-110.971625	1.5	10.103516	0.116	13	93	11.3254
2010	1	18	20	43	48.30	44.560906	-110.962222	1.3	11.158203	0.104	14	91	11.0843
2010	1	18	20	46	2.94	44.560128	-110.962219	2.3	10.783203	0.135	22	92	11.1348
2010	1	18	20	47	30.44	44.560128	-110.962219	1.3	10.736328	0.119	15	124	11.1348
2010	1	18	20	50	48.27	44.555461	-110.965335	2.1	10.162109	0.140	25	94	11.6434
2010	1	18	20	59	9.34	44.560517	-110.979061	0.9	10.636719	0.066	8	144	12.071
2010	1	18	21	1	17.03	44.562462	-110.973977	2.1	9.763672	0.115	21	94	11.1203
2010	1	18	21	3	9.22	44.579574	-110.960723	1.5	9.775391	0.243	17	82	9.90412
2010	1	18	21	5	6.99	44.553906	-110.96063	0.9	9.611328	0.082	13	126	11.4581
2010	1	18	21	5	19.77	44.558573	-110.951248	0.4	10.970703	0.140	12	153	10.5538
2010	1	18	21	5	30.75	44.565184	-110.97438	1.0	8.902344	0.084	11	143	10.9643
2010	1	18	21	11	33.84	44.558573	-110.96143	1.4	10.220703	0.138	24	92	11.1876
2010	1	18	21	15	2.78	44.558573	-110.965347	0.2	10.302734	0.087	12	149	11.4371
2010	1	18	21	17	29.07	44.560128	-110.967702	2.1	10.044922	0.138	24	93	11.4889
2010	1	18	21	19	10.32	44.56324	-110.959881	0.6	11.216797	0.122	20	90	10.7825
2010	1	18	21	24	19.77	44.560128	-110.966919	0.1	10.900391	0.117	12	93	11.438
2010	1	18	21	34	9.11	44.557795	-110.970043	0.9	9.669922	0.098	12	148	11.6292
2010	1	18	21	34	53.04	44.548072	-110.964916		10.730469	0.109	10	250	12.1352
2010	1	18	21	45	36.39	44.560906	-110.970055	0.4	9.939453	0.103	14	93	11.4746
2010	1	18	21	59	55.41	44.560906	-110.970055	1.9	10.150391	0.127	21	93	11.4746
2010	1	18	22	5	16.32	44.558573	-110.96378	0.8	10.326172	0.113	13	150	11.3369
2010	1	18	22	5	44.53	44.561684	-110.966141	0.0	9.763672	0.101	11	147	11.2888
2010	1	18	22	20	9.02	44.557017	-110.962208	0.6	10.337891	0.122	13	151	11.3414
2010	1	18	22	20	21.80	44.558961	-110.96339	0.3	10.074219	0.103	11	149	11.2864
2010	1	18	22	22	17.54	44.564017	-110.963583	1.4	10.431641	0.110	18	90	11.041
2010	1	18	22	23	47.94	44.560128	-110.962219	0.0	9.693359	0.098	10	149	11.1348
2010	1	18	22	24	29.40	44.56674	-110.968119	1.1	10.542969	0.077	10	144	11.1136
2010	1	18	22	24	50.07	44.563628	-110.979074	0.1	9.207031	0.100	11	119	11.7269
2010	1	18	22	25	20.66	44.541071	-110.973504	0.5	9.054688	0.093	7	272	13.1599
2010	1	18	22	36	7.27	44.562462	-110.967711	1.0	10.232422	0.116	13	146	11.3433
2010	1	18	22	46	36.99	44.55585	-110.972777	1.4	10.402344	0.088	13	179	11.5392
2010	1	18	22	49	55.42	44.564795	-110.968503	1.8	10.408203	0.104	21	91	11.2541
2010	1	18	22	54	49.79	44.551183	-110.961795	0.3	8.199219	0.092	7	248	11.7225
2010	1	18	22	55	26.39	44.565962	-110.967332	0.2	10.085938	0.094	7	294	11.1063
2010	1	18	23	4	38.72	44.558573	-110.965347	1.3	10.150391	0.104	13	149	11.4371
2010	1	18	23	9	10.19	44.522403	-110.970301	0.6	12.242188	0.050	7	265	13.8579
2010	1	18	23	43	34.28	44.560128	-110.962219	1.7	10.126953	0.133	17	92	11.1348
2010	1	18	23	51	11.46	44.549627	-110.966488	0.8	9.441406	0.103	10	249	12.1191
2010	1	18	23	52	0.34	44.571407	-110.966569	0.0	14.925781	0.142	6	116	21.0578
2010	1	18	23	56	28.68	44.558573	-110.962213		8.697266	0.146	11	150	11.2372
2010	1	18	23	56	31.54	44.558961	-110.966523	2.7	10.144531	0.121	20	93	11.4874
2010	1	18	23	58	36.68	44.56674	-110.957151	0.8	11.339844	0.105	12	147	10.3832
2010	1	18	23	58	45.20	44.562073	-110.974368	0.7	8.597656	0.110	12	144	11.8089
2010	1	19	1	18	49.73	44.565184	-110.966546	1.0	10.566406	0.122	16	90	11.1001
2010	1	19	1	20	31.59	44.561295	-110.953215	0.1	11.328125	0.094	7	241	10.4863
2010	1	19	1	22	55.39	44.558961	-110.961823	0.6	10.074219	0.143	11	253	11.1866
2010	1	19	1	49	36.57	44.565184	-110.961846	0.6	10.824219	0.120	11	147	10.7885
2010	1	19	2	7	27.64	44.556239	-110.966121	2.0	9.880859	0.129	23	94	11.6408
2010	1	19	2	10	54.10	44.566351	-110.969292	0.7	9.330078	0.144	12	91	11.2154
2010	1	19	2	14	22.02	44.565573	-110.975556	1.0	9.353516	0.127	12	93	10.8618
2010	1	19	2	19	26.21	44.563628	-110.974374	0.4	9.863281	0.055	9	144	11.0366
2010	1	19	2	19	36.74	44.579574	-110.97326	0.2	9.599609	0.090	9	135	9.9225
2010	1	19	2	33	6.43	44.564795	-110.959886	0.5	10.900391	0.087	11	148	10.6841
2010	1	19	2	36	3.73	44.556239	-110.962988	1.0	9.318359	0.161	15	93	11.4431
2010	1	19	2	53	2.95	44.558573	-110.970829	1.5	8.650391	0.198	25	95	11.5345
2010	1	19	2	54	38.71	44.557406	-110.96965	1.5	9.277344	0.185	24	95	11.6766
2010	1	19	3	9	8.64	44.562462	-110.970061	0.8	11.216797	0.079	12	93	11.4005
2010	1	19	3	29	31.54	44.564795	-110.96537	0.8	10.068359	0.145	16	90	11.0454
2010	1	19	3	29	58.15	44.697416	-111.059687	0.1	7.894531	0.104	10	93	8.01099
2010	1	19	3	30	25.49	44.566351	-110.969292	0.9	9.939453	0.120	14	91	11.2154
2010	1	19	3	39	38.78	44.55935	-110.970049	3.0	9.447266	0.154	26	94	11.5509
2010	1	19	3	47	32.26	44.569073	-110.970478	0.9	9.898438	0.086	9	142	11.0756

<i>Yr</i>	<i>Mo</i>	<i>Day</i>	<i>Hr</i>	<i>Mn</i>	<i>Sec</i>	<i>Lat</i>	<i>Lon</i>	<i>Mag</i>	<i>Depth</i>	<i>RMS</i>	<i>Nphs</i>	<i>Gap</i>	<i>Dist</i>
2010	1	19	3	53	52.93	44.557795	-110.979442	1.2	9.658203	0.141	19	97	10.9734
2010	1	19	3	56	0.85	44.56324	-110.956747	0.8	10.033203	0.140	15	89	10.5805
2010	1	19	4	3	24.79	44.562462	-110.973977	1.6	9.751953	0.140	23	94	11.1203
2010	1	19	4	4	40.83	44.564795	-110.958319	0.0	9.904297	0.163	13	148	10.5819
2010	1	19	4	4	53.06	44.563628	-110.97124	0.7	9.839844	0.143	14	100	11.2617
2010	1	19	4	5	38.38	44.55935	-110.971616	0.3	9.189453	0.130	13	147	11.4401
2010	1	19	4	10	25.81	44.553128	-110.955928	1.1	10.103516	0.121	19	93	11.2281
2010	1	19	4	18	11.93	44.558961	-110.975922	0.1	8.902344	0.096	13	146	11.1569
2010	1	19	4	34	10.95	44.552739	-110.968066	0.0	9.253906	0.143	13	96	11.9999
2010	1	19	4	34	43.66	44.557795	-110.963777	0.5	8.955078	0.091	10	150	11.3883
2010	1	19	4	42	13.66	44.563628	-110.96654	2.8	9.019531	0.156	28	91	11.1942
2010	1	19	4	43	17.35	44.560128	-110.965352	1.1	10.080078	0.150	13	175	11.3365
2010	1	19	4	52	10.65	44.564017	-110.973983	0.4	9.810547	0.095	13	144	11.0465
2010	1	19	4	54	16.75	44.560128	-110.973185	1.5	10.220703	0.123	16	94	11.2904
2010	1	19	4	55	38.81	44.554683	-110.968465	0.9	9.482422	0.160	21	96	11.8933
2010	1	19	4	57	29.43	44.556239	-110.973954	0.6	8.779297	0.099	11	147	11.4369
2010	1	19	4	59	36.17	44.568295	-110.968124	0.2	9.746094	0.103	10	143	11.0242
2010	1	19	5	0	0.66	44.562462	-110.961444	1.0	10.466797	0.157	14	148	10.9337
2010	1	19	5	1	11.19	44.565962	-110.954798	0.3	11.773438	0.160	15	87	10.2788
2010	1	19	5	1	33.29	44.566351	-110.955975	0.1	11.251953	0.159	13	148	10.3307
2010	1	19	5	10	23.61	44.562462	-110.959094	1.0	10.830078	0.120	13	149	10.782
2010	1	19	5	12	7.54	44.56324	-110.963014	0.3	11.064453	0.114	13	90	10.9865
2010	1	19	5	15	2.60	44.557017	-110.97474	0.4	8.333984	0.152	14	96	11.341
2010	1	19	5	16	23.81	44.562073	-110.971234	0.0	9.699219	0.076	9	145	11.3347
2010	1	19	5	20	11.91	44.565573	-110.97869	0.7	9.646484	0.104	12	141	10.6362
2010	1	19	5	24	32.65	44.57024	-110.963823	0.1	10.478516	0.124	13	143	10.6206
2010	1	19	5	31	4.94	44.557017	-110.955159	0.7	10.056641	0.183	18	91	10.9032
2010	1	19	5	32	42.78	44.561684	-110.966141	0.3	10.197266	0.086	11	147	11.2888
2010	1	19	5	33	17.79	44.569851	-110.966563	0.3	10.121094	0.134	13	143	10.8296
2010	1	19	5	39	5.88	44.560128	-110.975535	2.1	9.634766	0.167	26	95	11.1246
2010	1	19	5	47	53.48	44.571018	-110.964609	0.8	11.755859	0.085	14	87	10.6304
2010	1	19	5	52	22.27	44.554683	-110.962199	2.0	9.705078	0.149	26	94	11.5006
2010	1	19	5	55	11.77	44.560906	-110.966138	0.8	10.033203	0.133	16	92	11.3378
2010	1	19	5	56	33.72	44.561684	-110.955958	0.6	11.404297	0.117	14	140	10.6329
2010	1	19	6	3	54.53	44.568295	-110.980659	0.2	5.996094	0.180	8	139	11.2243
2010	1	19	6	4	18.78	44.56324	-110.964581	0.4	10.478516	0.129	16	91	11.0891
2010	1	19	6	11	48.23	44.558573	-110.955947	0.1	10.666016	0.126	13	152	10.8435
2010	1	19	6	21	57.90	44.569851	-110.999467	0.7	8.199219	0.191	9	134	11.3204
2010	1	19	6	22	30.33	44.564795	-110.96302	1.5	9.822266	0.165	19	123	10.8899
2010	1	19	6	23	27.37	44.57374	-110.965794		10.390625	0.121	12	227	10.5478
2010	1	19	6	26	1.12	44.573351	-110.963051	0.7	10.572266	0.195	18	86	10.3944
2010	1	19	6	26	21.26	44.56324	-110.959097	0.3	9.939453	0.160	18	89	10.7318
2010	1	19	6	27	28.71	44.560906	-110.972405	0.9	9.623047	0.120	16	94	11.3074
2010	1	19	6	34	3.48	44.564795	-110.966936	0.8	10.595703	0.116	20	91	11.1496
2010	1	19	6	35	2.08	44.55935	-110.975532	0.5	9.412109	0.139	10	95	11.1643
2010	1	19	6	37	5.75	44.57024	-110.966957	0.5	10.279297	0.075	10	142	10.8347
2010	1	19	6	37	41.57	44.561684	-110.977108		9.330078	0.068	10	144	10.9358
2010	1	19	6	43	6.92	44.561684	-110.975541	0.3	9.658203	0.125	12	144	11.0468
2010	1	19	6	43	20.74	44.564017	-110.964583	1.4	9.458984	0.168	17	123	11.041
2010	1	19	7	0	8.39	44.56324	-110.963797	0.7	9.845703	0.183	19	91	11.0377
2010	1	19	7	1	34.25	44.569851	-110.960296	0.9	10.613281	0.169	18	121	10.4042
2010	1	19	7	4	52.55	44.564017	-110.973983	0.2	9.939453	0.108	13	93	11.0465
2010	1	19	7	10	19.15	44.573351	-110.95835	0.2	11.240234	0.219	12	143	10.0712
2010	1	19	7	10	42.50	44.567906	-110.963031	0.2	10.232422	0.123	14	88	10.7026
2010	1	19	7	12	39.33	44.560517	-110.963396	0.4	10.542969	0.143	13	92	11.1851
2010	1	19	7	17	51.32	44.57024	-110.962256	0.9	9.857422	0.169	21	87	10.5142
2010	1	19	7	23	56.56	44.557017	-110.959858	0.5	10.548828	0.109	14	92	11.1941
2010	1	19	7	25	30.64	44.565573	-110.957539	0.4	10.115234	0.138	18	138	10.4818
2010	1	19	7	26	34.54	44.571407	-110.954034	0.9	13.144531	0.149	8	146	9.89188
2010	1	19	7	28	34.21	44.553128	-110.972375	1.4	9.845703	0.115	18	97	11.7147
2010	1	19	7	34	56.16	44.55935	-110.965349	1.0	9.330078	0.122	14	104	11.3866
2010	1	19	7	40	45.76	44.556628	-110.976696	0.3	9.382812	0.079	9	146	11.2261

<i>Yr</i>	<i>Mo</i>	<i>Day</i>	<i>Hr</i>	<i>Mn</i>	<i>Sec</i>	<i>Lat</i>	<i>Lon</i>	<i>Mag</i>	<i>Depth</i>	<i>RMS</i>	<i>Nphs</i>	<i>Gap</i>	<i>Dist</i>
2010	1	19	7	43	17.30	44.558961	-110.980622	0.6	8.457031	0.098	9	144	10.8293
2010	1	19	7	49	13.99	44.56324	-110.967714	0.9	9.564453	0.097	13	102	11.2957
2010	1	19	7	58	6.02	44.554683	-110.973164	2.0	9.716797	0.136	24	97	11.5752
2010	1	19	8	2	10.33	44.560517	-110.975928	1.0	9.863281	0.100	14	95	11.0773
2010	1	19	8	6	44.20	44.557406	-110.975916	1.7	9.347656	0.095	14	96	11.2387
2010	1	19	8	7	19.25	44.561295	-110.972015	0.8	10.109375	0.103	11	137	11.3163
2010	1	19	8	14	0.22	44.550016	-110.969231	1.2	9.728516	0.078	15	98	12.1036
2010	1	19	8	15	34.22	44.55935	-110.969266	1.2	9.669922	0.089	15	94	11.6064
2010	1	19	8	17	8.74	44.55235	-110.970023	1.4	8.919922	0.161	18	97	11.919
2010	1	19	8	19	23.20	44.556239	-110.973954	1.2	9.916016	0.084	15	96	11.4369
2010	1	19	8	19	49.55	44.553128	-110.968459	1.3	10.185547	0.159	18	96	11.9842
2010	1	19	8	20	32.02	44.548072	-110.974314	0.6	8.527344	0.161	9	100	11.8746
2010	1	19	8	41	36.67	44.554683	-110.970031	0.9	9.810547	0.097	16	96	11.7919
2010	1	19	8	54	56.44	44.567129	-110.968512	1.7	9.458984	0.121	22	90	11.1175
2010	1	19	8	56	23.32	44.557017	-110.969257	1.9	9.763672	0.133	21	95	11.7241
2010	1	19	9	1	6.66	44.557017	-110.967691	0.4	9.892578	0.084	12	149	11.6892
2010	1	19	9	1	19.90	44.557795	-110.97161	0.9	9.330078	0.101	16	124	11.5192
2010	1	19	9	5	27.61	44.560517	-110.969662	0.5	10.238281	0.120	14	93	11.5214
2010	1	19	9	11	10.63	44.56674	-110.957151	0.8	10.425781	0.106	13	138	10.3832
2010	1	19	9	11	41.47	44.554683	-110.968465	1.4	9.623047	0.151	17	96	11.8933
2010	1	19	9	16	45.35	44.562462	-110.975544	1.3	9.716797	0.147	16	94	11.0086
2010	1	19	9	17	15.08	44.565184	-110.96968	0.0	10.144531	0.094	9	261	11.3099
2010	1	19	9	28	0.11	44.556239	-110.968471	1.7	9.939453	0.107	19	95	11.7903
2010	1	19	9	32	59.58	44.554683	-110.967682	0.3	9.892578	0.100	15	95	11.8438
2010	1	19	9	36	21.60	44.561295	-110.959482	0.7	10.296875	0.155	20	90	10.883
2010	1	19	9	39	50.58	44.557017	-110.970824		9.388672	0.138	14	95	11.6143
2010	1	19	9	39	56.41	44.558961	-110.979055	2.4	10.285156	0.118	13	97	10.9382
2010	1	19	9	40	44.40	44.560517	-110.957129	1.0	10.730469	0.061	9	173	10.7851
2010	1	19	9	42	53.30	44.62391	-110.984408	0.1	7.478516	0.126	13	105	5.20827
2010	1	19	9	43	5.16	44.56324	-110.949697	0.2	11.814453	0.165	14	152	10.1333
2010	1	19	9	45	20.62	44.55935	-110.966916	0.8	9.341797	0.126	18	93	11.4876
2010	1	19	9	55	0.36	44.569462	-110.956769	0.3	11.779297	0.138	15	122	10.191
2010	1	19	9	57	21.28	44.571018	-110.956775	0.2	11.005859	0.150	15	86	10.0987
2010	1	19	10	1	23.72	44.565573	-110.966156	1.0	10.619141	0.071	11	145	11.0508
2010	1	19	10	2	49.77	44.571018	-110.972444	1.0	10.455078	0.103	12	89	10.8583
2010	1	19	10	14	31.93	44.562073	-110.958701	0.9	10.941406	0.124	10	149	10.7821
2010	1	19	10	16	11.63	44.560128	-110.957519	1.1	10.830078	0.085	11	125	10.8359
2010	1	19	10	36	13.96	44.56324	-110.960664	2.3	9.716797	0.122	27	90	10.8333
2010	1	19	10	45	7.33	44.546516	-110.910093	0.8	8.480469	0.083	8	164	9.42054
2010	1	19	10	45	54.14	44.564795	-110.973203	1.6	9.705078	0.125	13	92	11.0669
2010	1	19	10	47	49.74	44.569851	-110.955596	0.1	11.949219	0.156	9	146	10.0894
2010	1	19	10	51	53.04	44.562462	-110.970061	0.8	10.279297	0.101	15	93	11.4005
2010	1	19	11	0	33.29	44.568295	-110.975958	0.2	9.605469	0.203	12	141	11.1884
2010	1	19	11	2	12.12	44.566351	-110.966942	0.6	10.384766	0.119	13	90	11.0571
2010	1	19	11	3	12.26	44.565573	-110.963022	0.6	10.595703	0.120	16	89	10.8424
2010	1	19	11	4	32.87	44.567518	-110.959504	0.1	10.671875	0.157	15	138	10.4906
2010	1	19	11	7	8.91	44.566351	-110.961458	1.1	10.935547	0.114	16	89	10.6913
2010	1	19	11	14	11.11	44.557406	-110.96965	1.7	9.371094	0.122	24	95	11.6766
2010	1	19	11	26	52.96	44.562851	-110.970454	0.1	10.039062	0.089	13	92	11.3542
2010	1	19	11	35	13.57	44.55235	-110.961408	1.1	9.494141	0.156	19	95	11.6157
2010	1	19	12	8	48.51	44.554683	-110.973164	0.2	9.025391	0.108	12	97	11.5752
2010	1	19	12	15	7.60	44.556239	-110.969254	0.7	9.365234	0.126	15	95	11.7643
2010	1	19	12	21	56.34	44.55935	-110.965349	0.6	10.150391	0.109	14	93	11.3866
2010	1	19	13	0	59.30	44.56324	-110.963797	1.1	9.939453	0.145	20	91	11.0377
2010	1	19	13	1	25.47	44.593186	-110.982325	0.1	13.753906	0.254	9	79	8.50162
2010	1	19	13	26	2.02	44.555072	-110.965725	0.3	9.734375	0.107	15	95	11.6943
2010	1	19	13	26	51.38	44.557406	-110.963384	2.4	9.652344	0.138	26	93	11.3894
2010	1	19	13	28	23.45	44.56324	-110.962231	0.1	9.435547	0.101	11	148	10.9353
2010	1	19	13	28	35.04	44.562462	-110.959094	0.5	10.267578	0.156	16	90	10.782
2010	1	19	13	30	5.57	44.560906	-110.962222	0.8	10.197266	0.084	15	91	11.0843
2010	1	19	13	32	29.66	44.56324	-110.963014	1.0	10.326172	0.122	20	90	10.9865
2010	1	19	13	39	12.48	44.56324	-110.961447	2.0	9.693359	0.134	27	90	10.8843

<i>Yr</i>	<i>Mo</i>	<i>Day</i>	<i>Hr</i>	<i>Mn</i>	<i>Sec</i>	<i>Lat</i>	<i>Lon</i>	<i>Mag</i>	<i>Depth</i>	<i>RMS</i>	<i>Nphs</i>	<i>Gap</i>	<i>Dist</i>
2010	1	19	13	44	35.51	44.569851	-110.957162	0.6	10.191406	0.079	8	146	10.1939
2010	1	19	13	48	11.46	44.553906	-110.964546	0.4	10.478516	0.104	17	95	11.7002
2010	1	19	13	57	0.12	44.55235	-110.96689	0.3	10.701172	0.118	18	96	11.9533
2010	1	19	14	2	27.52	44.548461	-110.963743	1.3	9.283203	0.141	22	97	12.0364
2010	1	19	14	7	53.82	44.553906	-110.966112	0.1	9.564453	0.105	12	95	11.7979
2010	1	19	14	15	21.90	44.55585	-110.966511	1.0	10.566406	0.088	20	94	11.6915
2010	1	19	14	15	39.39	44.557795	-110.962211	0.2	10.630859	0.084	16	93	11.2891
2010	1	19	14	16	2.13	44.557017	-110.962208	0.8	10.630859	0.120	20	93	11.3414
2010	1	19	14	39	20.07	44.564795	-110.970853	0.1	9.259766	0.112	12	92	11.2367
2010	1	19	15	16	42.79	44.568684	-110.963817	0.4	10.654297	0.134	19	88	10.7099
2010	1	19	15	40	41.42	44.562851	-110.957921	0.7	11.070312	0.117	15	139	10.6812
2010	1	19	16	15	58.57	44.569851	-110.96813	0.3	9.863281	0.081	9	142	10.9369
2010	1	19	16	20	31.22	44.56674	-110.961852	0.7	10.378906	0.092	9	146	10.6937
2010	1	19	16	21	3.69	44.571407	-110.965002	0.7	10.097656	0.093	9	142	10.6357
2010	1	19	16	21	37.79	44.554294	-110.946142	1.2	10.894531	0.063	10	90	10.5636
2010	1	19	16	27	55.78	44.560517	-110.961829	0.9	9.605469	0.114	13	124	11.0844
2010	1	19	16	47	0.96	44.562073	-110.969668	0.7	9.652344	0.091	9	146	11.4964
2010	1	19	16	48	31.09	44.561684	-110.966925	3.0	7.982422	0.190	28	92	11.34
2010	1	19	16	51	1.55	44.555461	-110.962985	1.1	10.654297	0.101	15	94	11.496
2010	1	19	17	1	20.36	44.549627	-110.964922	0.6	8.128906	0.037	8	152	12.0236
2010	1	19	17	25	5.86	44.560128	-110.969269	1.4	10.126953	0.112	12	93	11.5682
2010	1	19	17	28	50.22	44.557406	-110.958685	0.8	9.535156	0.088	8	152	11.0942
2010	1	19	17	50	34.93	44.55935	-110.969266	0.6	9.470703	0.082	11	103	11.6064
2010	1	19	18	5	18.34	44.558573	-110.971613	1.8	10.607422	0.122	17	95	11.4794
2010	1	19	18	22	14.56	44.556628	-110.967297	0.9	9.382812	0.093	11	104	11.6897
2010	1	19	18	28	20.33	44.557795	-110.977876	1.6	9.283203	0.122	17	97	11.0819
2010	1	19	19	1	7.04	44.55585	-110.966511	0.3	9.183594	0.093	11	150	11.6915
2010	1	19	19	1	34.31	44.558961	-110.964956	1.4	10.050781	0.115	12	242	11.3866
2010	1	19	19	6	31.12	44.558184	-110.962604	0.7	9.78125	0.092	11	150	11.2879
2010	1	19	19	6	57.78	44.564017	-110.959883	1.0	10.830078	0.167	14	123	10.7331
2010	1	19	19	12	40.91	44.553128	-110.974725	2.0	9.822266	0.122	23	98	11.5539
2010	1	19	19	14	25.18	44.553128	-110.971592	1.5	10.279297	0.099	17	97	11.7684
2010	1	19	19	14	53.32	44.562462	-110.963011	0.7	9.341797	0.125	13	91	11.0354
2010	1	19	19	19	30.40	44.55235	-110.96689	1.3	10.150391	0.114	16	96	11.9533
2010	1	19	19	22	48.01	44.551572	-110.966104	1.0	9.365234	0.072	13	96	11.9586
2010	1	19	19	23	36.01	44.556628	-110.967297	1.3	10.320312	0.133	15	94	11.6897
2010	1	19	19	27	17.29	44.559739	-110.967309	1.0	10.789062	0.139	12	124	11.4882
2010	1	19	19	32	3.68	44.560517	-110.974362	1.1	10.214844	0.062	12	145	11.1879
2010	1	19	19	32	57.85	44.555461	-110.965335	0.6	10.197266	0.126	16	94	11.6434
2010	1	19	19	34	7.62	44.558573	-110.971613	0.3	9.740234	0.150	12	102	11.4794
2010	1	19	19	40	59.26	44.564795	-110.966153	0.9	10.900391	0.111	19	91	11.0974
2010	1	19	19	43	27.03	44.553517	-110.964153	1.7	10.742188	0.096	19	95	11.7027
2010	1	19	19	44	2.68	44.557406	-110.964951	0.5	9.886719	0.092	9	150	11.4888
2010	1	19	19	50	41.56	44.571018	-110.970877	0.1	10.572266	0.054	10	141	10.8611
2010	1	19	19	51	35.89	44.558961	-110.95869	0.3	10.894531	0.114	11	151	10.9884
2010	1	19	19	51	48.24	44.555461	-110.963769	1.0	11.087891	0.102	17	94	11.545
2010	1	19	19	53	0.90	44.552739	-110.968066	0.1	9.300781	0.082	11	151	11.9999
2010	1	19	19	53	24.62	44.556239	-110.959855	0.2	10.185547	0.101	14	141	11.2475
2010	1	19	19	58	9.97	44.55235	-110.96454	0.6	10.525391	0.110	19	95	11.8078
2010	1	19	20	1	29.58	44.56674	-110.964985	0.9	10.824219	0.107	15	138	10.9028
2010	1	19	20	4	57.55	44.556239	-110.971604	0.8	10.185547	0.132	16	139	11.6003
2010	1	19	20	52	27.25	44.562073	-110.979068	0.2	8.246094	0.104	11	143	11.899
2010	1	19	20	54	34.80	44.547683	-110.966873	0.8	10.044922	0.109	16	98	12.2813
2010	1	19	20	58	3.13	44.551572	-110.968453	0.9	10.291016	0.088	19	97	12.0696
2010	1	19	21	1	18.04	44.547294	-110.96413	0.4	9.382812	0.168	14	97	12.1446
2010	1	19	21	1	32.93	44.557406	-110.96965	1.0	10.238281	0.096	17	95	11.6766
2010	1	19	21	7	4.76	44.546905	-110.973918	2.3	8.720703	0.161	22	100	11.9711
2010	1	19	21	10	17.01	44.57024	-110.968523	0.8	12.037109	0.087	16	89	10.9406
2010	1	19	21	11	9.12	44.562462	-110.964578	0.4	10.478516	0.143	13	91	11.1376
2010	1	19	21	17	51.25	44.549627	-110.968054	1.7	10.238281	0.099	18	97	12.2056
2010	1	19	21	31	15.24	44.549627	-110.966488	1.1	9.722656	0.100	15	97	12.1191
2010	1	19	21	32	10.04	44.560906	-110.967705	1.8	10.197266	0.115	21	93	11.4399

<i>Yr</i>	<i>Mo</i>	<i>Day</i>	<i>Hr</i>	<i>Mn</i>	<i>Sec</i>	<i>Lat</i>	<i>Lon</i>	<i>Mag</i>	<i>Depth</i>	<i>RMS</i>	<i>Nphs</i>	<i>Gap</i>	<i>Dist</i>
2010	1	19	21	32	30.81	44.557795	-110.97396	3.7	9.330078	0.166	27	96	11.3546
2010	1	19	21	33	23.62	44.550016	-110.966881	3.0	10.033203	0.090	16	143	12.1157
2010	1	19	21	34	22.60	44.550016	-110.975496	0.9	10.021484	0.116	18	184	11.6803
2010	1	19	21	37	38.93	44.565184	-110.975946	0.6	10.332031	0.107	14	93	10.8514
2010	1	19	21	40	46.56	44.562073	-110.969668	0.9	10.121094	0.125	14	146	11.4469
2010	1	19	21	41	31.16	44.556239	-110.968471	1.3	10.537109	0.104	17	95	11.7903
2010	1	19	21	42	3.67	44.557795	-110.966127	0.5	10.185547	0.132	15	94	11.5381
2010	1	19	21	42	53.77	44.557017	-110.966907	1.8	9.892578	0.126	22	94	11.6392
2010	1	19	21	50	3.20	44.557017	-110.975523	0.3	10.009766	0.113	11	147	11.2866
2010	1	19	21	51	47.63	44.549627	-110.97432	1.3	8.222656	0.125	12	150	11.7821
2010	1	19	21	55	10.94	44.554294	-110.975904	0.6	8.035156	0.097	9	148	11.4082
2010	1	19	21	56	54.24	44.555461	-110.969251	1.2	10.337891	0.086	15	95	11.805
2010	1	19	21	57	57.35	44.56324	-110.974764	1.4	9.810547	0.080	13	122	11.0271
2010	1	19	22	0	15.10	44.558961	-110.961823	0.7	9.253906	0.120	12	150	11.1866
2010	1	19	22	3	33.29	44.558961	-110.969656	1.2	10.589844	0.051	9	123	11.598
2010	1	19	22	5	22.81	44.562073	-110.964968	0.1	9.089844	0.074	8	149	11.1876
2010	1	19	22	11	14.84	44.553517	-110.964153	0.7	9.148438	0.061	8	152	11.7027
2010	1	19	22	15	57.35	44.55585	-110.969644	0.7	10.121094	0.056	9	149	11.7573
2010	1	19	22	16	42.49	44.551183	-110.966494	0.5	4.003906	0.064	7	117	23.2824
2010	1	19	22	18	0.22	44.555461	-110.970818	2.3	10.314453	0.136	24	96	11.696
2010	1	19	22	21	14.74	44.560517	-110.968095	0.7	10.167969	0.084	9	147	11.4899
2010	1	19	22	21	37.75	44.558573	-110.971613	0.4	8.955078	0.119	12	147	11.8423
2010	1	19	22	23	35.16	44.556239	-110.963771	0.6	10.232422	0.100	14	95	11.4924
2010	1	19	22	25	33.76	44.567129	-110.978696	0.1	9.271484	0.096	9	141	10.5647
2010	1	19	22	28	57.03	44.550405	-110.967274	0.7	8.492188	0.088	10	152	12.1124
2010	1	19	22	32	11.31	44.551572	-110.969237	0.8	10.162109	0.107	14	97	12.0159
2010	1	19	22	39	52.58	44.564017	-110.96615	1.4	10.583984	0.132	22	91	11.1446
2010	1	19	22	40	56.14	44.565184	-110.96968	0.3	9.746094	0.065	10	144	11.3099
2010	1	19	22	56	30.95	44.550016	-110.966098	0.5	9.013672	0.095	11	141	12.0677
2010	1	19	22	58	41.56	44.557017	-110.951242	0.5	9.623047	0.114	12	142	10.6646
2010	1	19	23	2	44.53	44.564017	-110.967717	1.3	10.208984	0.108	15	104	11.2485
2010	1	19	23	3	31.93	44.557795	-110.97396	2.0	8.755859	0.153	17	106	13.8445
2010	1	19	23	17	27.42	44.566351	-110.964592	0.2	10.490234	0.095	13	145	10.8997
2010	1	19	23	18	7.98	44.565573	-110.970856		10.103516	0.044	9	144	11.2019
2010	1	19	23	19	16.06	44.564795	-110.968503	0.4	9.951172	0.103	16	91	11.2541
2010	1	19	23	21	37.55	44.560128	-110.984935	0.9	10.033203	0.067	11	142	10.468
2010	1	19	23	22	6.79	44.568684	-110.974785	0.1	10.794922	0.129	11	118	11.1382
2010	1	19	23	34	41.77	44.564017	-110.971633	0.4	8.955078	0.087	11	144	11.2155
2010	1	19	23	35	37.99	44.562851	-110.967321	0.0	9.523438	0.125	7	296	11.2936
2010	1	19	23	36	16.55	44.562462	-110.966144	0.0	8.755859	0.085	11	147	11.2402
2010	1	19	23	36	35.64	44.564017	-110.96615	0.7	10.314453	0.076	13	146	11.1446
2010	1	19	23	59	40.92	44.557406	-110.96965	1.0	10.613281	0.108	15	95	11.6766
2010	1	20	1	1	37.61	44.560517	-110.972795	1.0	9.511719	0.085	10	146	11.2988
2010	1	20	1	11	50.90	44.556239	-110.967688	1.3	10.748047	0.109	14	95	11.7403
2010	1	20	1	35	36.25	44.556239	-110.969254	3.1	9.974609	0.123	25	95	11.7643
2010	1	20	1	40	37.98	44.550794	-110.964535	1.4	11.275391	0.121	18	96	11.917
2010	1	20	1	43	0.36	44.550794	-110.970017	0.8	9.517578	0.092	12	151	12.0061
2010	1	20	1	43	41.70	44.552739	-110.968066	1.4	9.628906	0.088	11	151	11.9999
2010	1	20	1	45	1.26	44.550016	-110.968448	1.3	10.033203	0.122	16	97	12.1569
2010	1	20	1	48	10.47	44.553128	-110.96376	1.5	10.595703	0.122	19	95	11.7054
2010	1	20	1	52	14.29	44.567129	-110.963811	0.8	10.455078	0.146	15	89	10.8011
2010	1	20	2	0	21.31	44.57024	-110.986542	0.7	9.880859	0.078	14	93	9.85775
2010	1	20	2	1	16.18	44.568684	-110.966951	0.3	10.431641	0.109	17	89	10.9222
2010	1	20	2	8	52.69	44.553906	-110.969245	0.7	9.716797	0.142	20	96	11.888
2010	1	20	2	16	39.66	44.552739	-110.974332	0.2	9.042969	0.085	11	149	11.6026
2010	1	20	2	32	9.40	44.561684	-110.967708	0.7	10.103516	0.120	20	92	11.3914
2010	1	20	3	20	38.91	44.553906	-110.968462	0.9	9.412109	0.156	19	96	11.9422
2010	1	20	3	23	1.20	44.556239	-110.971604	0.4	9.482422	0.149	13	96	11.6003
2010	1	20	3	35	34.67	44.562073	-110.975934	0.4	9.816406	0.175	14	94	10.9998
2010	1	20	3	53	55.99	44.558573	-110.966913	0.4	10.548828	0.091	13	93	11.5377
2010	1	20	4	10	31.46	44.562462	-110.974761	0.2	9.353516	0.100	11	144	11.0644
2010	1	20	4	11	48.88	44.551572	-110.966887	0.8	9.833984	0.118	14	106	12.007

<i>Yr</i>	<i>Mo</i>	<i>Day</i>	<i>Hr</i>	<i>Mn</i>	<i>Sec</i>	<i>Lat</i>	<i>Lon</i>	<i>Mag</i>	<i>Depth</i>	<i>RMS</i>	<i>Nphs</i>	<i>Gap</i>	<i>Dist</i>
2010	1	20	4	12	2.32	44.571796	-110.964612	1.6	10.630859	0.145	15	99	10.5873
2010	1	20	4	12	27.32	44.565573	-110.963806	2.2	9.587891	0.129	21	90	10.8943
2010	1	20	4	13	20.10	44.572962	-110.919567	1.0	14.363281	0.211	8	234	7.60767
2010	1	20	4	13	54.73	44.571018	-110.961475	0.6	11.111328	0.128	15	121	10.4166
2010	1	20	4	14	8.01	44.568684	-110.958333	0.7	10.630859	0.110	14	138	10.3421
2010	1	20	4	16	15.62	44.560906	-110.961439	1.2	9.962891	0.183	20	91	11.0339
2010	1	20	4	16	55.23	44.558573	-110.962997	0.8	9.951172	0.134	17	92	11.287
2010	1	20	4	20	30.68	44.574907	-110.965407	0.3	10.115234	0.125	14	136	10.4179
2010	1	20	4	32	28.53	44.565962	-110.967332	0.3	10.085938	0.124	14	138	11.1063
2010	1	20	4	37	20.65	44.577629	-110.95719	0.4	13.238281	0.181	10	141	9.75826
2010	1	20	4	41	2.60	44.564795	-110.963803	3.1	9.447266	0.139	24	90	10.9416
2010	1	20	4	41	42.26	44.559739	-110.954777	1.8	10.085938	0.044	7	242	10.6903
2010	1	20	4	42	17.87	44.562462	-110.960661	2.4	10.513672	0.127	18	90	10.883
2010	1	20	4	42	52.13	44.564017	-110.95205	1.6	11.673828	0.129	13	124	10.2293
2010	1	20	4	43	49.67	44.563628	-110.974374	1.6	10.378906	0.085	11	122	11.0366
2010	1	20	4	46	2.36	44.56674	-110.974386	0.2	9.300781	0.118	13	92	10.8943
2010	1	20	4	48	5.00	44.562073	-110.925802	1.2	12.699219	0.214	8	162	8.80639
2010	1	20	4	48	25.97	44.559739	-110.961043	0.7	10.320312	0.092	9	150	11.0853
2010	1	20	4	49	0.18	44.56324	-110.963797	1.5	10.126953	0.116	16	91	11.0377
2010	1	20	4	51	3.46	44.560517	-110.969662	0.1	10.707031	0.146	12	138	11.5214
2010	1	20	4	51	25.19	44.518514	-110.902189	0.2	11.785156	0.205	9	172	11.9527
2010	1	20	4	52	16.69	44.554294	-110.958673	1.6	10.894531	0.105	8	93	11.3108
2010	1	20	4	53	31.79	44.55935	-110.965349	0.9	10.630859	0.123	16	93	11.3866
2010	1	20	4	54	2.14	44.561684	-110.963008	0.4	11.544922	0.173	16	91	11.0849
2010	1	20	4	55	56.99	44.558573	-110.965347	0.6	10.560547	0.094	17	93	11.4371
2010	1	20	4	56	51.60	44.543405	-110.963333	0.9	9.277344	0.188	17	98	12.3867
2010	1	20	4	58	39.99	44.566351	-110.950491	0.3	12.916016	0.238	14	96	9.9759
2010	1	20	4	59	10.11	44.564017	-110.976334	0.7	9.400391	0.115	19	94	10.878
2010	1	20	5	1	33.72	44.550794	-110.965318	0.2	9.962891	0.102	12	96	11.9649
2010	1	20	5	5	48.98	44.569851	-110.974398	0.1	9.816406	0.092	10	140	10.7611
2010	1	20	5	7	16.72	44.564017	-110.971633	1.1	9.751953	0.109	19	92	11.2155
2010	1	20	5	9	7.07	44.569073	-110.973611	0.6	9.898438	0.105	15	90	10.8509
2010	1	20	5	17	6.51	44.55935	-110.974749	0.1	9.716797	0.103	12	101	11.2193
2010	1	20	5	38	28.39	44.56324	-110.959097	0.9	11.697266	0.137	14	89	10.7318
2010	1	20	5	40	32.82	44.564017	-110.970067	1.7	9.646484	0.132	22	92	11.3285
2010	1	20	5	41	48.81	44.565573	-110.969289	0.2	9.916016	0.096	11	144	11.2608
2010	1	20	5	58	15.75	44.574907	-110.959139	0.8	12.037109	0.152	16	84	10.0394
2010	1	20	5	58	33.54	44.543405	-110.969597	0.5	9.816406	0.109	11	186	12.4702
2010	1	20	5	59	46.34	44.546516	-110.952381	0.3	9.628906	0.191	10	156	11.5191
2010	1	20	6	8	44.10	44.560517	-110.953996	0.4	11.480469	0.087	9	152	10.5882
2010	1	20	6	14	27.47	44.556628	-110.954766	0.1	10.929688	0.103	11	153	10.9066
2010	1	20	6	22	20.49	44.56674	-110.961852	0.6	9.277344	0.071	8	146	10.6937
2010	1	20	6	23	11.24	44.566351	-110.956758	0.3	12.142578	0.218	13	88	10.3818
2010	1	20	6	35	48.94	44.562851	-110.967321	2.0	9.335938	0.118	22	92	11.2936
2010	1	20	6	42	27.72	44.56324	-110.97398	0.1	9.353516	0.125	14	93	11.0831
2010	1	20	6	43	47.40	44.564017	-110.967717	0.1	9.740234	0.151	15	91	11.2485
2010	1	20	6	46	24.29	44.564795	-110.969286	0.1	10.208984	0.102	13	100	11.3066
2010	1	20	6	53	50.66	44.553906	-110.95828	0.5	10.337891	0.155	15	93	11.3144
2010	1	20	6	55	34.37	44.55235	-110.959841	0.8	10.326172	0.085	13	94	11.5204
2010	1	20	7	0	32.68	44.564795	-110.968503	0.2	10.501953	0.089	13	91	11.2541
2010	1	20	7	0	54.98	44.558573	-110.962997	0.2	11.123047	0.112	13	92	11.287
2010	1	20	7	1	16.70	44.557406	-110.963384	0.1	10.496094	0.118	13	93	11.3894
2010	1	20	7	1	46.13	44.561684	-110.967708	0.6	10.466797	0.112	14	92	11.3914
2010	1	20	7	10	16.21	44.560517	-110.975928	0.2	8.339844	0.066	10	145	11.0773
2010	1	20	7	13	33.29	44.568684	-110.972435	0.4	9.611328	0.114	15	90	10.9534
2010	1	20	7	17	0.77	44.556239	-110.966121	0.4	9.740234	0.143	14	94	11.6408
2010	1	20	7	20	18.05	44.567129	-110.981829	0.2	9.095703	0.093	10	140	10.3386
2010	1	20	7	22	14.13	44.562851	-110.967321	0.6	9.570312	0.097	12	92	11.2936
2010	1	20	7	33	17.48	44.563628	-110.97124	1.2	9.652344	0.126	17	92	11.2617
2010	1	20	7	50	32.40	44.565962	-110.957932	0.5	11.820312	0.124	16	88	10.483
2010	1	20	7	55	23.38	44.558573	-110.967696	1.0	9.341797	0.145	18	94	11.5882
2010	1	20	8	1	26.30	44.573351	-110.977153	0.7	9.400391	0.104	16	89	10.4189

<i>Yr</i>	<i>Mo</i>	<i>Day</i>	<i>Hr</i>	<i>Mn</i>	<i>Sec</i>	<i>Lat</i>	<i>Lon</i>	<i>Mag</i>	<i>Depth</i>	<i>RMS</i>	<i>Nphs</i>	<i>Gap</i>	<i>Dist</i>
2010	1	20	8	2	59.60	44.564795	-110.973986	0.6	9.318359	0.149	17	93	11.0104
2010	1	20	8	4	59.12	44.568295	-110.964991	0.2	11.457031	0.133	11	144	10.8118
2010	1	20	8	27	24.31	44.558961	-110.968089	2.0	9.980469	0.133	23	94	11.5886
2010	1	20	8	27	47.38	44.555461	-110.970818	2.3	9.587891	0.143	21	96	11.696
2010	1	20	8	28	25.85	44.551572	-110.968453	1.1	9.517578	0.148	18	97	12.0696
2010	1	20	8	33	37.20	44.556628	-110.967297	0.4	10.226562	0.116	14	94	11.6897
2010	1	20	8	46	9.83	44.567906	-110.982616	0.4	10.830078	0.138	13	93	10.2464
2010	1	20	9	1	14.43	44.571796	-110.974013	0.0	10.091797	0.118	12	139	10.7117
2010	1	20	9	9	18.85	44.54496	-110.953941	0.1	11.574219	0.124	12	156	11.7287
2010	1	20	9	11	59.31	44.560906	-110.947339	0.2	11.873047	0.133	13	141	10.1497
2010	1	20	9	16	58.07	44.558961	-110.971223	0.2	10.191406	0.106	13	102	11.4873
2010	1	20	9	18	6.72	44.573351	-110.989689	0.4	9.740234	0.064	10	134	9.49433
2010	1	20	9	27	44.79	44.567906	-110.959897	0.1	10.841797	0.183	17	88	10.4932
2010	1	20	9	30	29.51	44.804756	-110.55369	0.2	5.832031	0.112	10	171	10.2372
2010	1	20	9	33	25.14	44.575685	-110.954441	0.3	12.189453	0.142	11	83	9.67302
2010	1	20	9	55	3.87	44.569462	-110.956769	0.1	12.037109	0.168	12	146	10.191
2010	1	20	10	25	6.93	44.567129	-110.957544	0.5	11.533203	0.156	14	87	10.3849
2010	1	20	10	25	39.99	44.56674	-110.966552	0.1	10.519531	0.096	10	90	11.008
2010	1	20	10	32	22.41	44.567129	-110.963028	0.3	10.724609	0.103	17	89	10.7487
2010	1	20	10	33	21.47	44.566351	-110.965375	0.4	10.794922	0.103	16	90	10.9521
2010	1	20	10	33	57.23	44.564017	-110.96615	0.1	10.560547	0.121	13	91	11.1446
2010	1	20	10	38	10.45	44.565573	-110.977123	0.6	8.544922	0.132	15	93	10.7489
2010	1	20	10	39	37.40	44.565184	-110.966546	0.2	10.027344	0.113	16	90	11.1001
2010	1	20	11	2	39.99	44.584241	-110.961524	0.6	10.970703	0.162	12	80	9.38397
2010	1	20	11	8	52.42	44.57024	-110.966173	0.6	11.205078	0.107	15	88	10.7811
2010	1	20	11	9	23.86	44.568684	-110.965384	0.6	11.017578	0.126	16	89	10.8158
2010	1	20	11	30	48.72	44.564017	-110.978684	0.8	9.681641	0.077	13	142	10.7101
2010	1	20	11	37	30.02	44.565184	-110.941479	1.0	11.339844	0.138	10	153	9.48871
2010	1	20	11	39	16.26	44.560517	-110.961829	0.8	10.355469	0.139	13	149	11.0844
2010	1	20	11	39	25.68	44.557795	-110.963777	1.0	9.669922	0.093	12	150	11.3883
2010	1	20	11	40	2.42	44.560517	-110.960262	0.8	10.332031	0.120	11	150	10.9841
2010	1	20	11	40	12.32	44.554294	-110.963373	1.5	9.324219	0.125	10	94	11.6004
2010	1	20	11	42	23.61	44.554683	-110.960633	1.2	10.513672	0.107	20	93	11.4037
2010	1	20	11	47	39.37	44.561684	-110.973191	0.7	9.505859	0.148	16	94	11.2137
2010	1	20	11	54	25.35	44.562073	-110.971234	1.2	9.324219	0.144	21	93	11.3347
2010	1	20	12	3	0.92	44.56324	-110.968497	0.0	9.107422	0.118	12	146	11.3476
2010	1	20	12	22	19.38	44.568684	-110.971651	0.5	9.833984	0.116	12	90	11.0108
2010	1	20	12	34	18.31	44.574129	-110.96227	0.4	11.673828	0.157	14	137	10.2982
2010	1	20	12	40	13.19	44.561684	-110.959092	0.0	11.169922	0.089	11	90	10.8325
2010	1	20	12	41	50.21	44.569851	-110.974398	0.1	10.261719	0.109	11	140	10.7611
2010	1	20	12	47	47.84	44.557795	-110.977876	1.4	9.458984	0.129	22	97	11.0819
2010	1	20	12	48	13.69	44.557017	-110.975523	2.0	9.529297	0.144	19	97	11.2866
2010	1	20	12	51	40.82	44.567906	-110.966948	1.1	10.947266	0.142	15	89	10.9667
2010	1	20	12	52	10.43	44.558573	-110.972396	0.6	8.427734	0.104	12	95	11.4243
2010	1	20	12	54	0.30	44.557017	-110.97004	0.8	9.224609	0.132	11	139	11.6691
2010	1	20	13	9	11.69	44.564795	-110.969286	1.8	9.869141	0.125	23	91	11.3066
2010	1	20	13	12	40.76	44.558573	-110.96378	0.3	8.861328	0.141	11	93	11.3369
2010	1	20	13	12	52.79	44.551183	-110.966494	0.2	10.472656	0.082	10	96	12.0099
2010	1	20	13	28	5.33	44.565573	-110.971639	0.4	9.939453	0.118	15	92	11.145
2010	1	20	13	30	27.46	44.566351	-110.968509	0.2	10.408203	0.106	11	90	11.1626
2010	1	20	13	47	7.93	44.560906	-110.982588	0.4	9.939453	0.107	12	97	10.5901
2010	1	20	13	55	6.34	44.572962	-110.97911	0.7	10.472656	0.047	9	137	10.2888
2010	1	20	13	55	33.51	44.568684	-110.982619	0.9	9.951172	0.064	11	139	10.2112
2010	1	20	13	58	46.50	44.569462	-110.97557	0.6	10.291016	0.116	11	140	10.691
2010	1	20	14	1	41.86	44.568295	-110.958724	1.1	10.894531	0.133	10	146	10.3916
2010	1	20	14	3	12.33	44.561684	-110.973191	1.9	9.880859	0.113	17	94	11.2137
2010	1	20	14	8	30.35	44.564017	-110.967717	2.0	9.494141	0.124	22	91	11.2485
2010	1	20	14	11	24.47	44.566351	-110.967725	1.8	10.326172	0.141	19	90	11.1098
2010	1	20	14	13	52.96	44.557795	-110.965344	1.3	9.822266	0.104	14	105	11.488
2010	1	20	14	23	16.78	44.566351	-110.967725	2.4	11.837891	0.085	15	90	11.1098
2010	1	20	14	27	22.31	44.557406	-110.966517	2.1	9.511719	0.134	22	94	11.5886
2010	1	20	14	30	7.94	44.55935	-110.9583	1.4	10.419922	0.135	13	125	10.9376

<i>Yr</i>	<i>Mo</i>	<i>Day</i>	<i>Hr</i>	<i>Mn</i>	<i>Sec</i>	<i>Lat</i>	<i>Lon</i>	<i>Mag</i>	<i>Depth</i>	<i>RMS</i>	<i>Nphs</i>	<i>Gap</i>	<i>Dist</i>
2010	1	20	14	34	49.54	44.550405	-110.97354	0.7	9.101562	0.043	6	249	11.7894
2010	1	20	14	34	57.78	44.560517	-110.968095	0.8	10.542969	0.117	11	147	11.4899
2010	1	20	14	38	16.54	44.557795	-110.981009	2.0	9.189453	0.139	18	98	10.8652
2010	1	20	14	39	54.81	44.558961	-110.988455	1.7	10.472656	0.052	11	100	10.2899
2010	1	20	14	41	2.80	44.565573	-110.984957	1.1	9.447266	0.064	11	95	10.1883
2010	1	20	14	42	9.87	44.564017	-110.983384	1.2	9.646484	0.097	14	96	10.3761
2010	1	20	14	47	10.42	44.574129	-110.972455	1.1	8.123047	0.170	11	139	10.5223
2010	1	20	15	0	6.06	44.562462	-110.963011	1.1	10.384766	0.122	13	148	11.0354
2010	1	20	15	2	47.95	44.565184	-110.98848	0.6	9.722656	0.051	9	139	9.95783
2010	1	20	15	10	5.62	44.567906	-110.973215	1.2	9.751953	0.090	13	98	10.929
2010	1	20	15	20	7.19	44.564795	-110.963803	0.8	10.572266	0.115	16	90	10.9416
2010	1	20	15	47	36.20	44.549627	-110.966488	1.9	9.441406	0.146	22	97	12.1191
2010	1	20	15	49	2.79	44.549627	-110.960223	0.6	10.496094	0.134	17	95	11.7405
2010	1	20	15	50	15.32	44.554683	-110.963766	0.6	11.099609	0.111	15	94	11.5981
2010	1	20	15	55	41.14	44.55235	-110.968456	0.7	9.974609	0.134	12	96	12.0267
2010	1	20	15	56	5.65	44.553517	-110.967286	0.1	8.632812	0.104	11	96	11.8979
2010	1	20	16	4	38.60	44.565573	-110.973206	0.5	9.658203	0.114	16	92	11.0316
2010	1	20	16	7	59.58	44.553517	-110.964153	1.3	10.648438	0.114	17	95	11.7027
2010	1	20	16	9	15.91	44.576463	-110.987351	0.3	9.634766	0.040	10	133	9.54298
2010	1	20	16	9	34.35	44.571407	-110.961869	0.1	10.308594	0.057	9	143	10.4212
2010	1	20	16	13	34.52	44.548461	-110.967659	0.8	9.236328	0.153	18	98	12.2734
2010	1	20	16	21	18.11	44.566351	-110.966942	0.1	10.560547	0.118	15	90	11.0571
2010	1	20	16	22	36.35	44.566351	-110.971642	1.7	9.576172	0.152	22	91	11.1106
2010	1	20	16	25	2.94	44.57024	-110.977925	0.4	9.833984	0.114	12	95	10.4861
2010	1	20	16	26	48.38	44.569462	-110.977922	0.1	9.634766	0.108	11	140	10.519
2010	1	20	17	0	9.65	44.627411	-110.98403	0.3	8.011719	0.123	12	103	4.82848
2010	1	20	17	5	0.90	44.557406	-110.964951	0.6	10.917969	0.116	15	95	11.4888
2010	1	20	17	12	22.85	44.551572	-110.960622	0.3	10.314453	0.091	13	95	11.6235
2010	1	20	17	17	52.88	44.564795	-110.97477	0.6	10.361328	0.132	13	99	10.954
2010	1	20	18	8	9.69	44.560128	-110.984935	0.6	9.599609	0.119	13	98	10.468
2010	1	20	18	38	50.52	44.562073	-110.964968	0.3	10.941406	0.100	15	139	11.1876
2010	1	20	18	51	1.93	44.56324	-110.977897	0.2	9.037109	0.074	11	143	10.8035
2010	1	20	18	53	36.64	44.560128	-110.967702	1.3	10.220703	0.093	19	93	11.4889
2010	1	20	18	57	15.26	44.567129	-110.982613	0.7	9.482422	0.140	15	94	10.2822
2010	1	20	19	16	4.38	44.562462	-110.968494	0.2	10.501953	0.106	13	92	11.395
2010	1	20	19	22	31.00	44.558573	-110.965347	1.7	11.041016	0.107	19	93	11.4371
2010	1	20	19	28	2.18	44.569073	-110.983012	0.7	10.929688	0.125	9	138	10.1654
2010	1	20	19	56	15.42	44.569851	-110.969697	0.6	10.050781	0.162	13	142	10.9868
2010	1	20	20	0	27.73	44.556628	-110.973563	2.3	9.335938	0.156	25	96	11.4434
2010	1	20	20	2	5.16	44.562073	-110.972801	0.8	9.042969	0.077	10	93	11.2228
2010	1	20	20	7	48.46	44.561684	-110.971625	1.5	10.021484	0.102	12	122	11.3254
2010	1	20	20	10	20.35	44.557795	-110.974743	2.2	9.845703	0.155	25	96	11.2999
2010	1	20	20	13	10.68	44.560128	-110.973969	2.0	10.044922	0.151	23	95	11.2351
2010	1	20	20	22	35.46	44.564017	-110.981817	1.4	9.798828	0.062	12	95	10.4871
2010	1	20	21	2	46.44	44.56324	-110.967714	1.7	10.279297	0.109	17	92	11.2957
2010	1	20	21	15	44.66	44.554683	-110.958283	0.9	10.349609	0.106	13	93	11.2594
2010	1	20	21	15	53.80	44.557795	-110.959078	0.7	9.904297	0.095	12	140	11.0921
2010	1	20	21	23	4.18	44.568295	-110.979092	1.1	10.542969	0.062	10	140	10.4841
2010	1	20	21	25	24.72	44.558573	-110.962997	0.4	11.158203	0.092	15	92	11.287
2010	1	20	21	25	38.78	44.562462	-110.966144	1.5	10.783203	0.155	15	92	11.2402
2010	1	20	21	30	30.51	44.556239	-110.962988	0.2	10.595703	0.114	14	93	11.4431
2010	1	20	21	43	0.44	44.567129	-110.973212	2.7	9.435547	0.130	29	91	10.9626
2010	1	20	21	46	29.29	44.563628	-110.969674	0.5	10.285156	0.106	17	92	11.3746
2010	1	20	21	48	0.34	44.556628	-110.951633	0.0	10.742188	0.144	9	153	10.7162
2010	1	20	21	53	17.16	44.572185	-110.961088	0.3	11.539062	0.168	15	94	10.324
2010	1	20	21	55	19.48	44.556239	-110.963771	1.7	10.384766	0.146	22	94	11.4924
2010	1	20	22	3	10.29	44.571796	-110.977931	0.1	10.583984	0.063	10	138	10.4222
2010	1	20	22	10	11.10	44.567906	-110.981049	0.7	10.513672	0.100	15	93	10.3596
2010	1	20	22	31	53.39	44.560906	-110.973188	0.5	9.166016	0.087	12	94	11.2518
2010	1	20	22	32	50.95	44.563628	-110.972807	0.3	9.628906	0.107	13	93	11.149
2010	1	20	22	48	14.71	44.565573	-110.97634	1.1	9.447266	0.160	20	93	10.8053
2010	1	20	22	53	38.81	44.562851	-110.976721	0.5	9.101562	0.102	10	99	10.9061

<i>Yr</i>	<i>Mo</i>	<i>Day</i>	<i>Hr</i>	<i>Mn</i>	<i>Sec</i>	<i>Lat</i>	<i>Lon</i>	<i>Mag</i>	<i>Depth</i>	<i>RMS</i>	<i>Nphs</i>	<i>Gap</i>	<i>Dist</i>
2010	1	20	23	3	45.88	44.567906	-110.973215	0.0	9.962891	0.057	11	142	10.929
2010	1	20	23	11	17.70	44.551572	-110.965321	0.8	10.583984	0.122	16	96	11.9104
2010	1	20	23	12	57.29	44.56324	-110.977114	0.0	8.427734	0.090	11	143	10.8593
2010	1	20	23	22	45.73	44.557795	-110.96691	0.2	10.326172	0.092	14	94	11.5882
2010	1	20	23	23	33.61	44.556239	-110.966121	1.5	10.396484	0.107	14	140	11.6408
2010	1	20	23	23	58.12	44.556239	-110.962988	0.5	11.287109	0.120	13	140	11.4431
2010	1	20	23	28	31.71	44.556239	-110.968471	0.4	9.833984	0.098	12	149	11.7903
2010	1	20	23	35	11.82	44.546127	-110.959819	1.1	9.869141	0.138	13	96	11.9766
2010	1	20	23	35	31.33	44.554294	-110.977471	1.0	11.292969	0.102	6	247	11.3011
2010	1	20	23	39	10.31	44.560517	-110.972795	0.5	8.832031	0.109	10	146	11.7987
2010	1	20	23	42	29.12	44.554294	-110.96024	0.5	10.074219	0.114	12	93	11.4068
2010	1	20	23	51	11.80	44.551572	-110.968453	1.1	9.986328	0.088	13	106	12.0696
2010	1	21	1	4	27.24	44.565962	-110.973599	1.4	9.804688	0.095	14	92	10.9857
2010	1	21	1	8	14.03	44.565184	-110.975946	0.5	9.535156	0.081	11	142	10.8514
2010	1	21	1	19	46.00	44.56324	-110.97163	2.5	9.669922	0.149	25	93	11.2516
2010	1	21	1	20	52.98	44.565184	-110.97438	1.2	10.097656	0.122	8	137	10.9643
2010	1	21	1	24	23.05	44.565184	-110.97438	0.8	9.769531	0.095	10	99	10.9643
2010	1	21	1	26	9.73	44.572962	-110.975977	0.9	10.449219	0.070	11	227	10.5211
2010	1	21	1	31	54.14	44.563628	-110.972807	0.7	9.746094	0.113	11	237	11.149
2010	1	21	1	32	34.91	44.562073	-110.974368		9.652344	0.102	11	238	11.1112
2010	1	21	1	56	3.35	44.562073	-110.977501	1.9	9.582031	0.126	22	95	10.8887
2010	1	21	1	58	6.19	44.572962	-110.97911	0.2	10.261719	0.045	10	137	10.2888
2010	1	21	2	0	10.55	44.564017	-110.97555	0.5	9.505859	0.105	13	93	10.9341
2010	1	21	2	1	18.44	44.564017	-110.97555	2.0	9.623047	0.145	24	93	10.9341
2010	1	21	2	3	47.23	44.557795	-110.979442	1.1	9.974609	0.121	18	97	10.9734
2010	1	21	2	4	59.56	44.564795	-110.973986	1.0	9.927734	0.145	19	93	11.0104
2010	1	21	2	6	14.74	44.556239	-110.984919	1.7	9.212891	0.150	21	100	10.6843
2010	1	21	2	9	28.14	44.567906	-110.984183	0.1	10.033203	0.053	10	139	10.1335
2010	1	21	2	12	48.27	44.571018	-110.985762	0.1	9.283203	0.066	10	137	9.88042
2010	1	21	2	30	50.01	44.560517	-110.983761	0.0	9.324219	0.060	10	142	10.5287
2010	1	21	2	34	38.08	44.566351	-110.977909	0.1	9.259766	0.098	11	141	10.6566
2010	1	21	2	36	12.01	44.563628	-110.982207	0.3	9.699219	0.065	10	141	10.4786
2010	1	21	2	53	51.96	44.561684	-110.977108	0.7	9.669922	0.140	17	95	10.9358
2010	1	21	2	57	30.20	44.553128	-110.962977	0.9	10.794922	0.082	17	95	11.657
2010	1	21	2	57	49.50	44.558573	-110.969263	2.1	9.962891	0.141	22	94	11.6451
2010	1	21	3	5	46.24	44.558573	-110.969263	1.3	10.197266	0.114	21	94	11.6451
2010	1	21	3	28	15.16	44.557795	-110.968477	0.3	10.408203	0.100	15	94	11.6889
2010	1	21	3	29	10.79	44.565184	-110.968113	0.6	8.527344	0.067	8	148	11.4182
2010	1	21	3	29	43.83	44.575296	-110.979903	0.9	9.757812	0.120	10	136	10.1412
2010	1	21	3	34	12.99	44.56674	-110.974386	0.5	9.839844	0.062	10	142	10.8943
2010	1	21	3	46	59.82	44.568295	-110.977525	0.8	9.699219	0.081	8	140	10.598
2010	1	21	3	47	58.47	44.567129	-110.974779	0.9	9.611328	0.122	14	92	10.8486
2010	1	21	3	55	51.60	44.560128	-110.966136	1.5	9.681641	0.146	20	93	11.3872
2010	1	21	3	58	36.09	44.562851	-110.973587	0.5	8.585938	0.111	9	144	11.7103
2010	1	21	4	8	57.03	44.571407	-110.968136	1.0	10.308594	0.089	13	88	10.8102
2010	1	21	4	13	20.80	44.571407	-110.97127	0.6	9.582031	0.099	11	140	10.8194
2010	1	21	4	13	31.30	44.574129	-110.970889	0.7	9.763672	0.123	14	135	10.5158
2010	1	21	4	17	56.69	44.564017	-110.9732	1.2	9.306641	0.109	12	144	11.1028
2010	1	21	5	4	50.44	44.557017	-110.960641	1.4	10.525391	0.120	15	92	11.2431
2010	1	21	5	6	12.74	44.555461	-110.957503	1.2	10.455078	0.105	15	92	11.1566
2010	1	21	5	9	20.09	44.543405	-110.845873	0.8	18.863281	0.248	8	179	8.4018
2010	1	21	5	14	19.38	44.571796	-110.965396	1.0	10.537109	0.093	13	120	10.6413
2010	1	21	5	27	28.01	44.567129	-110.974779	1.2	9.916016	0.110	15	92	10.8486
2010	1	21	5	48	48.68	44.571407	-110.974404	1.0	9.816406	0.077	10	89	10.6981
2010	1	21	5	51	54.69	44.563628	-110.974374	0.6	9.019531	0.112	9	144	11.0366
2010	1	21	6	1	49.92	44.557795	-110.974743	3.5	8.263672	0.178	29	96	11.2999
2010	1	21	6	3	59.39	44.549627	-110.969621	1.8	8.269531	0.077	9	152	12.0992
2010	1	21	6	5	41.85	44.561684	-110.979458	1.7	9.974609	0.090	12	143	10.7698
2010	1	21	6	12	27.28	44.564795	-110.977903	1.0	9.541016	0.086	11	142	10.729
2010	1	21	6	15	1.60	44.565184	-110.977513	1.2	9.769531	0.063	11	142	10.7388
2010	1	21	6	16	18.70	44.562851	-110.967321	3.7	9.429688	0.180	27	92	11.2936
2010	1	21	6	18	59.99	44.557017	-110.97004	2.2	10.091797	0.121	21	95	11.6691

<i>Yr</i>	<i>Mo</i>	<i>Day</i>	<i>Hr</i>	<i>Mn</i>	<i>Sec</i>	<i>Lat</i>	<i>Lon</i>	<i>Mag</i>	<i>Depth</i>	<i>RMS</i>	<i>Nphs</i>	<i>Gap</i>	<i>Dist</i>
2010	1	21	6	24	43.08	44.559739	-110.967309	1.1	11.257812	0.209	11	124	11.4882
2010	1	21	6	28	47.98	44.568295	-110.975958	0.8	9.019531	0.085	9	141	10.7122
2010	1	21	6	29	8.60	44.561684	-110.973191	1.4	9.892578	0.107	10	145	11.2137
2010	1	21	6	29	29.10	44.554294	-110.977471	0.4	9.253906	0.100	9	147	11.3011
2010	1	21	6	30	22.80	44.569462	-110.976355	0.9	9.224609	0.101	11	140	10.6337
2010	1	21	6	30	40.26	44.563628	-110.974374	0.9	9.558594	0.077	10	144	11.0366
2010	1	21	6	34	53.75	44.569851	-110.983799	1.3	9.417969	0.111	13	119	10.074
2010	1	21	6	36	30.17	44.565184	-110.986913	0.4	8.011719	0.098	7	139	11.6327
2010	1	21	6	36	43.81	44.556628	-110.854511	0.6	13.226562	0.237	6	209	6.94713
2010	1	21	6	37	8.11	44.562073	-111.001	0.8	-3.003906	0.135	6	137	12.1892
2010	1	21	6	39	6.97	44.571796	-110.976364	1.2	9.705078	0.117	13	110	10.5379
2010	1	21	6	42	17.21	44.565573	-110.969289	1.1	10.162109	0.093	12	144	11.2608
2010	1	21	6	45	48.22	44.54146	-110.966066	0.7	9.658203	0.163	15	100	12.6928
2010	1	21	6	51	30.42	44.569462	-110.978705	0.3	9.224609	0.101	13	91	10.4618
2010	1	21	6	52	23.82	44.547683	-110.970788	1.3	9.587891	0.134	20	99	12.1333
2010	1	21	6	53	15.73	44.569462	-110.994373	0.8	8.896484	0.128	13	96	9.33016
2010	1	21	6	56	18.76	44.564017	-110.96615	0.5	10.689453	0.097	12	91	11.1446
2010	1	21	6	56	51.65	44.567518	-110.972038	0.4	9.734375	0.162	12	91	11.0315
2010	1	21	7	4	47.04	44.562073	-110.977501	0.1	8.457031	0.023	8	144	10.8887
2010	1	21	7	5	15.44	44.572573	-110.97245	0.7	10.068359	0.097	13	88	10.6949
2010	1	21	7	6	17.41	44.57024	-110.988893	0.4	9.869141	0.049	11	94	9.68763
2010	1	21	7	18	21.38	44.562073	-110.960268	1.4	10.777344	0.174	19	90	10.8827
2010	1	21	7	23	30.51	44.574907	-110.976376	0.2	9.798828	0.116	14	88	10.4188
2010	1	21	7	23	48.80	44.553906	-110.964546	0.6	10.818359	0.182	12	106	11.7002
2010	1	21	7	25	59.00	44.561684	-110.966925	0.1	10.068359	0.100	13	92	11.34
2010	1	21	7	26	54.98	44.574129	-110.974806	0.2	10.396484	0.103	11	117	10.5349
2010	1	21	7	28	54.51	44.560906	-110.965355	0.9	10.349609	0.115	19	92	11.2868
2010	1	21	7	32	17.44	44.558573	-110.969263	0.4	9.787109	0.118	13	94	11.6451
2010	1	21	7	32	47.78	44.580352	-110.9858	0.4	9.623047	0.086	9	132	9.52232
2010	1	21	7	34	33.88	44.560906	-110.976321	1.5	9.705078	0.142	22	95	11.0301
2010	1	21	7	34	56.40	44.562462	-110.974761	1.2	9.189453	0.150	18	94	11.0644
2010	1	21	7	35	36.21	44.561684	-110.978674	0.4	8.498047	0.132	14	95	10.8251
2010	1	21	7	38	0.91	44.564795	-110.97947	0.0	9.669922	0.111	11	142	10.6168
2010	1	21	7	39	22.13	44.571796	-110.97558	0.1	9.763672	0.111	12	139	10.5958
2010	1	21	7	39	56.69	44.568684	-110.960684	0.5	10.431641	0.166	16	95	10.4991
2010	1	21	7	45	10.94	44.564795	-110.959103	0.9	11.216797	0.118	17	89	10.633
2010	1	21	7	47	46.41	44.560906	-110.974755	0.5	9.166016	0.130	14	95	11.1408
2010	1	21	7	48	6.85	44.562462	-110.979461	1.5	9.365234	0.140	20	95	10.7307
2010	1	21	7	48	33.34	44.562851	-110.976721	2.3	9.664062	0.132	23	94	10.9061
2010	1	21	7	49	31.26	44.568684	-110.968518	0.8	9.916016	0.141	20	89	11.0289
2010	1	21	7	51	26.79	44.573351	-110.966968	0.2	11.041016	0.142	12	97	10.5922
2010	1	21	7	52	13.93	44.556239	-110.976303	1.6	9.482422	0.161	22	97	11.2742
2010	1	21	8	3	15.96	44.556239	-110.970037	0.2	10.361328	0.126	12	95	11.7095
2010	1	21	8	4	9.10	44.55935	-110.974749	0.9	9.669922	0.142	20	95	11.2193
2010	1	21	8	8	2.42	44.564017	-110.9591	0.5	11.052734	0.153	16	89	10.6822
2010	1	21	8	8	36.75	44.56324	-110.958314	1.5	11.486328	0.142	15	124	10.6813
2010	1	21	8	12	52.02	44.569462	-110.963037	0.5	10.314453	0.139	15	88	10.6119
2010	1	21	8	17	47.72	44.550794	-110.971583	0.1	8.966797	0.069	12	98	11.8996
2010	1	21	8	20	10.36	44.562462	-110.972411	0.3	10.115234	0.119	14	93	11.2322
2010	1	21	8	21	28.82	44.549627	-110.971187	0.7	8.972656	0.098	11	151	11.9932
2010	1	21	8	23	59.83	44.562073	-110.977501	0.6	9.324219	0.055	10	144	10.8887
2010	1	21	8	27	1.00	44.572962	-110.97441	0.7	10.074219	0.098	12	95	10.6375
2010	1	21	8	28	22.89	44.569462	-110.981055	1.6	9.048828	0.149	22	92	10.2905
2010	1	21	8	31	22.27	44.562462	-110.967711	0.8	9.751953	0.127	15	92	11.3433
2010	1	21	8	35	58.70	44.560517	-110.977495	0.4	9.066406	0.113	13	95	10.967
2010	1	21	8	40	0.94	44.564795	-110.96537	0.6	10.970703	0.094	16	90	11.0454
2010	1	21	8	43	41.12	44.572573	-110.967749	1.6	10.572266	0.166	18	103	10.6798
2010	1	21	8	44	51.43	44.557406	-110.964951	0.8	9.136719	0.125	10	150	11.4888
2010	1	21	8	45	13.17	44.568295	-110.96029	0.4	10.285156	0.094	10	145	10.496
2010	1	21	8	46	48.86	44.436064	-110.336077	0.1	2.480469	0.168	8	112	6.38754
2010	1	21	8	47	6.48	44.558573	-110.962997	1.3	10.091797	0.119	19	92	11.287
2010	1	21	8	48	35.22	44.560517	-110.971228	1.1	10.027344	0.128	14	146	11.41

<i>Yr</i>	<i>Mo</i>	<i>Day</i>	<i>Hr</i>	<i>Mn</i>	<i>Sec</i>	<i>Lat</i>	<i>Lon</i>	<i>Mag</i>	<i>Depth</i>	<i>RMS</i>	<i>Npfs</i>	<i>Gap</i>	<i>Dist</i>
2010	1	21	8	50	26.45	44.566351	-110.971642	0.9	8.685547	0.113	13	91	11.1106
2010	1	21	8	53	18.04	44.561684	-110.967708	0.8	9.318359	0.099	12	147	11.3914
2010	1	21	8	53	38.55	44.562462	-110.953611	1.1	10.642578	0.102	14	124	10.4322
2010	1	21	8	55	4.29	44.561684	-110.963791	1.6	10.396484	0.103	19	91	11.1357
2010	1	21	8	56	13.04	44.561295	-110.965748	1.2	10.109375	0.139	13	123	11.2877
2010	1	21	8	56	43.21	44.562073	-110.963401	1.2	9.863281	0.122	13	123	11.0855
2010	1	21	8	58	48.56	44.556239	-110.968471	1.3	9.833984	0.119	15	95	11.7903
2010	1	21	9	4	53.94	44.564017	-110.9732	0.8	10.068359	0.122	13	174	11.1028
2010	1	21	9	5	6.36	44.560128	-110.970835	2.8	9.927734	0.134	24	94	11.4569
2010	1	21	9	8	45.62	44.571018	-110.96696	2.0	10.173828	0.117	23	88	10.7918
2010	1	21	9	12	18.49	44.578796	-110.981876	1.1	9.048828	0.065	12	87	9.87002
2010	1	21	9	14	13.17	44.558573	-110.964563	1.7	10.138672	0.117	21	93	11.3869
2010	1	21	9	22	25.53	44.565184	-110.961846	1.2	10.941406	0.124	12	103	10.7885
2010	1	21	9	22	54.29	44.576074	-110.963453	0.9	11.292969	0.132	13	97	10.2776
2010	1	21	9	23	34.20	44.581519	-110.957988	1.0	10.835938	0.097	10	219	9.61816
2010	1	21	9	24	41.01	44.611076	-111.009836	0.6	16.203125	0.129	6	143	7.3242
2010	1	21	9	26	15.88	44.557406	-110.955552	1.3	8.925781	0.173	17	91	10.9001
2010	1	21	9	28	24.94	44.573351	-110.988122	1.3	9.716797	0.130	16	92	9.60916
2010	1	21	9	29	59.87	44.557795	-110.96691	0.9	9.740234	0.091	12	149	11.5882
2010	1	21	9	32	39.70	44.574907	-110.988128	1.3	10.103516	0.119	15	91	9.54558
2010	1	21	9	35	12.80	44.56324	-110.960664	1.6	10.607422	0.112	19	90	10.8333
2010	1	21	9	37	7.11	44.566351	-110.966159	1.2	10.162109	0.126	16	90	11.0046
2010	1	21	9	42	37.52	44.564017	-110.953617	1.0	10.396484	0.098	12	140	10.3291
2010	1	21	9	42	54.03	44.565184	-110.963413	1.2	9.722656	0.149	16	93	10.892
2010	1	21	9	44	17.17	44.576463	-110.989702	1.2	10.091797	0.084	14	90	9.36837
2010	1	21	9	44	47.98	44.56674	-110.961852	0.8	10.214844	0.130	13	89	10.6937
2010	1	21	9	45	10.89	44.575685	-110.985781	0.9	9.623047	0.064	12	90	9.68916
2010	1	21	9	45	57.35	44.549627	-110.993115	1.5	9.535156	0.233	12	105	10.5496
2010	1	21	9	47	43.11	44.571796	-110.986549	1.6	9.224609	0.159	19	118	9.78968
2010	1	21	9	48	6.14	44.551183	-110.966494	1.0	9.113281	0.113	12	117	12.0099
2010	1	21	9	52	59.31	44.554683	-110.973164	1.2	9.787109	0.115	15	97	11.5752
2010	1	21	9	58	15.79	44.551183	-110.964928	0.7	9.042969	0.095	11	152	11.9136
2010	1	21	10	3	33.03	44.568684	-110.956767	0.7	11.181641	0.094	12	146	10.238
2010	1	21	10	4	16.21	44.562073	-110.971234	0.9	10.027344	0.126	19	93	11.3347
2010	1	21	10	8	17.27	44.564795	-110.976337	0.7	9.705078	0.117	13	93	10.8413
2010	1	21	10	13	16.02	44.557406	-110.972783	0.2	9.371094	0.071	12	96	11.457
2010	1	21	10	17	13.80	44.567129	-110.979479	1.1	9.201172	0.147	19	93	10.5081
2010	1	21	10	20	56.12	44.569462	-110.977138	0.6	9.951172	0.094	16	91	10.5763
2010	1	21	10	21	54.68	44.578796	-110.972473	0.4	10.666016	0.134	17	85	10.0047
2010	1	21	10	30	12.18	44.560906	-110.976321	1.3	9.705078	0.116	18	95	11.0301
2010	1	21	10	31	58.79	44.558573	-110.974746	0.9	9.611328	0.113	17	96	11.2594
2010	1	21	10	37	3.84	44.549239	-110.973927	1.6	9.810547	0.132	20	99	11.8313
2010	1	21	10	38	22.55	44.551572	-110.974719	2.3	9.669922	0.135	21	99	11.6425
2010	1	21	10	41	24.47	44.553128	-110.974725	1.7	10.712891	0.116	23	98	11.5539
2010	1	21	10	42	14.76	44.550794	-110.966101	1.5	10.337891	0.135	19	96	12.013
2010	1	21	10	42	38.66	44.546905	-110.971568	1.7	9.728516	0.135	21	100	12.1273
2010	1	21	10	44	58.23	44.543405	-110.97273	0.7	9.582031	0.095	10	152	12.2648
2010	1	21	10	46	58.22	44.55235	-110.975505	1.3	9.751953	0.137	20	99	11.5448
2010	1	21	10	47	33.77	44.562851	-110.973587	1.5	10.789062	0.113	17	93	11.1296
2010	1	21	10	49	14.99	44.554683	-110.969248	0.7	10.583984	0.112	16	96	11.8462
2010	1	21	10	53	4.29	44.557017	-110.969257	2.0	9.728516	0.142	17	95	11.7241
2010	1	21	10	53	45.09	44.551183	-110.966494	1.5	9.136719	0.113	12	126	12.0099
2010	1	21	10	54	4.50	44.546127	-110.964517	1.5	10.009766	0.111	17	98	12.2533
2010	1	21	10	54	28.54	44.57024	-110.959122	1.2	10.103516	0.149	17	86	10.3024
2010	1	21	11	3	48.37	44.564017	-110.96145	1.6	10.525391	0.136	16	123	10.8353
2010	1	21	11	7	24.01	44.549239	-110.973143	2.4	9.412109	0.141	23	99	11.8839
2010	1	21	11	10	24.78	44.568684	-110.973218	0.9	10.103516	0.102	16	90	10.8959
2010	1	21	11	16	22.28	44.56674	-110.979086	0.8	8.878906	0.123	11	141	11.3829
2010	1	21	11	16	48.46	44.569073	-110.973611	0.5	9.335938	0.103	10	141	11.0887
2010	1	21	11	18	28.22	44.552739	-110.974332	1.0	9.324219	0.095	10	149	11.6026
2010	1	21	11	19	50.94	44.551572	-110.970803	1.7	10.607422	0.118	16	97	11.9088
2010	1	21	11	22	6.74	44.561684	-110.963791	1.5	9.951172	0.098	15	91	11.1357

<i>Yr</i>	<i>Mo</i>	<i>Day</i>	<i>Hr</i>	<i>Mn</i>	<i>Sec</i>	<i>Lat</i>	<i>Lon</i>	<i>Mag</i>	<i>Depth</i>	<i>RMS</i>	<i>Nphs</i>	<i>Gap</i>	<i>Dist</i>
2010	1	21	11	23	1.70	44.565184	-110.961846	0.6	10.144531	0.115	10	147	10.7885
2010	1	21	11	23	49.41	44.564795	-110.97007	1.6	9.541016	0.152	16	104	11.3591
2010	1	21	11	26	47.32	44.565184	-110.977513	0.9	9.886719	0.050	8	142	11.5433
2010	1	21	11	28	24.86	44.567906	-110.955197	1.2	11.498047	0.153	16	87	10.1822
2010	1	21	11	29	49.38	44.569851	-110.977531	0.8	10.050781	0.049	9	139	10.5312
2010	1	21	11	30	48.42	44.554294	-110.979037	0.8	10.449219	0.069	8	246	11.1944
2010	1	21	11	36	23.85	44.548072	-110.971181	0.6	8.667969	0.092	10	152	12.0841
2010	1	21	11	39	59.30	44.551572	-110.966887	1.2	9.892578	0.125	16	96	12.007
2010	1	21	11	42	9.03	44.568295	-110.961857	0.6	10.355469	0.078	10	145	10.6008
2010	1	21	11	42	54.01	44.566351	-110.971642	1.4	9.728516	0.107	16	91	11.1106
2010	1	21	11	44	55.81	44.575685	-110.979513	1.1	9.833984	0.111	14	117	10.1561
2010	1	21	11	49	32.06	44.559739	-110.964176	1.2	9.851562	0.101	15	92	11.2858
2010	1	21	11	59	26.44	44.579574	-110.988147	0.5	9.330078	0.075	10	132	9.37141
2010	1	21	11	59	58.94	44.576463	-110.988918	1.0	10.291016	0.045	10	133	9.42653
2010	1	21	12	0	38.04	44.563628	-110.986907	0.4	8.199219	0.092	9	261	11.8036
2010	1	21	12	15	59.66	44.563628	-110.969674	0.8	8.972656	0.146	13	136	11.4022
2010	1	21	12	35	14.99	44.558961	-110.960257	1.1	9.582031	0.066	9	242	11.0872
2010	1	21	12	35	56.98	44.569851	-111.013569	0.2	10.261719	0.059	5	114	29.4971
2010	1	21	12	44	9.80	44.568684	-110.963817	0.9	10.291016	0.111	14	144	10.7099
2010	1	21	12	44	50.49	44.578018	-110.98579		9.658203	0.054	10	133	9.6026
2010	1	21	12	50	32.68	44.571407	-110.990072	0.3	9.253906	0.070	9	229	9.55013
2010	1	21	12	50	39.41	44.523181	-110.985177	0.7	6.980469	0.272	9	154	12.9445
2010	1	21	12	52	45.21	44.569851	-110.980665	0.3	8.691406	0.101	8	230	10.3022
2010	1	21	12	54	57.02	44.563628	-110.979074		10.542969	0.027	8	161	10.701
2010	1	21	12	54	59.89	44.562073	-110.979068	1.2	9.722656	0.076	8	257	10.7779
2010	1	21	13	1	47.49	44.557017	-110.965341	1.6	10.244141	0.105	19	94	11.5394
2010	1	21	13	2	38.59	44.560128	-110.964569	1.1	9.423828	0.084	12	92	11.2859
2010	1	21	13	7	36.98	44.568295	-110.964991	1.1	10.214844	0.095	12	137	10.8118
2010	1	21	13	16	2.27	44.563628	-110.97124	1.1	10.144531	0.113	12	145	11.2617
2010	1	21	13	16	26.01	44.565962	-110.976733	0.1	9.382812	0.113	11	142	10.7592
2010	1	21	13	20	54.39	44.562073	-110.969668	0.4	9.628906	0.115	10	239	11.4469
2010	1	21	13	22	34.10	44.558573	-110.982578	2.2	9.154297	0.143	23	98	10.7147
2010	1	21	13	23	30.72	44.577629	-110.974428	0.6	9.113281	0.056	10	222	10.1447
2010	1	21	13	23	42.66	44.564017	-110.98495	1.6	9.447266	0.106	16	96	10.2653
2010	1	21	13	30	18.19	44.563628	-110.97124	0.3	8.691406	0.083	9	145	11.2617
2010	1	21	13	30	47.68	44.563628	-110.94304	1.2	7.496094	0.130	10	153	9.69409
2010	1	21	13	31	24.63	44.569073	-110.979879	0.5	9.617188	0.141	10	145	11.1316
2010	1	21	13	41	24.92	44.558573	-110.979445	2.4	9.798828	0.136	21	97	10.9316
2010	1	21	13	42	17.13	44.551183	-110.964928	1.2	10.660156	0.125	10	142	11.9136
2010	1	21	13	42	31.10	44.673303	-110.890822	0.7	-0.015625	0.013	4	195	5.88503
2010	1	21	13	42	53.04	44.57024	-110.973224	1.0	10.701172	0.169	15	104	10.9574
2010	1	21	13	44	4.76	44.57024	-110.977925	1.3	9.810547	0.108	13	91	10.4861
2010	1	21	13	44	25.02	44.560517	-110.990028	0.3	8.410156	0.044	8	141	12.1841
2010	1	21	13	44	43.30	44.560128	-110.969269	0.6	9.798828	0.071	10	147	11.5682
2010	1	21	13	45	17.88	44.55935	-110.970832	1.6	10.291016	0.160	15	94	11.4955
2010	1	21	13	46	58.11	44.577629	-110.977562	0.5	8.761719	0.077	9	222	10.1666
2010	1	21	13	47	16.05	44.569851	-110.980665	0.1	9.183594	0.082	11	230	10.3022
2010	1	21	13	49	39.85	44.558961	-110.979055	0.2	8.597656	0.041	9	145	10.9382
2010	1	21	13	50	57.16	44.553517	-110.976684	0.5	8.726562	0.083	10	246	11.3985
2010	1	21	13	57	49.73	44.556239	-110.971604	1.3	9.376953	0.113	12	96	11.6003
2010	1	21	13	58	45.13	44.55585	-110.972777	1.4	9.558594	0.102	14	124	11.5392
2010	1	21	13	59	39.22	44.553517	-110.970419	0.2	7.554688	0.042	8	150	11.8279
2010	1	21	13	59	58.80	44.56324	-110.97633	1.2	9.962891	0.057	11	143	10.9152
2010	1	21	14	10	11.62	44.569462	-110.966954	1.7	9.845703	0.134	21	89	10.8782
2010	1	21	14	22	26.08	44.561684	-110.930892	1.9	8.169922	0.138	17	84	9.12157
2010	1	21	14	28	37.36	44.571407	-110.960302	0.3	10.800781	0.099	12	144	10.3145
2010	1	21	14	31	32.09	44.553906	-110.967679	1.7	10.373047	0.086	13	96	11.8962
2010	1	21	14	31	51.12	44.558961	-110.977489	0.6	10.167969	0.056	9	241	11.0474
2010	1	21	14	32	5.34	44.551183	-110.960229	1.0	10.378906	0.139	15	95	11.6278
2010	1	21	14	33	43.27	44.563628	-110.98534	1.2	8.597656	0.066	7	141	10.2574
2010	1	21	14	36	12.14	44.556239	-110.962205	1.1	10.595703	0.143	10	151	11.394
2010	1	21	14	36	49.59	44.523959	-110.978135	0.1	9.359375	0.247	11	155	13.2844

<i>Yr</i>	<i>Mo</i>	<i>Day</i>	<i>Hr</i>	<i>Mn</i>	<i>Sec</i>	<i>Lat</i>	<i>Lon</i>	<i>Mag</i>	<i>Depth</i>	<i>RMS</i>	<i>Nphs</i>	<i>Gap</i>	<i>Dist</i>
2010	1	21	14	38	59.79	44.55585	-110.950847	0.1	9.207031	0.079	8	154	10.7253
2010	1	21	14	39	10.73	44.556239	-110.969254	0.5	9.388672	0.116	13	149	11.7643
2010	1	21	14	43	18.26	44.549239	-110.962963	1.3	10.068359	0.124	17	96	11.9331
2010	1	21	14	48	2.47	44.556239	-110.962205	0.9	10.607422	0.087	10	93	11.394
2010	1	21	14	49	18.97	44.548461	-110.963743	1.2	10.162109	0.090	15	97	12.0364
2010	1	21	14	50	24.48	44.553128	-110.967676	0.7	9.693359	0.096	11	151	11.9489
2010	1	21	14	52	41.17	44.55935	-110.984931	1.8	9.294922	0.129	18	98	10.5102
2010	1	21	14	57	56.11	44.565184	-110.975946	0.7	8.902344	0.203	10	142	10.8514
2010	1	21	14	58	14.86	44.560517	-110.971228	0.5	10.777344	0.076	11	146	11.41
2010	1	21	14	59	3.65	44.56674	-110.983786	0.5	8.972656	0.082	10	139	10.2161
2010	1	21	15	13	13.61	44.571796	-110.963045	0.1	10.642578	0.115	12	143	10.4798
2010	1	21	15	13	42.23	44.56324	-110.966931	0.4	10.830078	0.104	10	146	11.2439
2010	1	21	15	24	51.60	44.583852	-110.982288	0.1	12.371094	0.204	8	130	9.52623
2010	1	21	15	25	12.89	44.574518	-110.968148	0.1	10.519531	0.124	8	140	10.4646
2010	1	21	15	25	24.17	44.556239	-110.970037	0.7	10.373047	0.101	13	95	11.7095
2010	1	21	15	26	14.65	44.558573	-110.964563	1.5	10.162109	0.105	15	93	11.3869
2010	1	21	15	26	52.24	44.548072	-110.974314	0.3	8.480469	0.080	9	151	11.8746
2010	1	21	15	30	29.35	44.550405	-110.992335	0.4	9.007812	0.057	6	301	13.3229
2010	1	21	15	32	25.32	44.564795	-110.963803	0.9	12.248047	0.201	16	90	10.9416
2010	1	21	15	38	20.62	44.56324	-110.97398	0.9	10.373047	0.107	15	100	11.0831
2010	1	21	15	39	0.42	44.563628	-110.979074	0.1	8.832031	0.162	11	237	10.701
2010	1	21	15	39	34.10	44.569851	-110.969697	1.2	10.191406	0.099	16	89	10.9868
2010	1	21	15	57	42.44	44.557017	-110.968474	0.2	10.080078	0.105	13	95	11.7394
2010	1	21	16	0	57.16	44.557017	-110.968474	0.5	10.314453	0.113	15	95	11.7394
2010	1	21	16	4	35.95	44.568684	-110.995937	0.6	12.998047	0.213	11	97	9.25675
2010	1	21	16	17	15.76	44.545349	-110.966081	0.3	9.728516	0.106	14	98	12.4035
2010	1	21	16	23	56.40	44.57024	-110.94267	1.0	9.177734	0.096	11	150	9.2202
2010	1	21	16	29	14.54	44.55235	-110.96689	0.7	10.537109	0.084	17	96	11.9533
2010	1	21	16	32	19.59	44.571796	-110.966962	0.3	11.029297	0.077	12	103	10.7493
2010	1	21	16	45	18.28	44.561684	-110.956742	0.6	9.541016	0.131	13	90	10.6826
2010	1	21	16	49	27.31	44.576463	-110.984217	0.3	8.826172	0.097	11	91	9.77644
2010	1	21	17	22	28.41	44.567906	-110.986533	0.3	9.822266	0.089	10	138	9.9646
2010	1	21	17	22	45.52	44.565184	-110.980647	0.9	9.863281	0.144	15	94	10.5143
2010	1	21	17	23	15.29	44.574129	-110.981074	1.0	8.861328	0.129	18	90	10.0981
2010	1	21	17	35	13.73	44.557795	-110.977093	0.3	9.587891	0.096	11	146	11.1363
2010	1	21	17	36	57.59	44.567129	-110.967728	1.7	10.455078	0.148	20	90	11.0646
2010	1	21	17	42	29.42	44.565962	-110.973599	0.9	10.648438	0.200	17	92	10.9857
2010	1	21	17	45	19.05	44.57024	-110.975574	1.1	10.361328	0.076	12	140	10.6587
2010	1	21	17	48	14.73	44.566351	-110.970859	0.9	9.833984	0.122	13	143	11.1676
2010	1	21	17	51	56.00	44.55935	-110.984148	1.9	9.189453	0.178	24	98	10.5643
2010	1	21	17	53	20.54	44.565573	-110.964589	1.0	10.806641	0.109	16	90	10.9464
2010	1	21	17	58	15.87	44.571018	-110.970093	0.4	10.595703	0.140	13	98	10.8585
2010	1	21	18	17	57.98	44.567129	-110.963811	0.3	9.787109	0.161	15	89	10.8011
2010	1	21	18	19	3.60	44.554683	-110.942619	0.5	10.560547	0.166	12	89	12.7836
2010	1	21	18	19	33.63	44.578018	-110.974821	0.2	12.587891	0.154	13	86	10.1041
2010	1	21	18	27	28.53	44.576463	-110.981867	1.7	9.998047	0.134	22	89	9.952
2010	1	21	18	32	6.61	44.568295	-110.969691	0.8	11.457031	0.079	10	93	11.131
2010	1	21	18	34	30.29	44.561684	-110.965358	1.7	10.080078	0.148	21	92	11.2376
2010	1	21	18	37	23.31	44.569462	-110.95912	0.3	11.404297	0.117	13	87	10.3481
2010	1	21	18	37	49.45	44.562462	-110.965361	1.0	10.501953	0.160	19	91	11.1889
2010	1	21	18	46	35.31	44.558573	-110.955947	0.9	9.763672	0.097	13	91	10.8435
2010	1	21	18	47	4.06	44.571018	-110.984195	1.2	9.634766	0.098	15	92	9.99467
2010	1	21	18	47	50.03	44.57724	-110.977952	1.5	9.517578	0.078	9	117	10.2182
2010	1	21	18	54	42.23	44.580352	-110.981098	0.6	9.564453	0.041	12	133	9.87818
2010	1	21	18	56	11.27	44.565184	-110.938345	0.0	8.621094	0.147	11	84	9.29742
2010	1	21	19	0	31.36	44.551183	-110.979025	0.3	8.925781	0.097	11	148	11.3751
2010	1	21	19	10	49.65	44.572962	-110.980677	0.0	9.394531	0.045	10	137	10.173
2010	1	21	19	11	9.89	44.564795	-110.966153	1.0	10.970703	0.111	17	91	11.0974
2010	1	21	19	11	38.91	44.560517	-110.964962	0.6	10.097656	0.109	15	92	11.2862
2010	1	21	19	13	41.69	44.562462	-110.969278	0.3	10.080078	0.108	13	92	11.4468
2010	1	21	19	21	27.04	44.550794	-110.94104	0.4	9.869141	0.122	16	90	10.5479
2010	1	21	19	26	6.03	44.547683	-110.965306	0.3	9.576172	0.097	12	97	12.1868

<i>Yr</i>	<i>Mo</i>	<i>Day</i>	<i>Hr</i>	<i>Mn</i>	<i>Sec</i>	<i>Lat</i>	<i>Lon</i>	<i>Mag</i>	<i>Depth</i>	<i>RMS</i>	<i>Nphs</i>	<i>Gap</i>	<i>Dist</i>
2010	1	21	19	28	28.43	44.569462	-110.987323	0.7	10.349609	0.056	12	94	9.83617
2010	1	21	19	33	39.73	44.568295	-110.988493	0.2	7.941406	0.123	9	137	9.80587
2010	1	21	19	44	40.48	44.568684	-110.969301	0.3	10.443359	0.117	13	116	11.0824
2010	1	21	19	46	32.05	44.560128	-110.969269	0.8	10.185547	0.098	13	93	11.5682
2010	1	21	19	54	1.34	44.550794	-110.955137	0.6	-3.994141	0.171	9	140	11.3526
2010	1	21	19	54	32.90	44.593964	-110.961167	0.1	11.304688	0.011	5	240	8.30508
2010	1	21	20	7	37.93	44.557017	-110.935577	2.1	7.748047	0.169	21	87	9.75063
2010	1	21	20	27	1.86	44.563628	-110.97594	0.4	9.207031	0.081	10	237	10.9245
2010	1	21	20	28	22.09	44.563628	-110.977507	0.3	9.605469	0.060	10	143	10.8126
2010	1	21	20	31	11.83	44.544572	-110.945718	0.6	10.068359	0.084	12	139	11.3054
2010	1	21	20	47	56.55	44.566351	-110.970859	0.4	9.611328	0.124	13	143	11.3214
2010	1	21	20	49	54.90	44.557795	-110.983359	0.6	9.142578	0.121	11	144	10.7035
2010	1	21	20	52	13.56	44.569851	-110.961863	0.5	10.683594	0.132	14	144	10.51
2010	1	21	21	44	6.01	44.569462	-110.960686	0.6	11.134766	0.097	13	145	10.4533
2010	1	21	21	57	16.37	44.560128	-110.968485	1.1	10.595703	0.081	14	93	11.54
2010	1	21	22	1	22.40	44.554683	-110.969248	2.0	9.494141	0.081	11	150	11.8462
2010	1	21	22	1	54.12	44.55935	-110.962216	0.8	8.896484	0.085	11	150	11.1858
2010	1	21	22	26	19.20	44.55935	-110.963783	1.9	10.501953	0.112	20	92	11.286
2010	1	21	22	27	10.76	44.557406	-110.975916	0.3	10.097656	0.052	10	243	11.2387
2010	1	21	22	27	52.76	44.556628	-110.97043	0.6	9.476562	0.109	10	148	11.6619
2010	1	21	22	28	25.29	44.555461	-110.966902	1.5	9.927734	0.092	18	95	11.7423
2010	1	21	22	30	8.89	44.562073	-110.966534	1.0	11.152344	0.125	19	92	11.2901
2010	1	21	22	38	21.45	44.575296	-110.983037	0.3	9.195312	0.039	9	225	9.90781
2010	1	21	22	44	27.04	44.564795	-110.971636	0.5	10.384766	0.079	12	144	11.18
2010	1	21	22	48	15.46	44.569073	-110.967344	0.0	10.273438	0.068	9	143	10.9268
2010	1	21	22	48	46.42	44.567906	-110.972432	0.1	9.705078	0.079	10	142	10.9862
2010	1	21	23	28	30.98	44.56324	-110.96928	0.1	9.974609	0.088	12	145	11.3996
2010	1	21	23	46	58.04	44.563628	-110.983774	0.6	9.910156	0.121	12	96	10.3678
2010	1	22	1	21	16.89	44.564017	-110.971633	0.4	10.736328	0.076	13	92	11.2155
2010	1	22	1	33	53.55	44.561684	-110.983374	0.3	9.857422	0.050	10	142	10.4947
2010	1	22	1	54	15.15	44.55935	-110.972399	0.1	9.916016	0.100	11	146	11.3848
2010	1	22	1	57	30.97	44.556239	-110.962205	0.5	10.443359	0.105	14	93	11.394
2010	1	22	2	2	43.00	44.561684	-110.967708	0.6	10.888672	0.113	15	92	11.3914
2010	1	22	2	19	24.09	44.573351	-110.981854	0.6	9.236328	0.090	13	93	10.0707
2010	1	22	2	19	52.68	44.567129	-110.972429	0.0	10.091797	0.127	13	98	11.0197
2010	1	22	2	24	1.89	44.556239	-110.968471	0.5	10.455078	0.127	14	95	11.7903
2010	1	22	2	33	33.96	44.571796	-110.951293	0.6	10.759766	0.128	10	104	9.68569
2010	1	22	2	50	44.57	44.567906	-110.958331	0.1	8.685547	0.103	11	146	10.3891
2010	1	22	2	53	47.96	44.567129	-110.954411	0.8	9.787109	0.154	18	87	10.1795
2010	1	22	3	23	20.78	44.555461	-110.987265	0.7	9.271484	0.128	17	101	10.5709
2010	1	22	3	29	15.00	44.55935	-110.931668	0.1	8.369141	0.131	14	85	9.34807
2010	1	22	3	29	49.47	44.551572	-110.961405	1.2	10.759766	0.108	17	95	11.671
2010	1	22	3	40	14.57	44.558573	-110.958297	0.9	10.513672	0.100	13	151	10.9902
2010	1	22	3	42	12.95	44.565184	-110.971246	0.6	11.152344	0.168	8	261	11.4154
2010	1	22	3	45	15.26	44.565962	-110.979866	0.3	9.148438	0.070	8	234	10.5337
2010	1	22	3	47	4.36	44.57024	-110.961473	0.8	8.474609	0.151	14	87	10.4611
2010	1	22	3	47	57.48	44.55935	-110.935585	2.3	8.263672	0.160	20	86	9.56926
2010	1	22	3	49	23.01	44.56674	-110.963418	1.2	11.902344	0.069	9	137	11.3256
2010	1	22	4	0	55.77	44.560517	-110.93833	1.3	7.355469	0.146	13	155	9.63911
2010	1	22	4	1	9.04	44.566351	-110.940307	0.7	7.255859	0.172	13	153	9.33488
2010	1	22	4	5	41.85	44.558961	-110.957124	0.9	11.035156	0.089	13	125	10.8901
2010	1	22	4	9	1.34	44.556239	-110.969254	2.4	9.470703	0.164	27	95	11.7643
2010	1	22	4	11	18.29	44.567518	-110.959504	1.0	10.296875	0.134	12	234	10.4906
2010	1	22	4	14	55.83	44.561684	-110.963791	0.8	9.822266	0.133	13	91	11.1357
2010	1	22	4	15	21.62	44.574129	-110.97794	1.1	9.248047	0.115	15	89	10.3309
2010	1	22	4	28	33.77	44.564017	-110.972417	1.7	9.974609	0.148	23	92	11.1591
2010	1	22	4	29	57.87	44.571796	-110.977147	0.1	9.822266	0.107	12	95	10.48
2010	1	22	4	32	15.85	44.56674	-110.972819	0.4	9.300781	0.143	11	117	11.3438
2010	1	22	4	34	54.13	44.571018	-110.96931	1.5	9.927734	0.144	18	88	10.8562
2010	1	22	4	35	30.92	44.55235	-110.965324	1.3	9.716797	0.169	20	96	11.8562
2010	1	22	4	44	5.23	44.572573	-110.966965	1.2	10.138672	0.145	22	87	10.6786
2010	1	22	4	48	24.33	44.566351	-110.957542	0.9	11.427734	0.104	16	123	10.4331

<i>Yr</i>	<i>Mo</i>	<i>Day</i>	<i>Hr</i>	<i>Mn</i>	<i>Sec</i>	<i>Lat</i>	<i>Lon</i>	<i>Mag</i>	<i>Depth</i>	<i>RMS</i>	<i>Nphs</i>	<i>Gap</i>	<i>Dist</i>
2010	1	22	4	49	1.96	44.544572	-110.973909	1.3	10.009766	0.136	14	127	12.1149
2010	1	22	4	55	52.45	44.550794	-110.969234	0.2	9.740234	0.117	14	97	12.0595
2010	1	22	4	56	56.26	44.560906	-110.970838	1.1	9.447266	0.174	21	93	11.4188
2010	1	22	4	59	54.75	44.569851	-110.979098	1.1	8.527344	0.125	21	91	10.4166
2010	1	22	5	1	22.98	44.571796	-110.977931	0.6	8.873047	0.108	16	91	10.4222
2010	1	22	5	3	39.15	44.571796	-110.97088	0.6	10.337891	0.109	13	97	10.7748
2010	1	22	5	4	29.27	44.546905	-110.962171	0.0	9.505859	0.220	12	97	12.0567
2010	1	22	5	10	46.98	44.546905	-110.976267	0.6	8.849609	0.155	16	101	11.8158
2010	1	22	5	12	24.77	44.562073	-110.983767	0.9	9.324219	0.129	16	97	10.4472
2010	1	22	5	22	5.21	44.546905	-110.970785	1.7	10.138672	0.138	22	99	12.1796
2010	1	22	5	24	15.00	44.571018	-110.974794	1.2	7.923828	0.149	19	90	10.6847
2010	1	22	5	26	8.88	44.550016	-110.966881	0.6	10.431641	0.130	17	97	12.1157
2010	1	22	5	38	39.55	44.545349	-110.972345	2.9	9.025391	0.185	26	100	12.1698
2010	1	22	5	39	27.34	44.554683	-110.970031	1.5	9.458984	0.097	14	96	11.7919
2010	1	22	5	39	54.08	44.550794	-110.96845	1.4	9.751953	0.102	15	97	12.113
2010	1	22	5	44	1.90	44.553906	-110.967679	1.8	10.595703	0.108	15	139	11.8962
2010	1	22	5	44	35.67	44.548461	-110.972357	1.0	9.095703	0.164	18	99	11.9823
2010	1	22	5	45	48.73	44.546127	-110.973132	1.1	10.291016	0.172	24	100	12.0704
2010	1	22	5	46	15.67	44.568295	-110.963424	0.5	11.292969	0.098	9	115	10.7061
2010	1	22	5	47	4.11	44.574129	-110.978723	1.9	10.044922	0.119	19	90	10.2727
2010	1	22	5	47	41.92	44.572573	-110.97245	1.6	8.240234	0.173	16	92	10.6949
2010	1	22	5	51	38.23	44.545349	-110.971562	1.6	10.208984	0.087	20	100	12.2215
2010	1	22	5	57	12.21	44.578796	-110.977175	1.6	9.787109	0.086	10	135	10.0346
2010	1	22	5	57	36.96	44.55935	-110.974749	1.7	9.705078	0.101	17	95	11.2193
2010	1	22	5	58	56.12	44.556239	-110.968471	1.5	10.173828	0.105	12	149	11.7903
2010	1	22	6	0	16.24	44.553128	-110.969242	1.1	9.974609	0.109	17	96	11.9301
2010	1	22	6	1	13.25	44.566351	-110.98496	1.0	9.025391	0.098	12	139	10.1506
2010	1	22	6	1	26.11	44.534849	-110.992271	1.1	5.726562	0.165	10	150	11.643
2010	1	22	6	1	45.83	44.57724	-110.974818	1.2	8.896484	0.112	20	91	10.1902
2010	1	22	6	3	5.79	44.576074	-110.969721	0.8	10.167969	0.083	9	224	10.2959
2010	1	22	6	3	25.88	44.543405	-110.974296	0.6	10.847656	0.060	8	254	12.1627
2010	1	22	6	4	7.81	44.581907	-110.977797	1.2	9.470703	0.082	14	133	9.69713
2010	1	22	6	4	26.71	44.574129	-110.981074	1.5	8.908203	0.125	19	90	10.0981
2010	1	22	6	6	10.72	44.562073	-110.979068	1.3	9.605469	0.128	13	143	10.7779
2010	1	22	6	6	54.90	44.571796	-110.979498	2.1	9.119141	0.142	29	90	10.3067
2010	1	22	6	9	18.16	44.573351	-110.966185	1.7	10.279297	0.120	23	87	10.5913
2010	1	22	6	10	24.41	44.55935	-110.979448	1.9	9.763672	0.149	22	97	10.8904
2010	1	22	6	12	29.71	44.580352	-110.97483	1.2	9.048828	0.070	12	133	9.84563
2010	1	22	6	18	20.13	44.578407	-110.979915	1.2	10.648438	0.029	8	221	10.0308
2010	1	22	6	21	26.88	44.550016	-110.966098	1.7	10.103516	0.113	22	97	12.0677
2010	1	22	6	22	36.00	44.54496	-110.966471	0.8	8.902344	0.095	10	153	12.4553
2010	1	22	6	26	53.88	44.550405	-110.967274	1.1	9.148438	0.112	11	97	12.1124
2010	1	22	6	43	2.21	44.543405	-110.968031	0.7	10.191406	0.074	9	253	12.5734
2010	1	22	6	43	54.50	44.55585	-110.98061	0.0	8.035156	0.014	6	244	10.9997
2010	1	22	6	44	29.83	44.578018	-110.982656	0.6	8.392578	0.081	11	134	9.83777
2010	1	22	6	47	39.57	44.561684	-110.977891	0.8	9.494141	0.175	13	99	10.8804
2010	1	22	6	59	39.05	44.571018	-110.980278	2.2	8.978516	0.135	23	91	10.2813
2010	1	22	7	1	10.71	44.575685	-110.979513	1.5	9.939453	0.100	13	90	10.1561
2010	1	22	7	1	34.02	44.568684	-110.973218	1.3	8.814453	0.131	13	92	10.8959
2010	1	22	7	2	35.19	44.557795	-110.970826	0.5	9.810547	0.119	10	148	11.5741
2010	1	22	7	2	48.74	44.574129	-110.977794	0.5	8.380859	0.062	10	134	10.3309
2010	1	22	7	4	34.96	44.552739	-110.971199	1.0	9.792969	0.090	12	139	11.8168
2010	1	22	7	7	39.07	44.530182	-110.95937	0.4	12.453125	0.270	11	198	13.2183
2010	1	22	7	7	55.96	44.538738	-111.0009	0.3	5.996094	0.094	8	260	10.8495
2010	1	22	7	8	12.80	44.56674	-110.977519	0.5	8.902344	0.122	11	141	11.3711
2010	1	22	7	8	28.57	44.574129	-110.968538	0.6	9.611328	0.112	12	140	10.5087
2010	1	22	7	9	32.34	44.556628	-110.97043	1.1	10.132812	0.120	12	148	11.8904
2010	1	22	7	12	19.69	44.557406	-110.941453	0.6	13.261719	0.152	8	243	10.0558
2010	1	22	7	12	49.87	44.550405	-110.929683	0.7	10.414062	0.112	11	247	9.97642
2010	1	22	7	13	51.57	44.541071	-110.926522	0.3	10.273438	0.054	5	252	10.6434
2010	1	22	7	14	8.19	44.541849	-110.927307	0.7	10.449219	0.106	11	251	10.6096
2010	1	22	7	19	8.21	44.559739	-110.929711	0.8	10.039062	0.105	17	144	9.20845


























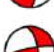
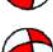
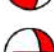


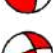

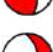

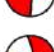
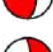

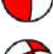
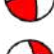
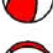
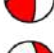

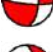

<i>Yr</i>	<i>Mo</i>	<i>Day</i>	<i>Hr</i>	<i>Mn</i>	<i>Sec</i>	<i>Lat</i>	<i>Lon</i>	<i>Mag</i>	<i>Depth</i>	<i>RMS</i>	<i>Nphs</i>	<i>Gap</i>	<i>Dist</i>
2010	1	22	7	20	8.48	44.562073	-110.972801	1.2	9.582031	0.118	11	238	11.2228
2010	1	22	7	21	4.11	44.600964	-110.941596	0.3	10.308594	0.215	10	198	7.63521
2010	1	22	7	29	29.82	44.557406	-110.96965	0.3	9.722656	0.092	11	243	11.6766
2010	1	22	7	49	19.67	44.551183	-110.928902	0.9	9.394531	0.084	9	233	9.87038
2010	1	22	7	56	16.53	44.562462	-110.961444	1.8	10.033203	0.153	20	90	10.9337
2010	1	22	7	57	3.23	44.558961	-110.969656	0.6	9.933594	0.097	9	265	11.6902
2010	1	22	7	59	25.60	44.562462	-110.965361	1.3	10.279297	0.106	15	91	11.1889
2010	1	22	8	16	12.34	44.562073	-110.969668	0.6	10.332031	0.080	10	239	11.4469
2010	1	22	8	17	50.93	44.557406	-110.968084	0.4	9.957031	0.114	11	243	11.6889
2010	1	22	8	23	50.07	44.539905	-110.966061	1.3	10.302734	0.140	16	100	12.8107
2010	1	22	8	29	52.01	44.548072	-110.971181	0.4	9.535156	0.086	10	152	12.0841









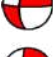
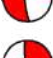


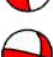














Appendix 4

Focal mechanism solutions of the Yellowstone volcanic plateau







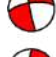
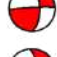
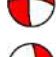
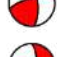
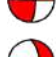

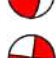

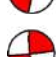

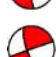
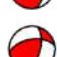











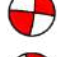
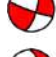
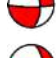


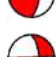

2010

Year, Month, Day, Hour, Minute, Seconds, Latitude, Longitude, Depth, Strike, Dip, Rake

 2010;1;19;13;39;12,48;44,56317;-110,9615;9,69;269;83;178	 2010;1;19;3;39;38,78;44,55933;-110,97;9,45;270;87;163
 2010;1;18;9;18;9,35;44,56017;-110,9615;10,48;80;90;177	 2010;1;18;11;56;12,33;44,55617;-110,9685;9,07;264;80;166
 2010;1;20;14;27;22,31;44,55733;-110,9665;9,51;265;85;175	 2010;1;20;14;8;30,35;44,564;-110,96767;9,49;265;77;173
 2010;1;25;6;9;45,48;44,562;-110,96333;9,79;267;85;172	 2010;1;24;9;55;45,99;44,56017;-110,95834;10,2;253;77;175
 2010;1;18;1;58;10,19;44,555;-110,96567;9,27;268;86;169	 2010;1;21;9;5;6,36;44,56017;-110,97083;9,93;269;84;169
 2010;1;18;5;54;53,16;44,5555;-110,9645;9;258;46;166	 2010;1;18;16;27;4,26;44,5625;-110,96533;10,94;268;68;177
 2010;1;18;19;16;22,26;44,56167;-110,96933;9,83;64;81;163	 2010;1;20;19;22;31;44,5585;-110,96533;11,04;93;90;178
 2010;1;19;22;18;0,22;44,5555;-110,97083;10,31;265;68;160	 2010;1;24;9;14;16,42;44,5625;-110,9615;10,63;258;72;179
 2010;1;24;17;21;23,99;44,56167;-110,95667;10,91;260;83;154	 2010;1;18;18;3;13,82;44,5555;-110,9685;9,76;267;70;176
 2010;1;22;5;47;4,11;44,57417;-110,97867;10,04;261;75;178	 2010;1;18;5;51;56,98;44,55383;-110,95834;9,65;249;71;174
 2010;1;20;21;43;0,44;44,56717;-110,97317;9,44;271;85;177	 2010;1;18;21;1;17,03;44,5625;-110,974;9,76;81;89;170
 2010;1;28;8;46;14,76;44,56717;-110,96933;8,93;273;83;175	 2010;1;19;21;7;4,76;44,54683;-110,974;8,72;264;68;165
 2010;1;25;12;34;9,74;44,56083;-110,95834;10,4;252;63;171	 2010;1;17;22;0;33,3;44,55467;-110,96217;10,2;264;87;163
 2010;1;31;6;55;1,2;44,56867;-110,95917;10,43;254;81;167	 2010;1;22;14;48;53,78;44,557;-110,96616;10,22;265;82;159
 2010;1;25;10;27;35,89;44,5605;-110,95866;9,89;260;82;163	 2010;1;18;2;44;36;44,55117;-110,96333;9,11;258;80;153
 2010;1;18;12;59;55,18;44,55783;-110,9685;9,33;255;55;161	 2010;1;18;17;31;37,18;44,56317;-110,967;10,02;270;85;147
 2010;1;18;13;25;50,9;44,55933;-110,9685;9,97;246;63;154	 2010;1;17;20;56;36,58;44,55267;-110,965;9,23;94;88;-136
 2010;1;19;7;58;6,02;44,55467;-110,97317;9,72;249;72;150	 2010;1;17;22;24;47,19;44,5585;-110,963;9,72;265;88;178
 2010;1;18;4;4;48,26;44,55467;-110,9645;9,07;261;85;145	 2010;1;17;23;35;49,79;44,5585;-110,963;9,9;270;89;175
 2010;1;25;6;13;28,61;44,56167;-110,95834;10,96;259;74;150	 2010;1;21;2;1;18,44;44,564;-110,9755;9,62;260;76;168
 2010;2;1;12;17;51,6;44,57917;-110,98067;8,01;266;85;168	 2010;1;18;15;17;3,09;44,56317;-110,97166;9,78;255;82;164
 2010;1;19;2;53;2,95;44,5585;-110,97083;8,65;240;52;145	 2010;1;17;22;18;56,02;44,55783;-110,96533;9,83;256;62;160
 2010;1;18;6;46;44,34;44,55967;-110,9705;9,52;135;75;-75	 2010;1;19;5;52;22,27;44,55467;-110,96217;9,71;263;69;153
 2010;1;25;11;31;7;44,56667;-110,95567;11,5;95;80;-146	 2010;2;2;11;54;37,17;44,56633;-110,97083;9,96;274;69;141
 2010;1;27;19;52;15,98;44,56783;-110,96467;9,56;91;84;-149	 2010;1;21;7;34;33,88;44,56083;-110,97633;9,71;270;89;161

 2010;1;27;1;46;17,22;44,55783;-110,963;10,2;255;67;-175	 2010;2;2;10;23;21,48;44,65967;-110,9885;6,26;248;71;178
 2010;1;20;20;0;27,73;44,55667;-110,9735;9,34;96;83;-167	 2010;1;25;7;54;38,57;44,56483;-110,96066;10,51;249;33;-157
 2010;1;25;17;32;15,58;44,55933;-110,94033;7,67;285;65;153	 2010;1;22;6;6;54,9;44,57183;-110,9795;9,12;302;32;-98
 2010;1;22;4;9;1,34;44,55617;-110,96933;9,47;87;84;-175	 2010;1;21;2;57;49,5;44,5585;-110,96933;9,96;265;57;-174
 2010;1;21;9;8;45,62;44,571;-110,967;10,17;268;73;-175	 2010;2;3;1;52;9,97;44,5555;-110,941;7,88;276;89;-169
 2010;1;19;11;14;11,11;44,55733;-110,96967;9,37;265;80;-177	 2010;2;1;17;3;11,07;44,58033;-110,978;8,57;86;86;-168
 2010;1;20;4;12;27,32;44,5655;-110,96384;9,59;269;72;-178	 2010;1;18;13;23;57,19;44,56017;-110,97083;9,79;264;71;-166
 2010;2;3;2;13;17,66;44,55317;-110,941;8,01;91;82;152	 2010;1;18;2;38;0,45;44,55617;-110,9685;8,72;81;87;-172
 2010;2;1;8;10;41,35;44,57883;-110,98267;8,26;269;63;-166	 2010;1;18;5;55;4,76;44,55383;-110,95983;9,35;257;66;-174
 2010;1;18;11;50;34,88;44,55467;-110,963;10,07;268;73;-170	 2010;2;2;22;44;50,47;44,55267;-110,92583;9,07;124;73;-139
 2010;1;25;22;43;31,45;44,5625;-110,93567;7,98;265;79;-173	 2010;1;17;21;15;55,69;44,55233;-110,9645;9,22;251;70;-168
 2010;1;19;21;42;53,77;44,557;-110,96684;9,89;85;85;-174	 2010;1;20;5;40;32,82;44,564;-110,97;9,65;264;75;-172
 2010;1;17;20;38;1,52;44,55233;-110,96384;9,19;265;78;-175	 2010;1;19;21;32;30,81;44,55783;-110,974;9,33;273;87;-174
 2010;2;2;22;33;34,71;44,55;-110,92533;7,67;284;83;139	 2010;1;24;14;32;21,04;44,56317;-110,95917;10,21;258;86;-176
 2010;1;19;21;32;10,04;44,56083;-110,96767;10,2;80;80;176	 2010;1;25;6;27;48,76;44,564;-110,96616;10,64;242;31;-174
 2010;1;24;8;58;34,21;44,56317;-110,95983;10,54;260;75;172	 2010;1;18;8;4;34,59;44,55467;-110,96767;9,62;267;82;-169
 2010;1;22;14;33;27,67;44,55783;-110,96217;10,04;265;71;167	 2010;1;28;18;3;35,16;44,56783;-110,96933;9,53;94;89;-148
 2010;1;21;7;48;33,34;44,56283;-110,97667;9,66;266;78;162	 2010;1;22;9;41;49,3;44,55733;-110,9665;9,32;257;85;-168
 2010;1;20;13;9;11,69;44,56483;-110,96933;9,87;266;67;155	 2010;1;22;3;47;57,48;44,55933;-110,93567;8,26;268;85;155
 2010;1;22;5;38;39,55;44,54533;-110,97234;9,03;272;88;148	 2010;1;27;23;45;31,37;44,56783;-110,95983;10,99;252;68;-175
 2010;1;25;6;57;5,63;44,56167;-110,95983;10,75;89;89;-140	 2010;1;19;16;48;31,09;44,56167;-110,967;7,98;274;87;-176
 2010;1;20;16;22;36,35;44,56633;-110,97166;9,58;85;90;-146	 2010;1;22;17;2;58,49;44,56083;-110,97083;9,76;78;84;-179
 2010;1;17;21;1;45,77;44,55117;-110,96183;8,6;266;66;-159	 2010;1;19;4;42;13,66;44,56367;-110,9665;9,02;268;83;-177
 2010;1;19;4;42;13,66;44,56367;-110,9665;9,02;268;83;-177	 2010;1;21;1;19;46;44,56317;-110,97166;9,67;260;79;-178
 2010;1;21;22;26;19,2;44,55933;-110,96384;10,5;262;75;-152	 2010;1;18;1;4;23,79;44,55617;-110,96384;8,29;266;73;-175










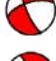






Year, Month, Day, Hour, Minute, Seconds, Latitude, Longitude, Depth, Strike, Dip, Rake

 2010;1;20;6;35;48,94;44,56283;-110,96733;9,34;264;76;-169	 2010;1;20;11;42;23,61;44,55467;-110,96066;10,51;86;85;-153
 2010;1;8;11;49;36,19;44,74833;-111,17117;6,25;247;69;-147	 2010;1;17;21;4;6,24;44,55117;-110,965;9,14;87;85;-156
 2010;1;21;1;56;3,35;44,562;-110,9775;9,58;257;66;-167	 2010;1;19;10;36;13,96;44,56317;-110,96066;9,72;85;81;-144
 2010;1;27;18;28;22,03;44,56783;-110,96384;10,27;85;87;-157	 2010;1;25;11;28;43,1;44,55783;-110,96533;10,43;262;68;13
 2010;1;24;7;56;42,13;44,5625;-110,9575;10,51;89;88;-148	 2010;1;28;23;56;4,56;44,56317;-110,97083;9,53;261;82;146
 2010;1;30;15;47;34,89;44,56867;-110,96467;10,15;262;69;-173	 2010;1;18;19;38;41,55;44,56017;-110,96217;10,6;267;86;152
 2010;1;21;6;16;18,7;44,56283;-110,96733;9,43;275;70;-169	 2010;1;19;2;54;38,71;44,55733;-110,96967;9,28;256;71;157
 2010;1;18;15;32;15,83;44,55933;-110,96767;10,09;92;89;-164	 2010;1;17;22;58;9,88;44,55783;-110,963;10,02;265;78;161
 2010;1;17;22;43;32,74;44,55267;-110,968;8,83;92;84;-149	 2010;1;23;5;41;15,86;44,56017;-110,9645;9,18;267;64;-170
 2010;1;20;20;10;20,35;44,55783;-110,97467;9,85;279;90;177	 2010;1;25;11;32;9,47;44,562;-110,9555;10,66;89;84;-142
 2010;1;21;20;7;37,93;44,557;-110,9355;7,75;84;88;173	 2010;1;26;10;39;15,75;44,5625;-110,98417;9,49;99;71;-134
 2010;1;21;2;6;14,74;44,55617;-110,985;9,21;70;90;163	 2010;1;21;6;18;59,99;44,557;-110,97;10,09;261;54;143
 2010;1;20;8;27;24,31;44,559;-110,96817;9,98;255;72;166	 2010;1;20;21;55;19,48;44,55617;-110,96384;10,38;265;84;149
 2010;1;21;8;55;4,29;44,56167;-110,96384;10,4;248;32;170	 2010;1;22;14;34;53,78;44,56083;-110,96533;9,74;267;88;153
 2010;1;19;19;12;40,91;44,55317;-110,97467;9,82;85;90;171	 2010;1;25;11;11;29,11;44,564;-110,95834;10,2;263;78;159
 2010;1;20;4;41;2,6;44,56483;-110,96384;9,45;268;80;174	 2010;1;22;6;59;39,05;44,571;-110,98033;8,98;261;89;158
 2010;1;24;7;56;0,13;44,559;-110,96183;10,03;272;70;-166	 2010;1;18;9;13;33,61;44,5585;-110,96533;9,05;241;40;162
 2010;2;3;3;25;15,73;44,55383;-110,94733;7,62;102;90;-155	 2010;1;27;1;28;41,44;44,56017;-110,96533;9,74;273;88;165
 2010;1;19;13;26;51,38;44,55733;-110,96333;9,65;264;79;176	 2010;1;18;20;50;48,27;44,5555;-110,96533;10,16;265;84;168
 2010;1;26;18;59;20,04;44,56633;-110,96066;10,47;260;81;177	 2010;1;21;6;1;49,92;44,55783;-110,97467;8,26;277;87;172
 2010;1;23;9;19;8,84;44,55083;-110,9715;10,2;109;83;-160	 2010;1;18;2;24;20,04;44,55433;-110,96017;10,14;251;74;176
 2010;1;25;6;21;33,21;44,56017;-110,96066;11,06;90;83;-147	
 2010;1;18;16;47;21,88;44,56483;-110,96467;11,1;270;79;141	
 2010;1;19;2;7;27,64;44,55617;-110,96616;9,88;255;63;147	
 2010;1;18;23;56;31,54;44,559;-110,9665;10,14;268;90;153	

Year, Month, Day, Hour, Minute, Seconds, Latitude, Longitude, Depth, Strike, Dip, Rake














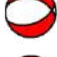


- | | |
|--|---|
|  2010;4;5;10;38;45;36;44,59433;-110,98983;7,69;36;73;-131 |  2010;11;7;3;51;47,42;44,55383;-110,99583;10,36;254;86;-179 |
|  2010;11;8;18;56;29,11;44,55083;-110,98967;10,28;309;35;-80 |  2010;4;6;3;32;9,36;44,59517;-110,99533;7,4;221;57;-169 |
|  2010;10;27;15;54;43,46;44,6045;-110,99617;10,88;220;38;-117 |  2010;11;6;14;48;6,25;44,5555;-110,99033;11,45;90;85;-162 |
|  2010;11;5;13;54;34,9;44,5555;-110,98883;11,52;255;69;156 |  2010;11;6;10;30;21,69;44,55783;-110,9865;12,25;87;88;-148 |
|  2010;5;18;11;29;10,51;44,74567;-111,2265;4,57;55;82;-158 |  2010;11;6;17;25;13,89;44,5535;-110,9955;10,6;87;80;-126 |
|  2010;12;24;9;51;29,69;44,77017;-111,22483;6,52;336;39;-30 |  2010;4;5;10;36;27,01;44,594;-110,9925;6,95;32;88;180 |
|  2010;4;27;4;26;7,03;44,7375;-111,0635;8,13;230;85;162 |  2010;11;28;15;42;12,52;44,73633;-111,19183;11,01;48;85;-167 |
|  2010;8;3;23;48;21,68;44,613;-110,65583;4,36;119;63;-80 |  2010;7;1;14;29;51,46;44,7585;-111,18217;7,35;50;76;159 |
|  2010;8;17;12;22;26,22;44,615;-110,65633;3,91;76;38;-67 |  2010;4;4;3;15;51,18;44,59317;-110,99333;7,33;227;38;-151 |
|  2010;10;7;7;50;44,34;44,61833;-110,65483;3,82;188;45;-106 |  2010;9;3;13;9;31,1;44,5485;-110,98183;10,62;107;81;-172 |
|  2010;10;7;7;32;14,51;44,61767;-110,652;4,07;2;34;-76 |  2010;10;27;4;33;23,94;44,60683;-111,00083;11,18;123;63;-139 |
|  2010;11;6;7;52;36,45;44,555;-110,99084;11,05;84;88;178 |  2010;6;24;4;46;5,18;44,557;-110,959;10,58;283;87;167 |
|  2010;11;6;12;12;35,97;44,55083;-110,988;10,6;270;85;145 |  2010;4;6;10;5;4,9;44,59283;-110,9945;8,16;57;60;-125 |
|  2010;11;7;4;14;9,59;44,55467;-110,992;11,06;268;86;174 |  2010;11;6;9;31;31,55;44,54917;-110,99583;9,44;259;81;-170 |
|  2010;6;29;6;3;36,96;44,71183;-111,1395;9,75;177;77;-118 |  2010;11;8;13;53;31,17;44,5515;-110,99267;9,82;249;64;-174 |
|  2010;9;27;10;22;40,36;44,711;-111,13483;8,51;264;83;-178 |  2010;11;6;12;15;38,63;44,54967;-110,99;10,24;91;80;-148 |
|  2010;6;24;4;42;24,07;44,559;-110,954;11,01;271;81;174 |  2010;11;7;10;56;5,71;44,55433;-110,9915;11,01;283;29;-130 |
|  2010;11;7;14;52;28,57;44,55383;-110,99033;11,28;334;32;-53 |  2010;11;7;4;50;25,11;44,55317;-110,99667;10,04;257;76;162 |

2011



- | | |
|---|---|
|  2011;11;5;20;21;58,98;44,73467;-110,874;10,14;240;66;-161 |  2011;3;1;16;1;21,22;44,79433;-111,0205;8,36;97;76;-177 |
|  2011;12;5;21;22;56,98;44,75467;-110,974;10,24;246;66;-161 |  2011;1;6;18;5;24,68;44,7515;-111,18616;9,72;248;61;-153 |
|  2011;1;27;7;46;44,17;44,77633;-111,3805;11,56;65;89;156 |  2011;1;1;16;53;46,9;44,76433;-111,1355;5,36;55;50;133 |
|  2011;6;19;9;14;26,33;44,52583;-111,05683;12,01;274;29;-91 |  2011;5;19;22;22;0,06;44,739;-111,19617;8,84;192;46;-128 |
|  2011;9;26;5;53;53,46;44,73483;-111,22017;5,5;260;54;138 |  2011;4;3;14;56;9,28;44,7255;-111,14616;11,53;253;63;-165 |
|  2011;6;2;21;9;48,48;44,7095;-111,06567;9,21;61;70;-118 |  2011;1;26;4;51;3,11;44,73833;-111,10817;5,98;65;87;-172 |
|  2011;1;31;21;31;5,21;44,28083;-110,42333;8,47;304;60;-123 |  2011;9;11;22;47;29,78;44,75817;-111,09933;5,86;91;66;-127 |
|  2011;2;25;12;2;3,77;44,73133;-110,77583;5,6;68;81;150 |  2011;2;18;1;30;55,68;44,78183;-110,94017;5,73;49;85;-175 |

Year, Month, Day, Hour, Minute, Seconds, Latitude, Longitude, Depth, Strike, Dip, Rake





2012

- | | |
|--|---|
|  2012;6;18;3;27;41,02;44,648;-110,43066;-0,17;354;68;170 |  2012;7;4;15;20;8,53;44,61533;-111,19133;11,29;120;53;-123 |
|  2012;7;12;7;29;17,8;44,61883;-110,67267;3,34;146;74;-108 |  2012;7;14;23;32;26,54;44,73667;-111,0965;7,33;345;31;70 |
|  2012;9;24;13;56;53,11;44,75533;-110,76717;6,79;337;39;-106 |  2012;8;7;5;7;14,36;44,73833;-111,09167;8,16;83;87;165 |
|  2012;9;6;8;51;52,33;44,77017;-110,93083;6,61;251;55;-106 |  2012;7;25;4;2;12,14;44,79267;-111,07317;7,3;73;30;-93 |
|  2012;3;29;8;9;20,62;44,55233;-110,95433;10,04;114;63;-90 |  2012;8;7;8;23;35,89;44,7375;-111,09717;7,1;69;87;-167 |
|  2012;8;7;11;16;6,59;44,58967;-111,14567;10,02;288;89;154 |  2012;3;3;8;59;13,57;44,75933;-111,13033;6,31;174;54;-77 |
|  2012;3;23;3;50;53,3;44,6115;-111,14433;7,57;171;58;-93 |  2012;3;3;10;5;31,76;44,76;-111,12883;5,77;282;43;-66 |
|  2012;7;20;1;57;11,66;44,61767;-111,1875;11,98;103;72;-116 |  2012;6;22;6;21;26,97;44,7445;-111,13583;11,51;251;73;-158 |




2013

- | |
|--|
|  2013;9;23;8;32;51,05;44,24667;-110,76633;3,12;90;84;-174 |
|  2013;9;27;15;38;53,58;44,7305;-111,10267;12,26;56;74;162 |


2014

- | |
|---|
|  2014;2;15;10;23;53,97;44,76;-111,084;5,25;268;42;-94 |
|  2014;2;13;23;37;41,88;44,70016;-110,65334;4,92;204;50;-89 |
|  2014;2;18;11;8;37,67;44,69117;-110,63883;4,87;302;86;177 |
|  2014;1;12;1;46;59,89;44,79583;-110,521;9,71;72;58;-136 |

2015

- | |
|--|
|  2015;2;2;5;17;4,37;44,75617;-111,07616;10,09;244;80;-178 |
|  2015;3;22;6;39;26,24;44,79817;-110,9835;5,56;286;37;-96 |
|  2015;5;18;23;0;51,63;44,584;-110,37683;2,14;1;25;-59 |

2016

- | |
|--|
|  2016;10;1;8;30;57,51;44,73133;-110,7735;9,35;266;87;-129 |
|--|

Bibliography

Abers, G.A., Gephart, J.W., 2001. Direct inversion of earthquake first motions for both the stress tensor and focal mechanisms and application to southern California. *J. Geophys. Res.* 106.

Abdallah, A., Courtillot, V., Kasser, M., Le Dain, A.Y., L epine, J.C., Robineau, B., Tarantola, A., 1979. Relevance of Afar seismicity and volcanism to the mechanics of accreting plate boundaries. *Nature* 282 (5734), 17.

Acocella, V., 2014. Structural control on magmatism along divergent and convergent plate boundaries: overview, model, problems. *Earth Sci. Rev.* 136, 226–288.

Acocella, V., Gudmundsson, A., Funicello, R., 2000. Interaction and linkage of extension fractures and normal faults: examples from the rift zone of Iceland. *J. Struct. Geol.* 22(9), 1233–1246.

Agisoft LLC (2018) PhotoScan usermanual, professional edition, version 1.4. http://www.agisoft.com/pdf/photoscan-pro_1_4_en.pdf. Accessed 1 Oct 2018

 g ustsd ottir, T., Woods, J., Greenfield, T., Green, R.G., White, R.S., Winder, T., Soosalu, H., 2016. Strike-slip faulting during the 2014 B ar arbunga-Holuhraun dike intrusion, central Iceland. *Geophys. Res. Lett.* 43 (4), 1495–1503.

Ali, S. T., Feigl, K. L., Carr, B. B., Masterlark, T., Sigmundsson, F., 2014. Geodetic measurements and numerical models of rifting in Northern Iceland for 1993–2008. *Geophysical Journal International*, 196(3), 1267-1280.

Allen, R.M., Nolet, G., Morgan, W.J., Vogfj rd, K., Nettles, M., Ekstr m, G., Bergsson, B.H., Erlendsson, P., Foulger, G.R., Jakobsd ottir, S., Julian, B.R., 2002. Plume-driven plumbing and crustal formation in Iceland. *Journal of Geophysical Research: Solid Earth*, 107(B8), pp.E5E-4.

Angelier, J., 1984. Tectonic analysis of fault slip data sets. *J. Geophys. Res.* 89 (B7), 5835–5848.

- Angelier, J., Bergerat, F., Dauteuil, O., Villedieu, T., 1997. Effective tension-shear relationships in extensional fissure swarms, axial rift zone of northeastern Iceland. *Journal of Structural Geology*, 19(5), 673-685.
- Antoniou, V., Paraskevi, N., Pavlina, B., Pantelia, S., Luca, B. F., Lemonia, R., Andreas, M., 2019. The Story Map for Metaxa Mine (Santorini, Greece): A Unique Site Where History and Volcanology Meet Each Other. GISTAM 2019. SciTePress.
- Armstrong, R.L., Leeman, W.P., Malde, H.E., 1975. K-Ar dating, Quaternary and Neogene volcanic rocks of the Snake River Plain Idaho. *Am. J. Sci.* 275, 225–251.
- Atwater, T., 1970. Implications for plate tectonics for the Cenozoic tectonic evolution of western North America. *Geol. Soc. Am. Bull.* 81, 3513–3536.
- Bjornsson, A., Semundsson, K., Einarsson, P., Tryggvason, E., Gronvold, K., 1977. Current rifting episode in north Iceland. *Nature*, 266, 318-323.
- Bjornsson, A., Johnsen, G., Sigurdsson, S., Thorbergsson, G., Tryggvason, E., 1979. Rifting of the plate boundary in north Iceland. *J. Geophys. Res.*, 84: 3029-3038.
- Bjornsson, A., 1985. Dynamics of crustal rifting in NE Iceland. *J. Geophys. Res.*, 90, 10151-10162.
- Blackwell, D. D., Richards, M. C., 2004. Geothermal Map of North America. American Association of Petroleum Geologists, 1 sheet, scale 1:6,500,000.
- Bonafede, M., Olivieri, M., 1995. Displacement and gravity anomaly produced by a shallow vertical dyke in a cohesionless medium. *Geophys. J. Int.* 123, 639–652.
- Bonali, F. L., Tibaldi, A., Marchese, F., Fallati, L., Russo, E., Corselli, C., Savini, A., 2019a. UAV-based surveying in volcano-tectonics: An example from the Iceland rift. *Journal of Structural Geology*, 121, 46-64.

Bonali, F.L., Tibaldi, A., Mariotto, F.P., Saviano, D., Meloni, A., Sajovitz, P., 2019b. Geometry, oblique kinematics and extensional strain variation along a diverging plate boundary: the example of the northern Theistareykir Fissure Swarm, NE Iceland. *Tectonophysics* 756, 57–72.

Bonali F.L., Corti N., Russo E., Marchese F., Fallati L., Pasquaré Mariotto F., Tibaldi A., 2020a. Commercial-UAV-based Structure from Motion for geological and geohazard studies. In *Building knowledge for geohazard assessment and management in the Caucasus and other orogenic regions*, NATO SPS Series; Bonali F.L., Tsereteli N., Pasquaré Mariotto F., Eds.; Springer: Heidelberg, Germany; in press.

Bonali, F. L., Tibaldi, A., Corti, N., Fallati, L., Russo, E., 2020. Reconstruction of Late Pleistocene-Holocene Deformation through Massive Data Collection at Krafla Rift (NE Iceland) Owing to Drone-Based Structure-from-Motion Photogrammetry. *Applied Sciences*, 10(19), 6759.

Bonnichsen, B., 1982. Rhyolite Lava Flows in the Bruneau-Jarbidge Eruptive Center, Southwestern Idaho. In: Bonnichsen, B., Breckenridge, R.M. (Eds.), *Cenozoic Geology of Idaho: Idaho Bureau of Mines and Geology Bulletin*, vol. 26, pp. 283–320. Moscow, ID.

Borgia, A., 1994. Dynamic basis of volcanic spreading. *Journal of Geophysical Research: Solid Earth* 99 (B9), 17791–17804.

Bott, M.H.P., 1982. Origin of the lithospheric tension causing basin formation. *Philosophical Transactions of the Royal Society of London. Series A, Mathematical and Physical Sciences* 305 (1489), 319–324.

Brandsdottir, B., Einarsson, P., 1979. Seismic activity associated with the September 1977 deflation of the Krafla central volcano in northeastern Iceland. *J. Volcanol. Geotherm. Res.*, 6: 197-212.

Brandsdottir, B., Menke, W. H., 2008. The seismic structure of Iceland. *Jokull*, 58, 17–34.

Buck, W.R., Einarsson, P., Brandsdóttir, B., 2006. Tectonic stress and magma chamber size as controls on dike propagation: constraints from the 1975–1984 Krafla rifting episode. *J. Geophys. Res.* 111, B12404.

Burns, J.H.R., Delparte, D., 2017. Comparison of commercial structure-from-motion photogrammetry software used for underwater three-dimensional modeling of coral reef environments. In *International Archives of the Photogrammetry, Remote Sensing and Spatial Information Sciences - ISPRS Archives* (Vol. 42, pp. 127–131).

Burov, E., Guillou-Frottier, L., 2005. The plume head-continental lithosphere interaction using a tectonically realistic formulation for the lithosphere: *Geophys. J. Int.* 161 (2), 469–490.

Burov, E., Guillou-Frottier, L., d'Acremont, E., Le Pourhiet, L., Cloetingh, S., 2007. The plume head lithosphere interactions near intra-continental plate boundaries. *Tectonophysics* 434, 15–38.

Camp, V.E., 1995. Mid-Miocene propagation of the Yellowstone mantle plume head beneath the Columbia River basalt source region. *Geology* 23 (5), 435–438.

Carr, W. J., Quinlivan, W. D., 1968. Structure of Timber Mountain resurgent dome, Nevada Test Site, in Eckel, E. B., ed., *Nevada Test Site: Geological Society of America Memoir* 110, p. 99-108.

Chang, W. L., Smith, R. B., Wicks, C. Farrell, J. M., Puskas, C. M., 2007. Accelerated uplift and magmatic intrusion of the Yellowstone caldera, 2004 to 2006, *Science*, 318, 952.

Chang, W. L., Smith, R. B., Farrell, J., Puskas, C.M., 2010. An extraordinary episode of Yellowstone caldera uplift, 2004-2010, from GPS and InSAR observations, *Geophysical Research Letters*, 37 (23).

Christiansen, R. L., 2001. The Quaternary and Pliocene Yellowstone plateau volcanic field of Wyoming, Idaho and Montana, *U.S. Geol. Surv. Profess. Pap.*, 729-G, 145.

Cook, K.L., 2017. An evaluation of the effectiveness of low-cost UAVs and structure from motion for geomorphic change detection. *Geomorphology*, 278, 195–208.

Crough, S.T., 1978. Thermal origin of mid-plate hot-spot swells. *Geophys. J. R. Astron. Soc.* 55, 451–469.

Crough, S.T., 1983. Hotspot swells. *Annu. Rev. Earth Planet. Sci.* 11, 165–193.

Currenti, G., Del Negro, C., Ganci, G., Williams, C. A., 2008. Static stress changes induced by the magmatic intrusions during the 2002–2003 Etna eruption. *Journal of Geophysical Research: Solid Earth*, 113(B10).

Darbyshire, F. A., White, R. S., Priestley, K. F., 2000. Structure of the crust and uppermost mantle of Iceland from a combined seismic and gravity study. *Earth and Planetary Science Letters*, 181(3), 409–428.

Darmawan, H., Walter, T.R., Brotopuspito, K.S., Nandaka, I.G.M.A., 2018. Morphological and structural changes at the Merapi lava dome monitored in 2012–15 using unmanned aerial vehicles (UAVs). *Journal of Volcanology and Geothermal Research*, 349, 256-267.

Dauteuil, O., Angelier, J., Bergerat, F., Verrier, S., Villemin, T., 2001. Deformation partitioning inside a fissure swarm of the northern Icelandic rift. *Journal of Structural Geology*, 23, 1359-1372.

Davies, G.F., 1988. Ocean bathymetry and mantle convection, 1, Large-scale flow and hotspots. *J. Geophys. Res.* 93, 10,467–10,480.

De Beni, E., Cantarero, M., Messina, A., 2019. UAVs for volcano monitoring: A new approach applied on an active lava flow on Mt. Etna (Italy), during the 27 February–02 March 2017 eruption. *Journal of Volcanology and Geothermal Research*, 369, 250-262.

Delaney, P.T., Pollard, D.D., 1981. Deformation of host rocks and flow of magma during growth of minette dikes and breccia bearing intrusions near Ship Rock, New Mexico. Professional Paper 1202. US Geological Survey, Denver, Colo.

DeMets, C., Gordon, R.G., Argus, D.F. Stein, S., 1994. Effect of recent revisions to the geomagnetic reversal time scale on estimates of current plate motions. *Geophys. Res. Lett.* 21 (20), 2191–2194.

DeMets, C., Gordon, R.G., Argus, D.F., 2010. Geologically current plate motions. *Geophys. J. Int.* 181 (1), 1–80.

DeNosaquo, K. R., Smith, R.B., Lowry, A.R., 2009. Density and lithospheric strength models of the Yellowstone–Snake River Plain volcanic system from gravity and heat flow data, *J. Volcanol. Geotherm. Res.*, 188, 108–127.

Doser, D. I., 1985. Source parameters and faulting processes of the 1959 Hebgen Lake, Montana, earthquake sequence. *Journal of Geophysical Research: Solid Earth*, 90(B6), pp.4537-4555.

Drouin, V., Sigmundsson, F., Ófeigsson, B.G., Hreinsdóttir, S., Sturkell, E., Einarsson, P., 2017. Deformation in the Northern Volcanic Zone of Iceland 2008–2014: an interplay of tectonic, magmatic, and glacial isostatic deformation. *J. Geophys. Res.: Solid Earth* 122 (4), 3158–3178.

Dzurisin, D., K. M. Yamashita, J. W. Kleinman, 1994. Mechanisms of crustal uplift and subsidence at the Yellowstone caldera, Wyoming, *Bull. Volcanol.*, 56, 261-270.

Eaton, G. P., Christiansen, R. L., Iyer, H. M., Pitt, A. M., Mabey, D. R., Blank, J. R., Jr., Zietz, I., Gettings, M. E., 1975. Magma beneath Yellowstone National Park: *Science*, v. 188, p. 787-796.

Einarsson, T., 1958. A survey of the geology of the area Tjörnes-Bárðardalur in northern Iceland including paleomagnetic studies. *Societas Scientiarum Islandica* 32, 1–79.

Einarsson, P., 1978. S-wave shadows in the Krafla Caldera in NE-Iceland, evidence for a magma chamber in the crust. *Bull Volcanol* 41:187–195.

Einarsson, P., 1991. Earthquakes and present-day tectonism in Iceland. *Tectonophysics* 189 (1–4), 261–279.

- Einarsson, P., 2008. Plate boundaries, rifts and transforms in Iceland. *Jokull* 58, 35–58.
- Einarsson, P., Brandsdóttir, B., 1980. Seismological evidence for lateral magma intrusion during the July 1978 deflation of the Krafla volcano in NE-Iceland. *J. Geophys. Res.* 47, 160–165.
- Einarsson, P., Eiriksson, J., 1982. Earthquake fractures in the districts Land and Rangarvellir in the South Iceland Seismic Zone. *Jokull*, 32,113–119.
- Einarsson, P., Saemundsson, K., 1987. Earthquake Epicenters 1982-1985 and Volcanic Systems in Iceland: Upptök Jarðskjálfta 1982-1985 Og Eldstodvakerfi á Íslandi. Menningarsjodur.
- Esposito, G., Mastrorocco, G., Salvini, R., Oliveti, M., Starita, P., 2017. Application of UAV photogrammetry for the multi-temporal estimation of surface extent and volumetric excavation in the Sa Pigada Bianca open-pit mine, Sardinia, Italy. *Environ. Earth Sci* , 76, 103.
- Fallati, L., Polidori, A., Salvatore, C., Saponari, L., Savini, A., Galli, P., 2019. Anthropogenic Marine Debris assessment with Unmanned Aerial Vehicle imagery and deep learning: A case study along the beaches of the Republic of Maldives. *Science of The Total Environment*, 693, 133581.
- Farrell, J., Smith, R.B., Taira, T.a., Chang,W. L., Puskas, C.M., 2010. Dynamics and rapid migration of the energetic 2008–2009 Yellowstone Lake earthquake swarm. *Geophys. Res. Lett.* 37 (19).
- Farrell, J. M., 2013. Seismicity and tomographic imaging of the Yellowstone crustal magmatic-tectonic system (Doctoral dissertation, The University of Utah).
- Farrell, J., Smith, R.B., Husen, S., Diehl, T., 2014. Tomography from twenty-six years of seismicity reveals the spatial extent of the Yellowstone crustal magma reservoir extends well beyond the Yellowstone caldera, University of Utah Dept. of Geology and Geophysics, Salt Lake City.
- Favalli, M., Fornaciai, A., Nannipieri, L., Harris, A., Calvari, S., Lormand, C., 2018. UAV-based remote sensing surveys of lava flow fields: a case study from Etna’s 1974 channel-fed lava flows. *Bulletin of Volcanology*, 80 (3), 29.

Fink, J.H., Pollard, D.D., 1983. Structural evidence for dikes beneath silicic domes, Medicine Lake Highland Volcano, California. *Geology* 11 (8), 458–461.

Fjäder, K., Gudmundsson, A., Forslund, T., 1994. Dikes, minor faults and mineral veins associated with a transform fault in North Iceland. *Journal of Structural Geology*, 16 (1), 109-119.

Forslund, T., Gudmundsson, A., 1991. Crustal spreading due to dikes and faults in SW Iceland. *Journal of Structural Geology*, 13: 443-457.

Foulger, G.R., Jahn, C.H., Seebet, G., Einarsson, P., Julian, B.R., Heki, K., 1992. Post-rifting stress relaxation at the divergent plate boundary in Northeast Iceland. *Nature*, 358, 488-490.

Fournier, R.O., 1989. Geochemistry and dynamics of the Yellowstone National Park hydrothermal system. *Annu. Rev. Earth Planet. Sci.* 17, 13–53.

Fournier, R. O., White, D.E., Truesdell, A.H., 1976. Convective heat flow in Yellowstone National Park, in Second United Nations Symposium on Development and Use of Geothermal Resources, U.S. Govt. Print. Off., Washington D.C., 731-739.

Fournier, M., Petit, C., 2007. Oblique rifting at oceanic ridges: relationship between spreading and stretching directions from earthquake focal mechanisms. *Journal of Structural Geology* 29, 201–208.

Garcia, S., Dhont, D., 2005. Structural analysis of the Húsavík–Flatey Transform Fault and its relationships with the rift system in Northern Iceland. *Geodin. Acta* 18, 31–41

Garcia S, Angelier J, Bergerat F, Homberg, C., 2002. Tectonic analysis of an oceanic transform fault zone revealed by fault slip data and earthquake focal mechanisms: the Husavik-Flatey Fault, Iceland. *Tectonophysics* 344:157-174.

Gardner, J. K., Knopoff, L., 1974. Is the sequence of earthquakes in Southern California, with aftershocks removed, Poissonian?. *Bulletin of the Seismological Society of America*, 64(5), 1363-1367.

Gephart, J.W., Forsyth, D.W., 1984. An improved method for determining the regional stress tensor using earthquake focal mechanism data: application to the San Fernando earthquake sequence. *J. Geophys. Res.* 89 (B11), 9305–9320.

Gerloni, I.G., Carchiolo, V., Vitello, F.R., Sciacca, E., Becciani, U., Costa, A., Riggi, S., Bonali, F.L., Russo, E., Fallati, L., Marchese, F., Tibaldi, A., 2018. Immersive Virtual Reality for Earth Sciences. In 2018 Federated Conference on Computer Science and Information Systems (FedCSIS) (pp. 527-534). IEEE.

Glen, J.M.G., Ponce, D.A., 2002. Large-scale fractures related to the inception of the Yellowstone hotspot. *Geology* 30 (7), 647–650.

Gudmundsson, A., Bäckström, K., 1991. Structure and development of the Sveinagja graben, northeast Iceland. *Tectonophysics* 200 (1–3), 111–125.

Gudmundsson, A., 1992. Formation and growth of normal faults at the divergent plate boundary in Iceland. *Terra. Nova* 4 (4), 464–471.

Gudmundsson, A., Brynjólfsson, S., Jónsson, M. Th., 1993. Structural analysis of a transform fault-rift zone junction in North Iceland. *Tectonophysics*, 220, 205–221.

Gudmundsson, A., 1995a. Infrastructure and mechanics of volcanic systems in Iceland. *J. Volcanol. Geotherm. Res.*, 6, 1-22.

Gudmundsson, A., 1995b. The geometry and growth of dykes. In *Physics and Chemistry of Dykes* ; Baer, G., Heimann, A., Eds; A.A. Balkema: Rotterdam, Netherlands; pp. 23-44

Gudmundsson, A., 2007. Infrastructure and evolution of ocean-ridge discontinuities in Iceland. *Journal of Geodynamics*, 43 (1), 6-29.

- Gudmundsson, A., Friese, N., Galindo, I., Philipp, S.L., 2008. Dike-induced reverse faulting in a graben. *Geology* 36 (2), 123–126.
- Gudmundsson, M.T., Jónsdóttir, K., Hooper, A., Holohan, E.P., Halldórsson, S.A., Ófeigsson, B.G., et al., 2016. Gradual caldera collapse at Bárðarbunga volcano, Iceland, regulated by lateral magma outflow. *Science* 353 (6296), aaf8988.
- Hainzl, S., Scherbaum, F., Beauval, C., 2006. Estimating background activity based on interevent-time distribution. *Bulletin of the Seismological Society of America*, 96(1), 313-320.
- Hamling, I.J., Ayele, A., Bennati, L., Calais, E., Ebinger, C.J., Keir, D., Yirgu, G., 2009. Geodetic observations of the ongoing Dabbahu rifting episode: new dyke intrusions in 2006 and 2007. *Geophys. J. Int.* 178 (2), 989–1003.
- Hampel, A., Hetzel, R., 2008. Slip reversals on active normal faults related to the inflation and deflation of magma chambers: Numerical modeling with application to the Yellowstone-Teton region. *Geophysical research letters*, 35(7).
- Hardarson, B. S., Fitton, J. G., Ellam, R. M., Pringle, M. S., 1997. Rift relocation: A geochemical and geochronological investigation of a palaeo-rift in northwest Iceland. *Earth and Planetary Science Letters*, 153, 181–196.
- Hardebeck, J. L., Shearer, P.M., 2002. A new method for determining first-motion focal mechanisms. *Bull. Seismol. Soc. Am.*, 92, 2264-2276.
- Hardebeck, J.L., Shearer, P.M., 2003. Using S/P amplitude ratios to constrain the focal mechanisms of small earthquakes. *Bull. Seismol. Soc. Am.* 93 (6), 2434–2444.
- Hardebeck, J.L., 2006. Homogeneity of small-scale earthquake faulting, stress, and fault strength. *Bull. Seismol. Soc. Am.* 96 (5), 1675–1688.

Heidbach, O., Tingay, M., Barth, A., Reinecker, J., Kurfess, D., Mler, B., 2008. " World Stress Map. A Project of the Heidelberg Academy of Sciences and Humanities." Commission for the Geological Map of the World.

Helgason, J., Zentilli, M., 1985. Field characteristics of laterally emplaced dikes: anatomy of an exhumed Miocene dike swarm in Reydarfjörður, eastern Iceland. *Tectonophysics* 115 (3–4), 247–274.

Heki, K., Foulger, G.R., Julian, B.R., Jahn, C.H., 1993. Plate dynamics near divergent plate boundaries: Geophysical implications of post-rifting crustal deformation in NE Iceland. *J. Geophys. Res.*, 98, 14,279-14,297.

Hey, R. N., Duennebieer, F. K., Morgan, W. J., 1980. Propagating rifts on mid-ocean ridges. *Journal of Geophysical Research*, 85(B7), 3647–3658.

Hjartardóttir, Á. R., Einarsson, P., Bramham, E., Wright, T. J., 2012. The Krafla fissure swarm, Iceland, and its formation by rifting events. *Bulletin of Volcanology*, 74(9), 2139-2153.

Hjartardottir, A.R., Einarsson, P., Bramham, E., Wright, T.J., 2012. The Krafla fissure swarm, Iceland, and its formation by rifting events. *Bull. Volcanol.* 74 (9), 2139–2153.

Hjartardottir, A.R., 2013. Fissure Swarms of the Northern Volcanic Rift Zone, Iceland (Ph.D. thesis), University of Iceland (122 pp.).

Hjartardóttir, Á. R., Einarsson, P., 2015. The interaction of fissure swarms and monogenetic lava shields in the rift zones of Iceland. *Journal of Volcanology and Geothermal Research*, 299, 91-102.

Hjartardóttir, Á., Einarsson, P., Gudmundsson, M.T., Högnadóttir, T., 2016a. Fracture movements and graben subsidence during the 2014 Bárðarbunga dike intrusion in Iceland. *J. Volcanol. Geother. Res.* 310, 242–252.

Hjartardóttir, Á.R., Einarsson, P., Björgvinsdóttir, S.G., 2016b. Fissure swarms and fracture systems within the Western Volcanic Zone, Iceland—Effects of spreading rates. *Journal of Structural Geology*, 91, 39-53.

Hjartardóttir, Á. R., Einarsson, P., Magnúsdóttir, S., Björnsdóttir, P., Brandsdóttir, B., 2016c. Fracture systems of the Northern Volcanic Rift Zone, Iceland: an onshore part of the Mid-Atlantic plate boundary. *Geological Society, London, Special Publications*, 420 (1), 297-314.

Hill, A. C., Limp, F., Casana, J., Laugier, E. J., Williamson, M., 2019. A New Era in Spatial Data Recording: Low-Cost GNSS. *Advances in Archaeological Practice*, 7(2), 169-177.

Hofton, M. A., Foulger, G. R., 1996. Postdrifting anelastic deformation around the spreading plate boundary, north Iceland: 1. Modeling of the 1987–1992 deformation field using a viscoelastic Earth structure. *Journal of Geophysical Research: Solid Earth*, 101(B11), 25403-25421.

Hollingsworth, J., Leprince, S., Ayoub, F., Avouac, J. P., 2013. New constraints on dike injection and fault slip during the 1975–1984 Krafla rift crisis, NE Iceland. *Journal of Geophysical Research: Solid Earth*, 118(7), 3707-3727.

Horiuchi, S., Rocco, G., Hasegawa, A., 1995. Discrimination of fault planes from auxiliary planes based on simultaneous determination of stress tensor and a large number of fault plane solutions. *J. Geophys. Res. Solid Earth* 100 (B5), 8327–8338.

Horst, A. J., Karson, J. A., Varga, R. J., 2018. Large rotations of crustal blocks in the Tjornes Fracture Zone of northern Iceland. *Tectonics*, 37(6), 1607-1625.

Husen, S., Smith, R. B., 2004. Probabilistic earthquake relocation in three-dimensional velocity models for the Yellowstone National Park region, Wyoming. *Bulletin of the Seismological Society of America*, 94(3), 880-896.

Husen, S., Smith, R.B., Waite, G.P., 2004. Evidence for gas and magmatic sources beneath the Yellowstone volcanic field from seismic tomographic imaging, *J. Volcanol. Geotherm. Res.*, 131, 397–410.

Ito, G., van Keken, P.E., 2007. Hotspots and melting anomalies. In: Bercovici, D. (Ed.), *Mantle Dynamics, Treatise on Geophysics*, vol. 7. Elsevier Press, Amsterdam, The Netherlands.

Jackson, E.D., Shaw, H.R., Bargar, K.E., 1975. Calculated geochronology and stress field orientations along the Hawaiian Chain. *Earth Planet. Sci. Lett.* 26, 145–155.

Jahn, C.H., Seeber, G., Foulger, G.R., Einarsson, P., 1994. GPS epoch measurements panning the mid-Atlantic plate boundary in northern Iceland 1987-1990. In *Gravimetry and Space Techniques Applied to Geodynamics and Ocean Dynamics*, *Geophys. Monogr. Ser.*, 82, Ed. B.E. Schutz et al., 109-123, AGU, Washington D.C.

James, M.R., Robson, S., 2012. Straightforward reconstruction of 3D surfaces and topography with a camera: accuracy and geoscience application. *J. Geophys. Res.* 117, F03017.

James, M.R., Robson, S., 2014. Mitigating systematic error in topographic models derived from UAV and ground-based image networks. *Earth Surf. Process. Landforms* 39 (10), 1413–1420.

Javernick, L., Brasington, J., Caruso, B, 2014. Modeling the topography of shallow braided rivers using Structure-from-Motion photogrammetry. *Geomorphology* 2014, 213, 166–182.

Jóhannesson, H., Sæmundsson, K., 1998. Geological map of Iceland, 1:500,000, Tectonics, Icelandic Institute of Natural History, Reykjavik.

Jónasson K., 1994. Rhyolite volcanism in the Krafla central volcano, north-east Iceland. *Bull. Volcanol.*, 56, 516–528.

Karson, J. A., Kelley, D. S., Fornari, D. J., Perfit, M. R., Shank, T. M., 2015. *Discovering the deep: A photographic atlas of the seafloor and oceanic crust*. London, UK: Cambridge University Press.

Karson, J. A., 2017. The Iceland plate boundary zone: Propagating rifts, migrating transforms and rift-parallel strike-slip faults. *Geochemistry, Geophysics, Geosystems*, 18, 4043–4054.

Karson, J. A., Farrell, J. A., Chutas, L. A., Nanfity, A. F., Proett, J. A., Runnals, K. T., Sæmundsson, K., 2018. Rift-parallel strike-slip faulting near the Iceland plate boundary zone: Implications for propagating rifts. *Tectonics*, 37, 4567–4594.

Kavanagh, J.L., Menand, T., Sparks, R.S.J., 2006. An experimental investigation of sill formation and propagation in layered elastic media. *Earth and Planetary Science Letters*, 245, 799–813.

Khodayar, M., Einarsson, P., 2002. Strike-slip faulting, normal faulting, and lateral dike injections along a single fault: Field example of the Gljufur_a fault near a Tertiary oblique rift-transform zone, Borgarfjodur, west Iceland. *Journal of Geophysical Research*, 107(B5), 2103.

Khodayar, M., Björnsson, S., Kristinsson, S., Karlsdóttir, R., Ólafsson, M., Víkingsson, S., 2018. Tectonic Control of the Theistareykir Geothermal Field by Rift and Transform Zones in North Iceland: A Multidisciplinary Approach. *Open Journal of Geology*, 8, 543-584.

Kilb, D., Hardebeck, J. L., 2006. Fault Parameter Constraints Using Relocated Earthquakes: A Validation of First-Motion Focal-Mechanism Data. *BULLETIN OF THE SEISMOLOGICAL SOCIETY OF AMERICA*, 96(3), 1140-1158.

King, G.C.P., Stein, R.S., and Lin, J., 1994, Static stress changes and the triggering of earthquakes: *Bulletin of the Seismological Society of America*, v. 84, no. 3, p. 935-953.

Kirkham, V. R., 1931. Snake River downwarp. *The Journal of Geology*, 39(5), 456-482.

Krokos M., Bonali F., Vitello F., Antoniou V., Becciani U., Russo E., Marchese F., Fallati L., Nomikou P., Kearn M., Sciacca, E., Whitworth M., 2019. Workflows for virtual reality visualisation and navigation scenarios in earth sciences. In 5th International Conference on Geographical Information Systems Theory, Applications and Management: GISTAM 2019. SciTePress.

Kuntz, M.A., Covington, H.R., Schorr, L.J., 1992. An overview of basaltic volcanism of the eastern Snake River Plain. In: Link, P.K., Kuntz, M.A., Platt, L.B. (Eds.), *Regional Geology of Eastern Idaho and Western Wyoming*: Geo. Soc. Amer., Memoir, vol. 179. Geological Society of America, Boulder, CO, pp. 227–267.

LaFemina, P. C., Dixon, T. H., Malservisi, R., Arnadottir, T., Sturkell, E., Sigmundsson, F., Einarsson, P., 2005. Geodetic GPS measurements in south Iceland: Strain accumulation and partitioning in a propagating ridge system. *Journal of Geophysical Research*, 110, B11405.

Lahitte, P., Gillot, P.Y., Courtillot, V., 2003. Silicic central volcanoes as precursors to rift propagation: the Afar case. *Earth and Planetary Science Letters*, 207, 103–116.

Leeman, W.P., 1982. Development of the Snake River Plain-Yellowstone Plateau province, Idaho and Wyoming: An overview and petrologic model. In: Bonnicksen, B., Breckenridge, R.M. (Eds.), *Cenozoic Geology of Idaho*: Idaho Bureau of Mines and Geology Bulletin, vol. 26. Idaho Bureau of Mines and Geology, Moscow, ID, pp. 155–178.

Lin, J., & Stein, R. S. (2004). Stress triggering in thrust and subduction earthquakes and stress interaction between the southern San Andreas and nearby thrust and strike-slip faults. *Journal of Geophysical Research: Solid Earth*, 109(B2).

Lomax, A., J. Virieux, P. Volant, C. Thierry-Berge, 2000. Probabilistic earthquake location in 3D and layered models, in *Advances in Seismic Event Location*, C.H. Thurber and N. Rabinowitz (Editors), Kluwer Academic Publishers, Dordrecht/Boston/London, 101-134.

Lomax, A., Curtis, A., 2001. Fast, probabilistic earthquake location in 3D models using Oct-Tree Importance sampling, *Geophys. Res. Abstr.*, 3.

Love, J. D., 1961. Reconnaissance study of Quaternary faults in and south of Yellowstone National Park, Wyoming. *Geological Society of America Bulletin*, 72(12), 1749-1764.

Machette, M. N., 2001. Map and data for Quaternary faults and folds in Wyoming (p. 153). US Geological Survey.

Magnúsdóttir, S., Brandsdóttir, B., 2011. Tectonics of the Peistareykir fissure swarm. *Jökull* 61:65-79

Malde, H. E., Powers, H. A., 1962. Upper Cenozoic stratigraphy of western Snake River Plain, Idaho. *Geological Society of America Bulletin*, 73(10), 1197-1220.

Malthe-Sørenssen, A., Planke, S., Svensen, H., Jamtveit, B., 2004. Formation of saucer-shaped sills. In: Breitzkreuz, C., Petford, N. (eds) *Physical Sill Morphology and Emplacement Mechanisms Geology of High-Level Magmatic Systems*. Geological Society, London, Special Publications, 234, 215–227.

Manighetti, I., Tapponnier, P., Courtillot, V., Gruszow, S., Gillot, P.Y., 1997. Propagation of rifting along the Arabia–Somalia plate boundary: The gulfs of Aden and Tadjoura. *Journal of Geophysical Research*, 102, 2681–2710.

Manighetti, I., King, G.C.P., Gaudemer, Y., Scholz, C.H., Doubre, C., 2001. Slip accumulation and lateral propagation of active normal faults in Afar. *Journal of Geophysical Research: Solid Earth*, 106(B7), 13667-13696.

Martinez, F., Hey, R.N., Johnson, P.D., 1997. The east ridge system 28.5°32”S East Pacific Rise: implication for overlapping spreading center development. *Earth and Planetary Science Letters*, 151, 13–31.

Massin, F., Farrell, J., Smith, R. B., 2013. Repeating earthquakes in the Yellowstone volcanic field: Implications for rupture dynamics, ground deformation, and migration in earthquake swarms. *Journal of Volcanology and Geothermal Research*, 257, 159-173.

Mastin, L.G., Pollard, D.D., 1988. Surface deformation and shallowdike intrusion processes at Inyo Craters, Long Valley, California. *J. Geophys. Res.* 93, 13221–13235.

Matthews, V., Anderson, C.E., 1973. Yellowstone convection plume and the break-up of the western United States. *Nature* 243, 158–159.

Mattsson H.B., Höskuldsson Á., 2011. Contemporaneous phreatomagmatic and effusive activity along the Hverfjall eruptive fissure, north Iceland: eruption chronology and resulting deposits. *J. Volcanol. Geotherm. Res.*, 201, 241–252, doi: 10.1016/j.jvolgeores.2010.05.015

Mavroulis, S., Andreadakis, E., Spyrou, N. I., Antoniou, V., Skourtsos, E., Papadimitriou, P., Kassaras, I., Kaviris, G., Tselentis, G.A., Voulgaris, N., Carydis, P., Lekkas, E., 2019. UAV and GIS based rapid earthquake-induced building damage assessment and methodology for EMS-98 isoseismal map drawing: The June 12, 2017 Mw 6.3 Lesvos (Northeastern Aegean, Greece) earthquake. *Int. J. Disaster Risk Reduct.*, 37, 101169.

Menke, W., Levin, V., 1994. Cold crust in a hot spot. *Geophysical Research Letters*, 21(18), 1967-1970.

Metzger, S., Jónsson, S., Geirsson, H., 2011. Locking depth and slip-rate of the Húsavík Flatey fault, North Iceland, derived from continuous GPS data 2006-2010. *Geophys. J. Int.* 187 (2), 564–576.

Metzger, S., Jónsson, S., Danielsen, G., Hreinsdóttir, S., Jouanne, F., Giardini, D., Villemin, T., 2013. Present kinematics of the Tjörnes Fracture Zone, North Iceland, from campaign and continuous GPS measurements. *Geophysical Journal International*, 192(2), 441-455.

Metzger, S., Jónsson, S., 2014. Plate boundary deformation in North Iceland during 1992–2009 revealed by InSAR time-series analysis and GPS. *Tectonophysics* 634,127–138.

Michael, A.J., 1987. Use of focal mechanisms to determine stress: a control study. *J. Geophys. Res.* 92 (B1), 357–368.

Mithen, D.P., 1982. Stress amplification in the upper crust and the development of normal faulting. *Tectonophysics* 83, 121-130.

Morgan, L. A., Shanks, W. C. P., Lowenstern, J. B., Farrell, J. M., Robinson, J. E., 2017. Geologic field-trip guide to the volcanic and hydrothermal landscape of the Yellowstone Plateau: U. S. Geological Survey Scientific Investigations Report 2017-5022-P, 100 p.

Morgan, W.J., 1971. Convection plumes in the lower mantle. *Nature* 230, 42–43.

Morgan, W.J., 1972. Plate motions and deep mantle convection. *Geol. Soc. Am. Memoir* 132, 7–22.

Morgan, L.A., Doherty, D.J., Leeman, W.P., 1984. Ignimbrites of the eastern Snake River Plain: Evidence for major caldera-forming eruptions. *J. Geophys. Res.* 89 (B10), 8665–8678.

Morgan, J.P., Morgan, W.J., Price, E., 1995. Hotspot melting generates both hotspot volcanism and a hotspot swell? *J. Geophys. Res.* 100, 8045–8062.

Müller, D., Walter, T.R., Schöpa A., Witt T., Steinke B., Gudmundsson, M.T., Dürig, T., 2017. High-resolution digital elevation modeling from TLS and UAV campaign reveals structural complexity at the 2014/2015 Holuhraun eruption site, Iceland. *Front. Earth Sci.*, 5-59.

Nagorsen-Rinke, S., Lee, J., Calvert, A., 2013. Pliocene sinistral slip across the Adobe Hills, eastern California–western Nevada: Kinematics of fault slip transfer across the Mina deflection. *Geosphere*, 9(1), 37-53.

Nanfity, A. F., 2011. Rift-parallel strike-slip faulting in Iceland: Kinematic analysis of the Gljúfurá Fault Zone (MS thesis, 61 p.). Syracuse, NY:Syracuse University.

Okada, Y., 1992. Internal deformation due to shear and tensile faults in a half-space. *Bulletin of the seismological society of America*, 82(2), 1018-1040.

Opheim, J.A., Gudmundsson, A., 1989. Formation and geometry of fractures, and related volcanism, of the Krafla fissure swarm, northeast Iceland. *Geological Society of America Bulletin*, 101 (12), 1608-1622.

Pálmason, G., Arnórsson, S., Fridleifsson, I.B., Kristmannsdóttir, H., Saemundsson, K., Stefánsson, V., Steingrímsson, B., Tómasson, J., Kristjánsson, L., 1979. The Iceland crust: Evidence from drillhole data on structure and processes. Deep drilling results in the Atlantic Ocean: Ocean crust, 2, pp.43-65.

Pang, G., Koper, K. D., Hale, J. M., Burlacu, R., Farrell, J., Smith, R. B., 2019. The 2017–2018 Maple Creek Earthquake Sequence in Yellowstone National Park, USA. *Geophysical Research Letters*, 46(9), 4653-4663.

Paquet, F., Dauteuil, O., Hallot, E., Moreau, F., 2007. Tectonics and magma dynamics coupling in a dyke swarm of Iceland. *J. Struct. Geol.* 29 (9), 1477–1493.

Pasquarè Mariotto, F., Bonali, F. L., Tibaldi, A., Rust, D., Oppizzi, P., Cavallo, A., 2015. Holocene displacement field at an emerged oceanic transform-ridge junction: the Husavik-Flatey fault Gudfinnugja fault system, North Iceland. *Journal of Structural Geology*, 75, 118-134.

Pelton, J. R., Smith, R. B., 1979. Recent crustal uplift in Yellowstone National Park. *Science*, 206(4423), 1179-1182.

Perkins, M.E., Nash, B.P., 2002. Explosive silicic volcanism of the Yellowstone hotspot: the ash fall tuff record. *Geol. Soc. Am. Bull.* 114 (3), 367–381.

Petit, J.P., 1987. Criteria for the sense of movement on fault surfaces in brittle rocks, *Journal of Structural Geology*, 9, 597-608.

Pierce, K. L., 1973. Surficial geologic map of the Mammoth quadrangle and part of the Gardiner quadrangle, Yellowstone National Park, Wyoming and Montana: U.S. Geological Survey Miscellaneous Geologic Investigations Map I-64I, scale 1:62,500.

Pierce, K.L., Morgan, L.A., 1990. The track of the Yellowstone hotspot: Volcanism, faulting, and uplift. U.S. Geol. Surv. Open-File Report 90-415. Geol. Surv, Denver, CO. 49 pp.

Pierce, K.L., Morgan, L.A., 1992. The track of the Yellowstone hot spot: Volcanism, faulting, and uplift. In: Link, P.K., Kuntz, M.A., Platt, L.B. (Eds.), *Regional Geology of Eastern Idaho and Western Wyoming: Geological Society of America Memoir 179*. Geological Society of America, Boulder, CO, pp. 1–53.

Pitt, A. M., Weaver, C.S., Spence, W., 1979. The Yellowstone Park earthquake of June 30, 1975, *Bull. Seismol. Soc. Am.*, 69(1), 187–205.

Pollard, D.D., Holzhausen, G., 1979. On the mechanical interaction between a fluid-filled fracture and the Earth's surface. *Tectonophysics* 53, 27–57.

Pollard, D.D., Delaney, P.T., Duffield, W.A., Endo, E.T., Okamura, A.T., 1983. Surface deformation in volcanic rift zones. *Tectonophysics* 94 (1–4), 541–584.

Proett, J. A., 2015. Enigmatic rift-parallel, strike-slip faults around Eyjafjörður, Northern Iceland, (M.S. thesis, 50 pp), Syracuse Univ., Syracuse, NY.

Puskas, C.M., Smith, R.B., Meertens, C.M., Chang, W.L., 2007. Crustal deformation of the Yellowstone Snake River Plain volcano-tectonic system: Campaign and continuous GPS observations, 1987-2004, *J. Geophys. Res.*, 112.

Puskas, C. M., Smith, R. B., 2009. Intraplate deformation and microplate tectonics of the Yellowstone hot spot and surrounding western US interior. *Journal of Geophysical Research: Solid Earth*, 114(B4).

Rea, D.K., 1978. Asymmetric sea-floor spreading and a non-transform axis offset: the East Pacific Rise 20° survey area. *Geological Society of America Bulletin*, 90, 836–844.

Reasenber, P., 1985. Second-order moment of central California seismicity, 1969–1982. *Journal of Geophysical Research: Solid Earth*, 90(B7), 5479-5495.

Rivera, L., Cisternas, A., 1990. Stress tensor and fault plane solutions for a population of earthquakes. *Bull. Seismol. Soc. Am.* 80 (3), 600–614.

Robinson, R., McGinty, P.J., 2000. The enigma of the Arthur's Pass, New Zealand, earthquake: 2. The aftershock distribution and its relation to regional and induced stress fields. *J. Geophys. Res.* 105 (B7), 16139–16150.

Rubin, A.M., 1992. Dike-induced faulting and graben subsidence in volcanic rift zones. *J. Geophys. Res.* 97 (B2), 1839–1858. <https://doi.org/10.1029/91JB02170>.

Rubin, A.M., Gillard, D., 1998. Dike-induced earthquakes: Theoretical considerations. *Journal of Geophysical Research: Solid Earth* 103 (B5), 10017–10030

Ruch, J., Wang, T., Xu, W., Hensch, M., Jónsson, S., 2016. Oblique rift opening revealed by reoccurring magma injection in central Iceland. *Nat. Commun.* 7, 12352.

Runnals, K. T., 2015. Multiple generations of faulting: A kinematic analysis of the Lagarfljót Region, northeast Iceland, (M.S. thesis, 72 pp), Syracuse Univ., Syracuse, NY.

Russo, E., Waite, G. P., Tibaldi, A., 2017. Evaluation of the evolving stress field of the Yellowstone volcanic plateau, 1988 to 2010, from earthquake first-motion inversions. *Tectonophysics*, 700, 80-91.

Russo, E., Tibaldi, A., Waite, G. P., Bonali, F. L., Massin, F., Farrell, J., 2020. Unraveling the complex deformation pattern at Yellowstone plateau through seismicity and fracture analysis. *Tectonophysics*, 778, 228352.

Saemundsson, K., 1974. Evolution of the axial rifting zone in northern Iceland and the Tjörnes fracture zone. *Geol Soc Am Bull* 85(4):495-504

Sæmundsson, K., 1978. Fissure swarms and central volcanoes of the neovolcanic zones of Iceland. *Geological Journal*, 10, 415–432.

- Sæmundsson, K., 1979. Outline of the geology of Iceland. *Jökull*, 29, 7–28.
- Sæmundsson, K., 1991. Jarðfræði Kröflukerfisins. In: Garðarsson A., Einarsson Á. (Eds), *Náttúra Mývatns*, Icelandic Nature Sci. Soc., Reykjavík, 24–95 (in Icelandic).
- Sæmundsson, K., Hjartarson, A., Kaldal, I., 2012. Geological map of the Northern Volcanic Zone, Iceland. Northern Part 1: 100.000. Reykjavik: Iceland GeoSurvey and Landsvirkjun.
- Savage, J.C., Cockerham, R.S., 1984. Earthquake swarm in Long Valley caldera, California, January 1983: evidence for dike inflation. *Journal of Geophysical Research: Solid Earth* 89 (B10), 8315–8324.
- Savage, J. C., Lisowski, M., Prescott, W. H., Pitt, A. M., 1993. Deformation from 1973 to 1987 in the epicentral area of the 1959 Hebgen Lake, Montana, earthquake ($M_s = 7.5$). *Journal of Geophysical Research*, 98, 2145–2153.
- Schouten, H., Klitgord, K. D., Gallo, D. G., 1993. Edge-driven microplate kinematics. *Journal of Geophysical Research*, 98(B4), 6689–6701.
- Shelly, D. R., Hill, D. P., Massin, F., Farrell, J., Smith, R. B., Taira, T. A., 2013. A fluid-driven earthquake swarm on the margin of the Yellowstone caldera. *Journal of Geophysical Research: Solid Earth*, 118(9), 4872-4886.
- Shelly, D.R., Ellsworth, W.L., Hill, D.P., 2016. Fluid-faulting evolution in high definition: Connecting fault structure and frequency-magnitude variations during the 2014 Long Valley Caldera, California, earthquake swarm. *Journal of Geophysical Research: Solid Earth* 121 (3), 1776–1795.
- Sigmundsson, F., Hooper, A., Hreinsdóttir, S., Vogfjörð, K.S., Ófeigsson, B.G., Heimisson, E.R., et al., 2015. Segmented lateral dyke growth in a rifting event at Bárðarbunga volcanic system, Iceland. *Nature* 517, 191–195.

Sleep, N.H., 1990. Hotspots and mantle plumes: some phenomenology. *J. Geophys. Res.* 95 (B5), 6715–6736.

Sleep, N.H., 1992. Hotspot volcanism and mantle plumes. *Annu. Rev. Earth Planet. Sci.* 20, 19–43.

Smith, M.W., Carrivick, J.L., Quincey, D.J., 2016. Structure from motion photogrammetry in physical geography. *Prog. Phys. Geogr.*, 40, 247–275.

Smith, R. L., 1968. Resurgent cauldrons. *Mem. Geol. Soc. Amer.*, 116, 613-662.

Smith, R.B., Sbar, M., 1974. Contemporary tectonics and seismicity of the Western United States with emphasis on the Intermountain Seismic Belt. *Geol. Soc. Am. Bull.* 85, 1205–1218.

Smith, R.B., 1977. Intraplate tectonics of the Western North American Plate. *Tectonophysics* 37, 323–336.

Smith, R.B., Braile, L.W., 1984. Crustal structure and evolution of an explosive silicic volcanic system at Yellowstone National Park. *Studies In Geophysics: Explosive Volcanism: Inception, Evolution, and Hazards*. National Academy Press, Washington, D.C, pp. 96–109.

Smith, R.B., Braile, L.W., 1994. The Yellowstone hotspot. *J. Volcanol. Geotherm. Res.* 61, 121–187.

Smith, R.B., Siegel, L., 2000. *Windows into the Earth's interior; The geologic story of Yellowstone and Grand Teton National Parks*. Oxford University Press. ISBN-13:9780195105971, 256 pp.

Smith, R. B., Jordan, M., Steinberger, B., Puskas, C. M., Farrell, J., Waite, G.P., Husen, S., Chang, W., O'Connell, R., 2009. Geodynamics of the Yellowstone hotspot and mantle plume: Seismic and GPS imaging, kinematics, and mantle flow, *J. Volcanol. Geotherm. Res.*, 188, 26–56.

Stal, C., Bourgeois, J., De Maeyer, P., De Mulder, G., De Wulf, A., Goossens, R., Hendrickx, M., Nuttens, T., Stichelbaut, B., 2012. Test case on the quality analysis of structure from motion in

airborne applications. In: 32nd EARSeL Symposium: Advances in Geosciences. European Association of Remote Sensing Laboratories (EARSeL).

Stefánsson, R., Böðvarsson, R., Slunga, R., Einarsson, P., Jakobsdóttir, S., Bungum, H., Gregersen, S., Havskov, J., Hjelme, J., Korhonen, H., 1993. Earthquake prediction research in the South Iceland Seismic Zone and the SIL project. *Bulletin of the Seismological Society of America*, 83(3), pp.696-716.

Stefansson, R., Gudmundsson, G. B., Halldorsson, P., 2008. Tjörnes fracture zone. New and old seismic evidences for the link between the North Iceland rift zone and the Mid-Atlantic ridge. *Tectonophysics* 447, 117–126.

Stovall, W. K., Cervelli, P. F., Shelly, D. R., 2014. Investigating Rapid Uplift and Subsidence Near Norris, Yellowstone, During 2013-2014. In AGU Fall Meeting Abstracts.

Taira, T., Smith, R. B., Chang, W. L., 2010. Seismic evidence for dilatational source deformations accompanying the 2004–2008 Yellowstone accelerated uplift episode. *Journal of Geophysical Research: Solid Earth*, 115(B2).

Takasu, T., 2009. RTKLIB: Open Source Program Package for RTK-GPS, FOSS4G 2009 Tokyo, Japan.

Tarantola, A., Valette, B., 1982. Inverse problems=quest for information, *J. Geophys. Res.*, 50, 159-170.

Tentler, T., Mazzoli, S., 2005. Architecture of normal faults in the rift zone of central north Iceland. *J. Struct. Geol.* 27 (9), 1721–1739.

Thoroddsen, T., 1925. Die Geschichte der isländischen Vulkane. D. Kgl. Danske Vidensk. Selsk. Skrifter. Naturvidensk. og Mathem. Afd. 8 (9), 1–458.

Tibaldi, A., 2015. Structure of volcano plumbing systems: a review of multi-parametric effects, *J Volcanol Geotherm Res*, 298, 85-135.

Tibaldi, A., Pasquaré Mariotto, F. A., Papanikolaou, D., Nomikou, P, 2008. Tectonics of Nisyros Island, Greece, by field and offshore data, and analogue modelling. *J. Struct. Geol.* , 30 , 1489-1506.

Tibaldi, A., Bonali, F.L., Pasquaré Mariotto, F., 2016a. Interaction between transform faults and rift systems: a combined field and experimental approach. *Frontiers Earth Sci* 4:33

Tibaldi, A., Bonali, F.L., Einarsson, P., Hjartardóttir, Á.R., Pasquaré Mariotto, F., 2016b. Partitioning of Holocene kinematics and interaction between the Theistareykir Fissure Swarm and the Husavik-Flatey Fault, North Iceland. *Journal of Structural Geology*, 83, 134-155.

Tibaldi, A., Bonali, F.L., 2018. Contemporary recent extension and compression in the central Andes. *J. Struct. Geol.* 107, 73–92.

Tibaldi, A., Bonali, F.L., 2018. A model to explain joint patterns found in ignimbrite deposits. *Bull. Volcanol.* 80 (3), 26.

Tibaldi, A., Bonali, F. L., Mariotto, F. P., Russo, E., Tenti, L. R., 2019. The development of divergent margins: Insights from the North Volcanic Zone, Iceland. *Earth and Planetary Science Letters*, 509, 1-8.

Tibaldi, A., Bonali, F. L., Russo, E., Fallati, L., 2020a. Surface deformation and strike-slip faulting controlled by dyking and host rock lithology: A compendium from the Krafla Rift, Iceland. *Journal of Volcanology and Geothermal Research*, 106835.

Tibaldi, A., Bonali, F. L., Pasquaré Mariotto, F., Corti, N., Russo, E., Einarsson, P., Hjartardóttir, Á. R., 2020b. Rifting Kinematics Produced by Magmatic and Tectonic Stresses in the North Volcanic Zone of Iceland. *Frontiers in Earth Science*, 8, 174.

Tizzani, P., Battaglia, M., Castaldo, R., Pepe, A., Zeni, G., Lanari, R., 2015. Magma and fluid migration at Yellowstone Caldera in the last three decades inferred from InSAR, leveling, and gravity measurements. *Journal of Geophysical Research: Solid Earth*, 120(4), 2627-2647.

Toda, S., Stein, R.S., Richards-Dinger, K., Bozkurt, S., 2005. Forecasting the evolution of seismicity in southern California: Animations built on earthquake stress transfer. *Journal of Geophysical Research: Solid Earth* 110, B05S16-17.

Toda, S., Stein, R.S., Sevilgen, V., Lin, J., 2011. Coulomb 3.3 Graphic-rich deformation and stress-change software for earthquake, tectonic, and volcano research and teaching—user guide. US Geological Survey open-file report, 1060, p.63.

Tonkin, T., Midgley, N., 2016. Ground-control networks for image based surface reconstruction: an investigation of optimum survey designs using UAV derived imagery and structure-from-motion photogrammetry. *Rem. Sens.* 8 (9), 786.

Tryggvason, E., 1973. Seismicity, earthquake swarms, and plate boundaries in the Iceland region. *Bull. Seismol. Soc. Am.* 63 (4), 1327–1348.

Tryggvason, E., 1978. Tilt observations in the Krafla-Mivatn area 1976-1977. Nordic Volcanological Institute, Report 78-02, 45 pp.

Tryggvason, E., 1984. Widening of the Krafla fissure swarm during the 1975–1981 volcano- tectonic episode. *Bull. Volcanol.* 47 (1), 47–69.

Tryggvason, E., 1994. Surface deformation at the Krafla volcano, north Iceland, 1982–1992. *Bull. Volcanol.* 56 (2), 98–107.

Turner, D., Lucieer, A., Watson, C., 2012. An automated technique for generating georectified mosaics from ultra-high resolution unmanned aerial vehicle (UAV) imagery, based on structure from motion (SfM) Point clouds. *Rem. Sens.* 4, 1392–1410.

Vavryčuk, V., 2014. Iterative joint inversion for stress and fault orientations from focal mechanisms. *Geophysical Journal International*, 199(1), 69-77.

Waite, G. P., Smith, R. B., 2002. Seismic evidence for fluid migration accompanying subsidence of the Yellowstone caldera. *Journal of Geophysical Research: Solid Earth*, 107(B9).

Waite, G. P., Smith, R. B., 2004. Seismotectonics and stress field of the Yellowstone volcanic plateau from earthquake first-motions and other indicators. *Journal of Geophysical Research: Solid Earth*, 109(B2).

Waldrop, H. A., 1969. Late Quaternary faulting near Mirror Lake Yellowstone National Park, in *Abstracts for 1968: Geological Society of America Special Paper 121*, p. 643-644.

Walker, G.P.L., 1965. Evidence of crustal drift from Icelandic geology. *Phil. Trans. Roy. Soc. Lond.* 258 (1088), 199–204.

Ward, P. L., 1971. New interpretation of the geology of Iceland. *Geological Society of America Bulletin*, 82(11), 2991-3012.

Werner, C., Hurwitz, S., Evans, W.C., Lowenstern, J.B., Bergfeld, D., Heasler, H., Jaworowski, C., Hunt, A., 2008. Volatile emissions and gas geochemistry of Hot Springs Basin, Yellowstone National Park, USA, *J. Volcanol. Geotherm. Res.*, 178, 751–762.

Westoby, M.J., Brasington, J., Glasser, N.F., Hambrey, M.J., Reynolds, J.M., 2012. “Structure-from-Motion” photogrammetry: a low-cost, effective tool for geoscience applications. *Geomorphology* 179, 300–314.

White, D. E., Hutchinson, R. A., Keith, T. E. C., 1988. The geology and remarkable thermal activity of Norris Geyser Basin, Yellowstone National Park, Wyoming. U. S. Geological Survey Professional Paper 1456, 84p, <https://pubs.usgs.gov/pp/1456>.

White, R. S., McKenzie, D. P., 1989. Volcanism at rifts. *Scientific American*, 261(1), 62-71.

Wicks Jr., C., Thatcher, W., Dzurisin, D., 1998. Migration of fluids beneath Yellowstone caldera inferred from Satellite radar interferometry, *Science*, 282, 458-462.

Wicks, C., Thatcher, W., Dzurisin, D., 2006. Uplift, thermal unrest and magma intrusion at Yellowstone Caldera, *Nature*, 440, 72-75.

Wicks, C. W., Dzurisin, D., Lowenstern, J. B., Svarc, J., 2020. Magma intrusion and volatile ascent beneath Norris Geyser Basin, Yellowstone National Park. *Journal of Geophysical Research: Solid Earth*, 125, e2019JB018208.

Wright, T.J., Sigmundsson, F., Ayele, A., Belachew, M., Brandsdottir, B., Keir, D., Pedersen, R., Ayele, A., Ebinger, C., Einarsson, P., Lewi, E., Calais, E., 2012. Geophysical constraints on the dynamics of spreading centres from rifting episodes on land. *Nat. Geosci.* 5, 242–250.

Yang, W., Hauksson, E., Shearer, P. M., 2012. Computing a large refined catalog of focal mechanisms for southern California (1981–2010): Temporal stability of the style of faulting. *Bulletin of the Seismological Society of America*, 102(3), 1179-1194.

Zaliapin, I., Ben-Zion, Y., 2013. Earthquake clusters in southern California I: Identification and stability. *Journal of Geophysical Research: Solid Earth*, 118(6), 2847-2864.

Zhuang, J., Ogata, Y., Vere-Jones, D., 2002. Stochastic declustering of space-time earthquake occurrences. *Journal of the American Statistical Association*, 97(458), 369-380.

Ziegler, M., Rajabi, M., Heidbach, O., Hersir, G.P., Ágústsson, K., Árnadóttir, S., Zang, A., 2016. The stress pattern of Iceland. *Tectonophysics* 674, 101–113.

Zoback, M.L., Thompson, G.A., 1978. Basin and Range rifting in northern Nevada: Clues from a mid-Miocene rift and its subsequent offsets. *Geology* 6, 111–116.

Zoback, M.L., 1992. First and second-order patterns of stress in the lithosphere: The World Stress Map Project, *J. Geophys. Res.*, 97(B8), 11,703-11,728.